

The University of Sheffield
Department of Physics & Astronomy



The
University
Of
Sheffield.

Characterizing and Controlling the Morphology of Non-Fullerene Acceptor Based Organic Photovoltaics

A thesis submitted in partial fulfilment of the requirements for
the degree of Doctor of Philosophy

June 2022

Emma Louise Kaltenthaler Spooner



EPSRC CENTRE FOR DOCTORAL TRAINING
NEW AND SUSTAINABLE
PHOTOVOLTAICS

“Science is made up of mistakes, but they are mistakes
which it is useful to make, because they lead little by
little to the truth”

Jules Verne

Acknowledgements

Firstly, I would like to thank my supervisor, David Lidzey, for his advice, pragmatism, calm, & humour. Thank you for letting me keep organic PV alive in EPMM. Thank you also to Jenny Clark for always listening no matter how busy she was & for keeping me sane in the final years of my PhD. Thank you to the Centre for Doctoral Training in New and Sustainable Photovoltaics (CDT-PV), the University of Sheffield, and the Engineering and Physical Sciences Research Council (EPSRC) for funding my research. It has been wonderful and exciting time in my life. A big thank you to Ossila for your support, and for the opportunities to share my enthusiasm for science with the world.

Thank you to all EPMM members past and present, for all of the fun in the lab, the Uni Arms snooker room, and Akbars. A big thanks to the senior members who always had time to help me and offer advice- Mike, James, Tom, Claire, Joel & Onkar. A special thanks to Claire for paving the way for myself and all of the other women in EPMM. Thank you to those of you who have taken this journey alongside me- Rachel, Kezia, Tarek, Mary, Kirsty, Tim & Peter. A special thanks to Rachel for her hard work on our many projects together, scattering wisdom, and for keeping the OPV faith. Thank you to Matt, for keeping everything running smoothly, for rescuing me in many crises, and for being generally hilarious. Thank you also to my CDT-PV cohort, C4- David, Leo, Laurie, Lewis, Tomi, Alan, Kilian, Liam & Sam- for welcoming me so wholeheartedly and for some amazing times up and down the country.

Thank you to my friends- Helen, Lizzie, Abby, Bettina, Anne, Fran, Kat & Sarah- for letting me complain about my thesis continually, for putting up with my haphazard communication skills, and for always making me happy.

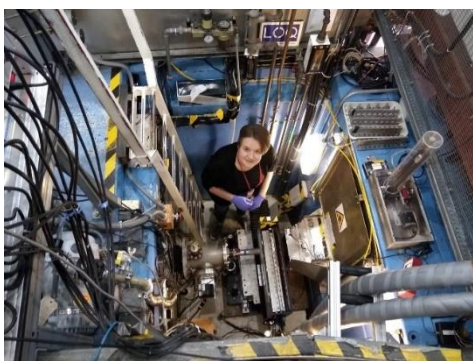
Thank you to my family for their unconditional support. Mum & Dad, thank you for your wisdom, patience, and kindness- you will always be my heroes & my guiding lights. Thank you for showing me how to be a good person, and how great science is, and for letting me be myself. Joanna & Katie, you have always been there to lift me up, inspire me, and put a smile on my face in hard times. Thank you also for bringing the great joys of Jacob, Helena & Jemi into my life. I especially appreciate the time you have spent reading and correcting my horribly long sentences and comma misuse. Gareth, Musonda & Reece, for your kindness, and for being the best additions to the family I could have asked for. Abs, you will always be my partner in crime & sharing platters. Thank you for helping me navigate life, for your patience & love, and for reading and correcting the worst chapter of all, usually long after I had gone to sleep. Love you long time.

Last of all, thank you to Elena. I could fill a thesis with things I have to thank you for, and another with reasons why I love you, and they would both be longer than this one. You are a constant source of inspiration, strength, and joy, and I would be lost without you. Thank you for believing in me and remaining steady when I could do neither. In this world, we're just beginning.

Abstract

Organic photovoltaics (OPVs) are a promising solar cell technology that have shown a slow but steady increase in performance since their initial development. OPVs hold potential for solar energy that is cheap, lightweight, and flexible- perfectly suited for the ever-growing global need for versatile energy sources. They also hold unique advantages, such as excellent infrared absorption, a band gap that can be tuned, and toxic-chemical free processing. As efficiencies approach those required for large-scale commercialisation, the need for OPV systems that are also scalable and stable is increasingly vital. This thesis aims to tackle these issues by characterizing and controlling the morphology of efficient non-fullerene acceptor (NFA) based OPVs in a range of contexts. By learning more about how these systems behave, they can be tuned to achieve the ideal trinity of efficiency, scalability, and stability.

In **Chapter 4**, a high performance NFA is adapted for fabrication using low-waste ultrasonic spray coating. Here an air-knife was used to tune the morphology and control the drying of the final film. This process achieved efficiencies of 14%, which is state-of-the-art for spray coated OPVs. In **Chapter 5**, the focus was shifted to device processing using a common solvent additive. Here a NFA system was found to show inferior performance and stability compared to that of a fullerene acceptor, when a solvent additive was used. This indicated processing routes for fullerene and NFA based systems need to be tuned to suit the properties of the acceptor. In **Chapter 6** the intrinsic stability of devices based on a range of NFAs were characterised, and it was found that both miscibility and crystallization temperature play a role in determining stability. Chemically related acceptors were found to have different stabilities in a blend, suggesting each OPV system must be characterised in turn to ensure optimal stability.



Front Matter

This thesis is a summary of work undertaken in the Department of Physics and Astronomy at the University of Sheffield from October 2017 to June 2022, under the supervision of Professor David Lidzey.

I, the author, confirm that the Thesis is my own work. I am aware of the University's Guidance on the Use of Unfair Means. This work has not been previously presented for an award at this, or any other, university.

All work contained within is my own, unless explicitly stated in the 'author contributions' section of each chapter. This work is within the 80,000 word limit and includes an abstract within the 300 word limit.

References are specific to each chapter, with figures, equations, and page numbers continued throughout the entire thesis. Supplementary information for each chapter is presented straight after the main text.

A list of abbreviations of chemical compounds can be found on the following page, with all other abbreviations defined within their appropriate chapter.

Abbreviations

2FIC: 2-(5,6-difluoro-3-oxo-2,3-dihydro-1H-inden-1-ylidene)malononitrile

BDT: Benzodithiophene

BT: Benzothiadiazole

BT-CIC: 4,4,10,10-tetrakis(4-hexylphenyl)-5,11-(2-ethylhexyloxy)-4,10-dihydrodithienyl[1,2-b:4,5b']benzodithiophene-2,8-diyl)bis(2-(3-oxo-2,3-dihydroinden-5,6-dichloro-1-ylidene)malononitrile)

BTP-4F (Y6): 2,2'-((2Z,2'Z)-((12,13-bis(2-ethylhexyl)-3,9-diundecyl-12,13-dihydro-[1,2,5]thiadiazolo[3,4-e]thieno[2'',3'':4',5']thieno[2',3':4,5]pyrrolo[3,2-g]thieno[2',3':4,5]thieno[3,2-b]indole-2,10-diyl)bis(methanylylidene))bis(5,6-difluoro-3-oxo-2,3-dihydro-1H-indene-2,1-diylidene))dimalononitrile

BTP-4F-12: 2,2'-((2Z,2'Z)-((12,13-bis(2-butyloctyl)-3,9-diundecyl-12,13-dihydro-[1,2,5]thiadiazolo[3,4-e]thieno[2'',3'':4',5']thieno[2',3':4,5]pyrrolo[3,2-g]thieno[2',3':4,5]thieno[3,2-b]indole-2,10-diyl)bis(methanylylidene))bis(5,6-difluoro-3-oxo-2,3-dihydro-1H-indene-2,1-diylidene))dimalononitrile

BTP-BO-4Cl: 2,2'-((2Z,2'Z)-((12,13-bis(2-butyloctyl)-3,9-diundecyl-12,13-dihydro-[1,2,5]thiadiazolo[3,4-e]thieno[2'',3'':4',5']thieno[2',3':4,5]pyrrolo[3,2-g]thieno[2',3':4,5]thieno[3,2-b]indole-2,10-diyl)bis(methanylylidene))bis(5,6-dichloro-3-oxo-2,3-dihydro-1H-indene-2,1-diylidene))dimalononitrile

BTP-eC9: 2,2'-[[12,13-Bis(2-butyloctyl)-12,13-dihydro-3,9-dinonylbisthieno[2'',3'':4',5']thieno[2',3':4,5]pyrrolo[3,2-e:2',3'-g][2,1,3]benzothiadiazole-2,10-diyl]bis[methylidyne(5,6-chloro-3-oxo-1H-indene-2,1(3H)-diylidene)]]bis[propanedinitrile]

DTQx: Dithieno[3,2-f:2'', 3''-h]quinoxaline

DTY6: 2,2'-((2Z,2'Z)-((12,13-bis(2-decylteradecyl)-3,9-diundecyl-12,13-dihydro-[1,2,5]thiadiazolo[3,4-e]thieno[2'',3'':4',5']thieno[2',3':4,5]pyrrolo[3,2-g]thieno[2',3':4,5]thieno[3,2-b]indole-2,10-diyl)bis(methanylylidene))bis(5,6-difluoro-3-oxo-2,3-dihydro-1H-indene-2,1-diylidene))dimalononitrile

eC9-2Cl: 2,2'-[[12,13-Bis(2-butyloctyl)-12,13-dihydro-3,9-dinonylbisthieno[2'',3'':4',5']thieno[2',3':4,5]pyrrolo[3,2-e:2',3'-g][2,1,3]benzothiadiazole-2,10-diyl]bis[methylidyne(2 or 3-chloro-3-oxo-1H-indene-2,1(3H)-diylidene)]]bis[propanedinitrile]

EH-IDTBR: 5,5'-[[4,4,9,9-tetrakis(2-ethylhexyl)-4,9-dihydro-s-indaceno[1,2-b:5,6-b']dithiophene-2,7-diyl]bis(2,1,3-benzothiadiazole-7,4-diylmethylidyne)]bis[3-ethyl-2-thioxo-4-thiazolidinone]

GS-ISO: No name given, see publication referenced at first mention for structure

IC-SAM: 4-((1,3-dioxo-1,3-dihydro-2H-inden-2-ylidene)methyl)benzoic acid

IDT: Indacenodithiophene

IDTT: Indacenodithienothiophene

INCN: 2-(2,3-dihydro-3-oxo-1H-inden-1-ylidene)propanedinitrile

ITIC: 3,9-bis(2-methylene-(3-(1,1-dicyanomethylene)-indanone))-5,5,11,11-tetrakis(4-hexylphenyl)-dithieno[2,3-d:2',3'-d']-s-indaceno[1,2-b:5,6-b']dithiophene

ITIC-2F: 2,2'-[[6,6,12,12-Tetrakis(4-hexylphenyl)-6,12-dihydrodithieno[2,3-d:2',3'-d']-s-indaceno[1,2-b:5,6-b']dithiophene-2,8-diyl]bis[methylidyne(5,6-difluoro-3-oxo-1H-indene-2,1(3H)-diylidene)]]bis[propanedinitrile]

ITIC-M: 3,9-bis(2-methylene-((3-(1,1-dicyanomethylene)-6/7-methyl)-indanone))-5,5,11,11-tetrakis(4-hexylphenyl)-dithieno[2,3-d:2',3'-d']-s-indaceno[1,2-b:5,6-b']dithiophene

O-IDTBR: (5Z,5'Z)-5,5'-((7,7'-(4,4,9,9-tetraoctyl-4,9-dihydro-s-indaceno[1,2-b:5,6-b']dithiophene-2,7-diyl)bis(benzo[c][1,2,5]thiadiazole-7,4-diyl))bis(methanylylidene))bis(3-ethyl-2-thioxothiazolidin-4-one)

P3HT: Poly(3-hexylthiophene-2,5-diyl)

PBDB-T: Poly[(2,6-(4,8-bis(5-(2-ethylhexyl)thiophen-2-yl)-benzo[1,2-b:4,5-b']dithiophene))-alt-(5,5-(1',3'-di-2-thienyl-5',7'-bis(2-ethylhexyl)benzo[1',2'-c:4',5'-c']dithiophene-4,8-dione)]

PBDB-TF: Poly[[4,8-bis[5-(2-ethylhexyl)-4-fluoro-2-thienyl]benzo- [1,2-b:4,5-b']dithiophene-2,6-diyl]-2,5-thiophenediyl- [5,7-bis(2-ethylhexyl)-4,8-dioxo-4H,8H-benzo[1,2-c:4,5-c']- dithiophene-1,3-diyl]-2,5-thiophenediyl]

PBDTTT-CF: Poly[1-(6-{4,8-bis[(2-ethylhexyl)oxy]-6-methylbenzo[1,2-b:4,5-b']dithiophen-2-yl})-3-fluoro-4-methylthieno[3,4-b]thiophen-2-yl)-1-octanone]

PBQx-TF: No name given, see publication referenced at first mention for structure

PC₆₀BM: [6,6]-Phenyl-C61-butyric acid methyl ester

PC₇₀BM: [6,6]-Phenyl-C71-butyric acid methyl ester

PCDTBT: Poly[[9-(1-octylonyl)-9H-carbazole-2,7-diyl]-2,5-thiophenediyl-2,1,3-benzothiadiazole-4,7-diyl-2,5-thiophenediyl], Poly[N-9'-heptadecanyl-2,7-carbazole-alt-5,5-(4',7'-di-2-thienyl-2',1',3'-benzothiadiazole)]

PDINN: N,N'-Bis{3-[3-(Dimethylamino)propylamino]propyl}perylene-3,4,9,10-tetracarboxylic diimide

PEDOT:PSS: Poly(3,4-ethylenedioxythiophene):polystyrene sulfonate

PEIE: Polyethylenimine ethoxylate

PffBT4T-2OD: Poly[(5,6-difluoro-2,1,3-benzothiadiazol-4,7-diyl)-alt-(3,3''-di(2-octyldodecyl)-2,2';5',2'';5'',2'''-quaterthiophen-5,5''''-diyl)]

PFN-Br: Poly(9,9-bis(3'-(N,N-dimethyl)-N-ethylammonium-propyl-2,7-fluorene)-alt-2,7-(9,9-dioctylfluorene))dibromide

PM6: Poly[(2,6-(4,8-bis(5-(2-ethylhexyl-3-fluoro)thiophen-2-yl)-benzo[1,2-b:4,5-b']dithiophene))-alt-(5,5-(1',3'-di-2-thienyl-5',7'-bis(2-ethylhexyl)benzo[1',2'-c:4',5'-c']dithiophene-4,8-dione)]

PNDIT-F3N: Poly[[2,7-bis(2-ethylhexyl)-1,2,3,6,7,8-hexahydro-1,3,6,8-tetraoxobenzo[lmn][3,8]phenanthroline-4,9-diyl]-2,5-thiophenediyl[9,9-bis[3-(dimethylamino)propyl]-9H-fluorene-2,7-diyl]-2,5-thiophenediyl]

PTB7: Poly[[4,8-bis[(2-ethylhexyl)oxy]benzo[1,2-b:4,5-b']dithiophene-2,6-diyl][3-fluoro-2-[(2-ethylhexyl)carbonyl]thieno[3,4-b]thiophenediyl]]

PTB7-Th: Poly([2,6-4,8-di(5-ethylhexylthienyl)benzo[1,2-b;3,3-b]dithiophene}{3-fluoro-2[(2-ethylhexyl)carbonyl]thieno[3,4-b]thiophenediyl})

PTQ10: Poly [[6,7-difluoro[(2-hexyldecyl)oxy]-5,8-quinoxalinediyl]-2,5-thiophenediyl]]

TT: Thieno[3,2-*b*]thiophene

Y6-BO: No name given, see publication referenced at first mention for structure

Publications

1. E. L. K. Spooner,* E. J. Cassella,* J. Smith, T. E. Catley, D. G. Lidzey, *Air-Knife Assisted Spray Coating of Organic Solar Cells*, **2022**, In preparation. Target Journal: Nat. Comm. Expected Submission: June 2022. (*Authors contributed equally. This work is described in **Chapter 4**).
2. M. O’Kane, J. A. Smith, R. C. Kilbride, E. L. K. Spooner, C. P. Duif, N. Mahmodi, T. E. Catley, A. L. Washington, S. M. King, S. R. Parnell, A. J. Parnell, *Exploring Nanoscale Structure in Perovskite Precursor Solutions Using Neutron and Light Scattering*, Chem. Mater, **2022**, Submitted.
3. K. Sasitharan, R. C. Kilbride, E. L. K. Spooner, J. Clark, A. Iraqi, D. G. Lidzey, J. A. Foster, *Metal-organic Framework Nanosheets as Templates to Enhance Performance in Semi-Crystalline Organic Photovoltaic Cells*, Adv. Sci., **2022**, Early Access, 2200366, DOI: 10.1002/advs.202200366.
4. E. J. Cassella, E. L. K. Spooner, T. Thornber, M. E. O’Kane, T. E. Catley, J. E. Bishop, J. A. Smith, O. S. Game, D. G. Lidzey, *Gas-Assisted Spray Coating of Perovskite Solar Cells Incorporating Sprayed Self-Assembled Monolayers*, Adv. Sci., **2022**, 9, 14, 2104848, DOI: 10.1002/advs.202104848.
5. J. A. Smith, O. S. Game, J. E. Bishop, E. L. K. Spooner, R. C. Kilbride, C. Greenland, R. Jayaprakash, T. I. Alanazi, E. J. Cassella, A. Tejada, G. Chistiakova, M. Wong-Stringer, T. J. Routledge, A. J. Parnell, D. B. Hammond, D.G. Lidzey, *Rapid Scalable Processing of Tin Oxide Transport Layer for Perovskite Solar Cells*, ACS Appl. Energy Mater., **2020**, 3, 6, 5552 - 5562.
6. W. Li, Z. Xiao, J. A. Smith, J. Cai, D. Li, R. C. Kilbride, E. L. K. Spooner, O. S. Game, X. Meng, D. Liu, R. A. L. Jones, D. G. Lidzey, L. Ding, T. Wang, *Enhancing the Efficiency of PTB7-Th:COi8DFIC-based Ternary Solar Cells With Versatile Third Components*, Appl. Phy. Rev., **2019**, 6, 041405.
7. M. Chen, Z. Zhang, W. Li, J. Cai, J. Yu, E. L. K. Spooner, R. C. Kilbride, D. Li, B. Du, R. S. Gurney, D. Liu, W. Tang, D. G. Lidzey, T. Wang, *Regulating the*

Morphology of Fluorinated Non-Fullerene Acceptor and Polymer Donor Via Binary Solvent Mixture for High Efficiency Polymer Solar Cells, Sci. China Chem, **2019**, *62*, 1221 – 1229.

8. W. Li, Z. Xiao, J. Cai, J. A. Smith, E. L. K. Spooner, R. C. Kilbride, O. S. Game, X. Meng, D. Li, H. Zhang, M. Chen, R. S. Gurney, D. Liu, R. A. L. Jones, D. G. Lidzey, L. Ding, T. Wang, *Correlating the Electron-Donating Core Structure With Morphology and Performance of Carbon-Oxygen-Bridged Ladder-Type Non-Fullerene Acceptor Based Organic Solar Cells*, Nano Energy, **2019**, *61*, 318 – 326.
9. M. Chen, D. Liu, W. Li, R. S. Gurney, D. Li, E. L. K. Spooner, R. C. Kilbride, J. D. McGettrick, T. M. Watson, Z. Li, R. A. L. Jones, D. G. Lidzey, T. Wang, *Influences of Non-Fullerene Acceptor Fluorination on Three-Dimensional Morphology and Photovoltaic Properties of Organic Solar Cells*, ACS Appl. Mater. Interfaces, **2019**, *11*, 26194 – 26203.
10. W. Li, M. Chen, J. Cai, E. L. K. Spooner, H. Zhang, R. S. Gurney, D. Liu, Z. Xiao, D. G. Lidzey, L. Ding, T. Wang, *Molecular Order Control of Non-Fullerene Acceptors for High-Efficiency Polymer Solar Cells*, Joule, **2019**, *3*, 819 – 833.

Presentations

Oral Presentations

- **Photovoltaics Science, Applications and Technology (PVSAT) 2021:** ‘The Impact of Solvent Additives on the Morphology and Stability of Fullerene and Non-Fullerene Acceptor Based Organic Solar Cells’ (*Virtual*)

Poster Presentations

- **Next Generation Materials for Solar Photovoltaics 2020:** ‘Stability of Non-Fullerene Acceptors in Organic Solar Cells’ (*London, UK*)
- **Conference on Hybrid and Organic Photovoltaics (HOPV) 2021:** ‘The Impact of Solvent Additives on the Morphology and Stability of Fullerene and Non-Fullerene Acceptor Based Organic Solar Cells’ (*Virtual*)
- **Centre of Doctoral Training in New and Sustainable Photovoltaics Showcase 2021:** ‘Air-Knife Assisted Spray Coating of Organic Solar Cells’ (*Sheffield, UK*)
- **HOPV 2022:** ‘Air-Knife Assisted Spray Coating of Organic Solar Cells’ (*Valencia, Spain*)

Table of Contents

Chapter 1 Introduction.....	1
1.1 Thesis Aims	4
1.2 Thesis Overview	4
1.3 References.....	6
Chapter 2 Background Theory	7
2.1 The Basics of Photovoltaics	7
2.1.1 The Photovoltaic Effect	7
2.1.2 Inorganic Crystalline Semiconductors	7
2.1.3 Organic Semiconductors	8
2.1.4 The Shockley-Queisser limit.....	10
2.2 Organic Photovoltaic Physics	13
2.2.1 The Basics of an Organic Photovoltaic Cell	13
2.2.2 Exciton Formation in Organic Semiconductors	13
2.2.3 Exciton Transport in Organic Semiconductors	13
2.2.4 Exciton Dissociation in Organic Semiconductors.....	14
2.2.5 Charge Carrier Transport in Organic Semiconductors.....	15
2.2.6 Types of Recombination	16
2.3 The Bulk Heterojunction.....	16
2.3.1 The Introduction of the Bulk Heterojunction.....	16
2.3.2 Bulk Heterojunction Morphology	17
2.4 A Brief History of Organic Photovoltaics.....	21
2.5 Organic Photovoltaic Architecture.....	24
2.5.1 Basic OPV Structure and Energy Level Cascades	24
2.5.2 Active Layer Components	25
2.5.3 Charge Transport Layers.....	27
2.5.4 Specialist Systems.....	29
2.6 Characterizing Organic Photovoltaics.....	31
2.6.1 The Equivalent Circuit Model.....	31
2.6.2 Modifications of the Equivalent Circuit Model for OPVs	33
2.6.3 Solar Cell Testing Parameters	33
2.6.4 Space Charge Limited Region	38
2.6.5 External Quantum Efficiency.....	39
2.7 Fabrication of Organic Photovoltaics	39
2.7.1 Spin Coating.....	39

2.7.2	Scalable Deposition Methods	40
2.7.3	Optimisation of OPV Efficiency	44
2.8	Stability of Organic Photovoltaics	45
2.8.1	Burn-In	45
2.8.2	Intrinsic Degradation Factors	46
2.8.3	Extrinsic Degradation Factors	48
2.8.4	Characterization of Degradation.....	51
2.9	The Future of Organic Photovoltaics.....	53
2.9.1	Commercial Prospects	53
2.9.2	Niche Applications	54
2.10	References	56
Chapter 3 Experimental Methods		61
3.1	Introduction	61
3.2	Materials	61
3.2.1	Substrates.....	61
3.2.2	Materials Used in Device Fabrication	62
3.2.3	Hole Transport Layers	62
3.2.4	Electron Transport Layers	63
3.2.5	Acceptors.....	64
3.2.6	Donors	66
3.2.7	Solvents	66
3.2.8	Summary.....	67
3.3	Deposition Methods.....	68
3.3.1	Spin Coating	68
3.3.2	Spray Coating	68
3.3.3	Thermal Evaporation	70
3.4	Device Fabrication.....	71
3.4.1	Architecture	71
3.4.2	Cleaning.....	71
3.4.3	Bottom CTL.....	72
3.4.4	Patterning.....	72
3.4.5	Active Layer	73
3.4.6	Top CTL	74
3.4.7	Thermal Evaporation	74
3.4.8	Encapsulation.....	75
3.5	Device Characterization	75
3.5.1	Charge Transport in the Completed Device	75

3.5.2	Current Voltage Measurements	76
3.5.3	Light Dependant Measurements	77
3.5.4	Photocurrent (J_{ph}) measurements	77
3.5.5	External Quantum Efficiency.....	77
3.5.6	Light beam induced current mapping	78
3.6	Device Stability.....	79
3.6.1	Shelf Life Testing.....	79
3.6.2	Illuminated stability	79
3.7	Film Characterization.....	80
3.7.1	Ultraviolet-Visible Absorption & Photoluminescence	80
3.7.2	Atomic Force Microscopy	82
3.7.3	Profilometry	82
3.7.4	Contact Angle Goniometry	82
3.7.5	Grazing Incidence Wide Angle X-ray Scattering	83
3.7.6	Visible Light Microscopy	87
3.8	Other Techniques	87
3.8.1	Differential Scanning Calorimetry.....	87
3.8.2	Nuclear Magnetic Resonance Spectroscopy	88
3.9	References.....	89
Chapter 4 Air Knife-Assisted Spray Coating of Organic Photovoltaics		91
4.1	Author Contributions	91
4.2	Abstract.....	91
4.3	Introduction.....	92
4.4	Results and Discussion	93
4.4.1	Methodology	93
4.4.2	Device Fabrication and Performance.....	94
4.4.3	Optical Characteristics	99
4.4.4	GIWAXS.....	100
4.4.5	Optoelectronic Measurements.....	103
4.4.6	Larger Scale Morphology	105
4.5	Conclusions.....	106
4.6	Experimental Methods	107
4.6.1	Device Fabrication	107
4.6.2	UV-Vis absorption & photoluminescence measurements	107
4.6.3	GIWAXS.....	107
4.6.4	Light dependent measurements.....	108
4.6.5	Atomic Force Microscopy	108

4.7	Supplementary Information	109
4.8	References	114
Chapter 5 Comparing the Influence of Solvent Additive Processing on Fullerene and Non-Fullerene Acceptors		116
5.1	Author Contributions	116
5.2	Abstract	116
5.3	Introduction	117
5.4	Results and Discussion	119
5.4.1	Initial Morphology	119
5.4.2	Device Studies	130
5.4.3	Dark Stability	138
5.4.4	Illuminated Stability	140
5.5	Conclusions	144
5.6	Experimental	145
5.6.1	GIWAXS	145
5.6.2	AFM	145
5.6.3	UV-Vis Absorption	145
5.6.4	Device Fabrication	145
5.6.5	NMR	146
5.6.6	Contact Angle	146
5.6.7	Dark Stability	146
5.6.8	Illuminated Stability	146
5.7	Supplementary Information	147
5.7.1	Component GIWAXS	147
5.7.2	Component AFM	150
5.7.3	Device Performance	153
5.7.4	NMR	155
5.7.5	Contact Angle Data	158
5.7.6	Dark Device Stability	160
5.7.7	Illuminated Device Stability	163
5.8	References	173
Chapter 6 Examining the Driving Factors of Positive Burn-in in Organic Photovoltaics		175
6.1	Author Contributions	175
6.2	Abstract	175
6.3	Introduction	175
6.4	Results and Discussion	181
6.4.1	Device Fabrication & Morphological Stability	181

6.4.2	Kinetic Factors: Exploration of Thermal Characteristics.....	184
6.4.3	Thermodynamic Factors: Assessment of the Flory-Huggins Interaction Parameter	189
6.4.4	Relation of Kinetic and Thermodynamic Factors to Stability.....	203
6.5	Conclusions.....	205
6.6	Experimental	206
6.6.1	Flory Huggins Binodal Curve	206
6.6.2	Devices.....	206
6.6.3	Differential Scanning Calorimetry.....	207
6.6.4	Grazing Incidence Wide Angle X-Ray Scattering	207
6.6.5	Determination of $\chi(T)$ via UV-Vis.....	207
6.7	Supplementary Information	209
6.7.1	Device Stability.....	209
6.7.2	Example Calculation of χ via Melting Point Depression	212
6.7.3	VLM images	213
6.7.4	Fitting of UV-Vis Spectra.....	225
6.8	References.....	227
Chapter 7 Conclusions and Future Work.....		228
7.1	Discussion of Conclusions	228
7.2	References.....	231

Chapter 1 | Introduction

Global warming, leading to widespread climate change, is an irrefutable presence in modern life. On the 4th April 2022, the intergovernmental panel on climate (IPCC) released their latest climate report, stating ‘climate change is a threat to human well-being and planetary health’.¹ Climate forecasting has shown that widespread flooding of coastal cities,² mass coral bleaching,³ and severe deterioration of ecosystems⁴ are all likely within the next few decades. Temperatures exceeding the upper limit of human survivability have also been predicted in several areas of the world by the end of the 21st century.^{5,6} To mitigate these severe risks, and irreversible change, there is a consensus that the final global temperature rise must be kept below 1.5°C.¹ In order for the globe to limit to this level of warming, humanity must transform how it produces and uses energy. The energy system must transition from that based on fossil fuels, to one based on efficient renewable sources, electrification, and alternate, clean fuels. The IPCC predicts that greenhouse gas emissions across the world must be reduced by 43% before 2030, and be at net zero by 2050, and that ‘any further delay in global action...will miss a brief and rapidly closing window of opportunity to secure a liveable and sustainable future for all’.¹

It is therefore clear that the way we produce and consume energy must change, at a pace rapid enough to keep up with increasing energy demand and increasing climate change risk. Whilst it is likely one single technology cannot solve humanity’s energy crisis; solar power holds arguably the greatest potential. In just 1.5 hours, 480 EJ of energy hits the Earth surface from the sun, a comparable number to the entire worldwide energy consumption in the year 2001. While not all of this is extractable, compared to other renewable technologies, such as wind or hydropower, solar energy has been predicted to have the highest easily accessible energy potential.⁷ Indeed, models suggest that the entire predicted global energy consumption in 2050 (27.6 TW) could be generated by 10% efficient solar systems on only 0.33% of the Earth’s surface area.⁷

Global adoption of solar energy has so far been restricted by several factors. Energy output from a solar system is limited by irradiance, time of day, and time of year. This means that without other technologies providing a baseline, solar power must be accompanied by suitable energy storage.⁸ Fluctuating costs of solar have also influenced adoption. The solar market has been almost uniformly dominated by silicon solar cells since their introduction in 1954,⁹ with efficiencies of these cells now exceeding 26%.¹⁰ Increases in Chinese production, compounded with global economic crisis, saw huge drops in the price of silicon solar in 2009.¹¹ These low prices remained for several years, however, drops in demand and supply chain issues, as a result of the COVID-19 pandemic in 2020 have begun to trigger increased

prices once more. Similarly, whilst UK subsidies once encouraged homeowners to install solar, their cuts in 2019 have been linked to drops in solar installations.¹²

Raw material cost is not the only factor that influences the adoption of solar, and installation of solar systems. Usually, the cost of the components and equipment (except the main module) are encompassed as ‘balance of system’ (BoS) costs. In general, the total cost of a silicon solar installation is considered to be roughly 50:50 module:BoS costs.¹³ As weight will influence the BoS (due to supporting frameworks), the efficiency and weight per area will contribute significantly to final price. Silicon does not absorb particularly well and so requires relatively thick, heavy active layers to produce efficient solar cells that therefore yield a high BoS costs.

Beyond simple installation cost, the future of solar must be considered in terms of its economic viability. This is typically discussed using energy payback time (EPT), defined as the time a solar panel will take to generate as much energy as was consumed in its production,¹⁴ and levelized cost of electricity (LCoE), defined as the total lifetime cost of a solar installation, divided by its lifetime electricity production.¹⁵ Silicon requires high temperature, energy intensive, manufacturing, therefore yielding a high EPT and LCoE.

In order to overcome the intrinsic limits on BoS, EPT, and LCoE for silicon, there have been huge research efforts into finding alternative solar cell technologies. The most successful of these have been based on nm – μm scale films, and are therefore known as ‘thin film’ technologies. Thin film solar technologies can be divided into 2nd and 3rd generation technologies, depending on their maturity. 2nd generation technologies include cadmium telluride (CdTe), copper indium gallium selenide (CIGS), amorphous silicon (a-Si), and gallium arsenide (GaAs). 3rd generation solar technologies include copper zinc tin sulphide (CZTS), dye sensitized solar cells (DSSCs), quantum dot solar cells (QDs), perovskite solar cells (PSCs), and organic photovoltaics (OPVs). An overview of the historic efficiencies obtained by these technologies can be seen in **Figure 1.1**, produced by the National Renewable Energy Laboratory (NREL).¹⁶

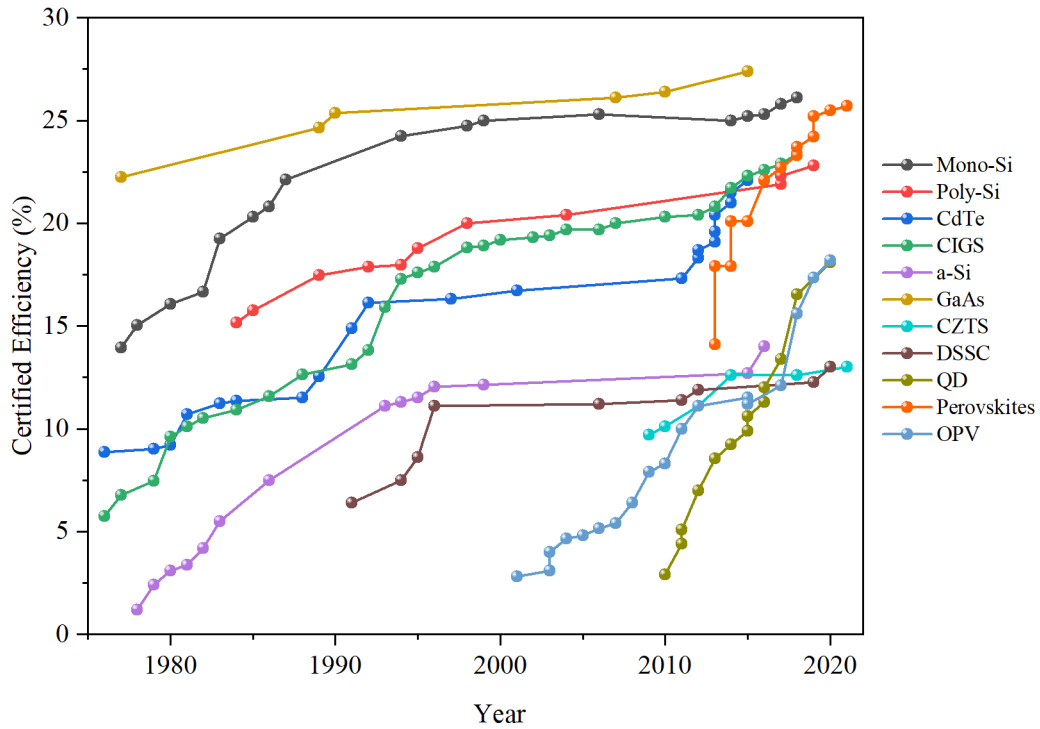


Figure 1.1: Historic certified efficiencies for a range of solar cell technologies.¹⁶

Each type of solar cell technology has its own balance of EPT, BoS, and LCoE, depending on its efficiency, manufacturing process, material abundance, stability, and a host of other factors. This thesis focuses on OPVs, a particularly promising type of 3rd generation technology. First introduced in 1986 with an efficiency of 0.95%,¹⁷ state-of-the-art OPVs now exceed 19%.¹⁸ Whilst these efficiencies lag behind that of silicon, OPVs hold several key advantages.

OPVs are usually fabricated via solution processing, using organic semiconductors (OSCs). Solution processability means they have the potential to be rapidly and cheaply ‘printed’ using roll-to-roll compatible methods such as slot-die coating.¹⁹ The active layer is usually very thin, and therefore the cell can be flexible and lightweight. The potential for flexibility is also compounded by the ability to manufacture efficient OPVs (~15%) without heat altogether,²⁰ opening up a new family of previously inaccessible, temperature sensitive substrates. The absorption of the active layer of an OPV can also be precisely tuned to allow through specific wavelengths of light, meaning they hold immense promise for applications such as solar windows. The combination of these factors has led to OPV projections with a fast EPT, and low BoS costs.²¹ This is especially true in niche contexts where efficiency is not the most important metric, such as building integrated PV.

With module scale efficiencies of OPVs now well exceeding 10%,²² a key benchmark identified for commercialization,²³ the main obstacles towards wide spread adoption are long term operational stability, and low-waste, scalable manufacture. Many OPV materials suffer from a host of degradation pathways, including morphological instability,²⁴ thermal instability,²⁵ moisture instability,²⁶ and UV-instability.²⁷ Careful choice of material and protecting layers has shown to go some way to combating this, with recent reports suggesting projected lifetimes exceeding 30 years.²⁸ Regardless, understanding of these degradation mechanisms, and how to mitigate them, remains a key area of research.

Scalable deposition is the other major stream of OPV research, as it is for many solution processed thin film technologies. Lab scale research is dominated by spin coating, but this is wasteful and cannot be upscaled to large areas. In contrast, techniques such as spray coating,²⁹ slot-die coating,¹⁹ and blade coating,³⁰ offer low-waste fabrication that can be applied to large scale, roll-to-roll systems. Whilst efficiencies using these methods are rising, they still lag behind that of spin coated cells, in part due to inferior film quality. Improvement of scalable performance, especially over increasing active areas, is potentially the most significant remaining hurdle of OPV research.

1.1 Thesis Aims

This thesis aims to contribute to overcoming these obstacles by focusing on improving the stability and scalability of high efficiency OPVs, through control of their morphology. Morphology describes the arrangement of OSCs molecules, aggregates, and phases, in the active layer of a cell, and has arguably the greatest influence on performance of any parameter. As unfavourable changes in morphology drive several degradation routes, and inferior scalable performance, this is an important unifying factor, and its optimisation and control key to commercialization of OPVs. Here, several combinations of solvent and OSC materials are explored, their morphology characterised, and techniques for improvement of scalable or stable performance suggested. This work allows the initialization of a framework for a commercially viable OPV system.

1.2 Thesis Overview

Chapter 2 details the foundational theory for the rest of the thesis. The history and working mechanisms of organic semiconductors and their charge transport is discussed, along with application of this theory to organic photovoltaics. A brief history of OPVs is given, to provide context to the results chapters, alongside their working principles, fabrication, and

details of stability and scalable deposition. Possible commercial applications of OPVs are discussed, including the current main obstacles to their fruition.

Chapter 3 outlines the experimental methods used in all results chapters. Here, film and device fabrication and testing are detailed, alongside techniques specific to characterizing morphology. Where required, the background theory and analysis for the techniques is explained.

Chapter 4 details an investigation into deposition of a high efficiency OPV using ultrasonic spray coating. Spray coated devices were successfully manufactured using careful choice of component and solvent. This work was performed with the aim of improving scalable OPV efficiencies, and marks a significant improvement in spray coated performance for the field as a whole. Differences in performance and morphology were characterised using a combination of device-based measurements, and grazing incidence wide angle X-ray scattering (GIWAXS).

Chapter 5 describes assessment of the performance and stability differences for two different OPV systems, where the acceptor molecule and solvent additive content were varied. Subtleties in how the solvent additive interacted with, and influenced the morphology of, each acceptor differently were explored. How these differences then influenced stability were assessed under a range of degradation conditions. As solvent additives are common in high performance OPV systems, the complexities in their influence on morphology and stability are important to understand.

Chapter 6 dives deeper into one specific type of OPV stability- namely morphological changes over time. Here the thermodynamic and kinetic factors influencing morphological stability for several different acceptors were assessed. Using Flory-Huggins theory, the dependence of donor:acceptor miscibility on acceptor chemical structure is analysed. As morphological stability underpins resistance to all other degradation routes, understanding the factors influencing this, and their control, is vital.

Chapter 7 finishes this work with a discussion of the conclusions of each chapter, how they fulfil the initial aims laid out here, and how they fit into the wider field of research. Future directions of research are proposed, along with the challenges that still remain.

1.3 References

1. Hans-O. Pörtner *et al.*, *Climate Change 2022 - Impacts, Adaptation and Vulnerability - Summary for Policymakers*. Ipcc (2022).
2. Dahl, K. A., Spanger-Siegfried, E., Caldas, A. & Udvardy, S. Effective inundation of continental United States communities with 21 st century sea level rise. *Elementa* **5**, (2017).
3. Hughes, T. P. *et al.* Global warming impairs stock–recruitment dynamics of corals. *Nature* **568**, 387–390 (2019).
4. IPBES. *Summary for policymakers of the global assessment report on biodiversity and ecosystem services*. *Intergovernmental Science-Policy Platform on Biodiversity and Ecosystem Services* **45**, (2019).
5. Im, E. S., Pal, J. S. & Eltahir, E. A. B. Deadly heat waves projected in the densely populated agricultural regions of South Asia. *Sci. Adv.* **3**, 1–8 (2017).
6. Kang, S. & Eltahir, E. A. B. North China Plain threatened by deadly heatwaves due to climate change and irrigation. *Nat. Commun.* **9**, 1–9 (2018).
7. Tsao, J., Lewis, N. & Crabtree, G. Solar FAQs. *US Dep. Energy* 1–24 (2006). Available at: https://science.osti.gov/-/media/bes/pdf/reports/files/Basic_Research_Needs_for_Solar_Energy_Utilization_rpt.pdf (Accessed Jan 2022).
8. Alva, G., Liu, L., Huang, X. & Fang, G. Thermal energy storage materials and systems for solar energy applications. *Renew. Sustain. Energy Rev.* **68**, 693–706 (2017).
9. Chapin, D. M., Fuller, C. S. & Pearson, G. L. A New Silicon p-n Junction Photocell for Converting Solar Radiation into Electrical Power. *J. Appl. Phys.* **25**, 676–677 (1954).
10. Yoshikawa, K. *et al.* Silicon heterojunction solar cell with interdigitated back contacts for a photoconversion efficiency over 26%. *Nat. Energy* **2**, 17032 (2017).
11. Bernreuter. Polysilicon price trend. 2022 Available at: <https://www.bernreuter.com/polysilicon/price-trend/>. (Accessed Jan 2022)
12. EDIE. One year on: How has the solar feed-in-tariff closure impacted renewables in the UK? (2020). Available at: <https://www.edie.net/one-year-on-how-has-the-solar-feed-in-tariff-closure-impacted-renewables-in-the-uk/>. (Accessed Jan 2022)
13. Zhou, Z. & Carbajales-Dale, M. Assessing the photovoltaic technology landscape: Efficiency and energy return on investment (EROI). *Energy Environ. Sci.* **11**, 603–608 (2018).
14. Sofia, S. E. *et al.* Economic viability of thin-film tandem solar modules in the United States. *Nat. Energy* **3**, 387–394 (2018).
15. Mulligan, C. J., Bilén, C., Zhou, X., Belcher, W. J. & Dastoor, P. C. Levelised cost of electricity for organic photovoltaics. *Sol. Energy Mater. Sol. Cells* **133**, 26–31 (2015).
16. NREL. Best Cell Efficiencies. (2021). Available at: <https://www.nrel.gov/pv/cell-efficiency.html>. (Accessed 9th May 2022)
17. Tang, C. W. Two-layer organic photovoltaic cell. *Appl. Phys. Lett.* **48**, 183–185 (1986).
18. Cui, Y. *et al.* Single-Junction Organic Photovoltaic Cell with 19% Efficiency. *Adv. Mater.* **2102420**, 2102420 (2021).
19. Zhao, H. *et al.* Hot Hydrocarbon-Solvent Slot-Die Coating Enables High-Efficiency Organic Solar Cells with Temperature-Dependent Aggregation Behavior. *Adv. Mater.* **32**, 1–10 (2020).
20. Wan, J., Wen, R., Xia, Y. & Dai, M. All annealing-free solution-processed highly flexible organic solar cells. *J. Mat. Chem. A* **9**, 5425–5433 (2021).
21. Anctil, A., Lee, E. & Lunt, R. R. Net energy and cost benefit of transparent organic solar cells in building-integrated applications. *Appl. Energy* **261**, 114429 (2020).
22. Sun, R. *et al.* A Layer-by-Layer Architecture for Printable Organic Solar Cells Overcoming the Scaling Lag of Module Efficiency. *Joule* **4**, 407–419 (2020).
23. Du, X. *et al.* Efficient Polymer Solar Cells Based on Non-fullerene Acceptors with Potential Device Lifetime Approaching 10 Years. *Joule* **3**, 215–226 (2019).
24. Qin, Y. *et al.* The performance-stability conundrum of BTP-based organic solar cells. *Joule* **5**, 2129–2147 (2021).
25. Yang, W. *et al.* Simultaneous enhanced efficiency and thermal stability in organic solar cells from a polymer acceptor additive. *Nat. Commun.* **11**, 1–10 (2020).
26. Planes, E. *et al.* Encapsulation Effect on Performance and Stability of Organic Solar Cells. *Adv. Mater. Interfaces* **7**, 1–13 (2020).
27. Classen, A. *et al.* Revealing Hidden UV Instabilities in Organic Solar Cells by Correlating Device and Material Stability. *Adv. Energy Mater.* **9**, 1–11 (2019).
28. Li, Y. *et al.* Non-fullerene acceptor organic photovoltaics with intrinsic operational lifetimes over 30 years. *Nat. Commun.* **12**, 1–9 (2021).
29. Tao, W. *et al.* Fabricating High Performance, Donor–Acceptor Copolymer Solar Cells by Spray-Coating in Air. *Adv. Energy Mater.* **3**, 505–512 (2013).
30. Dong, S. *et al.* Single-Component Non-halogen Solvent-Processed High-Performance Organic Solar Cell Module with Efficiency over 14%. *Joule* **4**, 2004–2016 (2020).

Chapter 2 | Background Theory

2.1 The Basics of Photovoltaics

2.1.1 The Photovoltaic Effect

All solar cells operate by converting light energy into electrical energy, known as the photovoltaic effect. This phenomenon was first discovered in 1839 by Edmond Becquerel¹ and broadly describes how the absorption of a photon of light by a semiconductor can excite an electron within the material, allowing the generation of an electrical current.

2.1.2 Inorganic Crystalline Semiconductors

The simplest case of a semiconductor can be defined as a material with electrical conductivity in-between that of a conductor and that of an insulator. These materials are bonded together by covalent bonds and, with the input of energy, some of the electrons in these bonds have enough energy to become delocalised, allowing electrical conduction. Therefore, conductivity of a semiconductor increases exponentially with temperature and at temperatures close to absolute zero it will behave as an insulator. The energy required for an electron to become delocalised is known as the band gap of the material, with the bound lower energy state known as the valence band and the delocalised higher energy state known as the conduction band. Generally, semiconductors will have a band gap energy in the region of 0.5-3 eV.² Upon electron excitation, there will be an empty space left in the valence band, commonly approximated as a positively charged particle known as a hole, shown in **Figure 2.1**. The excited electron and hole pair are known collectively as an exciton. Both the electron and hole can act as charge carriers and facilitate conduction. If the electron relaxes back down the valence band, annihilating the hole to release a photon, the absorbed energy will be lost in a process known as radiative recombination. This, and other forms of recombination are discussed in **Section 2.2.6**.

Intrinsic semiconductors have a sufficiently small band gap that a number of electrons exist in the conduction band at room temperature. This in contrast to the case of insulators (where the band gap is too large for electron excitation at room temperature) and conductors (where there is no band gap separating the valence and conduction bands). As well as temperature, light of sufficient energy can excite electrons into the conduction band, known as photoconductivity, which is the basis for the photovoltaic effect.

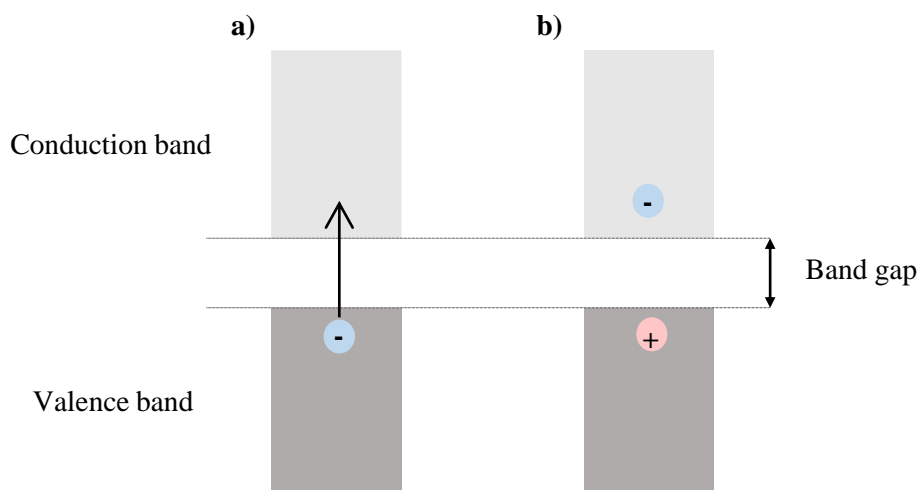


Figure 2.1: An approximation of **a)** electron excitation in a semiconductor from valence to conduction band, **b)** leaving behind a hole.

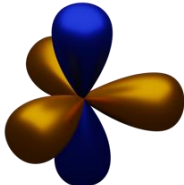
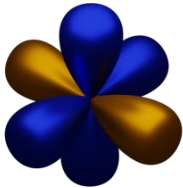
Typically, inorganic semiconductors are doped, i.e. a small amount of another material is added to promote either p-type behaviour, where there are more holes than electrons, or n-type behaviour, where there are more electrons than holes. The more predominant charge carrier is known as the majority carrier and the less common the minority carrier. A solar cell can then be formed by generating a ‘p-n’ junction between the two types of material. The higher work function of the p-type material will generate an electric field at the junction, which will drive electrons towards the n-type material and holes towards the p-type material, whilst promoting minority carriers to diffuse across the interface and be collected, generating a current.

The motion of charge carriers in an electric field is known as a drift current, whereas motion due to a concentration gradient is known as a diffusion current. Both types of current will be at play in semiconductor charge transport, and discussed more fully in works on the drift-diffusion model.³

2.1.3 Organic Semiconductors

Organic semiconductors (OSCs) are semiconductor materials based on carbon that take the form of polymers or small molecules and cannot be described by traditional inorganic-semiconductor models. To understand these materials, we must first consider the hybridisation of carbon orbitals upon bonding, which differs depending on the number of bonds formed and is described in **Table 2.1**.

Table 2.1: A visualisation of the hybrid bonding orbitals formed in different organic molecules, where gold represents the hybrid sp orbitals and blue represents the p orbitals.

Structure	Hybridisation	Visualization
$\begin{array}{c} \\ -C- \\ \end{array}$	sp^3	
$\begin{array}{c} \diagup \\ C= \\ \diagdown \end{array}$	sp^2	
$\begin{array}{c} -C\equiv \\ \\ =C= \end{array}$	sp	

OSCs always contain some form of conjugation, meaning a portion of the material has a section of alternating double and single bonds. This repeated sp^2 hybridisation causes the π -bonding electrons, contained within the p -orbitals, to be delocalised across the conjugated section. A visualization of this for the simple conjugated aromatic molecule, benzene, can be seen in **Figure 2.2**.

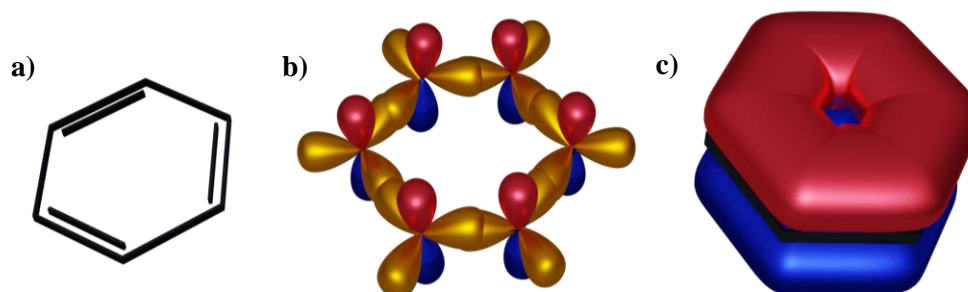


Figure 2.2: a) A skeletal representation of conjugated molecule benzene, b) sp^2 orbitals in the lowest energy molecular orbital for benzene, c) delocalisation of the electrons in the p -orbitals.

This electron delocalisation can lead to semiconducting properties that are similar to those found in inorganic semiconductors. The π -bonding molecular orbitals of the OSC, i.e. the highest occupied molecular orbital (HOMO) and the lowest unoccupied molecular orbital (LUMO), can be considered respectively analogous to the valence and conduction band of an inorganic semiconductor. The LUMO is roughly equivalent to the electron affinity (EA) of the OSC and the HOMO is roughly equivalent to its ionization energy (IE). The energy gap between the HOMO and LUMO is described as the band gap of the OSC, even though it does not form bands in the same manner as an inorganic semiconductor.

Not all conjugated materials can act as OSCs and in reality most that do will be insulating at room temperature without charge injection from electrodes, doping or photoexcitation.⁴

2.1.4 The Shockley-Queisser limit

While all semiconductors can be described by their band gap, not all will be suitable for application as a solar cell, as this depends on the wavelengths of light that they absorb. The spectrum of blackbody irradiation emitted by the sun is known as the AM0 ('air mass') spectrum. Once this radiation has passed through the Earth's atmosphere, and undergone scattering and absorption losses, it is known as the AM1.5 spectrum. This can be further divided into AM1.5 global (g) (including both direct and diffuse radiation), and AM1.5 direct (d) (including only direct diffusion). For the planar solar cells discussed in this thesis, AM1.5g will be used, which is normalized to 1000 W m^{-2} , known as '1 sun'. These spectra can be seen in **Figure 2.3**.

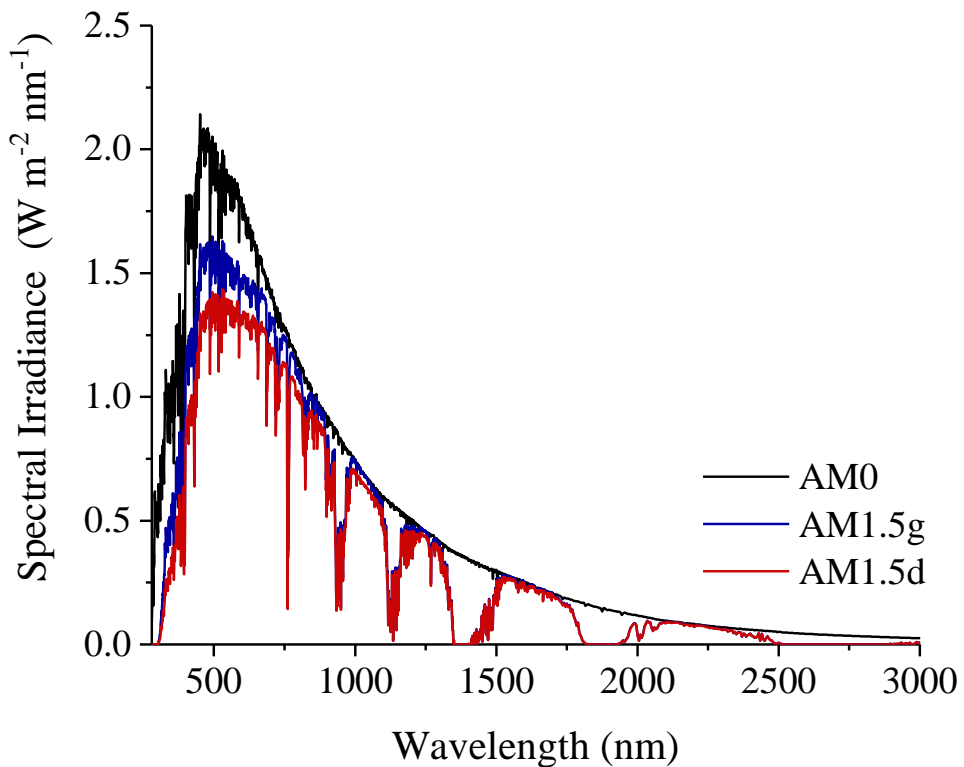


Figure 2.3: The AM0 and AM1.5 spectra, representing the blackbody irradiation emitted by the sun before and after the Earth's atmosphere. Accessed from the NREL website November 2021.⁵

The band gap of a semiconductor will dictate which wavelengths of light from the AM1.5 spectrum it can successfully absorb. Light with wavelengths above the band gap will not have sufficient energy to excite an electron within the valence band and so will not be absorbed. Light with wavelengths below the band gap will be absorbed but the excess energy is wasted as heat (or 'thermalisation'). As a result, semiconductor selection based on band gap is a careful balance of maximum absorption and minimal losses. The performance of a solar cell is quantified by power conversion efficiency (PCE), which is discussed in **Section 2.6.3.4** and is often referred to simply as 'efficiency.'

A landmark discussion of the fundamental efficiency limits for p-n junction solar cells based on their band gap was published in 1961 by Shockley and Queisser.⁶ Here, the authors propose a theoretical 'detailed balance limit', depending on several factors including the energy gap of the material and the degree of radiative recombination, known as the 'Shockley-Queisser (SQ) limit.' Under this model, an ideal solar cell would have a band gap of 1.34 eV, leading to a maximum efficiency of 34% under blackbody radiation. A representation of a range of modern solar cell technologies and how their record efficiencies compare to

maximum possible efficiencies predicted by the Shockley-Quiesser limit can be seen in **Figure 2.4**.

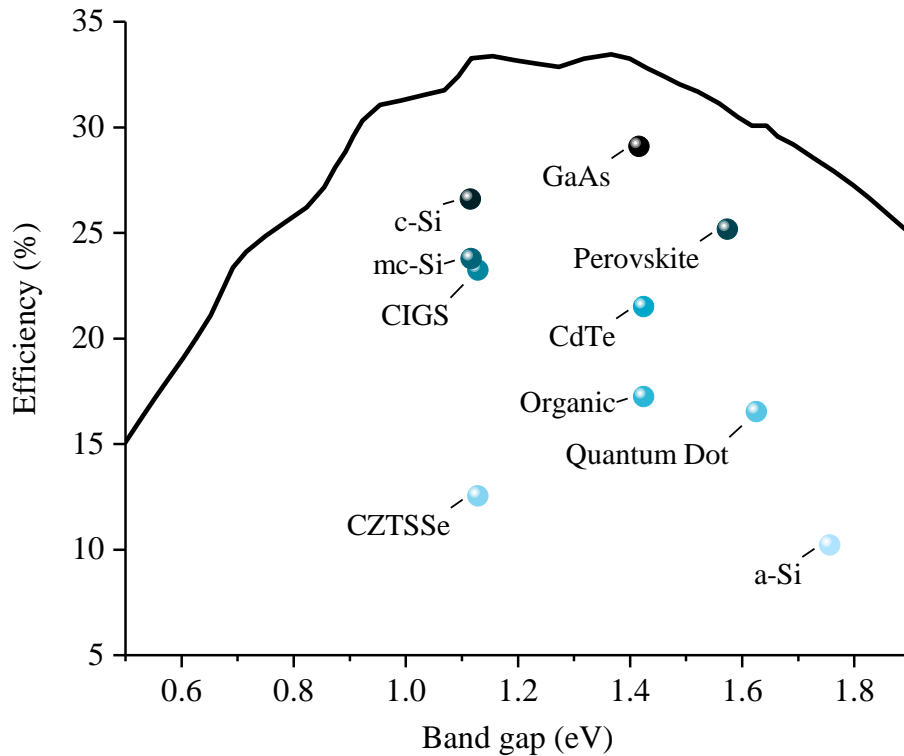


Figure 2.4: Record efficiencies (as of July 2020) for a range of solar cell types compared to the theoretical limit for the band gap of the photoactive material, according to the SQ limit. Figure adapted from Ehrler et al.⁴

The SQ model follows a number of assumptions, namely:

1. Only photons with energy above the band gap are absorbed and this absorption is perfect.
2. Energy above the band gap is lost as heat.
3. Only radiative recombination occurs.
4. The electrodes in the cell are ideal contacts without losses.

In reality, not all of these assumptions will hold true and incomplete absorption, other forms of recombination, and interface losses are all common, leading to the losses seen in **Figure 2.4**. Despite this, there are also technologies that can allow cells to exceed the SQ limit, including combining solar cells to absorb a wider portion of AM1.5 (tandem solar cells) and various charge carrier management methods⁴ which are beyond the scope of this work.

2.2 Organic Photovoltaic Physics

2.2.1 The Basics of an Organic Photovoltaic Cell

Organic photovoltaic cells (OPVs) are a type of solar cell that use OSCs as their photoactive material. For reasons discussed shortly, these OSCs must be in the form of thin films, usually on the order of ~100 nanometres. The active layer will be sandwiched between metal electrodes used to extract the current. In the following section, the mechanisms of generation and extraction of this current under illumination are discussed.

2.2.2 Exciton Formation in Organic Semiconductors

Illumination of an OSC will generate an exciton in the same way as an inorganic semiconductor but in contrast to the latter, excitons in OSCs are not easily dissociated into electrons and holes. Instead, the electron and hole are strongly bound together and known as a Frenkel exciton, in contrast to the weakly bound Wannier-Mott exciton in an inorganic semiconductor. The formation of Frenkel excitons in OSCs is a result of the low dielectric constant of these materials ($\epsilon \sim 3$),⁷ leading to little shielding between the electron and hole and so a significant binding energy (0.5 - 1 eV), greater than the available thermal energy at room temperature (~26 meV).⁴ This means that a Frenkel exciton cannot be easily dissociated to allow charge carrier transport and so further steps must be taken, detailed in **Section 2.2.4**.

The electronic energy levels of an organic semiconductor are usually described according to the spin of the electrons. Where electrons are paired with opposite spin, this is known as a singlet, whereas if they have the same spin this is known as a triplet. Generally, in OSCs, excitation will occur from a ground state singlet (S_0 , the HOMO) to the first excited single state (S_1 , the LUMO).

2.2.3 Exciton Transport in Organic Semiconductors

Before an exciton can be dissociated it must diffuse. Upon excitation of the electron in the OSC the distribution of electrons in the bonding orbitals will be changed, leading to a change in bond lengths and a distortion of the geometry of the material. The combination of a charge carrier (electron or hole) and its corresponding geometric distortion is known as a polaron. Charge carriers are usually localised across a few atoms of the material and so diffuse (in the form of a polaron) via 'hopping' along or between OSCs moieties.⁷

The exciton diffusion between OSC molecules or chains will occur by two possible mechanisms. Firstly, Förster resonance energy transfer (FRET) may occur, where coulombic energy coupling occurs between moieties. Alternatively, Dexter energy transfer (DET) may

take place, where charge carriers are transferred directly. FRET is considered to be the main mechanism of exciton diffusion in OPVs within a single material⁸ and operates over longer length scales than DET, leading to a typical ‘exciton diffusion length’ (referring to the distance the exciton can travel before recombination will occur) of ~10 nm in an OSC.⁹ A representation of FRET compared to DET can be seen in **Figure 2.5**.

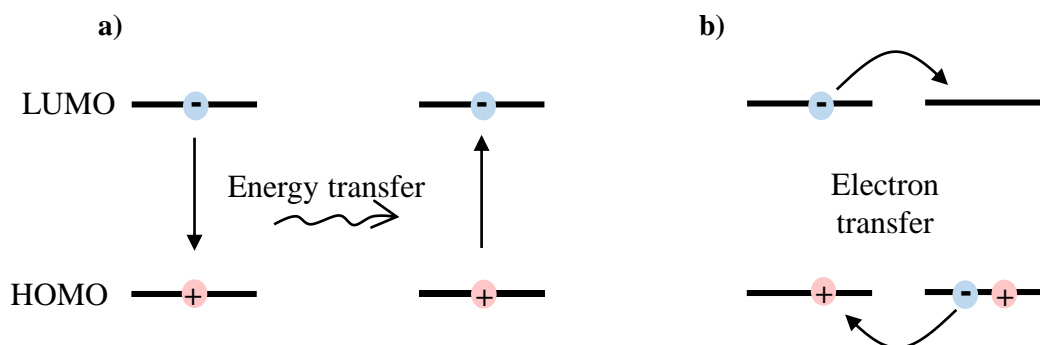


Figure 2.5: a) FRET and b) DET modes of exciton diffusion. Figure adapted from Feron et al..⁹

2.2.4 Exciton Dissociation in Organic Semiconductors

In order to facilitate the dissociation of the exciton into its constituent charge carriers in an OPV, the chemical potential difference between two OSCs can be used, with materials selected to act as an electron donor or acceptor. The most commonly used examples of these are P3HT and PCBM respectively. For electron transfer from donor to acceptor to occur it is generally assumed that the LUMO of the acceptor and donor should have an offset greater than that of the exciton binding energy. This provides a thermodynamic driving force for dissociation (see **Section 2.6.3.2.3** for a short discussion of systems where this may not apply). A HOMO offset is also required to prevent unwanted hole transfer to the acceptor and to drive hole transfer from acceptor to donor in the cases where this occurs.¹⁰ These HOMO & LUMO offsets can be seen in **Figure 2.6**.

Upon exciton diffusion to a donor acceptor interface, which must be within the exciton diffusion length of the OSC to avoid exciton recombination, the electron will be transferred from donor to acceptor. It is generally accepted that at this stage the electron and hole are still coulombically bound and so form a charge transfer (CT) state, sometimes known as a polaron-polaron pair. The electron and hole will remain as a CT state until they separate sufficiently for the distance between them to overcome the exciton binding energy. At this point, the charge carriers are now free and can be extracted from the cell after diffusing to the appropriate electrodes.

In recent years there has been some debate whether charge transfer states are always formed and evidence that in some cases excitons dissociate directly into free charges, possibly co-existing with or even dominating over CT states.¹¹ Conversely, it has also been suggested FRET of excitons may compete with charge carrier transfer between the donor and acceptor domains.¹²

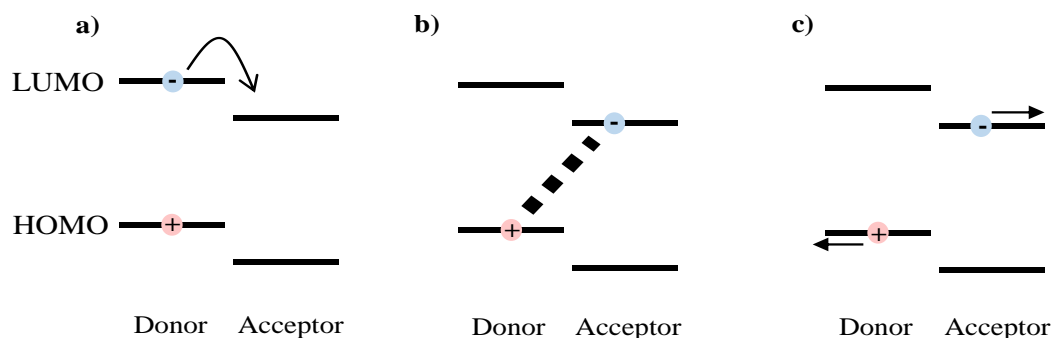


Figure 2.6: A depiction of **a)** electron transfer from donor to acceptor at the interface, **b)** formation of a charge transfer state across the interface, **c)** complete dissociation and extraction of charge carriers.

2.2.5 Charge Carrier Transport in Organic Semiconductors

After dissociation, free charge carriers will hop through from molecule to molecule. This is influenced by both the built-in field within the cell, and external applied bias, discussed further in **Section 2.6.1**. The speed of the charge carrier diffusion is described by the charge carrier mobility, defined in **Equation 2.1**, where μ represents mobility ($\text{cm}^2 \text{V}^{-1} \text{s}^{-1}$), E represents electric field (V) and v_d represents drift velocity ($\text{cm}^2 \text{s}^{-1}$):

$$\mu = \frac{E}{v_d} \quad (\text{Eq. 2.1})$$

Methods of calculating mobility are discussed in **Section 2.6.4**. Charge carrier mobility in an OSC will be different depending on the structure and morphology of the material, discussed further in **Section 2.3.2**.

2.2.6 Types of Recombination

At all stages discussed above, an excited electron and hole can recombine, with the energy used in their initial excitation being ‘lost’. Recombination is categorised as either geminate, where the recombination occurs between the initial electron and hole pair; or non-geminate, where any electron and hole can recombine regardless of their initial source. Both of these types of recombination can be radiative, where a photon is released; or non-radiative, where the energy is eventually converted to heat.

Common sub-categories of non-geminate recombination include bimolecular recombination, which is a radiative process sometimes referred to as Langevin recombination; and non-radiative trap-assisted recombination, sometimes referred to as Shockley-Read-Hall (SRH) recombination, where structural defects generate sub-band gap states.¹³

2.3 The Bulk Heterojunction

2.3.1 The Introduction of the Bulk Heterojunction

Whilst using two OSC components in the active layer of an OPV will encourage exciton dissociation, it took several years before the optimum mixing of these was understood. To maximise exciton dissociation a large donor-acceptor interface is required. However, excitons and free charge carriers can only travel a certain distance before recombination. A film having a sufficiently large optical thickness is also required to ensure effective light absorption. In general, a simple donor-acceptor bilayer cannot be used to generate both efficient light absorption and effective charge extraction.

A solution to this was proposed in 1995^{14,15} and is known as a ‘bulk heterojunction’ (BHJ). A BHJ consists of a nanoscale interpenetrating network of donor and acceptor material, meaning the layer can be made both sufficiently thick to absorb light and maintain a short distance interface to electrode distance for charge carriers to travel. This is shown in **Figure 2.7**.

Whilst early OPVs were fabricated via evaporation methods^{16, 17} vacuum techniques are typically limited in their ability to generate complex morphologies and are also restricted to small molecule materials. BHJs based on material-blends that include donor polymers are most often solution processed, with this type of structure now dominating the field. Here, such donor and acceptor materials are typically dissolved together in a single solvent and deposited via methods such as spin coating to form the BHJ. Further discussion of this fabrication process can be found in **Section 2.7**.

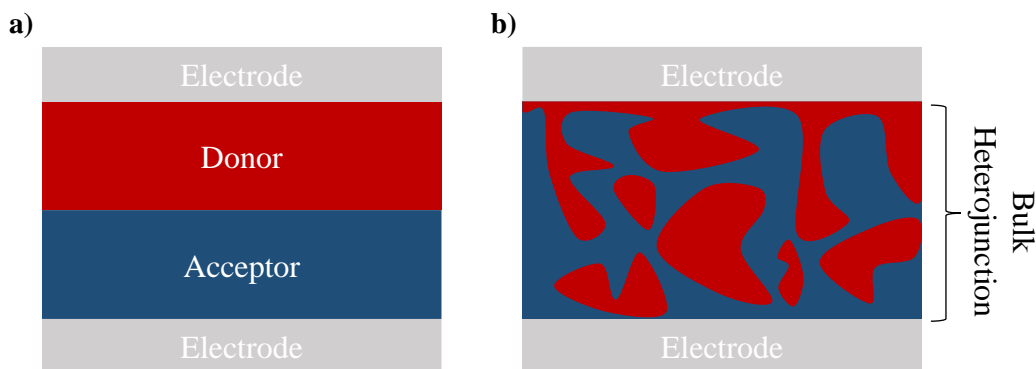


Figure 2.7: An approximation of **a)** a bilayer donor acceptor structure, **b)** a bulk heterojunction structure. Thicknesses here and in other figures are not displayed to scale.

2.3.2 Bulk Heterojunction Morphology

The way the donor and acceptor materials in the BHJ organize will have a significant impact on the performance of the OPV, with organization occurring over a number of length scales. These include the organization of OSCs within a domain of pure material, to the mesoscopic intermixing and phase-separation between the donor and acceptor.

On the smallest length scale, the organization of individual OSC molecules or chains is important. OSCs are usually polymers, oligomers or small molecules, all of which can be amorphous, crystalline or form a mixture of both. In crystalline domains, OSC moieties stack via π - π bonding between aromatic centres and lamellar stacking between non-conjugated portions, with the two mechanisms combining in a myriad of ways. A depiction of this can be seen in **Figure 2.8**.

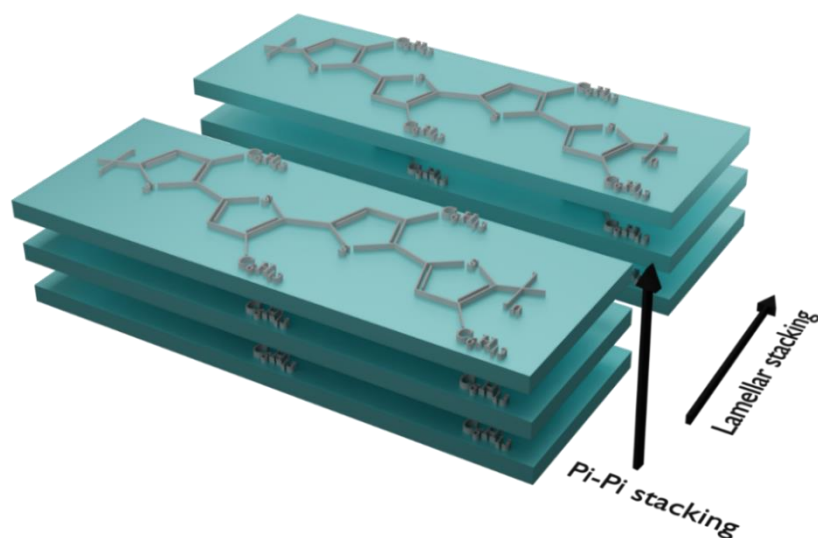


Figure 2.8: A depiction of the two main modes of stacking in conjugated organic molecules, with common donor polymer P3HT used as an example.

This stacking will influence charge carrier mobility, as differing levels of orbital overlap and order will change the rate at which hopping can occur. Generally, the highest mobility occurs along the polymer or molecular backbone (i.e. directly along the conjugation), followed by transport in the direction of π - π stacking, with hopping along the lamellar direction leading to the lowest mobility.¹⁸

This anisotropic mobility means orientation of the OSC moieties with respect to the substrate dictates the efficiency of charge carrier transport to the electrodes. Orientation of the π - π stacking parallel to the substrate is known as ‘face-on’ orientation, and is favourable for efficient device performance. In contrast π - π stacking perpendicular to the substrate is known as ‘edge-on’ orientation and results in reduced charge carrier mobility perpendicular to the device substrate. These orientations can be seen in **Figure 2.9**. The adoption of face or edge-on orientations has been shown to be influenced by OSC molecular structure¹⁹ and the surface energy of the underlying layers.²⁰

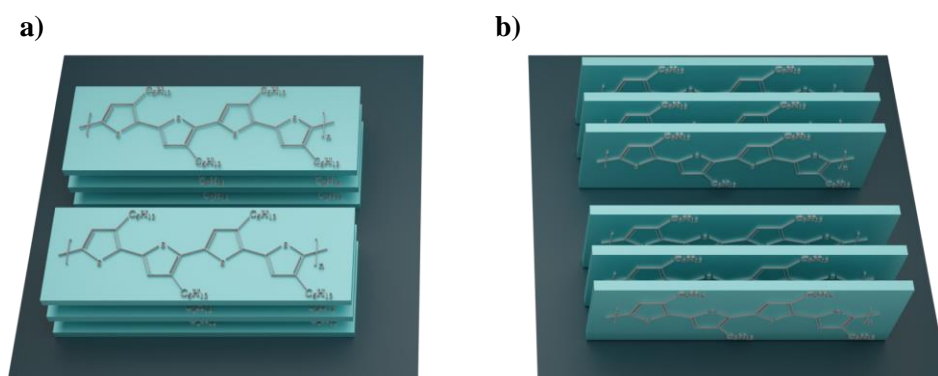


Figure 2.9: P3HT stacking in either **a)** face-on or **b)** edge-on modes.

Beyond molecular orientation, the relative fraction of crystalline or amorphous domains within each molecular phase is important, as crystalline regions will have improved mobility. Crystallinity can be promoted through molecular design and processing conditions.²¹ Generally, crystallinity is used to describe the amount of crystalline regions, rather than the quality of ordering within those regions, although both are important.²² A representation of a mixture of amorphous and crystalline regions of a donor polymer in a BHJ is shown in **Figure 2.10**. In systems where the acceptor is not a spherical molecule such as PCBM, acceptor crystallinity will play a more significant role. This is discussed in more depth in **Chapter 6**.

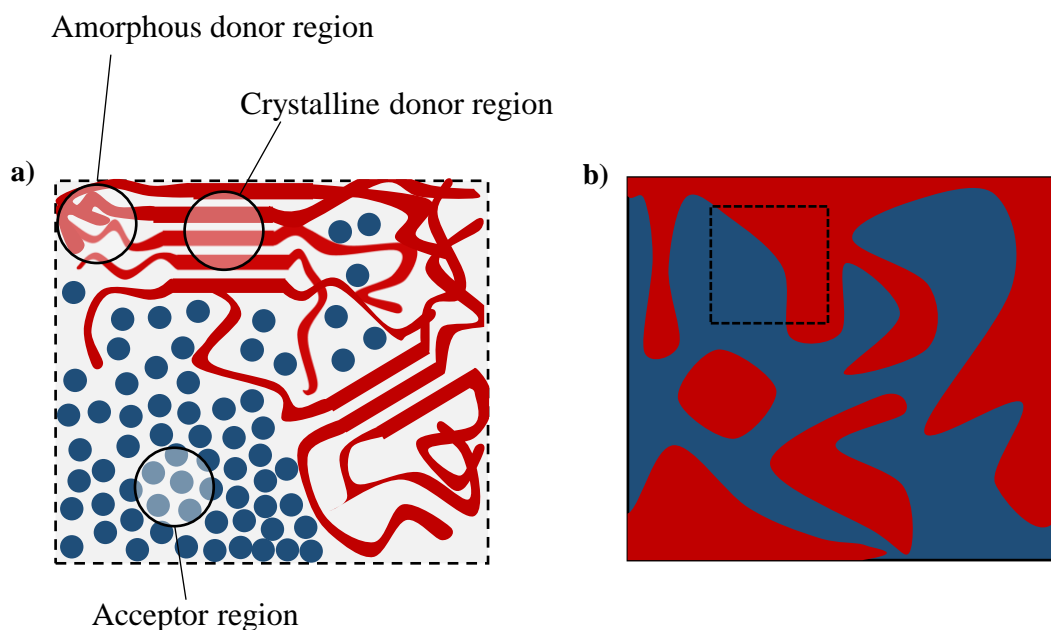


Figure 2.10: **a)** An approximation of how amorphous and crystalline regions of a donor polymer might be distributed in a BHJ. Here, the acceptor is in the form of a spherical molecule, such as in the case of PCBM, so acceptor crystallinity is ignored. **b)** A depiction of how (a) (the area of which is represented by the white box) would fit into an overall BHJ. Figure adapted from Radchenko *et al.*²³

Whilst mobility will be higher in crystalline regions, it is important to balance this with some fraction of amorphous regions to allow intermixing between donor and acceptor and create charge carrier transport pathways. For example, a small amount of acceptor within a donor phase will facilitate electron transport to the pure acceptor region and form a ‘percolation pathway,’ as shown in **Figure 2.11**. Too much intermixing will clearly encourage recombination, however too little acceptor in the mixed domain will also not allow percolation, so a balance of domain purity is required. The minimum amount of acceptor within donor regions to facilitate good electron transport is known as the percolation threshold.²⁴

Whilst amorphous regions facilitate intermixing, this is principally controlled by the miscibility between donor and acceptor, which is in turn dictated by their chemical structure. Miscibility will also dictate how the BHJ morphology changes over time and is discussed in greater depth in **Section 2.8.2**.

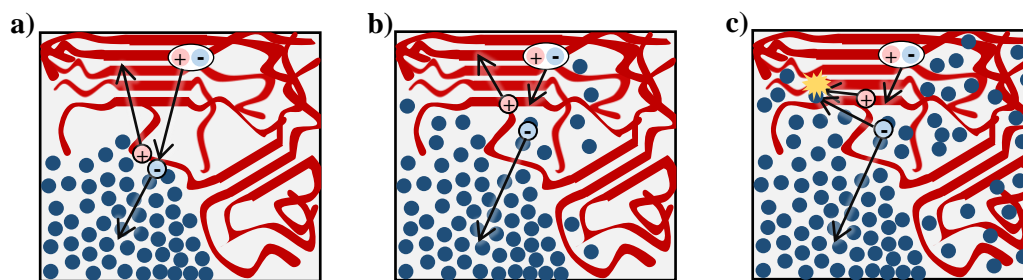


Figure 2.11: *a) A depiction of too high domain purity leading to improper percolation pathways, meaning excitons have too far to travel to an interface, b) the ideal percolation threshold, balancing exciton dissociation and recombination, c) too low domain purity, leading to increased recombination (an example of which is shown by the star). For these images the controlling factor is miscibility, rather than changes in crystallinity.*

The size of the phase separated domains is a critical parameter. Systems that are immiscible or have high crystallinity will form a reduced number of larger domains. This will lead to excitons having to travel a large distance before they can undergo dissociation at an interface. It will also result in extended pathways for dissociated charge carriers to travel before they can be extracted. Clearly, if domains are too small it will lead to the formation of poor percolation pathways and will cause reduced charge carrier mobility. For this reason, domain size must be carefully optimised.

On the largest scale, vertical segregation of components within a film, as shown in **Figure 2.12**, will play an important role in determining device performance. This can have both a positive and negative impact, depending on the degree of segregation and the architecture of the cell. Vertical segregation can be influenced by a range of factors, including solvent choice, the surface energy of each component and the surface energy of the layers below the BHJ.²⁵ Surface energy is discussed further in **Chapter 3**.

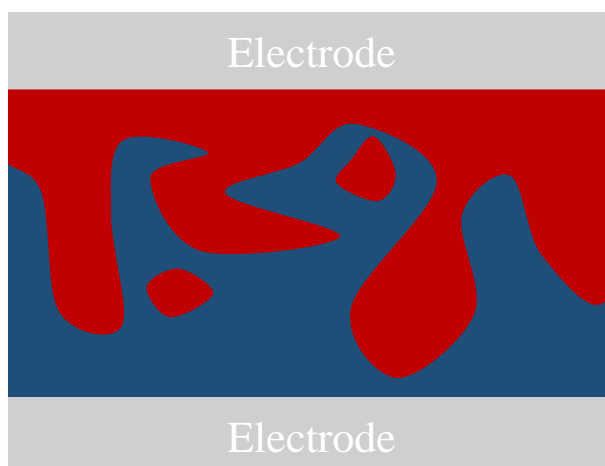


Figure 2.12: *A depiction of a BHJ with significant vertical segregation of the donor at the surface.*

The morphological properties of OSCs, such as crystallinity, can be described by various thermal transitions. As OSCs are generally partially disordered, they undergo a glass transition temperature, T_g . This describes the temperature at which amorphous portions of the OSC are no longer brittle, but become rubbery, and can partially diffuse in the same manner as a viscous liquid. T_g has been linked to speed of diffusion of a component within a BHJ,²⁶ which is discussed further in **Section 2.8.2**. Heating materials above T_g can trigger crystal growth, with this process known as cold crystallization (T_c) as it occurs below the material melting temperature (T_m). Both T_c and T_m values have been linked to properties associated with crystallization, such as tendency to crystallize.²⁷ All of these transitions can be determined using differential scanning calorimetry (DSC), discussed further in **Chapter 3**.

2.4 A Brief History of Organic Photovoltaics

Before discussing the structure and characterization of OPVs in detail, it is helpful to provide some context to the field.

The photovoltaic effect in OSCs was first established in 1959 by Kallman and Pope.²⁸ A two component solar cell was then demonstrated in the seminal work by C. W. Tang in 1986.¹⁶ Here a combination of a Copper Phthalocyanine (CuPc) acceptor and Perylene tetracarboxylic (PV) derived donor (both thermally evaporated) were fabricated into a simple bilayer structure and achieved an efficiency of 0.95%.

Photo-induced electron transfer to fullerene was discovered in 1992.²⁹ This discovery was followed by the use of a fullerene as an acceptor in an OPV the following year.³⁰ The first solution processable OPVs were shown in 1994,³¹ with solution processing offering improved device performance and accessibility compared to vacuum processing. The following year saw further success with the development of soluble fullerene derivatives³² such as PCBM, together with the introduction of a BHJ morphology.^{14,15}

For several years the field focused on optimising devices using a P3HT polymer-donor and PCBM acceptor, achieving efficiencies of 2-5%.³³ This was then followed by the development of several new donor polymers which subsequently led to improved device efficiencies. These include PCDTBT³⁴ and PBDTTT-CF³⁵ in 2009, leading to efficiencies exceeding 6% and 7% respectively; and PTB7 yielding an efficiency of 8.37% in 2011³⁶ and 9.2% in 2012.³⁷ The first device demonstrating an efficiency of 10% came following the synthesis of PffBT4T-2OD ('PCE11') in 2015,³⁸ followed by a derivative that had a 11.7% PCE in 2016.³⁹ Since then the efficiency of fullerene based OPVs have plateaued at ~12%.⁴⁰ The structures of some of the donor polymers mentioned here are shown in **Figure 2.13**.

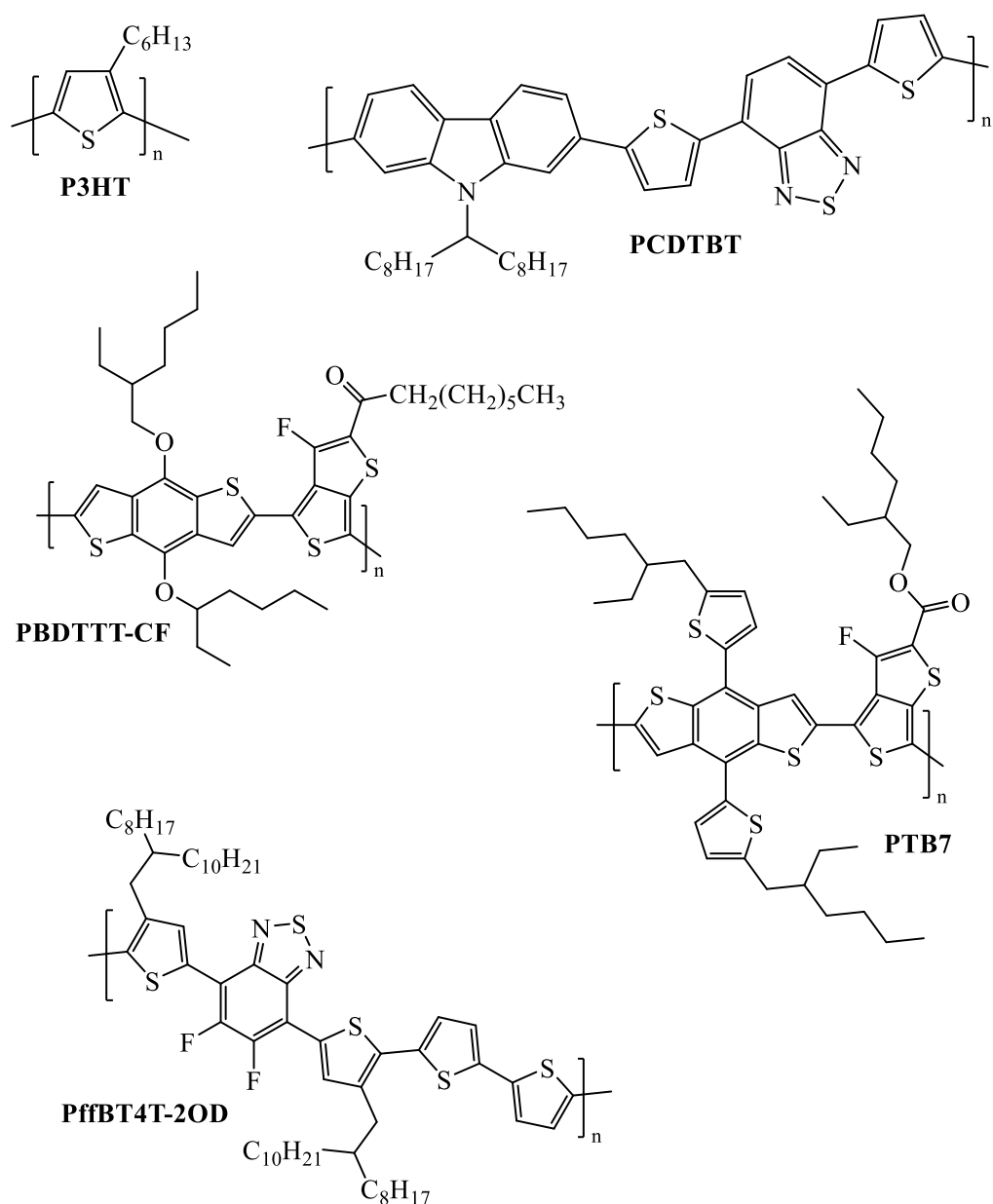


Figure 2.13: The chemical structure of a range of record setting polymer donors.

The OPV research field has recently been re-energised following the development of high efficiency acceptors that are not based on fullerenes, so-called non-fullerene acceptors (NFAs). Whilst NFAs have been studied for many years, they did not achieve comparable efficiencies to their fullerene counterparts until the development of the IDTT based acceptor ITIC in 2015, which realised devices having efficiencies exceeding 6% when combined with a PTB7-Th donor.⁴¹ NFA efficiencies then increased rapidly, reaching 11% in 2016⁴² and then 13% by 2017,⁴³ with both systems based on ITIC-derivatives.

The most recent improvements in efficiency have resulted from the use of a new type of NFA based on a BT core, known as the ‘Y-series’ of acceptors. First introduced in 2019 with BTP-4F (‘Y6’), the efficiency of devices based on these acceptors have risen from 15%⁴⁴ to around 19%. The current certified OPV record stands at a PCE of 18.7% and utilises the Y-series acceptor eC9-2Cl.⁴⁵ The structures of some of the small molecule acceptors discussed here are shown in **Figure 2.14**.

Recent work on NFA based OPVs have demonstrated very long exciton diffusion lengths⁴⁶ and charge separation between molecules with very low energy level offsets,⁴⁷ with the mechanism of both such effects still being under discussion.

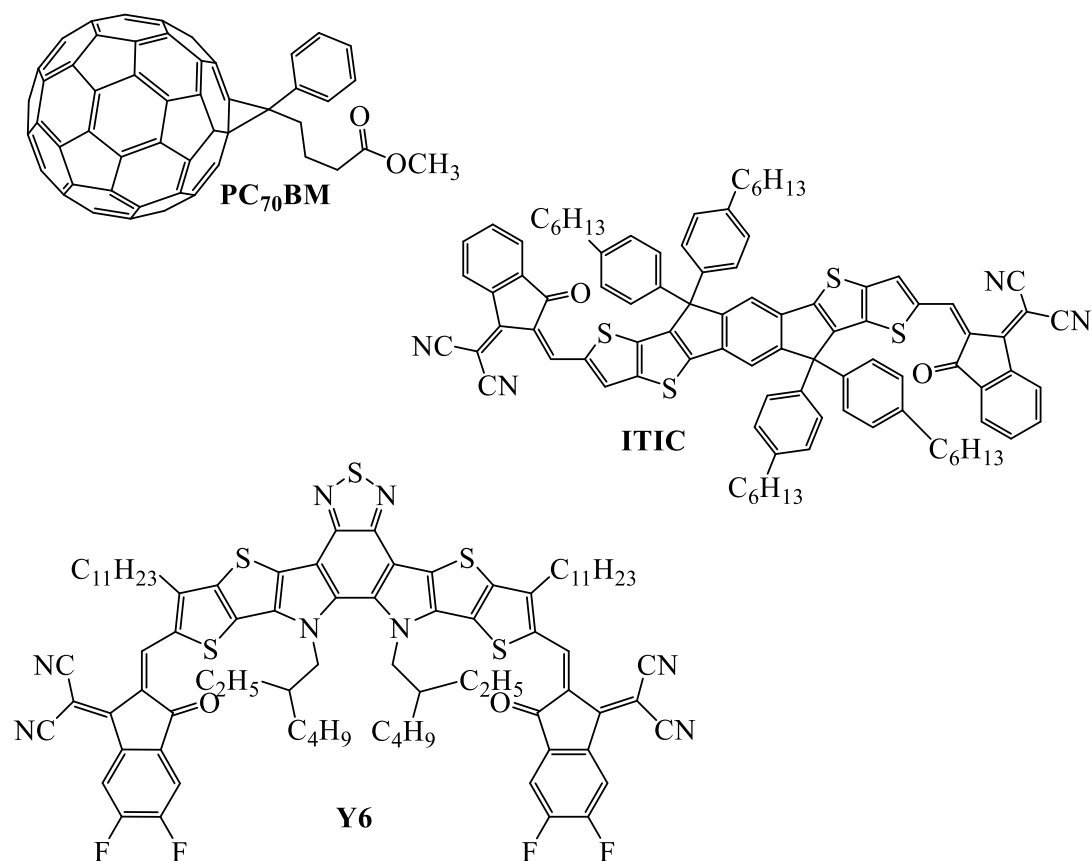


Figure 2.14: The chemical structure of a range of record setting small molecule acceptors.

Whilst other solar cell technologies may offer superior performance, OPVs remain an area of interest due to their potential for cheap, low temperature deposition from solution, allowing them to be coated on flexible substrates. Devices can also be created using fast printing technologies as will be discussed in **Section 2.7.2**. It is clear that other thin film solar

technologies also offer similar strengths, (namely perovskite solar cells). We discuss specific applications in which OPVs hold unique advantages in **Section 2.9.2**.

2.5 Organic Photovoltaic Architecture

2.5.1 Basic OPV Structure and Energy Level Cascades

As discussed above, the photoactive part of an OPV consists of a BHJ thin film, with an electrode on either side to extract charges. Usually, these electrodes sandwich charge transporting layers (CTLs), which are typically charge carrier selective and facilitate transport to the correct electrode. The arrangement of the CTLs will dictate whether the OPV is “inverted”, with the electron transporting layer (ETL) below the active layer; or “conventional” with the hole transporting layer (HTL) positioned below the active layer. These architectures are shown in **Figure 2.15**. In most cases OPVs are fabricated onto Indium-doped Tin Oxide (ITO) coated glass, which acts as the bottom electrode, with the top electrode almost exclusively formed from silver or aluminium.

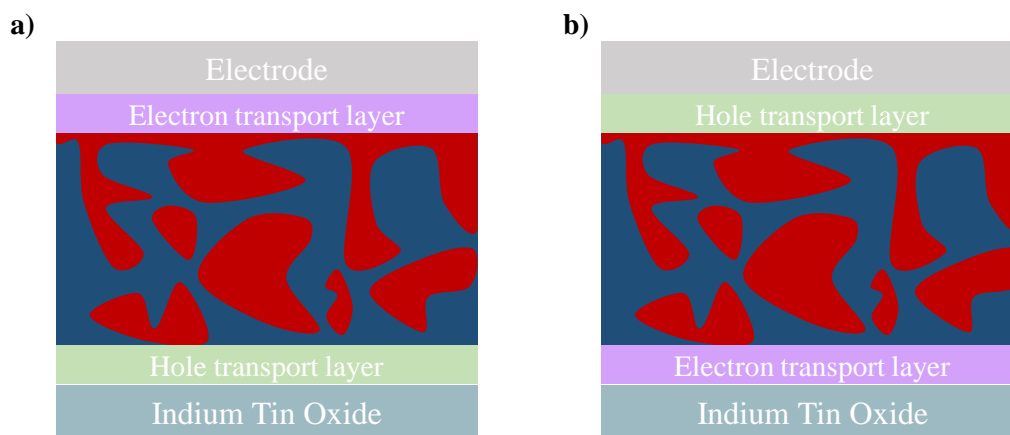


Figure 2.15: The architecture of a **a) conventional OPV**, **b) inverted OPV**.

The choice of the CTL is dictated by the material energy levels, which will ideally facilitate an energy ‘cascade’, as shown in **Figure 2.16**, and encourage the formation of a built-in field, as discussed in **Section 2.6.2**. This cascade encourages the movement of electrons to the cathode and holes to the anode.

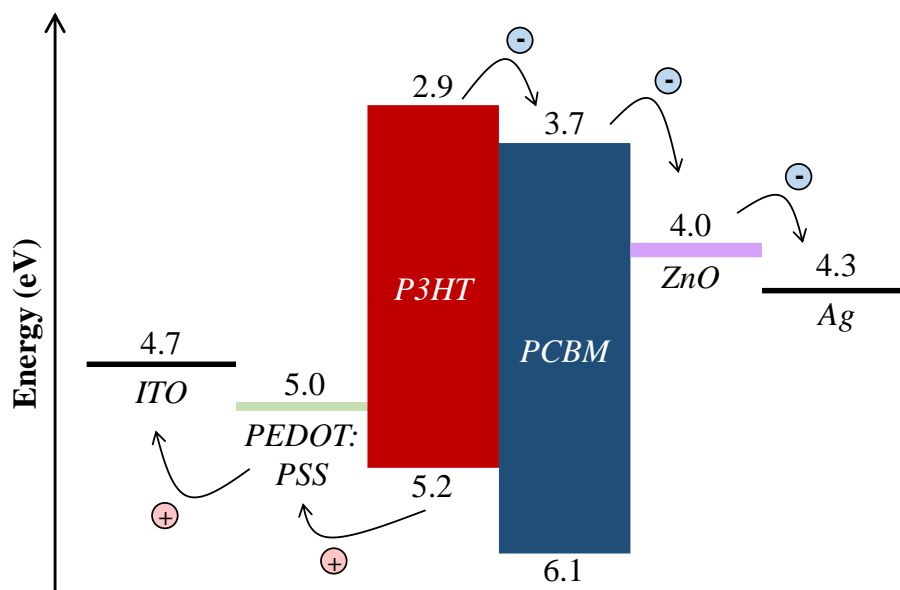


Figure 2.16: An example of the energy cascade produced by appropriate CTL choice in a conventional architecture P3HT:PCBM system. Here PEDOT:PSS acts as the HTL, zinc oxide (ZnO) as the ETL, ITO as the anode and silver as the cathode.

2.5.2 Active Layer Components

The choice of OSCs in the active layer of an OPV is determined by several factors, including the desired level of crystallinity, stability, absorption range, miscibility, and the relative offsets between donor and acceptor energy levels. Ideally, the combined absorption of the donor and acceptor should cover as much of the visible regime as possible. OSCs are classified according to their band gap, and are divided into wide band gap materials (>1.8 eV) such as P3HT; medium band gap materials (1.6 -1.8 eV) such as PCDTBT; or narrow band gap materials (>1.6 eV) such as PTB7.

Generally, high performing donors and NFAs have an extended conjugated “core” which facilitates electron delocalisation and allows close molecular packing due to their planar nature.⁴⁸ There is now a growing trend to reduce the synthetic complexity of active layer materials or choose those that can be made using cheaper and less demanding routes (see **Section 2.9**). Whilst small molecule donors and polymer acceptors have seen some success,⁴⁹ the majority of research focuses on polymer donors and small molecule acceptors, and such materials will be discussed exclusively in this thesis.

2.5.2.1 Acceptor Considerations

Whilst fullerene-based acceptors (such as PCBM) dominated the OPV field for many years, they have a number of key weaknesses including low absorption in the visible regime,

limited energy level tuneability (restricting donor choice), expensive purification requirements and poor photo- and thermal stability.⁴⁸ The use of NFAs has allowed many of these limitations to be overcome. For example, Y-series based acceptors absorb well into the infrared,⁴⁵ some materials have been designed with easy synthesis in mind,⁵⁰ and several have shown excellent long-term stability.⁵¹

Typically, NFAs are designed around alternating ‘acceptor’ and ‘donor’ units. The NFA ITIC is a classic example of this and is based on an electron-donating IDTT core which is positioned between electron-withdrawing INCN units. The Y-series of acceptors takes this concept further, and uses an A-D-A’-D-A structure. Indeed, Y6 consists of a fused core D-A’-D core of TT-BT-TT which is positioned between two 2FIC A units. Such structures are shown in **Figure 2.17**.

Beyond conjugated core choice, acceptor molecules can be modified via changing end groups (usually with the aim of tuning the energy levels), and through side chain modification (usually with the aim of tuning solubility).⁵²

2.5.2.2 Donor Considerations

Most recently reported highly performance donor polymers are based around a ‘donor-acceptor’ structure. These are often based on a BDT electron-donating group together with a variety of other electron-withdrawing moieties.⁴⁸ The record efficiency for OPV (18.7%)⁴⁵ was reached using a PBQx-TF donor that incorporated alternate BDT and DTQx units. Again, chemical modification to tune energy levels and solubility of polymer donors is a commonplace research strategy.⁴⁸

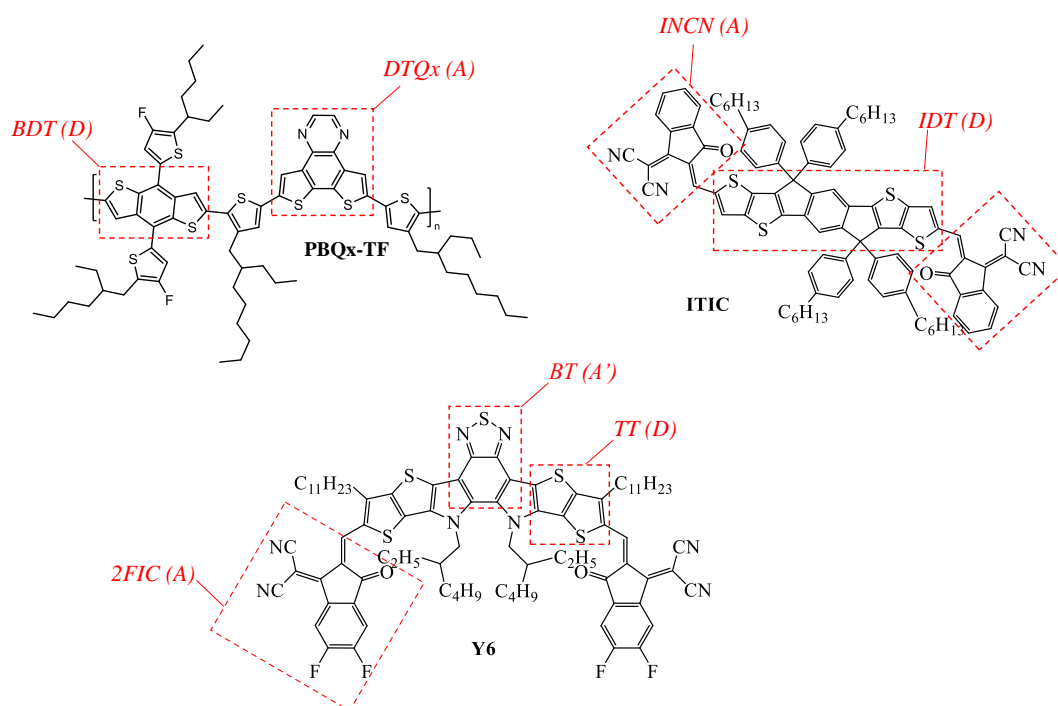


Figure 2.17: A visualization of how high performing donor and acceptor materials are made of alternating donor & acceptor sub-units.

2.5.3 Charge Transport Layers

CTLs primarily facilitate the transport of the correct charge carrier to the appropriate electrode. However, they can also perform multiple additional functions, including acting as charge carrier blocking layers, surface energy modifiers and protective or stabilising layers.⁵³ Often CTLs are solution processed from solvents that are orthogonal from those used to process the active layer. However, they can also be deposited via thermal evaporation.

Typically, CTLs are either organic semiconductors (polymers or small molecules), metal oxides, or electrolytes. Materials selected on the basis of their energy levels and charge transporting properties.

2.5.3.1 Hole Transport Layers

The most commonly used HTL is the polymer blend PEDOT:PSS, which can be processed in aqueous solutions and has good charge transporting properties. PEDOT:PSS is still used in many record breaking papers⁴⁵ but has known instabilities, including undergoing reactions with ITO as a result of its acidic nature. It can also absorb water which can lead to reactions with the active layer.⁵⁴

More stable alternatives to PEDOT:PSS include metal oxides such as MoO_x, NiO_x and VO_x. These are typically deposited via thermal evaporation but in some cases can be solution processed.⁵⁵⁻⁵⁷ Generally OPVs conventionally use PEDOT:PSS as the bottom HTL, with inverted OPVs using evaporated MoO_x on top of the active layer. Such a strategy avoids potentially detrimental contact between water and the photoactive layer.

A recent and exciting development in the area of HTLs is the use of carbozole based self assembled monolayers (SAMs); an approach that has yielded great success in the area of perovskite solar cells.⁵⁸ Such SAMs have only recently been applied to OPVs, specifically the use of the SAM 2PACz,⁵⁹ and show exceptional promise in terms of charge transporting abilities, high-stability and cheap, facile, processing.

2.5.3.2 Electron Transport Layers

A wider variety of organic materials are used as ETLs with promising properties observed in amino containing polymers such as PFN-Br,⁶⁰ PDINN⁶¹ and PNDIT-F3N⁶² (see **Figure 2.18**). These materials usually exhibit good stability and are all soluble in alcohol, and so easily processed. Generally, polymeric ETLs are favoured for deposition on top of the active layer.

For inverted OPVs, ZnO is favoured as the bottom ETL due to the fact that it is generally used as a thicker film (~40 nm compared to ~5 nm for an amino polymer) allowing it to be used to planarize the ITO.⁵³ However ZnO has been shown to undergo UV induced instability,⁶³ especially when used with NFAs. There has been some exploration of alternative inorganic ETLs such as SnO₂,⁶⁴ but this is not widespread. Generally, ZnO is not used on top of the OPV active layer due to high temperature requirements in its deposition.

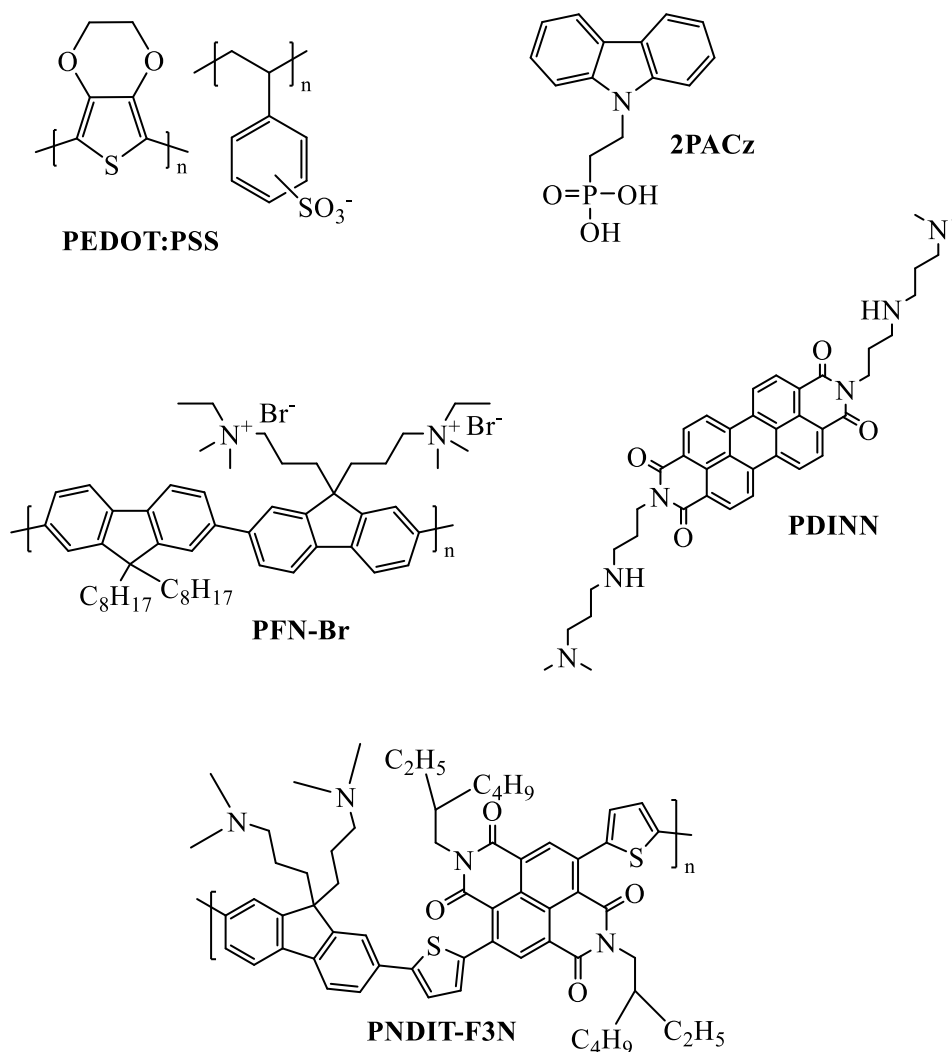


Figure 2.18: The chemical structures of a range of organic CTLs.

2.5.4 Specialist Systems

Some systems do not follow the typical BHJ stack detailed above and a selection of notable examples of this are discussed below.

2.5.4.1 Layer by Layer Systems

Despite the dominance of the BHJ structure over a bilayer planar heterojunction (PHJ), there have been recent developments in the use of highly efficient pseudo-PHJ systems. These have been partially driven by the increased exciton diffusion lengths of modern OSCs, such as Y6 and PM6.⁶⁵ In these systems, (which are fabricated using a so called ‘layer by layer’ technique), the donor and acceptor are deposited sequentially, followed by some degree of mixing. This method is particularly useful for cell fabrication over a larger area as it negates the need for careful morphology control of the active layer and may play a role in OPV scale up in the future.⁶⁶

2.5.4.2 Single Component Systems

In an attempt to improve morphological stability and reduce material complexity, there is a small but growing interest in OPVs fabricated from a single component active layer, the efficiencies of which have recently reached 11%.⁶⁷ The processes of exciton generation and dissociation in these materials has not yet been fully explored but is presumed to operate via transfer between donor and acceptor style ‘blocks’ along a single molecule chain.

2.5.4.3 Tandems

As mentioned in **Section 2.1.4**, a tandem solar cell uses two different solar cell active layers, (usually separated by an interconnecting layer) to maximise the region of the solar spectrum that is absorbed. Recent developments of tandem solar cells include a record 23.5% perovskite-organic tandem⁶⁸ and a record 20.3% organic-organic tandem,⁶⁹ the structure of which is shown in **Figure 2.19**.

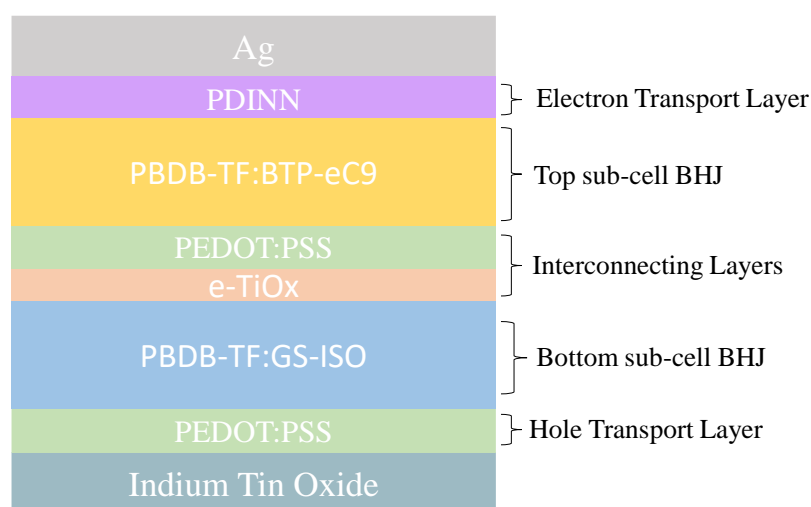


Figure 2.19: The cell architecture of the current organic-organic tandem record holder, using PBDB-TF as a donor polymer and BTP-eC9 and GS-ISO as two different small molecule acceptors.

2.5.4.4 Ternary Systems

Beyond a simple two component system, great success has been found by introducing a third OSC into the active layer in a so called ‘ternary’ system. This approach was first reported in 2010⁷⁰ and recently used in the current 19% PCE record OPV device.⁴⁵

The third component of a ternary cell is typically chosen to extend the absorption regime of the active layer but can also perform multiple additional functions. These include generating an energy cascade, facilitating charge transport, morphological control, and acting as a morphological stabiliser.⁷¹

A third component acting in a charge transport role is normally categorised in one of three ways, shown in **Figure 2.20**. Firstly, and most commonly, it can perform charge transfer, where it both generates excitons and provides charge transport pathways between donor and acceptor. Alternatively, the third component can be used to facilitate energy transfer (FRET or DET) between donor and acceptor without generating its own excitons. Lastly, it can also be used in a parallel-linkage strategy where it alloys with another component. Here, it will be primarily performing another function, such as extending absorption, but is miscible enough with the donor or acceptor to form essentially one phase. This allows it to participate in charge transport in the same manner as the component it is alloyed with.⁷²

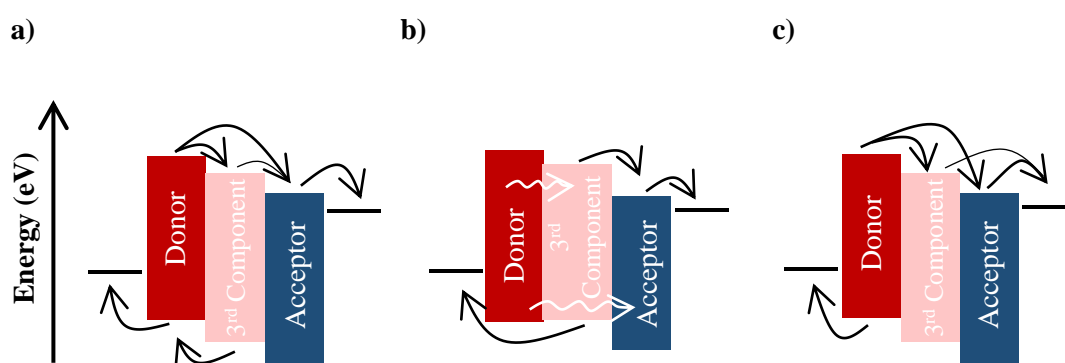


Figure 2.20: Examples of possible mechanisms of a ternary system: **a)** charge transfer, **b)** energy transfer, **c)** parallel-linkage, where the third component is alloyed with the acceptor. Figure adapted from Yu et al.⁷²

2.6 Characterizing Organic Photovoltaics

2.6.1 The Equivalent Circuit Model

In order to characterise an OPV, we must first consider the model of a simple p-n junction solar cell. All p-n junctions will have both a diffusion current (movement of carriers from high to low concentration) and drift current (movement of carriers driven by the in-built field) which act in opposition to each other. In the dark, the junction will act as a diode, meaning current will only flow in one direction. This is because upon application of a sufficient forward bias, the in-built electric field is overcome and the diffusion current increases. Upon application of a reverse bias, however, the diffusion current is significantly reduced. The drift current is small in both bias directions as it is limited by the production of

minority carriers, and so upon reverse bias very little current flows. In contrast, upon forward bias the diffusion current dominates. This current is known as the diode current, symbolised as J_D .

Without bias, under illumination, the minority carriers on both sides of the junction increase. This correspondingly increases drift current and generates a photocurrent, defined as J_{ph} . We can model this relationship between J_{ph} and J_D using the Shockley ideal photodiode equation:⁷³

$$J = J_{ph} - J_D = J_{ph} - J_0 \left[\exp\left(\frac{qV}{k_B T}\right) - 1 \right] \quad (\text{Eq. 2.2})$$

Here J is the current generated by the device, J_0 the diode reverse saturation current, q the elementary charge, V the applied voltage, k_B Boltzmann's constant and T the temperature.

In order to account for 'real world' losses, the ideal photodiode equation is normally modified with two sources of resistive losses. This is formalised by an equivalent circuit model⁷⁴ as shown in **Figure 2.21**.

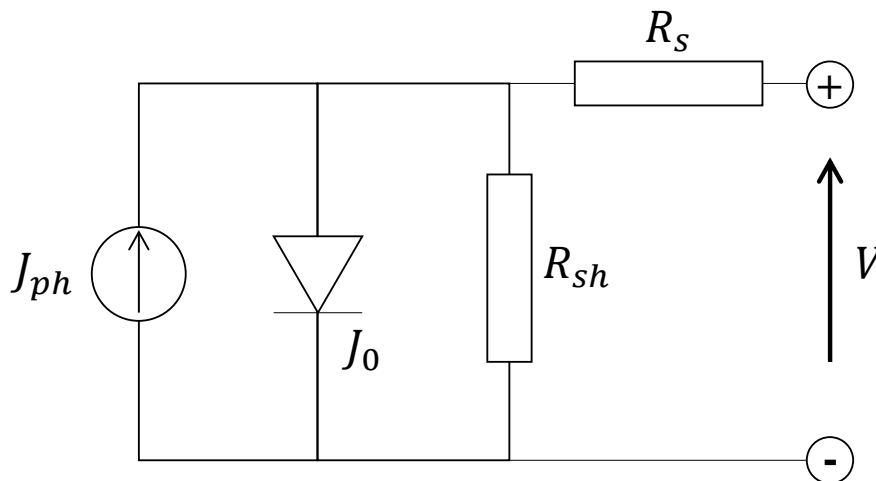


Figure 2.21: An equivalent circuit model for a solar cell, with two sources of resistive losses impacting the voltage generated as a result of the photocurrent.

The description of the solar cell is then expressed using:

$$J = J_0 \left[\exp\left(\frac{q(V - JR_s)}{nk_B T}\right) - 1 \right] + \frac{V - JR_s}{R_{sh}} - J_{ph} \quad (\text{Eq. 2.3})$$

here R_s is the series resistance, R_{sh} the shunt resistance and n the diode ideality factor.

The first of these new terms, R_s , expresses the resistance within the cell to current flow and so is ideally small. R_{sh} is the resistance to current leaking within the device and so is ideally large. These terms are discussed further in **Section 2.6.3.3**. The term n , is a measure of recombination. For an ideal diode $n = 1$, but in reality, it can exceed 2. Methods of estimating ideality factor for a PV device can be seen in **Section 2.6.3.2.1**.

2.6.2 Modifications of the Equivalent Circuit Model for OPVs

There are important differences in OPVs that must be considered for the equivalent circuit model to apply. Unlike in a p-n junction, free charge carriers are not initially formed in an OSC and the exciton must diffuse to the donor acceptor interface before dissociation. The free charge carriers (electrons / holes) will then be located mostly within the ETL / HTL respectively where they can be considered majority carriers.

Whilst there is no traditional p-n junction depletion region within an OPV, the energy level cascade shown in **Figure 2.16** will generate a built-in electric field in the same way, meaning drift current will dominate at low applied bias. At higher applied bias however the diffusion current will dominate as the built-in field is overcome.⁷⁵

2.6.3 Solar Cell Testing Parameters

By using the equivalent circuit model and measuring the photocurrent produced by a device under illumination, several important parameters can be extracted. A typical current density-voltage (or ‘*JV* sweep’) can be seen in **Figure 2.22**. Current density is the current per unit area produced by the cell, to allow for comparison of cells of different area. Standard illumination procedure is the AM1.5 spectrum, using a light-source at an intensity of 1000 W m⁻². Four main parameters are derived from such a *JV* sweep and are then used to compare devices. These terms will each be discussed in turn below.

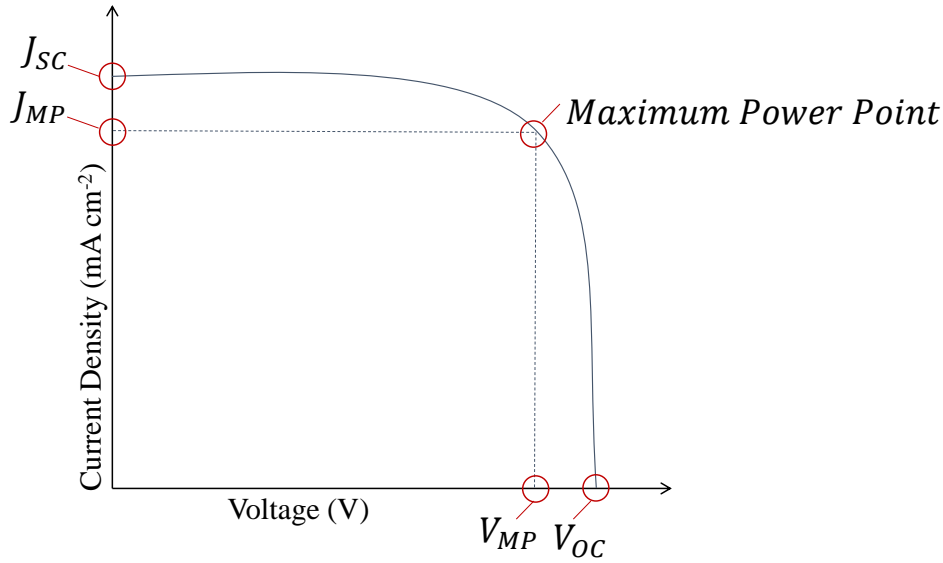


Figure 2.22: An illustration of a typical 'JV' sweep for a solar cell, with several important parameters labelled.

2.6.3.1 Short Circuit Current Density

The short circuit current density (J_{SC}), is defined as the current output of the cell without any applied voltage. The only contribution to current output here is the cell photocurrent however J_{SC} will differ from J_{ph} as a result of various loss mechanisms, such as recombination and charge extraction losses. In an OPV, charge carrier transport at J_{SC} will be dominated by drift due to the built-in field within the device. State of the art NFA based devices demonstrate J_{SC} values in excess of 25 mA cm^{-2} .⁴⁵

As the J_{SC} is dependent on the number of free charges generated, it is influenced by material band gap and film thickness, as well as charge carrier mobility and morphology. Clearly a sufficient active-layer thickness is required to maximise light absorption, however too thick an active layer will result in increased recombination which will correspondingly reduce charge generation and J_{SC} .

Measuring the light intensity dependent J_{SC} can be useful, which usually has a dependence given by:

$$J_{SC} \propto P_{in}^S \quad (\text{Eq. 2.4})$$

where P_{in} is light intensity and S is an exponential factor that can be extracted from the plot of J_{SC} vs P_{in} . The closer S is to 1, the lower the rate of bimolecular recombination is within in the device.⁷⁶

2.6.3.2 Open Circuit Voltage

2.6.3.2.1 The Origin of Open Circuit Voltage

The open circuit voltage (V_{OC}) is defined as the point where drift and diffusion currents are equal and the net device current output is zero. From the equivalent circuit model (neglecting resistance), V_{OC} can be expressed using:⁷³

$$V_{OC} = \frac{nk_B T}{q} \ln \left(\frac{J_{ph}}{J_0} + 1 \right) \quad (\text{Eq. 2.5})$$

This indicates that V_{OC} is directly proportional to the ideality factor, n , a relation that can be extracted from illumination dependent V_{OC} measurements, which have the form:

$$V_{OC} \propto \frac{nk_B T}{q} \ln (P_{in}) \quad (\text{Eq. 2.6})$$

Consequently, n can be extracted from a plot of V_{OC} vs P_{in} when plotted on a lin-log scale. In an ideal diode, $n \approx 1$, however, as n increases towards 2 it suggests the device becomes dominated by trap-assisted recombination rather than bimolecular recombination. When $n < 1$, it suggests that surface recombination dominates.⁷⁷ The ideality factor can also be calculated from dark JV curves, which will not be discussed here. A comparison of the validity of these methods has been discussed by Kirchartz *et al.*⁷⁸

2.6.3.2.2 Relationship between V_{OC} and the Effective Energy Gap

The maximum achievable V_{OC} for an OPV device is usually approximated as the energy gap between the LUMO (or electron affinity) of the acceptor and the HOMO (or ionisation energy) of the donor.⁷⁹ This is shown in **Figure 2.23**, with this energy difference being known as the effective energy gap (E_g^{eff}). The origin of this relationship is linked to the energy of the CT state of the system and is defined through the energy gaps of the donor and acceptor and their relative offsets. There is clearly a balance between maximising E_g^{eff} (to improve V_{OC}), using narrow band gap materials (to maximise the wavelengths of light absorbed and improve J_{SC}) and ensuring a sufficient energy level offset to drive exciton dissociation.⁸⁰

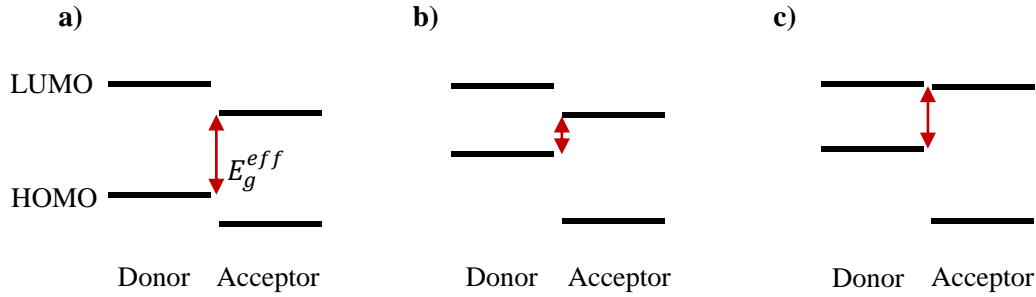


Figure 2.23: **a)** The effective energy gap of a system, which is roughly equivalent to the maximum obtainable V_{OC} of that donor acceptor combination, **b)** the impact of a narrower band gap donor, which will broaden light absorption but reduce effective energy gap, **c)** the impact of reducing LUMO offset, which will increase effective energy gap but reduce exciton dissociation driving force.

In reality, V_{OC} will differ from E_g^{eff} due to a multitude of factors, including recombination, temperature and morphology of the BHJ.⁷³

2.6.3.2.3 Energy Level Offset Requirements

In fullerene based systems, the minimum required LUMO-LUMO (or ‘EA’) offset between donor and acceptor has been experimentally determined to be ~ 0.3 eV.⁸¹ However, it has been shown in some state of the art NFA systems that an offset is not required for efficient charge generation.^{47,82} This result remains controversial and a recent comprehensive study¹² of this phenomenon in NFA based systems concluded that the use of cyclic voltammetry to determine the energy levels of the solid films is often unreliable, meaning offsets may be underestimated. The work also concluded that whilst an EA offset was not always necessary in high efficiency NFA systems, an IE offset was necessary to facilitate hole transfer from NFA to donor.

2.6.3.2.4 Voltage Loss in OPVs

The voltage losses (V_{loss}) in an OPV are quantified using:

$$V_{loss} = \frac{E_{gap}}{q} - V_{OC} \quad (\text{Eq. 2.7})$$

where E_{gap} is the smallest band gap among the donor and acceptor. V_{loss} includes losses due to energy level offsets (as without an offset, E_{gap} and V_{OC} would technically be equivalent), together with losses from non-radiative recombination. V_{loss} in state-of-the-art OPVs varies but typically exceeds 0.7 V; a loss that is much higher than many other solar cell technologies, and as such is an active area of research.⁸³

2.6.3.3 Fill Factor

The fill factor (FF) of a PV device is effectively an assessment of the ‘squareness’ of the JV curve and can be defined using the maximum power point shown in **Figure 2.22**:

$$FF = \frac{J_{MP}V_{MP}}{J_{SC}V_{OC}} \quad (\text{Eq. 2.8})$$

For an ideal cell, the FF approaches 100%. In reality the presence of series and shunt resistances reduces the value to ~80% for state-of-the-art systems.⁸⁴ The influence of each type of resistance can be seen in **Figure 2.24**.

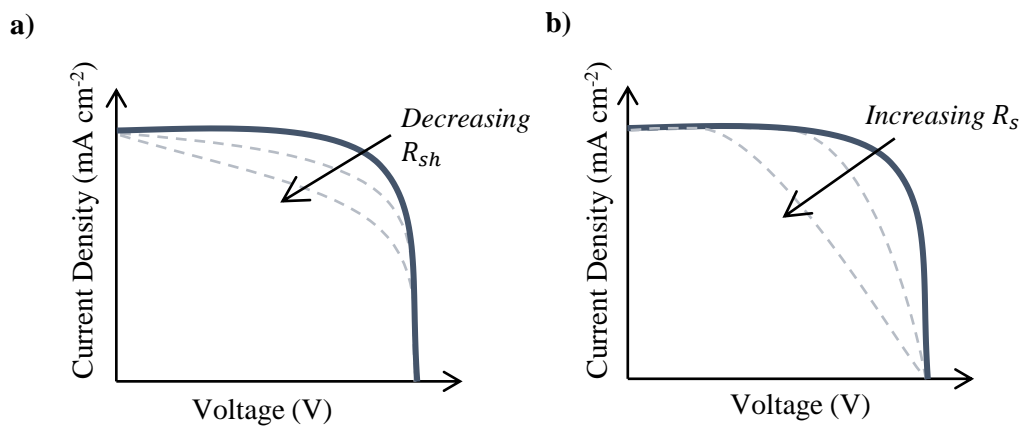


Figure 2.24: The influence on a JV sweep of **a)** shunt resistance, where the curve is mostly affected near J_{SC} , **b)** series resistance, where the curve is mostly affected near V_{OC} .

The series and shunt resistance values can be estimated by the slope of different parts of the JV curve, with the slope at J_{SC} defining the inverse shunt resistance while the slope at V_{OC} defines the inverse series resistance.

Because of the effect of resistance on JV curve shape, the FF can be improved by either reducing series resistance - for example by reducing layer thickness or reducing traps, or by increasing shunt resistance - for example by improving layer quality and reducing pinholes. Domain purity has been shown to have a strong influence on FF due to its influence on bimolecular recombination.⁸⁵

2.6.3.4 Power Conversion Efficiency

The power conversion efficiency (PCE) is defined by a combination of V_{OC} , J_{SC} and FF and compares the power generated by a cell with the power of the incident light:

$$PCE = \frac{V_{OC} J_{SC} FF}{P_{in}} \quad (\text{Eq. 2.9})$$

here, P_{in} is usually 1000 W m^{-2} . It is clear from **Equation 2.9** that PCE is equally dependent on each of the parameters discussed, meaning high efficiency values can only be obtained by optimising V_{OC} , J_{SC} and FF simultaneously.

2.6.4 Space Charge Limited Region

JV sweeps can be used to estimate charge carrier mobility if the charge transporting layers on either side of the active layer are chosen carefully. To study the movement of just one type of charge carrier, both CTLs must be of the same type (e.g. both HTLs to study hole mobility), in order to block the movement of the opposite carrier. Such types of device are known as hole-only or electron-only, or collectively as unipolar devices. In unipolar devices at high applied electric fields, the current is dependent on the charge carrier mobility, as opposed to the charge carrier concentration as in normal devices. This is known as the space charge limited region, further discussion of which can be found in the literature.⁸⁶

To extract mobility in the space charge limited region, the Mott-Gurney equation can be used:

$$J = \frac{9}{8} \varepsilon_r \varepsilon_0 \mu \frac{V^2}{L^3} \quad (\text{Eq. 2.10})$$

here ε_r represents the relative permittivity of the material (assumed to be 3 typically in literature),⁸⁷ ε_0 is the permittivity of the free space, μ is the charge carrier mobility, L is the thickness of the active layer and V represents the voltage across the device, typically defined as:

$$V = V_{applied} - V_{built-in} - V_{series} \quad (\text{Eq. 2.11})$$

where $V_{built-in}$ and V_{series} can be estimated from other measurements which will not be discussed here.⁸⁸

Commonly the Mott-Gurney law is modified using the Poole-Frenkel model⁸⁶ to account for the dependence of charge carrier mobility on electric field in OSCs, as defined by **Equation 2.12**:

$$J = \frac{9}{8} \varepsilon_r \varepsilon_0 \mu \frac{V^2}{L^3} \exp\left(0.89\beta \frac{\sqrt{V}}{\sqrt{L}}\right) \quad (\text{Eq. 2.12})$$

here β is the field-activation factor, which is fitted alongside mobility.

2.6.5 External Quantum Efficiency

An important characteristic of an OPVs is its external quantum efficiency (EQE). This is defined as:

$$EQE = \frac{Jhc}{P(\lambda)\lambda q} \quad (\text{Eq. 2.13})$$

where h is Planck's constant, c the speed of light, λ the wavelength of light and $P(\lambda)$ the incident power of the light as a function of wavelength. The EQE measures the percentage of extracted charges relative to the number of incident photons at any specific wavelength. EQE encompasses a range of losses, including parasitic absorption, reflection, recombination and losses of light below the band gap. It can be performed by monitoring the photocurrent of a device as a function of wavelength. As the EQE represents the spectral response of the cell, it can be used to provide an estimate for J_{SC} by integrating EQE over visible and NIR wavelengths.⁸⁹

2.7 Fabrication of Organic Photovoltaics

OPVs are typically processable from solution. This is a significant advantage as it potentially allows for 'roll to roll' processing. Here, devices would be fabricated onto a flexible substrate passed between large rollers whilst layers are printed, permitting fast and cheap large-scale PV manufacture. The most common method of lab scale device fabrication is spin coating, however there is growing interest in the exploration of scalable techniques appropriate for roll-to-roll manufacture. While most lab scale devices typically have active areas $<1 \text{ cm}^2$, work on scalable techniques has now realised OPV modules having an area of 36 cm^2 with efficiencies exceeding 14%.⁹⁰

2.7.1 Spin Coating

Spin coating is a widespread technique used to fabricate thin films from solution. Here, a solution is deposited onto a substrate, typically via pipette, whilst (or before) the

substrate is spinning. Centrifugal forces then distribute the solution across the surface, with rapid airflow accelerating solvent evaporation. This leads to rapid drying and the creation of a thin film. The process is shown in **Figure 2.25**.

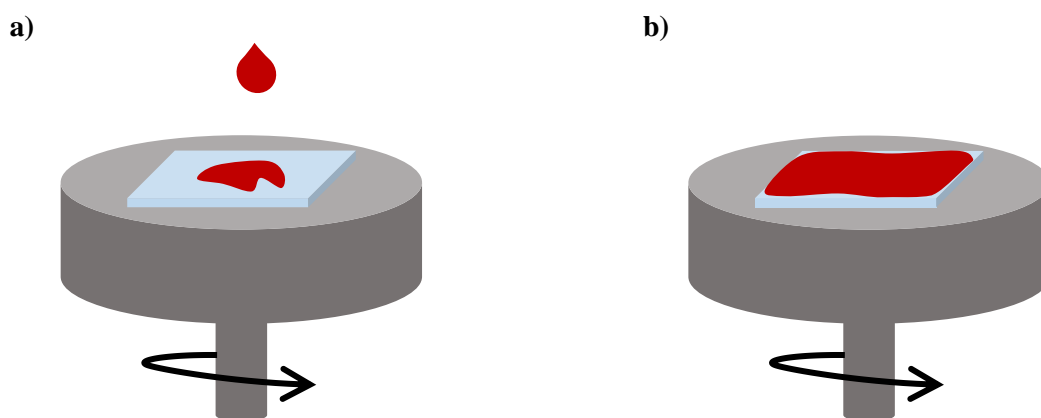


Figure 2.25: A depiction of spin coating: **a)** the solution is dropped onto a spinning substrate, **b)** the spinning forces spread the solution out into a thin film.

Film thickness is mostly influenced by the speed of the rotation, expressed in **Equation 2.14**:⁹¹

$$d = k\omega^\alpha \quad (\text{Eq. 2.14})$$

Here d is film thickness, k and α are empirical constants related to the solution properties and ω is the angular velocity. Whilst spin coating is a reliable processing technique, it can waste a significant amount of expensive material and so is not appropriate for large scale manufacture.

2.7.2 Scalable Deposition Methods

Scalable deposition methods are those associated with reduced solution waste compared to spin coating, and are therefore considered more appropriate for large-scale OPV manufacture. Such methods can be broadly divided into meniscus-based methods (where solution is spread via movement of the meniscus) and droplet-based techniques (where the film is formed by deposition of many individual droplets).⁷⁷

Most experiments on lab scale scalable deposition methods have concentrated on meniscus-based techniques, as these can often be used to create high efficiency devices. However, the precise control of head height and head to substrate distance places limitations on large scale manufacture, especially over non-planar substrates.⁷⁷ Many meniscus-based techniques are also slow which may restrict their industrial relevance. Furthermore, precise

control of the coating-area is difficult (for example creating a pattern rather than a continuous film).

Droplet-based techniques are less common in lab-scale research due to cost and a wider range of parameters that must be controlled. Here, factors such as solution viscosity and surface tension are important and optimisation of the film deposition process can be more difficult. However, once established, droplet-based techniques are compatible with non-planar substrates as close contact between head and substrate is not required. Furthermore, such techniques can potentially reach higher coating speeds than can be achieved using meniscus-based alternatives.⁷⁷

2.7.2.1 Meniscus-Based Techniques

2.7.2.1.1 Blade Coating

The most commonly used meniscus-based technique is blade coating, where a solution is deposited onto a substrate and then spread into a thin film via a blade being dragged across the surface. The distance between the blade and surface is the main parameter that controls thickness, as expressed in **Equation 2.15**:⁹¹

$$d = \frac{1}{2} \left(g \frac{c}{\rho} \right) \quad (\text{Eq. 2.15})$$

Here g is the blade to surface gap, c is the solid concentration of the solution and ρ is the density of the material. Blade coating has many advantages, including reduced waste. Indeed some estimates indicate that blade coating only uses 20% of the material that is used in spin coating,⁹² and as little as 5% of the initial solution is lost.⁹¹ This technique can be used to create high efficiency devices, with small scale devices having a PCE of 17%⁹³ and module-scale devices having PCEs of over 14%⁹⁴.

2.7.2.1.2 Slot-Die Coating

Slot-die coating is a similar technique to blade coating, and has also been explored extensively in lab scale research. Here, a solution is pumped through a head onto the substrate, with a blade moving a solution meniscus across a substrate. This process is shown in **Figure 2.26**.

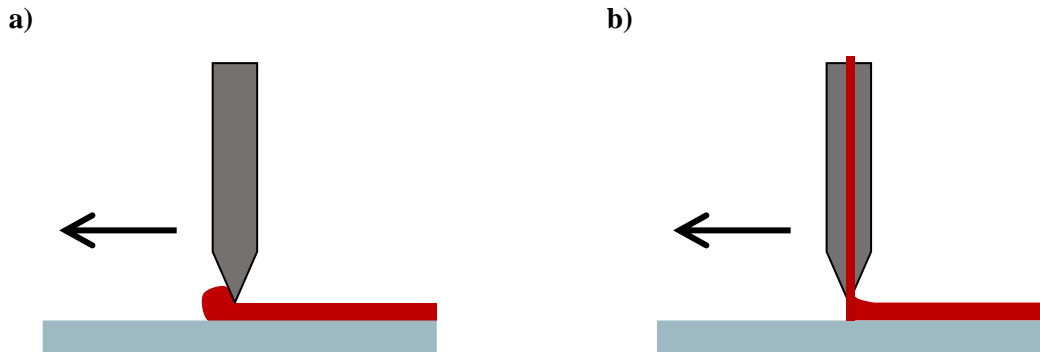


Figure 2.26: A depiction of **a)** blade coating, **b)** slot-die coating, where the arrow represents the movement of the blade or head.

As all the ink supplied to the head is coated onto the surface, slot-die coating has very little solution loss.⁹¹ Several factors will control the film thickness (d):

$$d = \frac{f}{Sw} \frac{c}{\rho} \quad (\text{Eq. 2.16})$$

where f is the flow rate of the ink, S the speed of the head (or substrate if this moves instead) and w is the coated-film width. As with blade coating, slot-die coating has achieved high efficiencies in lab-scale experiments, with devices created having a PCE exceeding 15%.⁹⁵

2.7.2.2 Droplet-Based Techniques

2.7.2.2.1 Ink-jet Printing

Ink-jet printing is a technique in which a motorised head is fitted with a piezoelectric transducer that delivers droplets of a solution to a substrate.⁹¹ Such droplets then coalesce and dry to form a continuous film. Here, film thickness is dependent on properties of the droplets:

$$d = N_d V_d \frac{c}{\rho} \quad (\text{Eq. 2.17})$$

here N_d is the number of droplets delivered per unit area and V_d is droplet volume. Whilst reports of ink-jet printing are considerably less common than blade or slot-die coating, this technique has been used to create devices having efficiencies in excess of 12%.⁹⁶ Typically, ink-jet printing can be very efficient at patterning substrates but has rather low substrate coating speeds.

2.7.2.2.2 *Spray Coating*

Spray coating is a droplet-based coating method that can be divided into several categories, including ultrasonic, electrospray, pneumatic and vibrating mesh atomization (VMA) printing.⁷⁷ In all of these techniques, a solution is atomised into droplets which are then carried to a substrate surface where they coalesce into a film. For example, in ultrasonic spray coating, a solution is atomised using a vibrating piezoelectric tip, with the droplets guided to the substrate using a shaping gas.⁹⁷ In vibrating mesh atomization techniques, a vibrating mesh is used to form the droplets which are again transported to a surface using a carrier gas.⁷⁷ A basic illustration of droplet based coating techniques can be seen in **Figure 2.27**.

There are many parameters that influence film-thickness in spray coating, meaning it cannot be described by a simple equation. Such parameters include solution surface tension, material density, droplet velocity, droplet size and droplet viscosity.

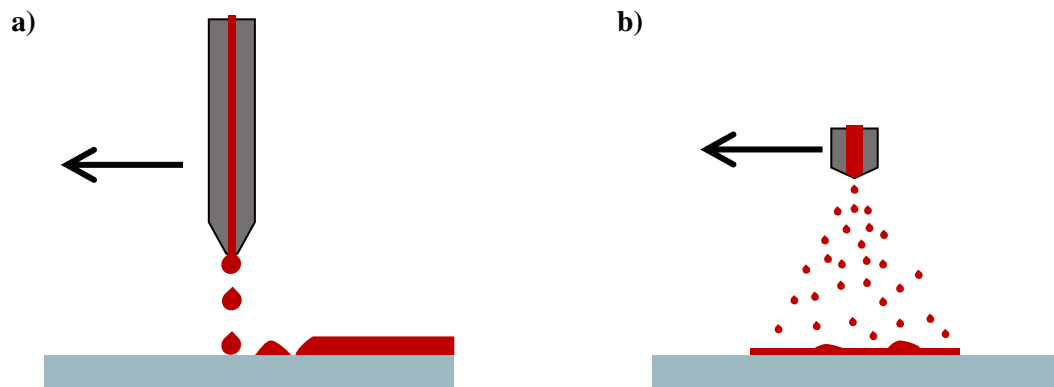


Figure 2.27: A depiction of **a)** Ink-jet coating, **b)** Spray coating, where the arrow represents the movement of the coating head.

Despite the wide range of parameters that must be controlled, spray coating can be successfully used to create PV devices. Indeed, ultrasonic spray coating has been used to create devices with efficiencies exceeding 12%⁹⁸ with VMA creating devices whose efficiency exceeds 15%.⁷⁷ It is worth noting that whilst spray coating is associated with high deposition speeds (estimated as being greater than twice that of slot-die⁹⁹), this depends on the exact method of spray coating. Many lab-scale, high efficiency demonstrations of spray coating in fact use very slow speeds. As a result, true high-speed scalable deposition of OPVs having high efficiencies is yet to be demonstrated. Addressing this challenge will be a key objective of **Chapter 4**.

2.7.3 Optimisation of OPV Efficiency

In order to maximise OPV efficiency, several parameters must be optimised. These are mainly discussed in the context of the active layer but this discussion also applies to the CTLs.

2.7.3.1 Solvent Choice & Solvent Additives

The properties of the deposition solution will play a vital role in dictating film quality and thickness. Such properties include solvent viscosity, solvent surface tension, solvent volatility, solid concentration and solubility of solute in solvent. For example, while volatile solvents often produce high efficiency devices when spin coated, such solvents are difficult to apply using droplet-based techniques. Furthermore, the solubility of each component in a molecular blend needs to be carefully considered.²³

There is a growing movement away from traditional, toxic, halogenated solvents, towards non-halogenated solvents which are less toxic. This is likely to be important for and future manufacture of OPVs. Widely used halogenated solvents include chlorobenzene and chloroform and common non-halogenated alternatives include *o*-Xylene and toluene. Switching to green alternatives has associated challenges, with many Y-series acceptors having poor solubility in non-halogenated solvents.¹⁰⁰ Despite this, devices deposited from non-halogenated OPVs have efficiencies that approach that of their halogenated counterparts, with the current record standing at 18.25% for a ternary PM6:Y6-10:BO-4Cl system deposited from *o*-Xylene.¹⁰¹

To tune solution properties, it is common practise to add a small quantity of another solvent, such as 1,8 diiodooctane (DIO), diphenyl ether (DPE) or 1-chloronaphthalene (CN), known as a solvent additive. The impact of this varies widely and includes selectively dissolving one component to tune morphology,²⁵ encouraging domain coarsening through extended drying,¹⁰² facilitating favourable vertical segregation¹⁰³ and altering surface tension of the solution.¹⁰⁴ While solvent additives are typically added at a concentration of 0.1 - 3%, solvent blends containing additive at higher concentration are also not uncommon, especially when the properties of multiple non-halogenated solvents are used to mimic the solubility of a halogenated solvent.¹⁰⁵

Solvent properties can also be tuned by adjusting solution temperature; a process known as 'hot casting'. This is particularly useful when dealing with polymers that exhibit temperature dependent aggregation¹⁰⁶ or in systems with non-ideal solubility, such as non-halogenated solvents.¹⁰¹

2.7.3.2 Post Deposition Treatment

After deposition of the active layer, various post deposition treatments can be used to further tune film morphology. The most common example of this is thermal annealing which is used to freeze or ‘quench’ the film morphology²⁴ or induce some degree of crystallization.¹⁰⁷ The impact of annealing will depend on the T_g of the components,¹⁰⁸ and the temperature and time of the applied process.

Another process used to modify film morphology is solvent vapour annealing. Here a film is exposed to a solvent vapour (often during thermal annealing) to facilitate molecular rearrangement.¹⁰⁹ The use of this technique was common in the early days of OPV research, but has since fallen out of favour as this is not a scalable process.

2.8 Stability of Organic Photovoltaics

The stability, or performance over time, of an OPV is vitally important for successful commercialisation. A number of different degradation pathways can occur. These can be broadly divided into intrinsic degradation (degradation that occurs without external factors) and extrinsic degradation (degradation caused by external factors such as oxygen or light).

2.8.1 Burn-In

Typically, OPV efficiency will exhibit a ‘burn-in’ as it is run, meaning there is a rapid initial decrease in device performance which then reaches a plateau, shown in **Figure 2.28**. This has been attributed to several different factors, depending on the exact nature of the device.¹¹⁰ The time taken for a cell to reach 80% of its initial PCE is known as T_{80} , and often quoted as the device ‘lifetime’, whether measured or extrapolated. In some cases, T_{80} is not quoted as 80% of the initial PCE, but instead 80% of the cell’s PCE after the burn-in period.

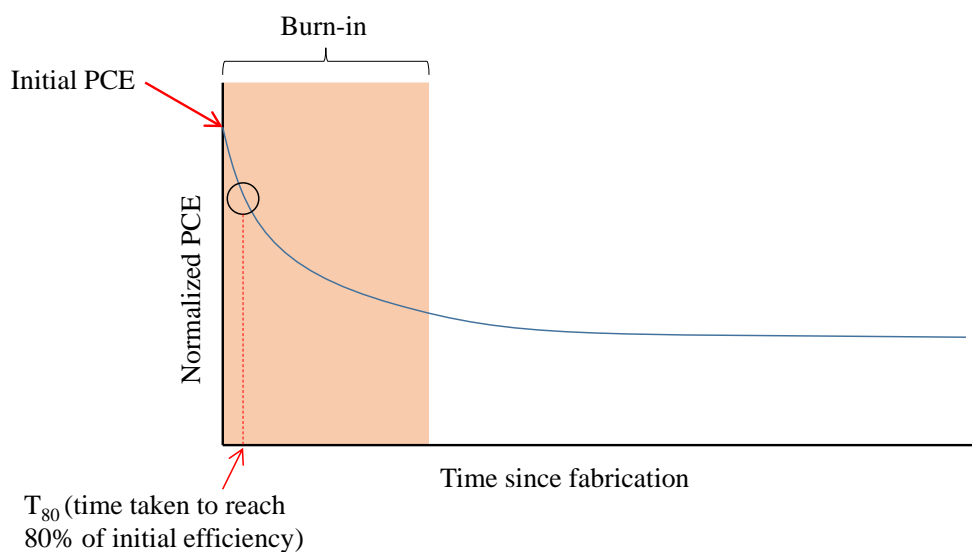


Figure 2.28: A depiction of what OPV degradation often looks like, featuring burn-in and a short T_{80} . Not all cells will show burn-in and some will have very long T_{80} values that must be extrapolated from measured data.

2.8.2 Intrinsic Degradation Factors

2.8.2.1 Morphological Degradation

Morphological degradation describes changes in the morphology of the active layer BHI over time that lead to decreased OPV performance. This type of degradation is the primary intrinsic degradation pathway for an OPV. Driving factors of morphological degradation can be divided into kinetic and thermodynamic factors.

The main thermodynamic factor that drives degradation is the miscibility between the donor and acceptor OSCs. In systems with organic components this miscibility is often described using Flory-Huggins theory. This is a lattice model that describes the total free energy of mixing, originally for a polymer and solvent:¹¹¹

$$f(\psi, \phi) = \phi f(\psi) + \frac{\phi}{N} \ln(\phi) + (1 - \phi) \ln(1 - \phi) + \chi_{effective} \phi(1 - \phi) \quad (\text{Eq 2.18})$$

Here $f(\psi, \phi)$ is the total free energy of mixing, ϕ is the volume fraction of the polymer, $f(\psi)$ is the variation of free energy of crystallization, N is the degree of polymerisation, and $\chi_{effective}$ is the effective Flory-Huggins (F-H) parameter. This equation can also be considered valid for a polymer-small molecule system, where the small molecule effectively acts as the ‘solvent’. As a negative free energy of mixing will yield spontaneous mixing, **Equation 2.18** therefore shows that for a given system, the higher the Flory-Huggins parameter χ , the higher the free energy of mixing, and the less favourable the mixing process is. Therefore, χ is often used as a measure of miscibility for polymer-small molecule OPV

blends. A high F-H parameter implies a mostly immiscible (or ‘hypo-miscible’) system. In contrast a low F-H value implies that a system mixes well (or is ‘hyper-miscible’).

Typically, high performance systems are hypo-miscible, as this is required to ensure sufficient phase separation to generate an ideal morphology. However, as a consequence such types of morphology have a thermodynamic tendency to de-mix and undergo excessive phase separation over time. Rapid immiscibility-induced phase-separation is often listed as a cause of burn-in.¹¹⁰ Vertical phase-segregation can also occur either in addition to, or instead of, smaller-scale phase separation.¹¹²

De-mixing will drive the BHJ towards a thermodynamic equilibrium composition, which is known as the binodal composition. This is usually expressed as the ratio of donor and acceptor, or as the volume fraction (ϕ) of one of the components. The higher the χ value, the more de-mixing occurs and the lower minority volume fraction in the binodal. The relationship between χ and ϕ is described by a binodal curve, modelled using Flory-Huggins theory. This is discussed further in **Chapter 6**.

The speed of de-mixing is dictated by kinetic factors such as the temperature, ease of diffusion of the OSC moieties, and their tendency to crystallize. Considering the role of temperature in diffusion, χ is normally considered to be a function of temperature, and quoted as $\chi(T)$. It has been recently shown that the diffusion constant of a material is also inversely proportional to its T_g (in the case of a small molecule), or elastic modulus (in the case of a polymer).¹¹³ As a result of this, even hypo-miscible systems can be stable against de-mixing if the T_g or elastic modulus are of appropriate values to give slow diffusion.²⁴

It is worth noting that a wide range of Y-series acceptors have been shown to have low T_g values, leading to rapid diffusion. This rapid diffusion, paired with high $\chi(T)$ values, means most high performance systems based on these acceptors display poor morphological stability.¹¹⁴ There has been some promising work on such systems,¹¹⁵ and others¹¹⁶ using a third component to stabilize the morphology against de-mixing, or by modifying materials to reduce their diffusion, for example with cross-linking.¹¹⁷ In spite of this progress, the development of materials systems having enhanced morphological stability, paired with high performance, remains an active area of OPV research.

2.8.2.2 Other Intrinsic Degradation

Other intrinsic pathways have been shown to exist in OPVs, most significantly diffusion of CTLs and electrodes into the active layer. Such effects can lead to the generation of charge traps and subsequent recombination.¹¹⁸ Some spontaneous reactions may also occur,

such as that between acidic PEDOT:PSS and ITO, or PEDOT:PSS and the INCN moieties in IDTT based acceptors.¹¹⁹ Both of these routes can be mitigated by careful choice of materials or the use of buffer layers, as shown in **Figure 2.30** and discussed below.

2.8.3 Extrinsic Degradation Factors

Extrinsic degradation factors in OPVs result from interaction with light, oxygen, moisture, heat and mechanical stress. Some extrinsic factors can be mitigated by encapsulation, but illumination and its associated heating cannot, meaning these degradation pathways must be directly addressed.

2.8.3.1 Photo-Degradation

The most significant extrinsic degradation pathway is that due to illumination, especially in combination with oxygen resulting in photo-oxidation. Illumination can induce a number of different reactions and affect multiple layers in the cell. Indeed, rapid photo-induced reactions are often listed as a possible cause of burn-in.¹²⁰

Under illumination, OSCs have been shown to undergo hydrogen abstraction that initiates a free-radical mediated reaction. These radicals move through the film, reacting with materials to cause a loss in electronic-conjugation and corresponding loss of function. To illustrate this point, **Figure 2.29** shows a hydrogen abstraction reaction in the donor-polymer PCDTBT. As electronic-conjugation is linked to the efficiency of light-absorption of OSCs, photo-degradation can cause loss of colour and so is known as ‘photo-bleaching.’ This reaction can happen in the absence of oxygen but has been shown to be accelerated by its presence.¹²¹

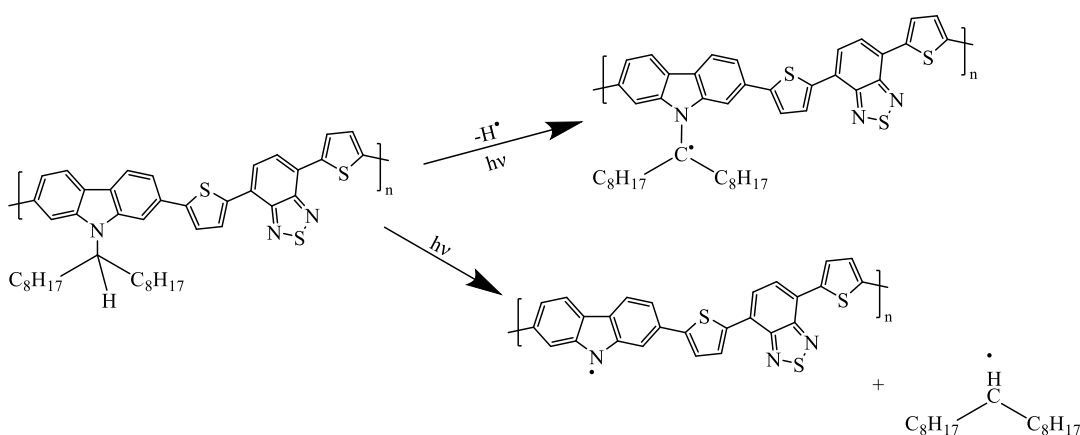


Figure 2.29: Hydrogen abstraction in the donor polymer PCDTBT which forms radicals that go on to react with other molecules. This eventually causes a loss in electronic-conjugation and performance. Reaction scheme adapted from Mateker et al.¹²¹

The chemical structure of the materials used in an OPV is important in dictating the impact of photo-degradation. For example, for the acceptor molecule PC₆₀BM, the process of photo-dimerization is well-established,¹²² with other instabilities also being common in NFAs. Indeed, IDTT based NFAs such as ITIC and ITIC-M have been shown to have poor photo-stability due to photo-induced conformational changes. However such instabilities have been shown to be reduced in derivatives such as ITIC-2F, which has an extrapolated lifetime approaching 10 years under illumination.⁵¹ Notably, other acceptors with an IDT core, such as EH-IDTBR,¹²⁰ have been shown to be among the most promisingly stable acceptors yet developed.

The UV portion of the AM1.5 spectrum has been shown to be particularly damaging in initiating photo-degradation pathways. In particular, it has been linked to photo-catalysed reactions between ZnO (when used as a CTL) and components in the active layer,¹²³ together with radical mediated reactions involving the solvent additive DIO.¹²⁴ As a result, photo-degradation has been shown to be reduced by application of an optical filter to remove the UV portion of the spectrum. For example, a recent study authored by Y. Li *et al.* demonstrated extrapolated lifetimes for a PTB7-Th:BT-CIC system approaching 30 years. In this study, a UV filter layer was combined with other ‘buffer layers’ to reduce reactions at the CTL active layer interfaces – see device stack shown in **Figure 2.30**.¹²⁵

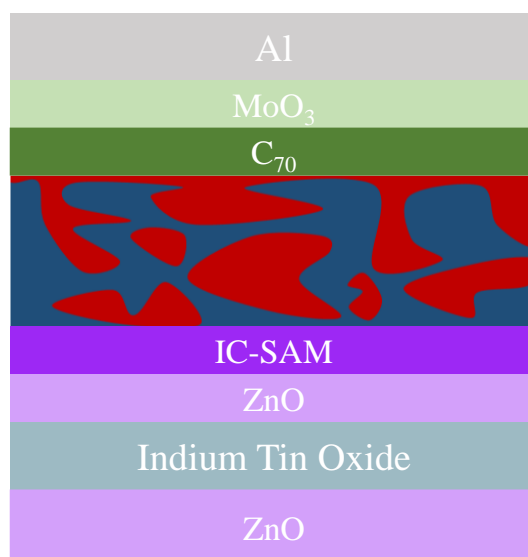


Figure 2.30: A recent example of an OPV system displaying high stability, with use of cathode and anode buffer layers (IC-SAM and ZnO respectively) and a UV filter layer (bottom ZnO).

2.8.3.2 Degradation Due to Moisture & Oxygen

Both moisture and oxygen that are present under ambient conditions can react with different components in a PV device, inducing processes such as oxidation of electrodes,¹²¹ photo-oxidation of active layer materials¹²⁶ and generation of oxidative defects.¹²⁷ A basic mechanism showing possible reactions with a thiophene group commonly found in OSCs can be seen in **Figure 2.31**.

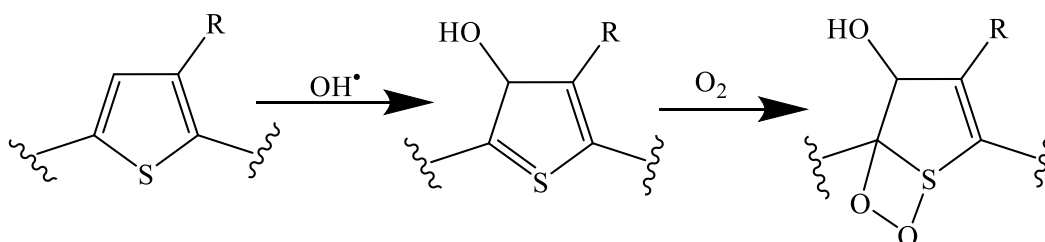


Figure 2.31: A reaction scheme showing how water and oxygen can react with a thiophene group, leading to loss of conjugation. Reaction scheme adapted from Sai et al.¹²⁶

Effective encapsulation provides the easiest route to restricting reactions with moisture and oxygen.^{128,129} However some materials are known to be particularly susceptible to such reactions. For example, the HTL PEDOT:PSS is hygroscopic and the absorption of water from the atmosphere will accelerate reactions within the device. As a result, the replacement of PEDOT:PSS has been shown to result in clear improvements in long term device stability.^{59,130} The careful choice of OSC materials is known to be critical to reduce photo-oxidation, for example material design should avoid the incorporation of susceptible side groups or bonds.¹²⁷

A high level of crystallinity and density in active layer components has also been linked to superior stability as close molecular packing restricts the diffusion of oxygen and moisture through a film.¹³¹ Indeed, the highest quoted extrapolated lifetime to date, 27,000 years¹³² is for a thermally evaporated OPV, a process known for producing dense films,¹³³ albeit often at the expense of performance.

2.8.3.3 Thermal Degradation

Ensuring the stability of OPVs under elevated temperatures is important, as operating temperatures for outdoor solar panels can often exceed 70°C. Indeed, thermal stress can accelerate other degradation pathways such as chemical-reactions, molecular-aggregation,

and phase-separation.¹¹⁷ Here, significant performance loss under heating has previously been seen in both fullerene¹³⁴ and NFA based systems.¹³⁵

It is known that thermal-energy will increase the movement of active layer components, and will lower kinetic barriers to de-mixing. The T_g of an OSC is inversely correlated with its diffusion constant,²⁶ and thus PV devices incorporating a high T_g material will have enhanced resistance to heating. Reducing the diffusion of components in a device via other methods such as through chemical design or the introduction of additives has also been an effective strategy used to minimize the impact of prolonged heating on cell performance.¹¹⁷ The relationship between crystallinity and thermal stability is complex, as whilst high levels of crystallinity have been linked to a reduction in OSC diffusion,¹³⁶ thermally induced aggregation and formation of large crystals in a device active layer will drastically reduce performance.¹³⁷ Other approaches to improve the stability of OPV devices include the use of layer by layer deposited materials, which have been shown to have improved morphological and thermal-stability over their BHJ counterparts.¹³⁸

2.8.3.4 Mechanical Stress

As thin film solar cells offer the potential for flexible operation, the performance of OPVs under mechanical stress, such as bending, is vital. Mechanical degradation will usually lead to either strain-induced morphological changes or cracks, or delamination between layers.¹¹⁸ Whilst crystallinity of OSCs has been linked to brittleness in the active layer¹³⁹ and a corresponding increase in the likelihood of mechanical failure, there has been moderate success in producing efficient, flexible OPVs. Strategies include the replacement of brittle layers such as ITO and increasing the relative amount of amorphous regions in the BHJ.¹⁴⁰ Using this approach, researchers have demonstrated device efficiencies exceeding 14% for flexible cells with good mechanical stability.¹⁴¹

2.8.4 Characterization of Degradation

To explore the impact of the degradation factors discussed above, OPVs are often tested under International Summit on Hybrid and Organic Photovoltaic Stability (ISOS) protocols, developed in 2011.¹⁴² While most published work does not strictly follow an ISOS protocol, there is growing movement towards stricter and more consistent testing. The protocols are summarised in **Table 2.2**, with greater detail available in the original publication.¹⁴²

Table 2.2: ISOS Protocols

	Protocol	Illumination	Temperature	Humidity	Characterization Source	Bias
Dark	ISOS-D-1	None	Ambient	Ambient	Solar Simulator	Open Circuit
	ISOS-D-2		65/85°C	Not controlled		
	ISOS-D-3		65/85°C	85%		
Light	ISOS-L-1	Solar Simulator (0.7-1 sun, close to AM1.5G)	Ambient	Ambient	Solar Simulator	MPP or open circuit
	ISOS-L-2		65/85°C	Not controlled		
	ISOS-L-3		65/85°C	Near 50%		MPP
Outdoor	ISOS-O-1	Sunlight	Ambient	Ambient	Solar Simulator	MPP or open circuit
	ISOS-O-2				Sunlight	
	ISOS-O-3				Sunlight + Solar Simulator	MPP
Thermal Cycling	ISOS-T-1	None	RT up to 65/85°C	Ambient	Solar Simulator	Open circuit
	ISOS-T-2			Not controlled		
	ISOS-T-3		-40 to 85°C	Near 55%		
Solar-Thermal Cycling	ISOS-LT-1	Solar Simulator	Ramping RT to 65°C	Not controlled	Solar Simulator	Open circuit or MPP
	ISOS-LT-2		Ramping 5°C to 65°C	Controlled at 50% beyond 40°C		
	ISOS-LT-3		Ramping -25 to 65°C	Controlled at 50% beyond 40°C		

We note that in the recently established ‘emerging photovoltaics reports initiative’,¹⁴² the recommended, best practise, stability test is 1000h of illumination under AM1.5 at 1 sun, 85°C, in a nitrogen atmosphere, with cells held at maximum power point.

2.9 The Future of Organic Photovoltaics

2.9.1 Commercial Prospects

Whilst OPV efficiencies lag behind that of silicon solar cells - and may always- they remain an attractive alternative due to their potential for significantly cheaper manufacture. Several factors still prevent widespread OPV commercialisation, namely poor stability, scalability issues and high synthetic costs,¹⁴⁴ so it is difficult to assess the commercial potential of existing systems. Instead, a number of quantitative models have been used to predict the feasibility or worth of large scale OPV manufacture.

Here, renewable energy technologies are assessed by their ‘energy payback time’ (EPBT), meaning the time required for devices to generate an equivalent energy to that used in their production. For silicon solar-cells the EPBT exceeds 2 years due to their industrially intensive production, whereas this is estimated to be as low as 0.5 years for OPVs, despite their inferior performance.¹⁴⁵

Another common term used to quantify PV technologies is the levelized cost of electricity (LCOE). This is calculated through its total manufacture cost divided by lifelong power output. A higher efficiency (and so higher power output), longer lifetime and lower materials cost will therefore all decrease LCOE.¹⁴⁶ The LCOE is currently at around 0.055 \$ kWh⁻¹ for a traditional silicon module,¹⁴⁵ with some estimates for the LCOE of an OPV system to be as low as 0.0028 \$ kWh⁻¹ for devices with a 10% power conversion efficiency over a 20 year lifetime.¹⁴⁷

There have also been a number of attempts to define figures of merit for OPVs that incorporate the elements of the ‘golden triangle’ of PV technology, namely efficiency, cost and lifetime.¹⁴⁸ The most recent of these was published in 2021¹⁴⁹ by Yang *et al.* and is defined as follows:

$$FOM = \frac{\text{PCE (\%)} \times \text{Stability (\% after 200h, 1 sun, 85°C, in N}_2\text{)}}{MC_{D:A} \text{ (material costs)}} \quad \text{(Eq. 2.19)}$$

Here material costs are calculated using a measure of the synthetic complexity, including quantifying the number of synthetic-steps, materials-yield and number of hazardous materials involved. Yang and co-authors describe market price competitiveness for OPVs as roughly equivalent to a system with 15% efficiency, 0.5 % degradation per year, 12.74 \$ m⁻² cost and a LCOE of 0.0346 \$ kWh⁻¹; values that are roughly equivalent to that of CIGS PV.

Whilst these efficiency and lifetime values have been achieved, albeit in separate systems, the synthetic cost, especially of the highest performing systems, still remains a significant barrier. For example, despite the high efficiencies obtained using the Y-class series of acceptors, they are notorious for their lengthy and low-yielding syntheses, meaning in assessments of FOM, lower efficiency material-systems may win out.¹⁴⁸

It is clear from these various estimates that with sufficient lifetime and low enough cost, OPVs should theoretically be competitive with existing technologies, however, considering the current low cost of silicon, the prospect of this seems distant. Indeed, in terms of cheap, solution-processed thin film technologies, perovskite solar cells have so far shown superior efficiencies despite their own stability issues, and are likely closer to commercial fruition. Instead, there is general consensus that OPVs must find their own niche for commercialisation over both silicon and perovskite technologies.

2.9.2 Niche Applications

Due to the tuneable band gap of OPVs, they hold particular promise for semi-transparent solar cells, meaning devices that let some of the visible portion of light through to allow for dual functionality. The incorporation of lightweight and/or semi-transparent solar cells into windows will create building integrated PV (BIPV). Other applications include the integration of OPV into wearable electronics and greenhouses.¹⁴⁸ Here, they not only can perform functions that silicon is unable to, i.e. semitransparency, application over non-planar surfaces, and light weight, they also hold advantages over perovskites, namely a more easily tuneable band gap and a reduction in toxicity for agricultural related applications.¹⁵⁰

Of these agricultural applications, a particularly promising avenue for OPVs is that of agrivoltaics; namely semi-transparent solar cells installed over plants or incorporated into greenhouses.¹⁵⁰ Here, additional electricity can be generated without increasing land use, taking full advantage of the tuneable band gap of OPVs to allow light of a favourable wavelength for plant growth. Not only are agrivoltaics beneficial for electricity production, they can also be used to reduce evaporation of water from crops and have been shown to

actually increase yield. Encouragingly, OPVs tuned to avoid absorbing light necessary for photosynthesis have been estimated to be capable of efficiencies as high as 17%.¹⁵⁰

Whilst it remains to be seen if OPVs will ever be commercialised on a large scale, they remain an ever-growing area of fascinating research with numerous avenues for exploration. This thesis aims to contribute towards this exploration by focusing on scalability and stability of OPVs. As many of the problems with these factors are linked to improper BHJ morphology, the strategy used in this work is to characterise and control the morphology of the BHJ, towards a better performing, or more stable system. The overall goal here is to use the theory explained above, a wide range of experimental techniques, and results interpreted in the context of the field, to contribute to establishing a commercially viable, stable, and scalable OPV.

2.10 References

1. Becquerel, A. E. Mémoire sur les effets électriques produits sous l'influence des rayons solaires. *Comptes Rendus L'Académie Des Sci* **9**, 145 (1839).
2. Nelson, J. *The physics of solar cells*. (Imperial College Press, 2003).
3. Doan, D. H., Glitzky, A. & Liero, M. Analysis of a drift-diffusion model for organic semiconductor devices. *Zeitschrift für Angew. Math. und Phys.* **70**, 1–18 (2019).
4. Ehrler, B. *et al.* Photovoltaics reaching for the Shockley-Queisser limit. *ACS Energy Lett.* **5**, 3029–3033 (2020).
5. NREL. NREL Reference AM1.5 Spectrum. Available at: <https://www.nrel.gov/grid/solar-resource/spectra-am1.5.html>. (Accessed Jan 2022)
6. Shockley, W. & Queisser, H. J. Detailed balance limit of efficiency of p-n junction solar cells. *J. Appl. Phys.* **32**, 510–519 (1961).
7. Bäessler, H. & Köhler, A. Charge Transport in Organic Semiconductors. in *Unimolecular and Supramolecular Electronics I* 1–65 (2012).
8. Schlenker, C. & Thompson, M. E. Current Challenges in Organic Photovoltaic Solar Energy Conversion. in *Unimolecular and Supramolecular Electronics I* 175–212 (2012).
9. Feron, K., Belcher, W. J., Fell, C. J. & Dastoor, P. C. Organic solar cells: Understanding the role of Förster resonance energy transfer. *Int. J. Mol. Sci.* **13**, 17019–17047 (2012).
10. Karuthedath, S. *et al.* Impact of Fullerene on the Photophysics of Ternary Small Molecule Organic Solar Cells. *Adv. Energy Mater.* **9**, 1901443 (2019).
11. Etzold, F. *et al.* Ultrafast exciton dissociation followed by nongeminate charge recombination in PCDTBT:PCBM photovoltaic blends. *J. Am. Chem. Soc.* **133**, 9469–9479 (2011).
12. Karuthedath, S. *et al.* Intrinsic efficiency limits in low-bandgap non-fullerene acceptor organic solar cells. *Nat. Mater.* **20**, 378–384 (2021).
13. Proctor, C. M., Kuik, M. & Nguyen, T. Q. Charge carrier recombination in organic solar cells. *Prog. Polym. Sci.* **38**, 1941–1960 (2013).
14. Halls, J. J. M., Walsh, C. A., Greenham, N. C., Marseglia, E. A., Friend, R. H., Moratti, S. C., Holmes, A. B. Efficient photodiodes from interpenetrating polymer networks. *Nature* **376**, 498–500 (1995).
15. Yu, G., Hummelen, J. C., Wudl, F., Heeger, A. J. Polymer photovoltaic cells—enhanced efficiencies via a network of internal donor-acceptor heterojunctions. *Science* **270**, 1789–1791 (1995).
16. Tang, C. W. Two-layer organic photovoltaic cell. *Appl. Phys. Lett.* **48**, 183–185 (1986).
17. Madduri, S., Katta, V. S., Raavi, S. S. K. & Singh, S. G. Annealing induced control of trap-assisted recombination in vacuum-deposited small-molecule solar cells. *Mater. Lett.* **300**, 130159 (2021).
18. Printz, A. D. & Lipomi, D. J. Competition between deformability and charge transport in semiconducting polymers for flexible and stretchable electronics. *Appl. Phys. Rev.* **3**, 021302 (2016).
19. Yang, L. *et al.* Modulating Molecular Orientation Enables Efficient Nonfullerene Small-Molecule Organic Solar Cells. *Chem. Mater.* **30**, 2129–2134 (2018).
20. Zaumseil, J. P3HT and other polythiophene field effect transistors. in *P3HT Revisited- from Molecular Scale to Solar Cell Devices* 107–137 (2014).
21. Qiu, D., Adil, M. A., Lu, K. & Wei, Z. The Crystallinity Control of Polymer Donor Materials for High-Performance Organic Solar Cells. *Front. Chem.* **8**, 1–21 (2020).
22. Peng, Z., Ye, L. & Ade, H. Understanding, quantifying, and controlling the molecular ordering of semiconducting polymers: from novices to experts and amorphous to perfect crystals. *Mater. Horizons* **9**, 11–13 (2022).
23. Radchenko, E. S. *et al.* Impact of the solubility of organic semiconductors for solution-processable electronics on the structure formation: A real-time study of morphology and electrical properties. *Soft Matter* **14**, 2560–2566 (2018).
24. Ye, L. *et al.* Quenching to the Percolation Threshold in Organic Solar Cells. *Joule* **3**, 443–458 (2019).
25. Kim, M. *et al.* Critical factors governing vertical phase separation in polymer-PCBM blend films for organic solar cells. *J. Mater. Chem. A* **4**, 15522–15535 (2016).
26. Ghasemi, M. *et al.* A molecular interaction-diffusion framework for predicting organic solar cell stability. *Nat. Mater.* **20**, 525–532 (2021).
27. Deng, M. *et al.* Fine regulation of crystallisation tendency to optimize the BHJ nanostructure and performance of polymer solar cells. *Nanoscale* **12**, 12928–12941 (2020).
28. Kallmann, H. & Pope, M. Photovoltaic effect in organic crystals. *J. Chem. Phys.* **30**, 585–586 (1959).
29. Sariciftci, N. S., Smilowitz, L., Heeger, A. J. & Wudl, F. Photoinduced electron transfer from a conducting polymer to buckminsterfullerene. *Science* **258**, 1474–1476 (1992).
30. Sariciftci, N. S., Smilowitz, L., Heeger, A. J. & Wudl, F. Semiconducting polymers (as donors) and buckminsterfullerene (as acceptor): photoinduced electron transfer and heterojunction devices. *Synth. Met.* **59**, 333–352 (1993).
31. Yu, G., Pakbaz, K. & Heeger, A. J. Semiconducting polymer diodes: Large size, low cost photodetectors with excellent visible-ultraviolet sensitivity. *Appl. Phys. Lett.* **64**, 3422–3424 (1994).
32. Hummelen, J. C. *et al.* Preparation and Characterization of Fulleroid and Methanofullerene

- Derivatives. *J. Org. Chem.* **60**, 532–538 (1995).
33. Brunetti, F. G., Kumar, R. & Wudl, F. Organic electronics from perylene to organic photovoltaics: Painting a brief history with a broad brush. *J. Mater. Chem.* **20**, 2934–2948 (2010).
 34. Park, S. H. *et al.* Bulk heterojunction solar cells with internal quantum efficiency approaching 100%. *Nat. Photonics* **3**, 297–303 (2009).
 35. Chen, H. Y. *et al.* Polymer solar cells with enhanced open-circuit voltage and efficiency. *Nat. Photonics* **3**, 649–653 (2009).
 36. He, Z. *et al.* Simultaneous enhancement of open-circuit voltage, short-circuit current density, and fill factor in polymer solar cells. *Adv. Mater.* **23**, 4636–4643 (2011).
 37. He, Z. *et al.* Enhanced power-conversion efficiency in polymer solar cells using an inverted device structure. *Nat. Photonics* **6**, 591–595 (2012).
 38. He, Z. *et al.* Single-junction polymer solar cells with high efficiency and photovoltage. *Nat. Photonics* **9**, 174–179 (2015).
 39. Zhao, J. *et al.* Efficient organic solar cells processed from hydrocarbon solvents. *Nat. Energy* **1**, 15027 (2016).
 40. Kumari, T., Lee, S. M., Kang, S. H., Chen, S. & Yang, C. Ternary solar cells with a mixed face-on and edge-on orientation enable an unprecedented efficiency of 12.1%. *Energy Environ. Sci.* **10**, 258–265 (2017).
 41. Lin, Y. *et al.* An Electron Acceptor Challenging Fullerenes for Efficient Polymer Solar Cells. *Adv. Mater.* **27**, 1170–1174 (2015).
 42. Lin, Y. *et al.* Mapping Polymer Donors toward High-Efficiency Fullerene Free Organic Solar Cells. *Adv. Mater.* **29**, 1604155 (2017).
 43. Zhao, W. *et al.* Molecular Optimization Enables over 13% Efficiency in Organic Solar Cells. *J. Am. Chem. Soc.* **139**, 7148–7151 (2017).
 44. Yuan, J. *et al.* Single-Junction Organic Solar Cell with over 15% Efficiency Using Fused-Ring Acceptor with Electron-Deficient Core. *Joule* **3**, 1140–1151 (2019).
 45. Cui, Y. *et al.* Single-Junction Organic Photovoltaic Cell with 19% Efficiency. *Adv. Mater.* **33**, 2101420 (2021).
 46. Tokmoldin, N. *et al.* Extraordinarily long diffusion length in PM6:Y6 organic solar cells. *J. Mater. Chem. A* **8**, 7854–7860 (2020).
 47. Liu, J. *et al.* Fast charge separation in a non-fullerene organic solar cell with a small driving force. *Nat. Energy* **1**, 16089 (2016).
 48. Fu, H., Wang, Z. & Sun, Y. Polymer Donors for High-Performance Non-Fullerene Organic Solar Cells. *Angew. Chemie - Int. Ed.* **58**, 4442–4453 (2019).
 49. Zhang, Z. *et al.* Efficient and thermally stable organic solar cells based on small molecule donor and polymer acceptor. *Nat. Commun.* **10**, 1–8 (2019).
 50. Yu, Z. P. *et al.* Simple non-fused electron acceptors for efficient and stable organic solar cells. *Nat. Commun.* **10**, 1–9 (2019).
 51. Du, X. *et al.* Efficient Polymer Solar Cells Based on Non-fullerene Acceptors with Potential Device Lifetime Approaching 10 Years. *Joule* **3**, 215–226 (2019).
 52. Zhao, J., Yao, C., Ali, M. U., Miao, J. & Meng, H. Recent advances in high-performance organic solar cells enabled by acceptor-donor-acceptor-donor-acceptor (A-DA'D-A) type acceptors. *Mater. Chem. Front.* **4**, 3487–3504 (2020).
 53. Sorrentino, R., Kozma, E., Luzzati, S. & Po, R. Interlayers for non-fullerene based polymer solar cells: Distinctive features and challenges. *Energy Environ. Sci.* **14**, 180–223 (2021).
 54. Abdulrazzaq, O. *et al.* Comparative Aging Study of Organic Solar Cells Utilizing Polyaniline and PEDOT:PSS as Hole Transport Layers. *ACS Appl. Mater. Interfaces* **7**, 27667–27675 (2015).
 55. Li, X., Choy, W. C. H., Xie, F., Zhang, S. & Hou, J. Room-temperature solution-processed molybdenum oxide as a hole transport layer with Ag nanoparticles for highly efficient inverted organic solar cells. *J. Mater. Chem. A* **1**, 6614–6621 (2013).
 56. Wong, K. H., Ananthanarayanan, K., Heinemann, M. D., Luther, J. & Balaya, P. Enhanced photocurrent and stability of organic solar cells using solution-based NiO interfacial layer. *Sol. Energy* **86**, 3190–3195 (2012).
 57. Alsulami, A. *et al.* Thermally stable solution processed vanadium oxide as a hole extraction layer in organic solar cells. *Materials* **9**, 235 (2016).
 58. Al-Ashouri, A. *et al.* Conformal monolayer contacts with lossless interfaces for perovskite single junction and monolithic tandem solar cells. *Energy Environ. Sci.* **12**, 3356–3369 (2019).
 59. Lin, Y. *et al.* Self-assembled monolayer enables hole transport layer-free organic solar cells with 18% efficiency and improved operational stability. *ACS Energy Lett.* **5**, 2935–2944 (2020).
 60. Park, H. S., Han, Y. W., Lee, H. S., Jeon, S. J. & Moon, D. K. 13.2% Efficiency of Organic Solar Cells by Controlling Interfacial Resistance Resulting from Well-Distributed Vertical Phase Separation. *ACS Appl. Energy Mater.* **3**, 3745–3754 (2020).
 61. Yao, J. *et al.* Cathode engineering with perylene-diimide interlayer enabling over 17% efficiency single-junction organic solar cells. *Nat. Commun.* **11**, 1–10 (2020).

62. Ding, S. *et al.* Boosting the Efficiency of Non-fullerene Organic Solar Cells via a Simple Cathode Modification Method. *ACS Appl. Mater. Interfaces* **13**, 51078–51085 (2021).
63. Soultati, A. *et al.* Suppressing the Photocatalytic Activity of Zinc Oxide Electron-Transport Layer in Nonfullerene Organic Solar Cells with a Pyrene-Bodipy Interlayer. *ACS Appl. Mater. Interfaces* **12**, 21961–21973 (2020).
64. Trost, S. *et al.* Tin Oxide (SnOx) as Universal ‘light-Soaking’ Free Electron Extraction Material for Organic Solar Cells. *Adv. Energy Mater.* **5**, 1–4 (2015).
65. Kang, H. *et al.* Strongly Reduced Non-Radiative Voltage Losses in Organic Solar Cells Prepared with Sequential Film Deposition. *J. Phys. Chem. Lett.* **12**, 10663–10670 (2021).
66. Sun, R. *et al.* A Layer-by-Layer Architecture for Printable Organic Solar Cells Overcoming the Scaling Lag of Module Efficiency. *Joule* **4**, 407–419 (2020).
67. Wu, Y. *et al.* A conjugated donor-acceptor block copolymer enables over 11% efficiency for single-component polymer solar cells. *Joule* **5**, 1800–1815 (2021).
68. Brinkmann, K. O *et al.* Perovskite-organic tandem solar cells with indium oxide interconnect, *Nature* **604**, 280–286 (2022).
69. Zheng, Z. *et al.* Tandem Organic Solar Cell with 20.2% Efficiency. *Joule* **6**, 171–184 (2022).
70. Koppe, M. *et al.* Near IR Sensitization of Organic Bulk Heterojunction Solar Cells: Towards Optimization of the Spectral Response of Organic Solar Cells. *Adv. Funct. Mater.* **20**, 338–346 (2010).
71. Gasparini, N., Salleo, A., McCulloch, I. & Baran, D. The role of the third component in ternary organic solar cells. *Nat. Rev. Mater.* **4**, 229–242 (2019).
72. Yu, R., Yao, H. & Hou, J. Recent Progress in Ternary Organic Solar Cells Based on Nonfullerene Acceptors. *Adv. Energy Mater.* **8**, 1702814 (2018).
73. Elumalai, N. K. & Uddin, A. Open circuit voltage of organic solar cells: An in-depth review. *Energy Environ. Sci.* **9**, 391–410 (2016).
74. Servaites, J. D., Ratner, M. A. & Marks, T. J. Organic solar cells: A new look at traditional models. *Energy and Environmental Science* **4**, 4410–4422 (2011).
75. Yu, H. *et al.* Effect of diffusion current on fill factor in organic solar cells. *J. Phys. D: Appl. Phys.* **49**, 205105 (2016).
76. Xie, Y. *et al.* Post-annealing to recover the reduced open-circuit voltage caused by solvent annealing in organic solar cells. *J. Mater. Chem. A* **4**, 6158–6166 (2016).
77. Yang, P. *et al.* Toward all aerosol printing of high-efficiency organic solar cells using environmentally friendly solvents in ambient air. *J. Mater. Chem. A* **9**, 17198–17210 (2021).
78. Kirchartz, T., Deledalle, F., Tuladhar, P. S., Durrant, J. R. & Nelson, J. On the differences between dark and light ideality factor in polymer:Fullerene solar cells. *J. Phys. Chem. Lett.* **4**, 2371–2376 (2013).
79. Widmer, J., Tietze, M., Leo, K. & Riede, M. Open-circuit voltage and effective gap of organic solar cells. *Adv. Funct. Mater.* **23**, 5814–5821 (2013).
80. Chen, S. *et al.* A Wide-Bandgap Donor Polymer for Highly Efficient Non-fullerene Organic Solar Cells with a Small Voltage Loss. *J. Am. Chem. Soc.* **139**, 6298–6301 (2017).
81. Hendriks, K. H., Wijkema, A. S. G., Van Franeker, J. J., Wienk, M. M. & Janssen, R. A. J. Dichotomous Role of Exciting the Donor or the Acceptor on Charge Generation in Organic Solar Cells. *J. Am. Chem. Soc.* **138**, 10026–10031 (2016).
82. Li, X. *et al.* Roles of Acceptor Guests in Tuning the Organic Solar Cell Property Based on an Efficient Binary Material System with a Nearly Zero Hole-Transfer Driving Force. *Chem. Mater.* **32**, 5182–5191 (2020).
83. Saito, T., Natsuda, S., Imakita, K., Tamai, Y. & Ohkita, H. Role of Energy Offset in Nonradiative Voltage Loss in Organic Solar Cells. *Sol. RRL* **4**, 2070095 (2020).
84. Zeng, Y. *et al.* Exploring the Charge Dynamics and Energy Loss in Ternary Organic Solar Cells with a Fill Factor Exceeding 80%. *Adv. Energy Mater.* **11**, 2101338 (2021).
85. Ye, L. *et al.* Quantitative relations between interaction parameter, miscibility and function in organic solar cells. *Nat. Mater.* **17**, 253–260 (2018).
86. Syed, A., Moiz, A. & Karimov, K. S. Space Charge – Limited Charge – Limited Current Current Model Space Model for for Polymers Polymers and. in *Conducting Polymers* 91–117 (2016).
87. Liang, Q. *et al.* Reducing the confinement of PBDB-T to ITIC to improve the crystallinity of PBDB-T/ITIC blends. *J. Mater. Chem. A* **6**, 15610–15620 (2018).
88. Röhr, J. A. Direct Determination of Built-in Voltages in Asymmetric Single-Carrier Devices. *Phys. Rev. Appl.* **11**, 1 (2019).
89. Saliba, M. & Etgar, L. Current density mismatch in Perovskite solar cells. *ACS Energy Lett.* **5**, 2886–2888 (2020).
90. Chen, H. *et al.* A guest-assisted molecular-organization approach for >17% efficiency organic solar cells using environmentally friendly solvents. *Nat. Energy* **6**, 1045–1053 (2021).
91. Krebs, F. C. Fabrication and processing of polymer solar cells: A review of printing and coating techniques. *Sol. Energy Mater. Sol. Cells* **93**, 394–412 (2009).

92. Wong, Y. Q. *et al.* Efficient semitransparent organic solar cells with good color perception and good color rendering by blade coating. *Org. Electron.* **43**, 196–206 (2017).
93. Guan, W. *et al.* Blade-coated organic solar cells from non-halogenated solvent offer 17% efficiency. *J. Semicond.* **42**, 030502 (2021).
94. Dong, S., Jia, T., Zhang, K., Jing, J. & Huang, F. Single-Component Non-halogen Solvent-Processed High-Performance Organic Solar Cell Module with Efficiency over 14%. *Joule* **4**, 2004–2016 (2020).
95. Zhao, H. *et al.* Hot Hydrocarbon-Solvent Slot-Die Coating Enables High-Efficiency Organic Solar Cells with Temperature-Dependent Aggregation Behavior. *Adv. Mater.* **32**, 1–10 (2020).
96. Corzo, D., Bihar, E., Alexandre, E. B., Rosas-Villalva, D. & Baran, D. Ink Engineering of Transport Layers for 9.5% Efficient All-Printed Semitransparent Nonfullerene Solar Cells. *Adv. Funct. Mater.* **31**, 1–10 (2021).
97. Bishop, J. E., Routledge, T. J. & Lidzey, D. G. Advances in Spray-Cast Perovskite Solar Cells. *J. Phys. Chem. Lett.* **9**, 1977–1984 (2018).
98. Cheng, J. *et al.* Intensification of Vertical Phase Separation for Efficient Polymer Solar Cell via Piecewise Spray Assisted by a Solvent Driving Force. *Sol. RRL* **4**, 1–11 (2020).
99. Bishop, J. E., Smith, J. A. & Lidzey, D. G. Development of Spray-Coated Perovskite Solar Cells. *ACS Appl. Mater. Interfaces* **12**, 48237–48245 (2020).
100. Dong, S., Jia, T., Zhang, K., Jing, J. & Huang, F. Single-Component Non-halogen Solvent-Processed High-Performance Organic Solar Cell Module with Efficiency over 14%. *Joule* **4**, 2004–2016 (2020).
101. Wang, D. *et al.* High-Performance Organic Solar Cells from Non-Halogenated Solvents. *Adv. Funct. Mater.* **2107827**, 1–8 (2021).
102. Zhang, Y. *et al.* Understanding and controlling morphology evolution via DIO plasticization in PffBT4T-2OD/PC 71 BM devices. *Sci. Rep.* **7**, 1–12 (2017).
103. Wang, L. M. *et al.* Quantitative Determination of the Vertical Segregation and Molecular Ordering of PBDB-T/ITIC Blend Films with Solvent Additives. *ACS Appl. Mater. Interfaces* **12**, 24165–24173 (2020).
104. Zheng, D., Huang, J., Zheng, Y. & Yu, J. High performance airbrush spray coated organic solar cells via tuning the surface tension and saturated vapor pressure of different ternary solvent systems. *Org. Electron.* **25**, 275–282 (2015).
105. Griffin, J. *et al.* Organic photovoltaic devices with enhanced efficiency processed from non-halogenated binary solvent blends. *Org. Electron.* **21**, 216–222 (2015).
106. Hu, H. *et al.* Aggregation and morphology control enables multiple cases of high-efficiency polymer solar cells. *Nat. Commun.* **5**, 1–8 (2014).
107. Sharenko, A., Kuik, M., Toney, M. F. & Nguyen, T. Q. Crystallization-induced phase separation in solution-processed small molecule bulk heterojunction organic solar cells. *Adv. Funct. Mater.* **24**, 3543–3550 (2014).
108. Qin, Y., Xu, Y., Peng, Z., Hou, J. & Ade, H. Low Temperature Aggregation Transitions in N3 and Y6 Acceptors Enable Double-Annealing Method That Yields Hierarchical Morphology and Superior Efficiency in Nonfullerene Organic Solar Cells. *Adv. Funct. Mater.* **30**, 1–10 (2020).
109. Jiang, M. *et al.* Two-Pronged Effect of Warm Solution and Solvent-Vapor Annealing for Efficient and Stable All-Small-Molecule Organic Solar Cells. *ACS Energy Lett.* **6**, 2898–2906 (2021).
110. Ghasemi, M. *et al.* Delineation of Thermodynamic and Kinetic Factors that Control Stability in Nonfullerene Organic Solar Cells. *Joule* **3**, 1328–1348 (2019).
111. Long, Y. *et al.* Miscibility-Function Relations in Organic Solar Cells: Significance of Optimal Miscibility in Relation to Percolation. *Adv. Ener. Mater.*, **8**, 1703058 (2018).
112. Wang, Y. *et al.* Stability of Nonfullerene Organic Solar Cells: from Built-in Potential and Interfacial Passivation Perspectives. *Adv. Energy Mater.* **9**, 1–9 (2019).
113. Ghasemi, M. *et al.* A molecular interaction–diffusion framework for predicting organic solar cell stability. *Nat. Mater.* **20**, 525–532 (2021).
114. Qin, Y. *et al.* The performance–stability conundrum of BTP-based organic solar cells. *Joule* **5**, 2129–2147 (2021).
115. Gasparini, N. *et al.* Exploiting Ternary Blends for Improved Photostability in High-Efficiency Organic Solar Cells. *ACS Energy Lett.* **5**, 1371–1379 (2020).
116. Zhu, Y. *et al.* Rational Strategy to Stabilize an Unstable High-Efficiency Binary Nonfullerene Organic Solar Cells with a Third Component. *Adv. Energy Mater.* **9**, 1–13 (2019).
117. Yang, W. *et al.* Simultaneous enhanced efficiency and thermal stability in organic solar cells from a polymer acceptor additive. *Nat. Commun.* **11**, 1–10 (2020).
118. Duan, L. & Uddin, A. Progress in Stability of Organic Solar Cells. *Adv. Sci.* **7**, 1903259 (2020).
119. Wang, Y. *et al.* Efficient and stable operation of nonfullerene organic solar cells: Retaining a high built-in potential. *J. Mater. Chem. A* **8**, 21255–21264 (2020).
120. Clarke, A. J. *et al.* Non-fullerene acceptor photostability and its impact on organic solar cell lifetime. *Cell Reports Phys. Sci.* **2**, 100498 (2021).

121. Mateker, W. R. & McGehee, M. D. Progress in Understanding Degradation Mechanisms and Improving Stability in Organic Photovoltaics. *Adv. Mater.* **29**, 1603940 (2017).
122. Inasaridze, L. N. *et al.* Light-induced generation of free radicals by fullerene derivatives: An important degradation pathway in organic photovoltaics? *J. Mater. Chem. A* **5**, 8044–8050 (2017).
123. Jiang, Y. *et al.* Photocatalytic effect of ZnO on the stability of nonfullerene acceptors and its mitigation by SnO₂ for nonfullerene organic solar cells. *Mater. Horizons* **6**, 1–6 (2019).
124. Classen, A. *et al.* Revealing Hidden UV Instabilities in Organic Solar Cells by Correlating Device and Material Stability. *Adv. Energy Mater.* **9**, 1–11 (2019).
125. Li, Y. *et al.* Non-fullerene acceptor organic photovoltaics with intrinsic operational lifetimes over 30 years. *Nat. Commun.* **12**, 1–9 (2021).
126. Sai, N., Leung, K., Zádor, J. & Henkelman, G. First principles study of photo-oxidation degradation mechanisms in P3HT for organic solar cells. *Phys. Chem. Chem. Phys.* **16**, 8092–8099 (2014).
127. Guo, J. *et al.* Suppressing photo-oxidation of non-fullerene acceptors and their blends in organic solar cells by exploring material design and employing friendly stabilizers. *J. Mater. Chem. A* **7**, 25088–25101 (2019).
128. Planes, E. *et al.* Encapsulation Effect on Performance and Stability of Organic Solar Cells. *Adv. Mater. Interfaces* **7**, 1–13 (2020).
129. Uddin, A., Upama, M. B., Yi, H. & Duan, L. Encapsulation of organic and perovskite solar cells: A review. *Coatings* **9**, 1–17 (2019).
130. Lan, W. *et al.* Toward improved stability of nonfullerene organic solar cells: Impact of interlayer and built-in potential. *EcoMat* **3**, 1–10 (2021).
131. Mateker, W. R. *et al.* Molecular Packing and Arrangement Govern the Photo-Oxidative Stability of Organic Photovoltaic Materials. *Chem. Mater.* **27**, 6345–6353 (2015).
132. Burlingame, Q. *et al.* Intrinsically stable organic solar cells under high-intensity illumination. *Nature* **573**, 394–397 (2019).
133. Burlingame, Q., Ball, M. & Loo, Y. L. It's time to focus on organic solar cell stability. *Nat. Energy* **5**, 947–949 (2020).
134. Landerer, D. *et al.* Enhanced thermal stability of organic solar cells comprising ternary D-D-A bulk-heterojunctions. *npj Flex. Electron.* **1**, 1–8 (2017).
135. Su, L. Y. *et al.* Enhancing Long-Term Thermal Stability of Non-Fullerene Organic Solar Cells Using Self-Assembly Amphiphilic Dendritic Block Copolymer Interlayers. *Adv. Funct. Mater.* **31**, 1–11 (2021).
136. Yi, X. *et al.* Effects of polymer crystallinity on non-fullerene acceptor based organic solar cell photostability. *J. Mater. Chem. C* **8**, 16092–16099 (2020).
137. Yu, L. *et al.* Diffusion-Limited Crystallization: A Rationale for the Thermal Stability of Non-Fullerene Solar Cells. *ACS Appl. Mater. Interfaces* **11**, 21766–21774 (2019).
138. Cheng, P. *et al.* Efficient and stable organic solar cells: Via a sequential process. *J. Mater. Chem. C* **4**, 8086–8093 (2016).
139. Huang, W. *et al.* Efficient and Mechanically Robust Ultraflexible Organic Solar Cells Based on Mixed Acceptors. *Joule* **4**, 128–141 (2020).
140. Fukuda, K., Yu, K. & Someya, T. The Future of Flexible Organic Solar Cells. *Adv. Energy Mater.* **10**, 1–10 (2020).
141. Yan, T. *et al.* 16.67% Rigid and 14.06% Flexible Organic Solar Cells Enabled by Ternary Heterojunction Strategy. *Adv. Mater.* **31**, 1902210 (2019).
142. Reese, M. O. *et al.* Consensus stability testing protocols for organic photovoltaic materials and devices. *Sol. Energy Mater. Sol. Cells* **95**, 1253–1267 (2011).
143. Almora, O. *et al.* Device Performance of Emerging Photovoltaic Materials (Version 1). *Adv. Energy Mater.* **11**, 2002774 (2021).
144. Riede, M., Spoltore, D. & Leo, K. Organic Solar Cells—The Path to Commercial Success. *Adv. Energy Mater.* **11**, 1–10 (2021).
145. Liu, H. *et al.* Technical Challenges and Perspectives for the Commercialization of Solution-Processable Solar Cells. *Adv. Mater. Technol.* **6**, 1–43 (2021).
146. Meng, L., You, J. & Yang, Y. Addressing the stability issue of perovskite solar cells for commercial applications. *Nat. Commun.* **9**, 1–4 (2018).
147. Guo, J. & Min, J. A Cost Analysis of Fully Solution-Processed ITO-Free Organic Solar Modules. *Adv. Energy Mater.* **9**, 1–9 (2019).
148. Moser, M., Wadsworth, A., Gasparini, N. & McCulloch, I. Challenges to the Success of Commercial Organic Photovoltaic Products. *Adv. Energy Mater.* **11**, 2100056 (2021).
149. Yang, W. *et al.* Balancing the efficiency, stability, and cost potential for organic solar cells via a new figure of merit. *Joule* **5**, 1209–1230 (2021).
150. Meitzner, R., Schubert, U. S. & Hoppe, H. Agrivoltaics—The Perfect Fit for the Future of Organic Photovoltaics. *Adv. Energy Mater.* **11**, 1–7 (2021).

Chapter 3 | Experimental Methods

3.1 Introduction

This chapter details the methods used to fabricate and characterise organic photovoltaic (OPV) devices, and the films and materials used in this thesis. Conditions and techniques specific to each experimental chapter are given in that chapter, with the basic principles outlined here.

3.2 Materials

3.2.1 Substrates

This thesis used three variations of substrate for the fabrication of thin films, all purchased from Ossila, measuring 20 x 15 mm (height x width):

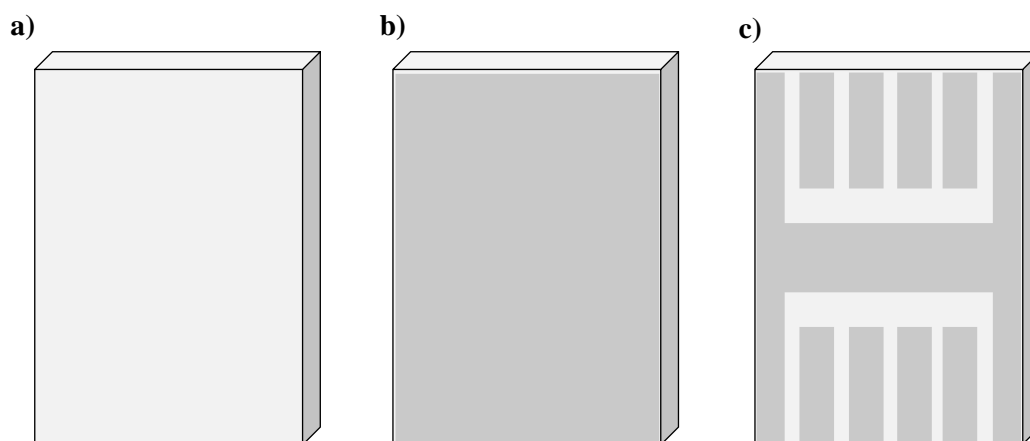


Figure 3.1: a) Quartz coated glass, b) indium-doped tin oxide coated glass, c) pre-patterned indium tin oxide coated glass.

Devices were made onto the pre-patterned indium-doped tin oxide (ITO) coated glass, where the ITO acted as a transparent electrode. Film characterization intended to be comparable to device conditions used un-patterned ITO coated glass, often with a charge transport layer (CTL) on top, in order to mimic the wetting of an active layer in a device. Characterization conditions where the ITO may have interfered with results used glass without ITO. Here the glass was instead coated with 20 nm of synthetic quartz, to provide a smooth layer for deposition.

Unless specified otherwise, ‘substrates’ in **Section 3.2 – 3.6** refers to the pre-patterned ITO coated glass.

3.2.2 Materials Used in Device Fabrication

As discussed in **Chapter 2**, OPVs were manufactured using hole and electron transporting layers, a blend of donor and acceptor organic semiconductor, and conducting electrodes. For charge carrier transport to be facilitated, the energy levels of the donor, acceptor and charge transport layers must be offset. The energy levels of the materials used in this thesis can be seen in **Figure 3.2**.

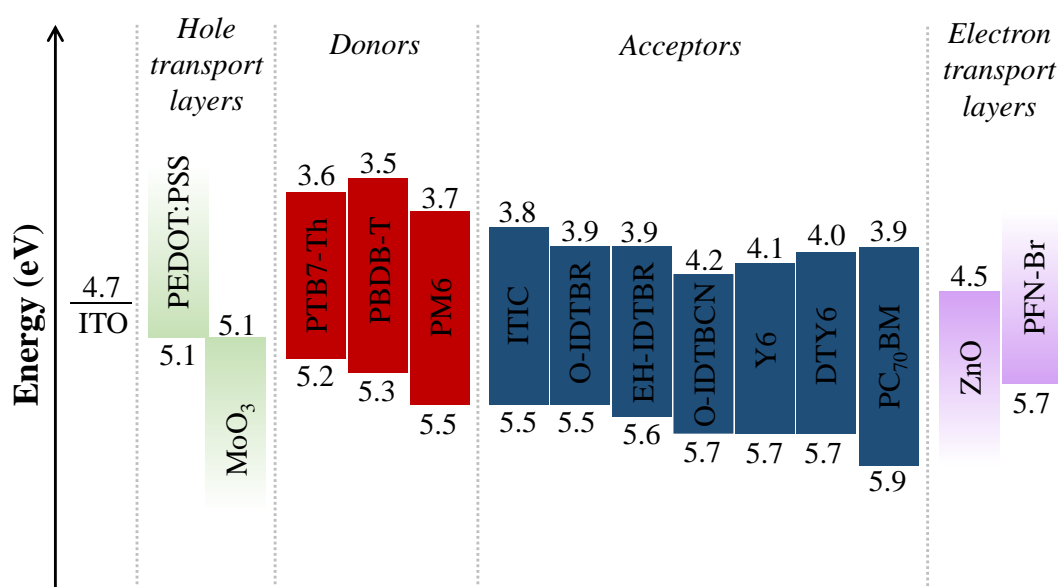


Figure 3.2: Energy levels of the materials used here. Values taken from literature.¹⁻¹⁰ Where only the work function (rather than HOMO & LUMO) is available, a single value is quoted. It is noted that PFN-Br acts more as a hole blocking layer.

3.2.3 Hole Transport Layers

This thesis used PEDOT:PSS and MoO₃ as hole transporting layers (HTLs). PEDOT:PSS, shown in **Figure 3.3**, is the most common of all solution processed HTLs, and consists of a mixture of two polymers in a water based solution. As a result, it is typically only used in conventional architecture devices (with the HTL on the bottom) to avoid moisture damage to the active layer. In inverted architecture devices, MoO₃ is favoured instead, and usually thermally evaporated. As PEDOT:PSS is hygroscopic,¹¹ there is a growing movement in the field towards replacing it with more stable HTLs, such as the self-assembled monolayer 2-PACz.¹²

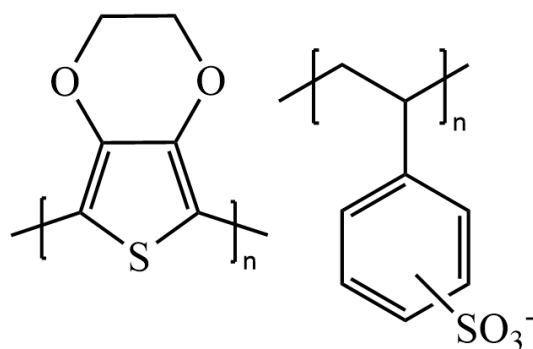


Figure 3.3: PEDOT:PSS, a common HTL.

3.2.4 Electron Transport Layers

This thesis used PFN-Br and ZnO as electron transporting layers (ETLs). In conventional architecture devices, alcohol soluble conjugated polymer electrolytes are particularly popular as ETLs. PFN-Br is a good example of this, shown in **Figure 3.4**, alongside more recent materials such as PDINN.¹³ In inverted cells a thicker, more planarising layer is usually favoured. The most common example of this is zinc oxide (ZnO). Here, the zinc oxide was processed via a sol-gel method, meaning a precursor (in this case zinc acetic dihydrate) was dissolved in an alcohol (here 2-methoxyethanol with a small amount of ethanolamine) before deposition. The thin film was then heated to a high temperature (in our case 150°C) to form the metal oxide. There have been recent works replacing this method with lower temperature nanoparticle alternatives.¹⁴

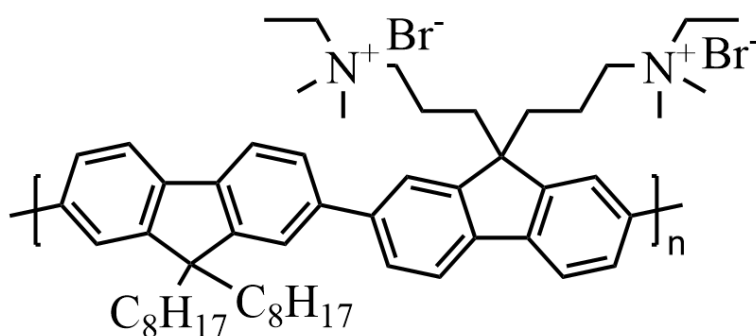


Figure 3.4: PFN-Br, a common conjugated polymer electrolyte ETL.

3.2.5 Acceptors

Whilst there is a growing movement in the field of OPVs to use polymeric electron acceptors,¹⁵ most works, and this thesis, focus exclusively on small molecule acceptors (SMAs). The structures of the acceptors used here can be seen in **Figure 3.5**. Fullerene derivatives, such as PC₆₀BM and PC₇₀BM, dominated the field for many years before being usurped by non-fullerene acceptors (NFAs). This thesis used several different types of NFA, including those based on a IDTT core (ITIC), an IDT core (O-IDBTR, EH-IDTBR and O-IDTBCN) and a BT core (Y6 and DTY6). Each type of core, and flanking groups, will yield different properties, such as solubility, crystallinity and charge carrier mobility.

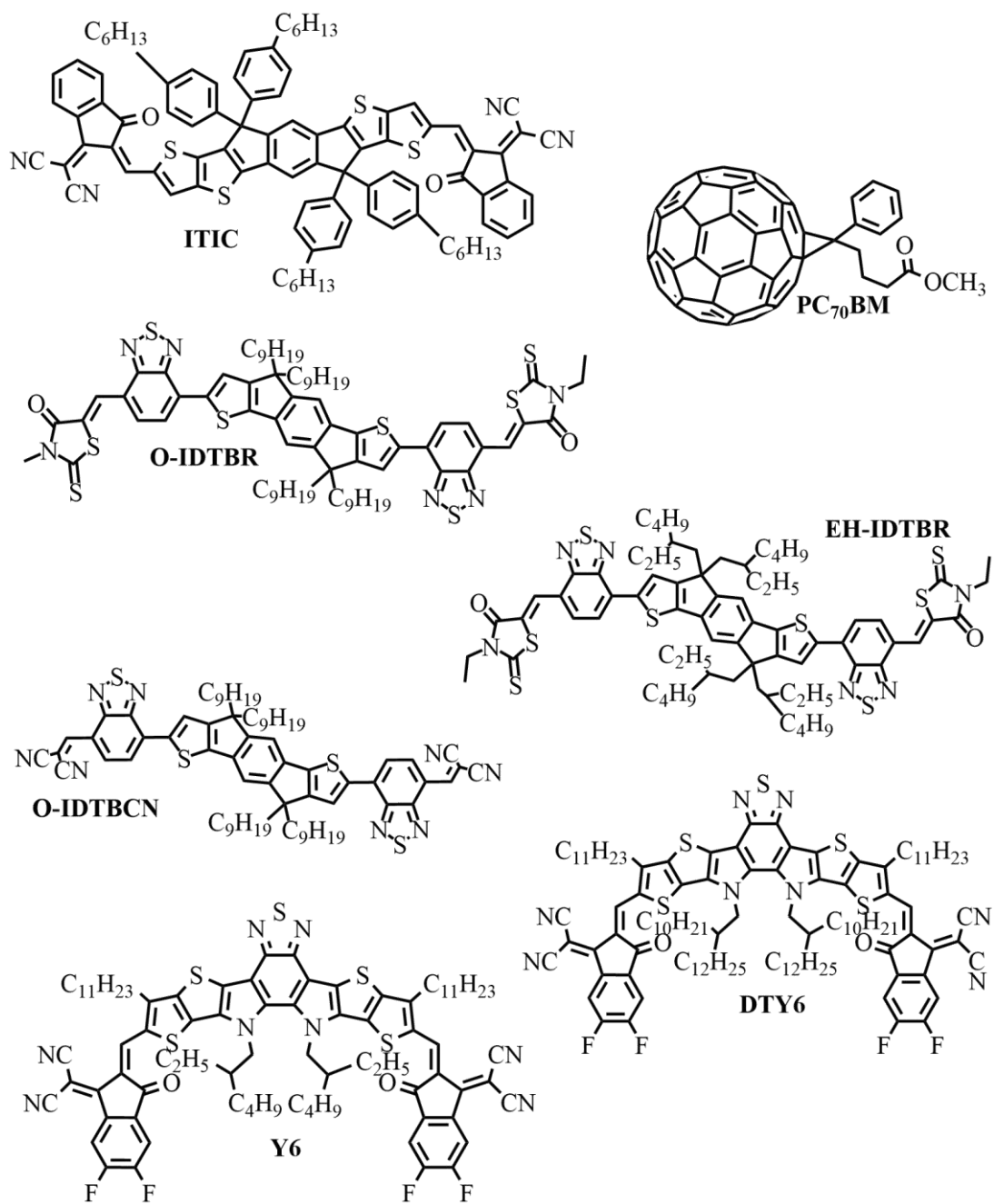


Figure 3.5: Acceptor molecules used.

3.2.6 Donors

This thesis used exclusively polymer donor materials, although there have been some recent works on high performance, all small molecule systems.¹⁶ The choice of donor is based on systems optimised in literature, where suitability of a donor acceptor combination is due to a number of factors including miscibility and energy level offsets. The donors used here can be seen in **Figure 3.6**.

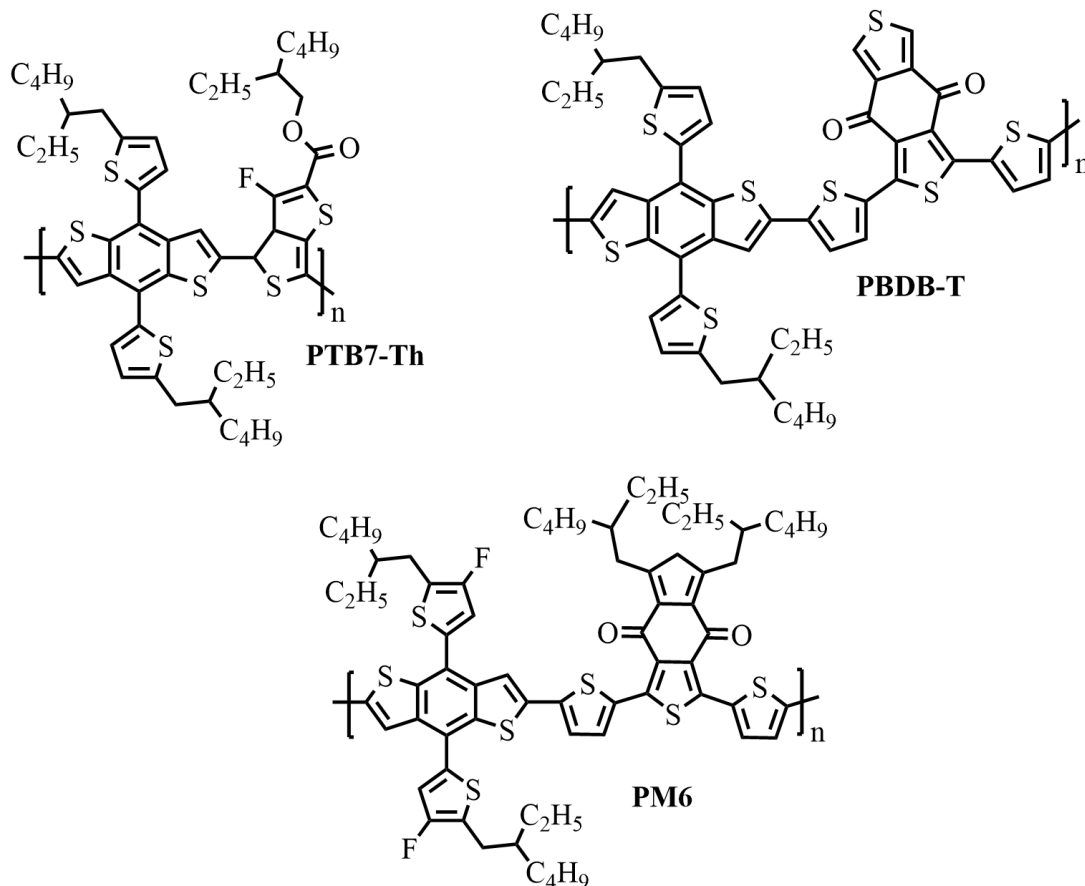


Figure 3.6: Donor polymers used.

3.2.7 Solvents

Solvent choice for an active layer or CTL system is based on solubility of the solutes, and properties such as the boiling point. Solvents suitable for spin coating may not be applicable for a different deposition technique, such as spray coating, as shown in **Chapter 4**. The toxicity of the solvent may also dictate its use, as non-halogenated solvents, such as *o*-Xylene, are usually considered more scalable than their halogenated alternatives. Here, *o*-Xylene, chlorobenzene and chloroform were used to dissolve various active layers, with methanol and 2-methoxyethanol used in CTL solutions.

Small amounts (~1%) of other solvents are sometimes added to the main solution to tune the final properties of the film, where these are known as ‘solvent additives’. This thesis

used two of these additives- 1,8-diiodooctane in **Chapter 5**, and ethanolamine in the ZnO solution in **Chapter 4** and **Chapter 6**. The chemical structures of the solvents and solvent additives used in this thesis are shown in **Figure 3.7**.

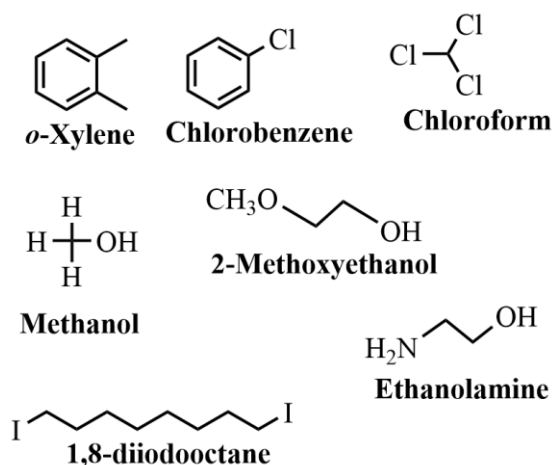


Figure 3.7: Solvents and solvent additives used in this thesis.

3.2.8 Summary

A summary of the batches and supplier of all materials used in this thesis can be found in **Table 3.1**.

Table 3.1: Supplier and batch number of all materials used.

Material	Supplier	Notes
PEDOT:PSS	Ossila	
PFN-Br		M _w : 165,000 g/mol
Zinc acetic dihydrate	Sigma Aldrich	
Molybdenum oxide		
ITIC	Ossila	
O-IDTBR	1-Material	
EH-IDTBR		
O-IDTBCN		
PC ₇₀ BM	Ossila	99% purity
Y6	1-Material	
DTY6	Ossila	
PBDB-T		
		1-Material

PTB7-Th	Ossila	M _w : 57,183 g/mol
PM6	1-Material	M _w : ~100,000 g/mol
Methanol	Sigma Aldrich	
2-methoxyethanol		
Ethanolamine		
Chlorobenzene		
<i>o</i> -Xylene		
Chloroform		
1,8-diiodooctane		

3.3 Deposition Methods

OPVs are thin film solar cells, meaning the CTLs, active layer, and electrodes are all on the order of nanometers. In general, solution processed techniques are favoured for their deposition as these can be theoretically extended to large scale, roll-to-roll fabrication. The theory behind the deposition methods discussed here can be found in **Chapter 2**.

3.3.1 Spin Coating

Spin coating is the most common lab-scale method of fabricating thin films from solution. Here, the substrate was held in place via either vacuum or an appropriately sized chuck. A small amount of solution (~30 – 40 μ L) was dropped onto the substrate via a micropipette, either before (static spin coating) or during (dynamic spin coating) the substrate spinning. This spinning was usually at several thousand revolutions per minute (rpm), and spread the solution out into a thin film via centrifugal forces. The choice of dynamic or static spin coating depended on the viscosity, volatility and wetting of the solution. A variety of spin coaters were used in this work, both in and out of a glovebox environment.

3.3.2 Spray Coating

Ultrasonic spray coating is a lower waste alternative to spin coating. In this thesis, a glovebox mounted Sonotek Exactacoat spray coater was used, shown in **Figure 3.8**. Coating inside a glovebox negated any negative impacts of oxygen or moisture on the quality of the final layer.

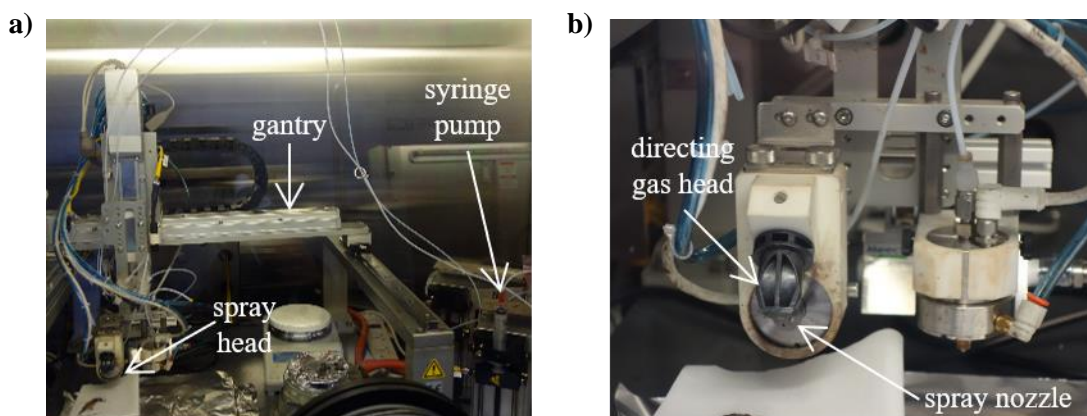


Figure 3.8: Ultrasonic spray coater used in this work. **a)** A full view of the system, including the syringe pump, lines, motorised gantry and spray head. **b)** A close-up view of the spray head, including the directing gas head and spray nozzle.

Here, the solution (often at a lower solid concentration than that used in spin coating) was driven by a syringe pump with a defined flow rate to the spray head. A piezoelectric nozzle in the spray head was vibrated in order to shear the solution used into a fine mist. A directing jet of nitrogen then guided this mist onto the substrate surface. The spray head was moved across the substrate via a motorised gantry to deposit solution across its entire surface. In an ideal process the droplets deposited then coalesced into a thin film that dried. In the spray coating process, several factors must be controlled, including the flow rate of solution, current (and so vibration) to the spray head, speed of the spray head movement, and distance between the head and substrate.

In our work, the film drying process was accelerated using an ‘air-knife’ attached to the gantry of the spray coater, pictured in **Figure 3.9**. Here a jet of moderately high-pressure nitrogen (~20 psi) was directed at the substrate after spray coating, with the gantry again moved across the substrate. The jet worked to accelerate the drying process, but has also been used by our group to induce perovskite formation in spray coated perovskite active layers.¹⁷ Again, the speed of movement and height of this air-knife will influence the quality and thickness of the final film.

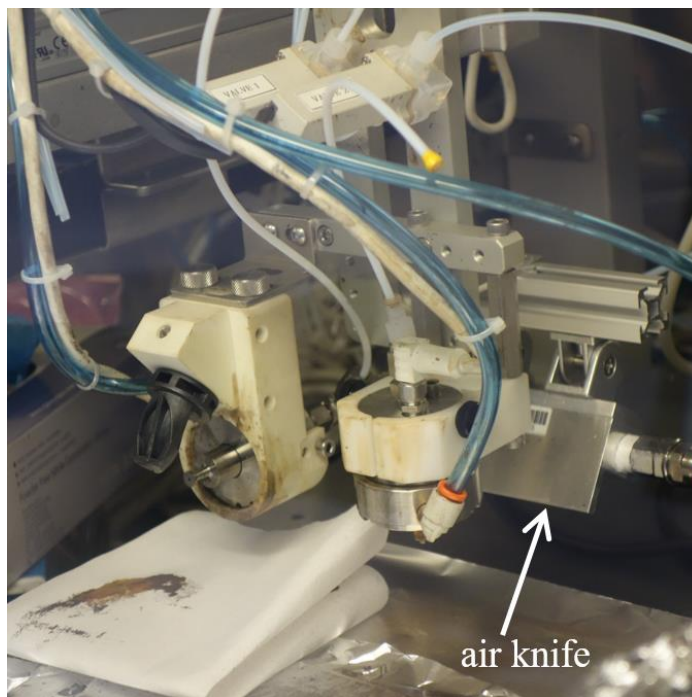


Figure 3.9: Air knife mounted to the same gantry as the spray head, although it is activated after (and not during) the spray process.

3.3.3 Thermal Evaporation

In this thesis the MoO₃ and Ag electrode were not deposited via a solution method, but instead thermal evaporation. Here, substrates were placed inside an evaporation mask with a defined area, and mounted in an evaporation chamber that was then pumped down to $\sim 2 \times 10^{-6}$ mBar. An Angstrom thermal evaporator was used for both materials. Small amounts of MoO₃ powder, and/or Ag pellets, were placed in the appropriate crucibles prior to pump down. These crucibles were then heated until the material began to vaporise, and travel onto the substrates. The rate of the deposition was measured using a calibrated quartz sensor, allowing the thickness of the evaporated layer to be finely controlled.

3.4 Device Fabrication

All devices were fabricated using a combination of solution processing and thermal evaporation. It is noted that most layers were subjected to a thermal anneal after deposition, the purpose of which depends on the layer.

3.4.1 Architecture

Devices were either fabricated in a conventional architecture, using PEDOT:PSS on the bottom and PFN-Br on the top of the active layer (**Chapter 5**), or an inverted architecture, using ZnO on the bottom and MoO₃ on the top (**Chapter 4 & Chapter 6**). In most cases, conventional and inverted cells using the same active layer will perform in a similar manner, although may show different stability. A visualization of these architectures can be seen in **Figure 3.10**.

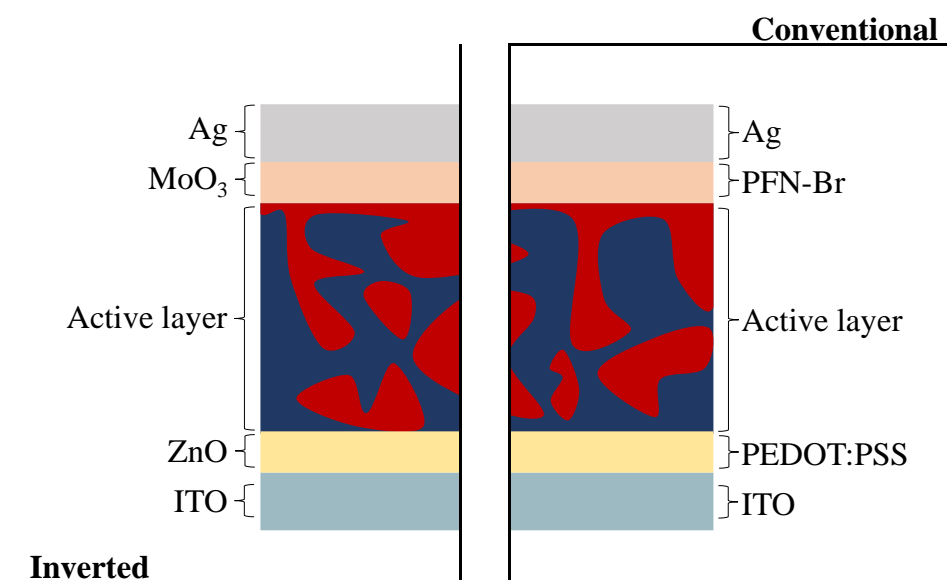


Figure 3.10: The layers used in the conventional and inverted architecture devices.

3.4.2 Cleaning

Prior to device manufacture, cleaning of substrates is important to remove any dust or contaminants that may impact the quality of the final thin film. As OPV CTLs are often on the order of only ~10 nm, dust can have a catastrophic impact. Here, ITO substrates were first labelled by number to allow identification during device fabrication. The substrates were then rubbed by hand with a small amount of a Hellmanex II soap solution, before rinsing under a tap. The substrates were then placed in a rack and sonicated in a dilute Hellmanex, boiling deionised (DI) water solution for 10 minutes. During this, and any subsequent sonication, the water bath was kept at ~50 °C. After sonication in Hellmanex, the substrate rack was dunk rinsed in boiling DI water twice, before a further 10 minute sonication in pure boiling DI water. Following this, substrates were sonicated in either acetone and isopropyl

alcohol for 10 minutes each (**Chapter 4 & Chapter 6**) or simply isopropyl alcohol (**Chapter 5**). After all sonication steps, the substrates were dried using a N₂ gun and subjected to an ultraviolet-ozone (UV-Ozone) treatment. In this process UV light dissociates oxygen present in the air to form ozone, which will react with any remaining organic compounds on the surface of the substrate, ensuring they are fully clean. UV-Ozone treatment will also improve the wetting of solutions onto the surface, as removal of organic contaminants will increase the surface energy. This is discussed further in **Section 3.7.4**.

3.4.3 Bottom CTL

After cleaning, the substrates were ready for the deposition of the first CTL. It was important for this to occur as soon after the UV-ozone treatment as possible to ensure good wetting and film quality. PEDOT:PSS was used as received from Ossila, after filtering through a 0.45µm polyvinylidene fluoride (PVDF) filter to remove aggregates. The solution was dynamically spin coated at 6000 rpm for 30 seconds in air to form a film of ~30 nm. After film fabrication, the substrates were then annealed at 110°C for 15 minutes in air, to remove any residual water. Films were then transferred to a nitrogen glovebox and annealed for a further 15 minutes under the same conditions.

ZnO was prepared via making a solution of zinc acetic dihydrate (219 mg) in 2-methoxyethanol (2 mL), with a small amount of ethanolamine (60.4 µL). This solution was stirred overnight, without heating, in order to ensure the material had dissolved. The next day the solution was filtered through a polytetrafluoroethylene (PTFE) filter to remove any undissolved material. It was then deposited via static spin coating at 4000 rpm for 30 seconds in air, before annealing at 150°C for 25 minutes. Here, the anneal was important to convert the zinc acetic dihydrate to the metal oxide, and so a high temperature and air environment were required. This formed a thin film of ~35 nm.

3.4.4 Patterning

In order to form a functional device, both electrodes must be able to be contacted. As a result, the deposited thin films needed to be ‘patterned’, i.e. partially removed, in order to expose the ITO underneath. An example of this can be seen in **Figure 3.11**, with a visualization of how this completes the electric circuit shown in **Figure 3.15**.

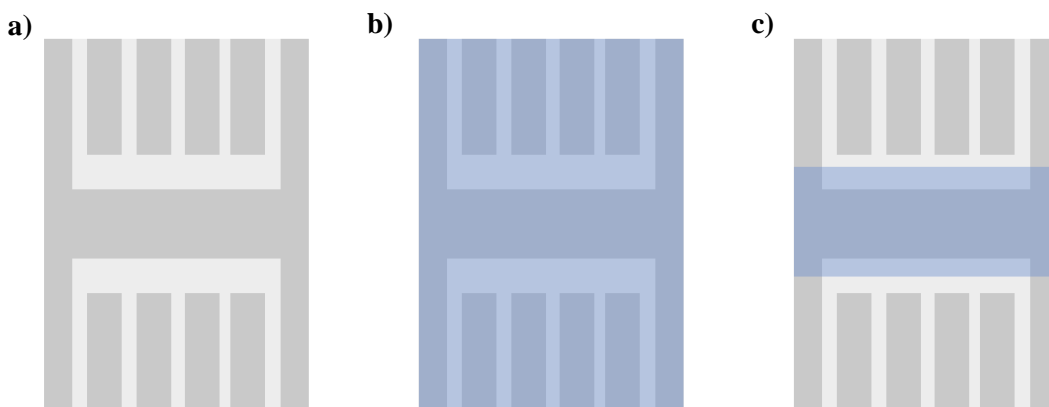


Figure 3.11: *a) A bare pre-patterned ITO substrate, b) after thin film deposition, c) after patterning of this thin film to allow exposure of the ITO.*

The patterning method depended on the layer involved. Ideally, all layers would be scraped off, for example using a razorblade, as was the case of the active layer. This avoided exposing the newly coated layer to any additional solvent, which may have damaged it. However, most layers were too soft or thin to allow scraping off, and instead most solution processed CTLs were patterned by ‘swabbing’ using a cotton bud dipped in an appropriate solvent. For PEDOT:PSS this was water, whereas for ZnO methanol was used. In both cases patterning was performed after spin coating, before the anneal. For PEDOT:PSS this was to allow all water to be evaporated in the anneal, whereas for ZnO this was because anneal would convert the precursor into the metal oxide, which is insoluble and difficult to remove via swabbing.

3.4.5 Active Layer

After deposition and patterning of the bottom CTL, the active layer was fabricated inside a glovebox. All active layer solutions were made by stirring the donor, acceptor and solvent overnight, whilst being heated, in a glovebox environment. The donor:acceptor ratio, solvent, solid concentration, and temperature of heating are all specified in the appropriate experimental chapters. As a general rule however, most systems were dissolved using ~1:1 donor:acceptor and a heating of ~60°C. No active layer solutions were filtered prior to deposition as in some cases high molecular weight donors may be unintentionally filtered out. The deposition conditions of the active layers are also given in the appropriate chapters; however, all active layers were subjected to a thermal anneal and patterned using a razor blade. For OPV active layers a thermal anneal is important to both remove solvent, and also improve the ordering of the components. It can also ‘freeze’ the film in a favourable morphology.

3.4.6 Top CTL

After active layer deposition, the final CTL was deposited. The PFN-Br was dissolved in methanol at a solid concentration of 0.5 mg/mL, and stirred overnight, in air, without heating. It was then spin coated dynamically at 3000rpm for 30 seconds, without anneal, inside a glovebox. Here, methanol was such a low boiling point solvent that an anneal was not required to remove it. This formed a layer of ~5 nm. As the PFN-Br was so thin, for conventional devices the active layer and PFN-Br were patterned simultaneously using a razor blade. MoO₃ was deposited via thermal evaporation.

3.4.7 Thermal Evaporation

Where MoO₃ was used, this was evaporated at a rate of 0.1 Å/s in order to form a film of ~ 10 nm. Cells of both architectures used an Ag top electrode, which was evaporated at 1.0 Å/s to yield a layer of ~ 100 nm. As evaporation was performed through a shadow mask within the pixel area, there was no need for patterning after deposition. An approximation of the evaporation mask and how this formed the pixels can be seen in **Figure 3.12**. As the evaporation mask was mounted in the top of the chamber, substrates were mounted with the coated layers facing down in the mask. The mask and substrates were slowly rotated during the evaporation to ensure even coverage.

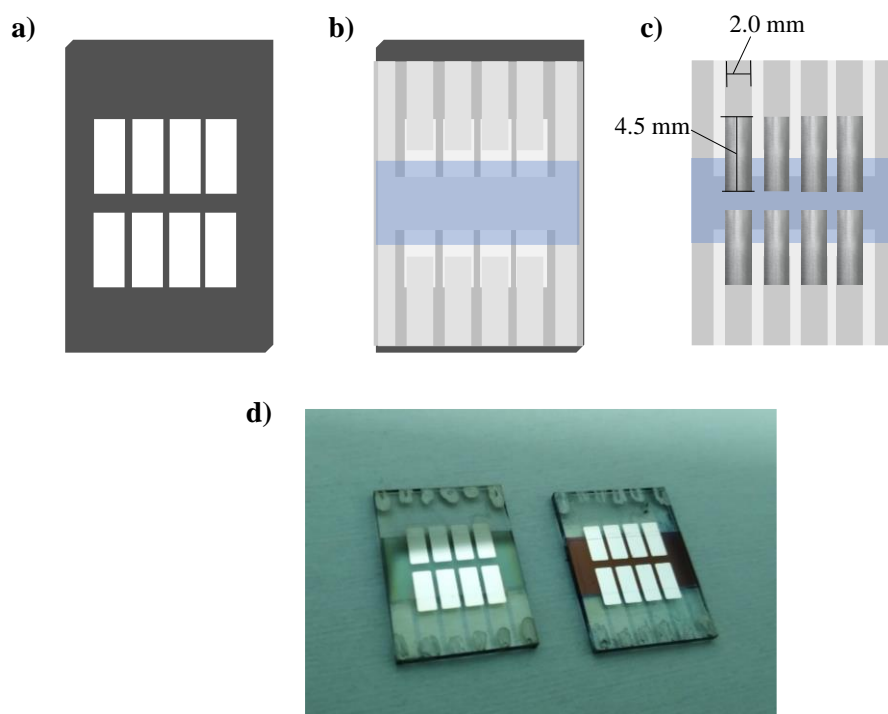


Figure 3.12: a) A single section of the evaporator mask, b) the coated substrate was mounted face-down into the mask, c) after evaporation 8 areas, each an individual device or 'pixel', were formed, d) a photo of real-life devices.

3.4.8 Encapsulation

In some cases, the devices were encapsulated in order to protect against oxygen and moisture. Here, a UV-curable epoxy from Ossila was used. A single drop was placed in the middle of the substrate, topped with a glass slide, and cured under a UV lamp at ~ 350 nm for 15 minutes. This epoxy then set and formed a hard barrier against extrinsic degradation. This can be seen in **Figure 3.13**. Prior to testing some devices were also painted with small amounts of silver paint on their ITO contacts to ensure good conduction (seen in **Figure 3.12d**).

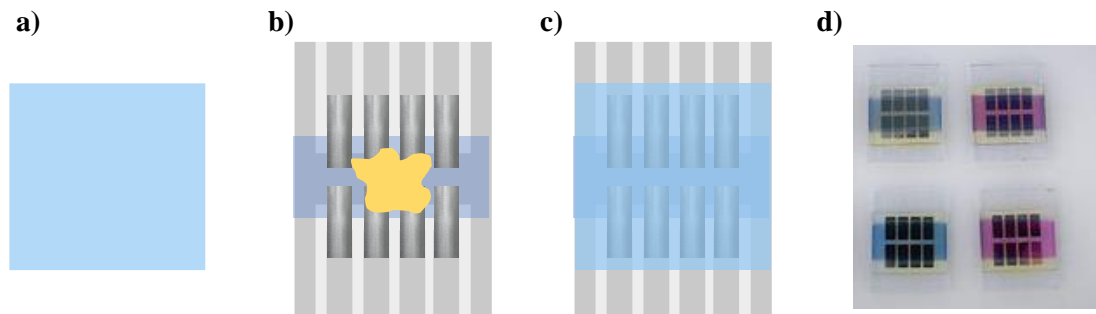


Figure 3.13: *a) Encapsulation glass slide, b) completed device with epoxy drop, c) device with encapsulation slide secured, d) photo of real-life devices after encapsulation.*

3.5 Device Characterization

3.5.1 Charge Transport in the Completed Device

In order to test the devices, an illumination mask was used that only allowed light through a small, defined area (2.5 mm^2) to the device. The devices were illuminated from the bottom (through the ITO), as shown in **Figure 3.14**.

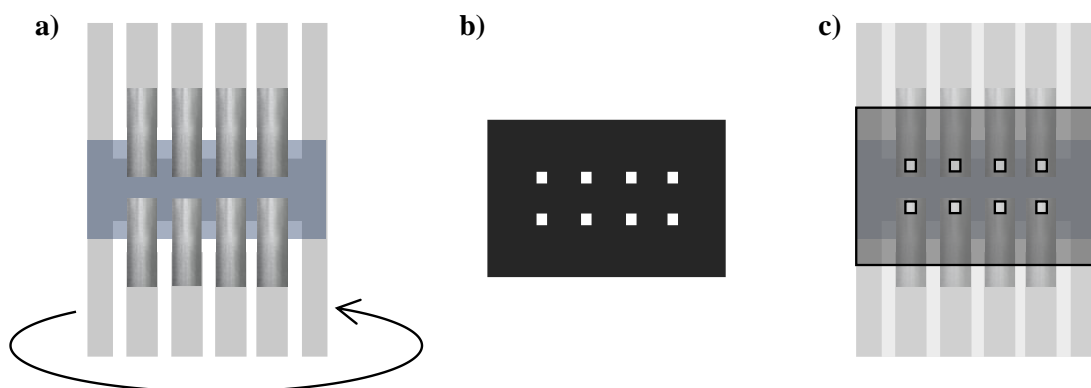


Figure 3.14: *a) Completed device was flipped to be illuminated through the glass/ITO, b) illumination mask, c) illumination mask mounted on facedown substrate.*

Charges were collected through the ITO on either side of the glass patterning, as depicted below in **Figure 3.15**. It is clear here that scratches, damage, or pinholes in the thin films or ITO that allow the metal and ITO beneath to contact would complete the circuit and short the device.

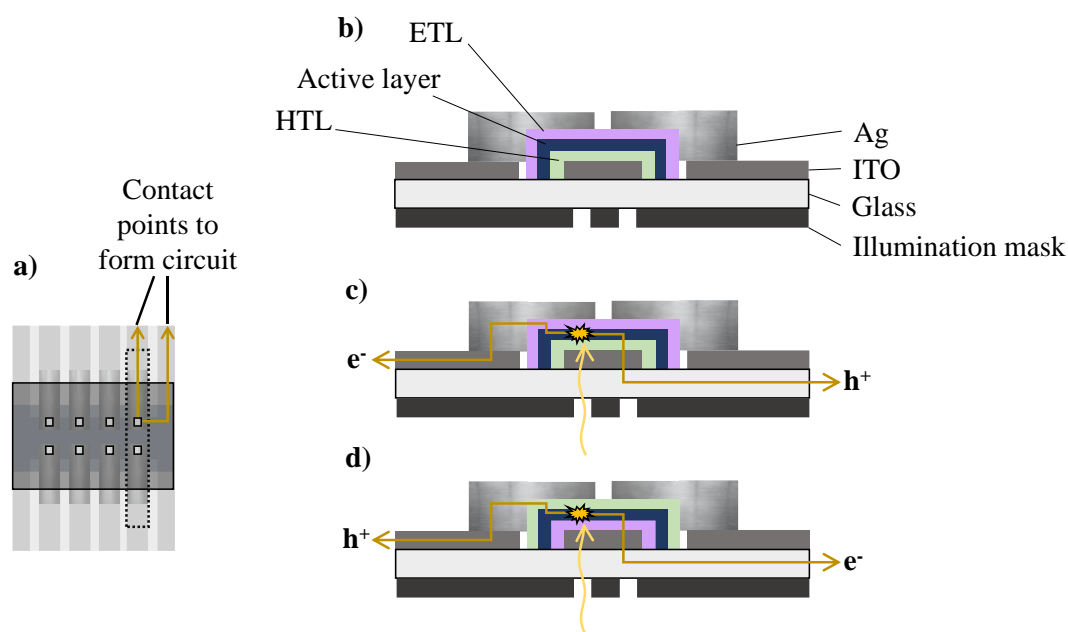


Figure 3.15: **a)** A completed device mounted with an illumination mask. The device is contacted at the corner, and at the ITO for the pixel being tested. The dotted box represents the area shown in **b-c**. **b)** A side on view of a device with illumination mask, **c)** direction of charge carriers for a conventional architecture device upon illumination. Note holes do not travel through glass, but instead the parallel ITO as shown in **a**). **d)** Direction of charge carriers for an inverted architecture device upon illumination.

3.5.2 Current Voltage Measurements

After fabrication, devices were tested using a Newport solar simulator (92251A-1000) that outputted a spectrum close to AM 1.5. Before testing, the solar simulator was calibrated using a silicon reference cell to ensure was outputting close to 1 Sun (1000 W/m^2). Current-voltage (JV) sweeps were performed both forward and reverse from 0 to 1.2 V at a speed of 0.2 V/s. This process was controlled by a MatLab code that outputted the JV sweep data and calculated short circuit current (J_{SC}), open circuit voltage (V_{OC}), fill factor (FF) and power conversion efficiency (PCE). These metrics were then recalculated from the sweeps using a homemade python code that also outputted the statistics for the 10 top performing devices (in terms of PCE), removed any devices that shorted or were non-functional, and

generated box plots of each metric. Unless specified, all metrics are an average of forward and reverse sweeps.

3.5.3 Light Dependant Measurements

As discussed in **Chapter 2**, light dependant V_{OC} and J_{SC} can provide useful information about the recombination in the device. As the Newport solar simulator was powered by a Xenon arc lamp, which is known to show spectral instability upon changing power,¹⁸ a light emitting diode (LED) solar simulator was instead used for light dependant measurements. Here an Oriel LSH-7320 ABA LED solar simulator was used to measure devices in the same manner as specified above, with the output varied from 0.1 to 1.0 sun in steps of 0.1. Fitting of this data to the models given in **Chapter 2** was performed in Origin.

3.5.4 Photocurrent (J_{ph}) measurements

By sweeping devices over a larger range (-1.5 to 1.5 V), in both the dark and under illumination, the ‘photocurrent density’ was extracted. This can provide a valuable measure of the exciton dissociation and collection efficiency, with further details given in **Chapter 4**.

3.5.5 External Quantum Efficiency

External quantum efficiency (EQE) measurements were taken using a Newport QuantX-300 Quantum Efficiency Measurement System, pictured below. Here a 100 W Xenon arc lamp was focused through an Oriel CS130B monochromator. Before each set of measurements, the system was calibrated with a silicon reference photodiode. The lamp was then focused on a single pixel, and the photocurrent measured as the wavelength was varied. The range of this is specified in the relevant experimental chapter, but was generally ~325 – 950 nm. Integrated J_{SC} values were obtained in Origin using an interpolated AM 1.5 spectrum available from NREL.¹⁹

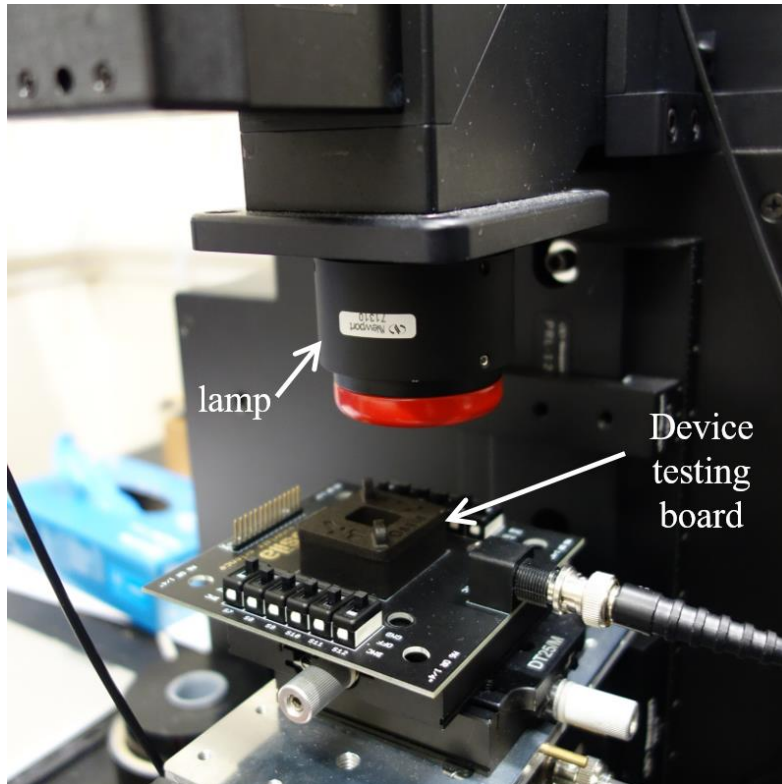


Figure 3.16: EQE set up used, where devices are mounted onto an Ossila test board for tracking photocurrent as the lamp wavelength is varied.

3.5.6 Light beam induced current mapping

Light beam induced current mapping (LBIC) is a technique that can be used to generate a 2D map of the photocurrent of a small area of a device, in order to identify defects or non-uniformities. In this thesis LBIC was performed using a custom set up with a 623 nm Thor Labs HRS015B laser, operating at 1.2 mW. This was passed through a 500 Hz chopper, and beam splitter, before being focused onto the device. The spot size was approximately 25 μm in diameter. Upon illumination, the photocurrent of the device was measured using a Stanford Research Systems SR830 lock-in amplifier. The device was mounted on a programmable XY stage, which translated it in steps of 25 μm during the measurement, allowing a 2D map of the photocurrent to be generated.

3.6 Device Stability

As a number of factors can influence the stability of devices, ideally their performance is tracked under a range of degradation stresses.

3.6.1 Shelf Life Testing

In this work, intrinsic stability was assessed using periodic testing of devices that were stored in the glovebox, in the dark. Here, only morphological degradation and reactions within the cell will degrade performance. In each case, devices were tested initially, stored, and removed from the glovebox for further testing every few days. The data over several devices was averaged and normalized to initial performance. The number of devices is specified for each case, but in general the top three initial pixels (in terms of PCE) were tracked.

3.6.2 Illuminated stability

Illuminated stability was assessed using an Atlas Suntest CPS+ lifetime tester, pictured below. Here, metal connection legs were mounted onto devices to allow them to be fitted to the testing board. This maintained the devices at V_{OC} and performed a JV sweep (0 to 1 V) on each pixel at ~20 minute intervals. A maximum of eight substrates (64 devices) could be mounted inside the Atlas at any one time.

The Atlas used a 1500 W Xenon lamp and was fitted with daylight extended infrared (IR) filters, and internal mirrors, to yield a spectrum that approximated AM 1.5. This illumination did have some associated heating, with the temperature found to stabilise at ~43°C. Data for this is shown in **Chapter 5**.

The Atlas outputted calculated device metrics, but these were not considered completely accurate as an aperture mask was not used during the illumination, and the spectrum differed to that of the Newport solar simulator. Instead, a python code was used to average the top two or three devices per type, and the metrics normalized to their initial performance.

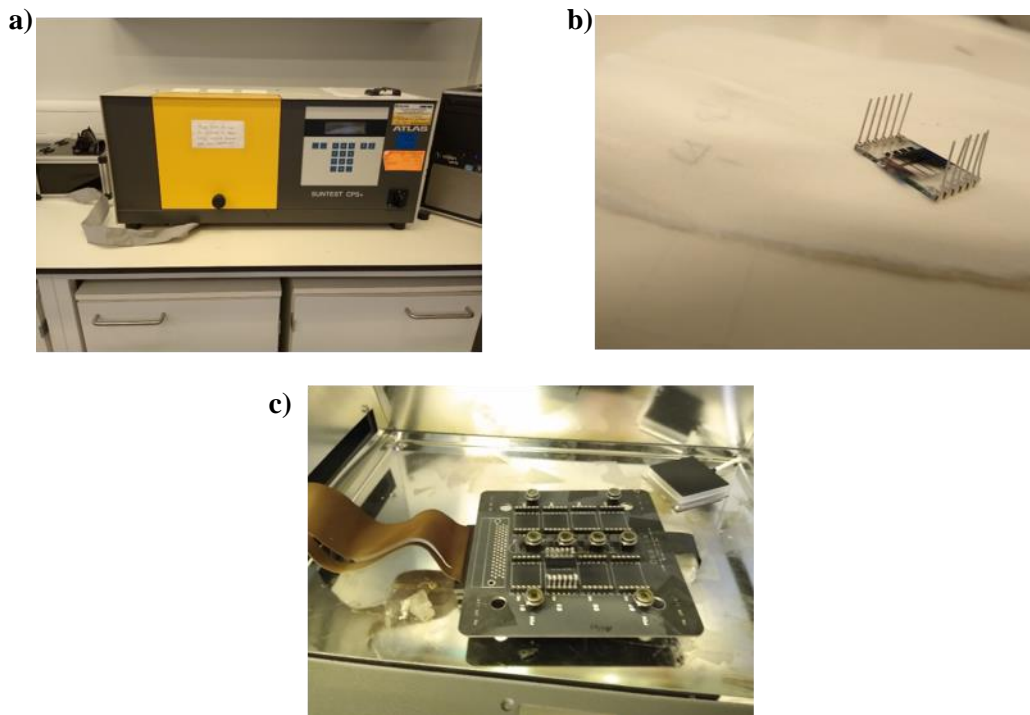


Figure 5.17: a) Atlas Suntest CPS+, b) device with legs mounted, c) device in lifetime testing board, in one of the eight slots. The spectrum of the Atlas tester can be found in Bovill *et al.*²⁰

3.7 Film Characterization

All characterization was performed on thin films prepared in the same manner as devices, with the substrate specified in the relevant experimental chapter.

3.7.1 Ultraviolet-Visible Absorption & Photoluminescence

Ultraviolet-visible (UV-Vis) absorption was performed on one of two set-ups depending on the chapter. That in **Chapter 5** was performed using an Ocean Optics light source (DH-2000-BAL) and spectrometer (HR2000+ES) in a custom set-up shown. Here, the sample was measured in transmission mode and corrected according to the background of the substrate (usually ITO or quartz). The spectrum was produced in Oceanview, and the absorbance outputted.

The absorbance in **Chapter 4** and **Chapter 6** was performed using a Horiba Fluoromax 4 flurometer, fitted with a Xe lamp and monochromator. Whilst the set-up above showed a superior signal to noise ratio in the infra-red region, the Fluoromax gave better results in the low wavelength region. Here, the background and transmission values were converted to absorbance using:

$$\text{Absorbance} = -\log_{10}\left(\frac{I}{I_0}\right) \quad (\text{Eq. 3.1})$$

The intensity of the transmission of the sample is represented here by I , with the intensity of the background represented as I_0 . The Fluoromax featured a detector both before (‘reference’) and after (‘signal’) the light hits the sample, allowing for removal of noise from the lamp.

The Fluoromax was also used for photoluminescence (PL) measurements. Here the sample was excited by a light of a specific wavelength (given in the relevant chapter), and the emitted light measured. In both these cases, a monochromator was used before the relevant detector. The direction of each of these monochromators and detectors can be seen in **Figure 3.18**.

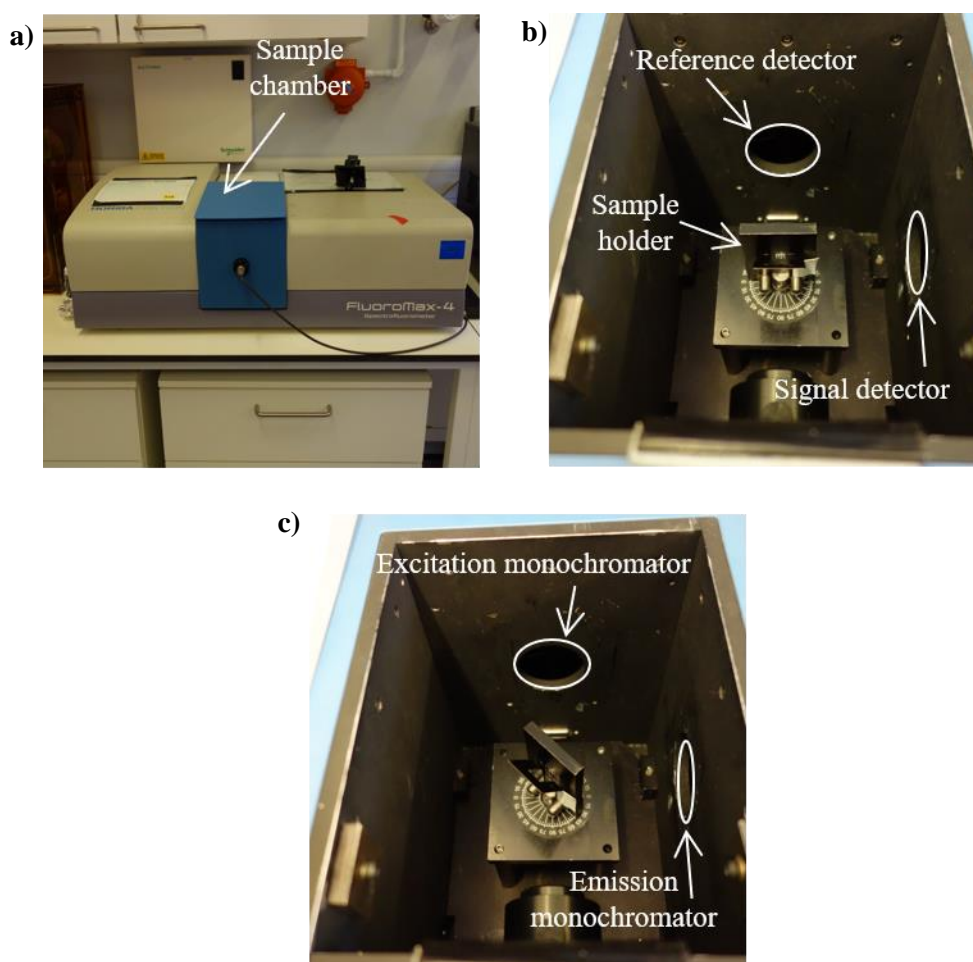


Figure 3.18: a) Fluoromax, b) sample chamber in the arrangement for absorption/transmission, with the outlets leading to both detectors labelled, c) arrangement for PL, with the sample at an angle to minimize the excitation signal on the signal detector.

3.7.2 Atomic Force Microscopy

Atomic force microscopy measurements were taken using a Veeco Dimension 3100, with samples prepared in the same manner as devices. In all cases, ITO coated glass was used. Samples were measured in tapping mode, over a small (e.g. 5 μm x 5 μm) area. The outputted files were processed in Gwyddion to step line correct and extract the root mean square roughness (RMS). Unless specified otherwise, all RMS values given in this thesis are an average of multiple measurements on the same film.

3.7.3 Profilometry

Film thicknesses were measured using a Bruker Dektak surface profilometer. Here, samples were scratched multiple times (usually using a razor blade), to create a trench of the same depth as the thickness of the film. A stylus was then scanned across the sample to produce a height profile, from which thickness was extracted. Unless specified otherwise, all thickness values given in this thesis are an average of line scans across at least three different scratches of the same film.

3.7.4 Contact Angle Goniometry

Contact angle measurements are a valuable measure of the wetting of a solution onto a given substrate, and can be used to calculate the surface energy of a film. Here, a syringe filled with the appropriate solvent was secured above the sample. An Ossila contact angle goniometer was used to film the sample as a drop of solvent was released. The video frame corresponding to the droplet hitting the surface was analysed to find the contact angle, as shown in **Figure 3.19**.

A high contact angle implies poor wetting, and a low surface energy, and vice versa. Several models can be used to calculate surface energy from contact angle, with further details given in the literature^{21,22} and **Chapter 5**.

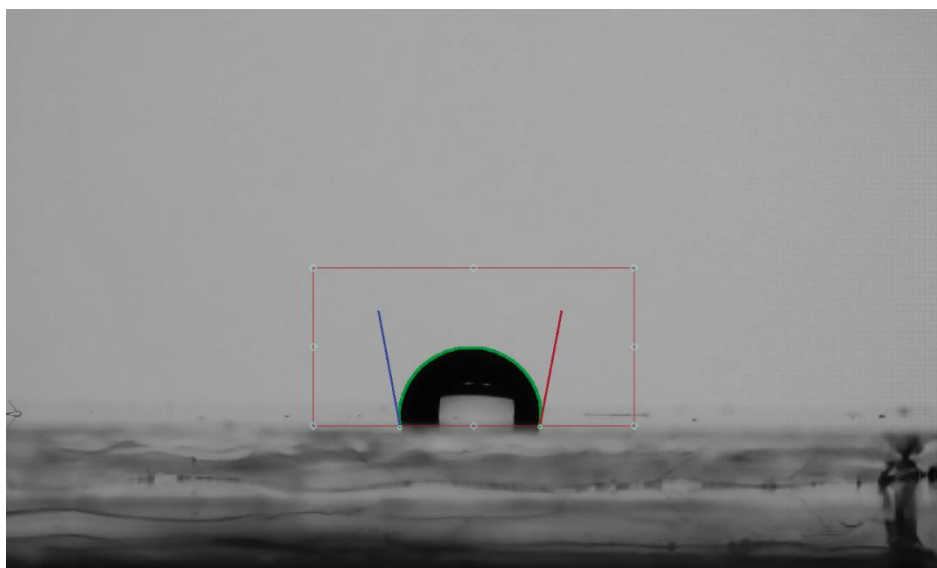


Figure 3.19: A screenshot from the ossila contact angle software. Here the area of analysis was defined and the software used python to identify the right and left angles the drop made with the film. In this case they were 100.5° and 100.7° respectively.

3.7.5 Grazing Incidence Wide Angle X-ray Scattering

Grazing incidence wide angle x-ray scattering (GIWAXS) is a scattering technique that can be used to gain information about the small scale (\sim nm), ordered features of a thin film. As crystallinity and orientation are key to high performing OPVs, this is a valuable characterization tool.

At its basis, X-ray diffraction techniques such as GIWAXS use an X-ray source to target X-rays onto a sample, and a detector to detect the scattering of these X-rays. Crystalline, repeating lattices in the sample will scatter the X-rays according to Bragg's law:²³

$$2d\sin\theta = n\lambda \quad (\text{Eq. 3.2})$$

Here θ is the angle of the X-ray beam, d is the spacing between the crystalline planes, n is an integer, and λ is the wavelength of the incident X-ray beam. The angle of the beam will dictate how deeply it penetrates into the sample, where a deeper angle penetrates deeper into the sample. GIWAXS is distinguished from non-grazing X-ray techniques by using a very shallow incident angle (e.g. 0.15°). The choice of angle will depend on the material, as at a 'critical angle' X-rays will interact with the bulk of the material. The critical angle for a given material is dependant on its electron and physical density.²⁴

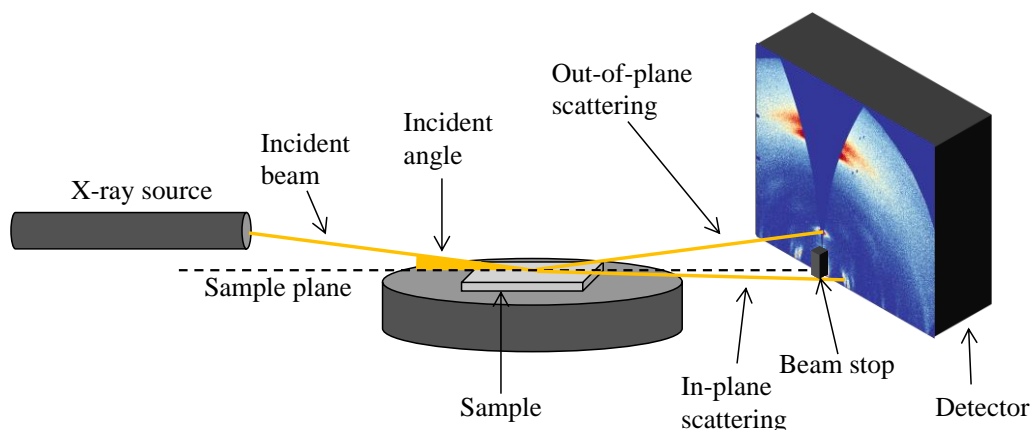


Figure 3.20: A simplified GIWAXS set up, where the X-ray is incident at a shallow angle on the sample, and this then scatters the X-rays onto a detector.

In GIWAXS, after the shallow angle X-ray hits the sample, it will scatter both in and out of the plane of the substrate, with the intensity of each depending on the orientation of the crystal planes on the substrate. The magnitude of the x-ray scattering is given by the scattering vector ‘ q ’, which can be expressed as:²⁵

$$q = \frac{4\pi \sin\theta}{\lambda} = \frac{2\pi}{d} \quad (\text{Eq. 3.3})$$

The scattering in and out of plane yields a two dimensional detector image, described by q_{xy} (in-plane) and q_z (out-of-plane). **Equation 3.3** illustrates that the position of the scattering vector is dependent on the spacing between the crystalline planes. As a result, this spacing (sometimes referred to as ‘ d -spacing’) can be calculated from the value of q , and is usually on the order of nanometres. The relationship between orientation and scattering is depicted in **Figure 3.21**. Here highly ordered planes in a single orientation will lead to narrow scattering in one plane, whereas randomly orientated planes will yield scattering rings.

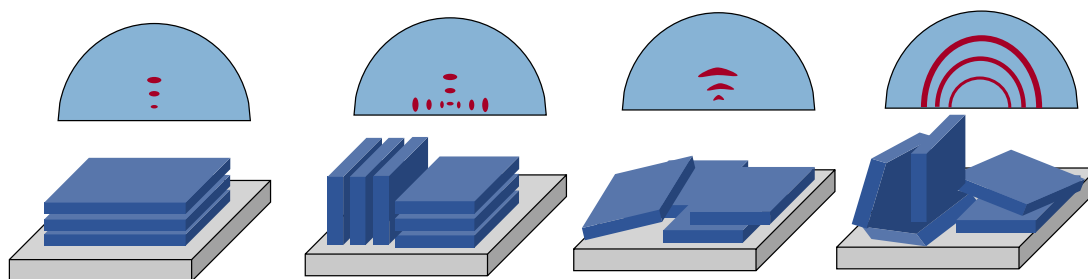


Figure 3.21: The relationship between orientation and scattering direction. Figure adapted from Müller-Buschbaum et al.²⁶

Crystal planes in inorganic materials are usually described using Miller indices, which describe the location of the plane in a Bravais lattice, via the form of three integers: h , k , and

l. The miller indices for a specific scattering peak are usually calculated using the unit cell of that system, or are often indexed automatically using GIWAXS analysis software. In this thesis all miller indices given are taken from similar systems in literature.

The 2D scattering patterns can be ‘linecut’ to 1D intensity profiles in either direction of scattering. In this work linecuts were produced via azimuthal integration, in the range of $-20^\circ < \chi < 20^\circ$ for out-of-plane and $-70^\circ < \chi < 90^\circ$ for in-plane. A visualization of this is shown in **Figure 3.22**. These 1D intensity profiles can then be fitted (usually with a Gaussian function) to obtain the full width half maximum (FWHM) of a specific feature. This FWHM can be used to obtain the average size of a crystal structure using Smilgies’ adaptation²⁷ of the Scherrer equation. This is referred to here as the crystal coherence length (CCL), although it has several names. It is noted that CCL is not directly translatable to phases or grains, and does not imply good crystallinity, but simply describes the size of an ordered region.

$$CCL = \frac{2\pi K}{FWHM} \quad (\text{Eq. 3.4})$$

Here K is the Scherrer constant. The exact value of this depends on the context, but here 1 is used for simplicity.

From **Equations 3.3 & 3.4** we can therefore know that in linecuts narrow peaks imply larger crystallite size than broad peaks, a larger q value implies a smaller d -spacing, and the position of the peak in q_z or q_{xy} gives information about its orientation.

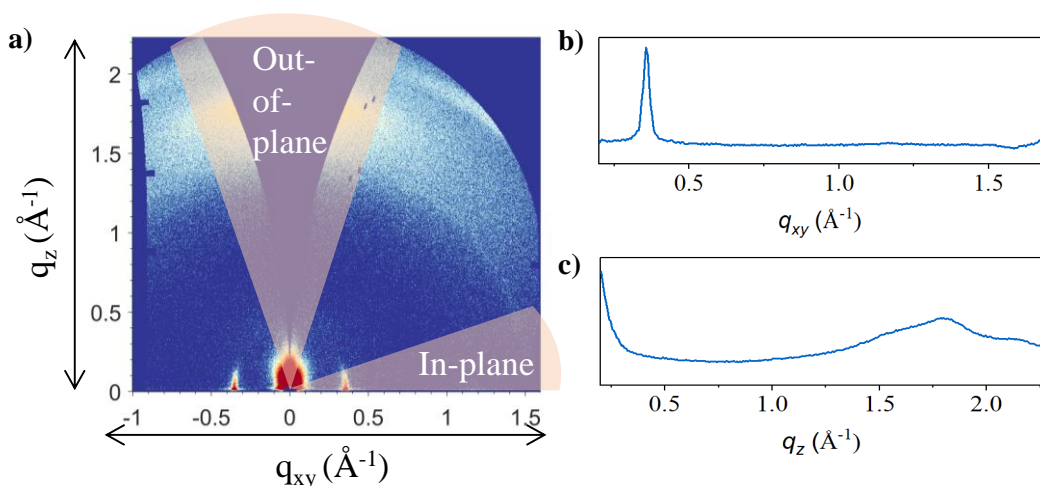


Figure 3.22: *a)* A visualization of the areas integrated to produce each type of linecut, and the corresponding graphs, *b)* in-plane, *c)* out-of-plane. Figure adapted from that produced by R. Kilbride in Sasitharan et al.²⁸

Using this information, GIWAXS can be used to probe the order in organic thin films. As detailed in **Chapter 2**, organic semiconductors pack in both lamellar stacks and π - π stacks,

with these having different inherent length scales of packing, and total aggregate size. GIWAXS can therefore show the orientation and size of these relative types of packing. As lamellar stacks will be larger than those based on π - π stacking, they will appear at lower q values, and vice versa. Typically lamellar features present at $\sim q = 0.5 \text{ \AA}^{-1}$, and π - π features at $\sim 1.7 \text{ \AA}^{-1}$. A depiction of how these features might appear in is shown in **Figure 3.23**.

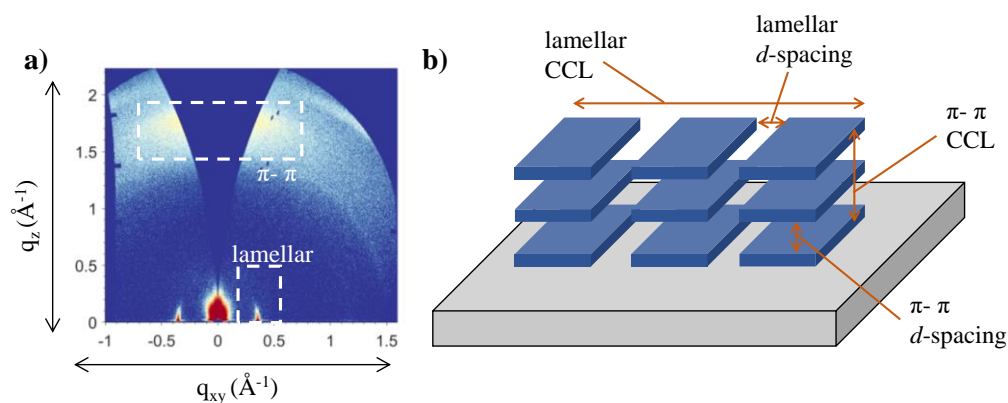


Figure 3.23: **a)** 2D GIWAXS pattern for a face-on structure, with the lamellar and π - π features highlighted. **b)** The face-on structure, with the features described by d -spacing and CCL illustrated.

In this figure, the lamellar stacking is in-plane with the substrate, and so appears in the in-plane direction (and the in-plane linecut shown in **Figure 3.22b**). The π - π stacking is out-of-plane with the substrate and so appears in the out-of-plane direction in the 2D pattern (and the linecut in **Figure 3.22c**). These positions are a strong indication of a face-on (e.g. with the π - π stacking parallel to the substrate) orientation, which is favourable for OPV performance.

In this thesis, GIWAXS measurements were performed on films prepared in the same manner as devices, with specifics detailed in the relevant experimental chapters. Data for **Chapter 5 & Chapter 6** was measured using a Xenocs Xeuss 2.0 system, with a liquid gallium MetalJet X-ray source. This source produced X-rays at an energy of 9.24 eV ($\lambda = 134 \text{ nm}$), with the incident angle quoted in the relevant chapters. A Pilatus 1M detector was used, at a sample to detector distance of $\sim 307 \text{ mm}$. The sample to detector distance was calibrated using silver behenate. All GIWAXS measurements were taken under vacuum to reduce background scatter. Data for **Chapter 4** was measured at the DL-SAXS beamline at the Diamond Light Source. All conditions were the same, except a Xenocs Xeuss 3.0 system was used instead.

Data in **Chapter 4** was processed by Dr Joel Smith via a custom-built python code, utilising the 'Python Fast Azimuthal Integration' (PyFAI) library.²⁹ Data in **Chapter 5** and **Chapter 6** was processed by Rachel Kilbride using GIXSGUI, a Matlab based visualization

and reduction toolkit published by Jiang *et al.*³⁰ All data was corrected, reshaped, and azimuthally integrated to yield the 2D patterns and 1D linecuts.

3.7.6 Visible Light Microscopy

Visible light microscopy (VLM) was performed using a Nikon Eclipse ME600 microscope, with the relevant scale quoted in the experimental chapters.

3.8 Other Techniques

3.8.1 Differential Scanning Calorimetry

Differential scanning calorimetry (DSC) involves heating a small amount of solid material, and measuring the difference in amount of heat required to increase the temperature of the sample compared to that of a reference. This yields a measure of heat flow against temperature. DSC can provide information about a range of thermal transitions, as these will disrupt the heat flow of the solid, in the form of peaks. Depending on the sample, and if the data is presented with exothermic features up or down, transitions such as glass transition, cold crystallization and melting may all be visible. An approximation of this can be seen in **Figure 3.24**.

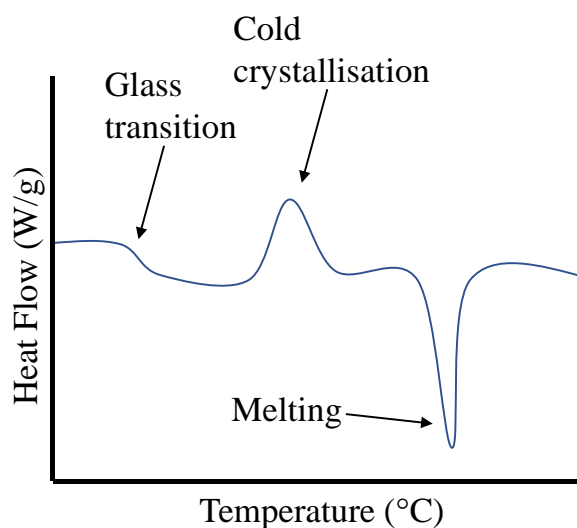


Figure 3.24: An approximate DSC curve for a semi-crystalline material. This is presented with exothermic features up, as with all other DSC data in this thesis.

As a glass transition and melting transition are both endothermic (i.e. they require heat), they will show as downward peaks if the data is presented with exotherms up. Cold crystallization is instead exothermic, as it is a bond-making process, meaning it will appear

as an upward peak. The enthalpy of a process can be obtained via integration of the appropriate peak.

DSC in this thesis was performed by preparing thin films in the same manner as devices, and then scraping these films into a vial to collect the corresponding solid. In this way the component transitions are representative of devices, as factors such as crystallinity and thickness can influence T_g .³¹

DSC was performed using a TA Instruments DSC25 with a RSC90 chiller unit. Here, the system was calibrated using an Indium standard, and the solid collected from the films placed into an aluminium pan. Data was corrected according to the weight of the sample, and processed in Trios.

3.8.2 Nuclear Magnetic Resonance Spectroscopy

Nuclear magnetic resonance (NMR) spectroscopy is a technique that can provide information about the chemical environments of specific elements in a solution. The NMR used in this thesis was ^1H (proton) NMR. Here the interaction of nuclear spins of the ^1H atoms, under a magnetic field, provide information about their bonding and adjacent atoms. This can be used to identify the presence and relative amounts of certain compounds in a solution.

To perform the ^1H NMR, thin film samples were prepared in the same manner as devices, dissolved, and the solution left to evaporate in order to obtain the solid. This solid was then re-dissolved in a deuterated solvent. A deuterated solvent was required to avoid ^1H atoms in the solvent swamping the NMR signal. In all cases in this thesis, *d*-chloroform was used, and the samples dissolved in $\sim 600\ \mu\text{L}$. Data was acquired using a Bruker Avance III 400MHz, and analysed using TopSpin.

3.9 References

1. Xu, H., Yuan, F., Zhou, D. & Chen, Y. Hole transport layers for organic solar cells- recent progress and prospects. *J. Mat. Chem. A*. **8**, 11478–11492 (2020).
2. Baik, S. *et al.* ITIC derivative acceptors for ternary organic solar cells: fine-tuning of absorption bands, LUMO energy levels, and cascade charge transfer. *Sustainable Energy & Fuels*. **6**, 110–120 (2022).
3. Hori, T., Moritou, H., Fukuoka, N., Sakamoto, J. & Fujii, A. Photovoltaic Properties in Interpenetrating Heterojunction Organic Solar Cells Utilizing MoO₃ and ZnO Charge Transport Buffer Layers. *Materials* **3**, 4915–4921 (2010).
4. Gong, Y. *et al.* Diverse applications of MoO₃ for high performance organic photovoltaics: fundamentals, processes and optimization strategies. *J. Mat. Chem. A*. **8**, 978–1009 (2020).
5. Links, D. A. Fullerene derivative acceptors for high performance polymer solar cells. *Phys. Chem. Chem. Phys.* **13**, 1970–1983 (2011).
6. Shin, Y. S. *et al.* Functionalized PFN - X (X = Cl, Br, or I) for Balanced Charge Carriers of Highly Efficient Blue Light-Emitting Diodes. *ACS Appl. Mater. Interfaces* **12**, 35740–35747 (2020).
7. Holliday, S. *et al.* High-efficiency and air-stable P3HT-based polymer solar cells with a new non-fullerene acceptor. *Nat. Commun.* **7**, 11585 (2016).
8. Wadsworth, A. *et al.* End Group Tuning in Acceptor–Donor–Acceptor Nonfullerene Small Molecules for High Fill Factor Organic Solar Cells. *Adv. Funct. Mater.* **29**, 1–8 (2019).
9. Lin, Y. *et al.* An electron acceptor challenging fullerenes for efficient polymer solar cells. *Adv Mater* **27**, 1170–1174 (2015).
10. Dong, S., Jia, T., Zhang, K., Jing, J. & Huang, F. Single-Component Non-halogen Solvent-Processed High-Performance Organic Solar Cell Module with Efficiency over 14%. *Joule* **4**, 2004–2016 (2020).
11. Wong-Stringer, M. *et al.* High-Performance Multilayer Encapsulation for Perovskite Photovoltaics. *Adv. Energy Mater.* **8**, 1–11 (2018).
12. Lin, Y. *et al.* Self-assembled monolayer enables hole transport layer-free organic solar cells with 18% efficiency and improved operational stability. *ACS Energy Lett.* **5**, 2935–2944 (2020).
13. Yao, J. *et al.* Cathode engineering with perylene-diimide interlayer enabling over 17% efficiency single-junction organic solar cells. *Nat. Commun.* **11**, 1–10 (2020).
14. Liu, C. & Xiao, C. Zinc oxide nanoparticles as electron transporting interlayer in organic solar cells. *J. Mat. Chem. C*. **9**, 14093–14114 (2021).
15. Zhang, Y. *et al.* Thermally Stable All-Polymer Solar Cells with High Tolerance on Blend Ratios. *Adv. Ener. Mater.* **8**, 1–10 (2018).
16. Jiang, M. *et al.* Two-Pronged Effect of Warm Solution and Solvent-Vapor Annealing for Efficient and Stable All-Small-Molecule Organic Solar Cells. *ACS Energy Lett.* **6**, 2898–2906 (2021).
17. Cassella, E. J. *et al.* Gas-Assisted Spray Coating of Perovskite Solar Cells Incorporating Sprayed Self-Assembled Monolayers. *Adv. Sci.* **2104848**, 1–10 (2022).
18. Matson, R. J., Emery, K. A. & Bird, R. E. Terrestrial solar spectra, solar simulation and solar cell short-circuit current calibration: A review. *Sol. Cells* **11**, 105–145 (1984).
19. NREL. NREL Reference AM1.5 Spectrum. Available at: <https://www.nrel.gov/grid/solar-resource/spectra-am1.5.html>. (Accessed Jan 2022)
20. Bovill, E. *et al.* The role of the hole-extraction layer in determining the operational stability of a polycarbazole:fullerene bulk-heterojunction photovoltaic device. *Appl. Phys. Lett.* **106**, 073301 (2015).
21. Zhang, Z. *et al.* Binary Liquid Mixture Contact-Angle Measurements for Precise Estimation of Surface Free Energy. *Langmuir* **35**, 12317–12325 (2019).
22. Vuckovac, M., Latikka, M., Liu, K., Huhtamäki, T. & Ras, R. H. A. Uncertainties in contact angle goniometry. *Soft Matter* **15**, 7089–7096 (2019).
23. Pope, C. G. X-ray diffraction and the bragg equation. *J. Chem. Educ.* **74**, 129–131 (1997).
24. Wang, W. *et al.* Influence of Solvent Additive 1,8-Octanedithiol on P3HT:PCBM Solar Cells. *Adv. Funct. Mater.* **28**, 1–9 (2018).
25. Rivnay, J., Mannsfeld, S. C. B., Miller, C. E., Salleo, A. & Toney, M. F. Quantitative determination of organic semiconductor microstructure from the molecular to device scale. *Chem. Rev.* **112**, 5488–5519 (2012).
26. Müller-Buschbaum, P. The active layer morphology of organic solar cells probed with grazing incidence scattering techniques. *Adv. Mater.* **26**, 7692–7709 (2014).
27. Smilgies, D. M. Scherrer grain-size analysis adapted to grazing-incidence scattering with area detectors. *J. Appl. Crystallogr.* **42**, 1030–1034 (2009).
28. Sasitharan, K. *et al.* Metal-organic framework nanosheets as templates to enhance performance in semi-crystalline organic photovoltaic cells, *Adv. Sci.*, Accepted (2022).
29. Kieffer, J. & Karkoulis, D. PyFAI, a versatile library for azimuthal regrouping, *J. Phys.: Conf. Ser.*

- 425**, 202012 (2013).
30. Jiang, Z. GIXSGUI: a MATLAB toolbox for grazing-incidence X-ray scattering data visualization and reduction, and indexing of buried three-dimensional periodic nanostructured films. *J. Appl. Cryst.* **48**, 917-926 (2015).
 31. Hamon, L., Grohens, Y. & Holl, Y. Thickness Dependence of the Glass Transition Temperature in Thin Films of Partially Miscible Polymer Blends. *Langmuir* **19**, 10399–10402 (2003).

Chapter 4 | Air Knife-Assisted Spray Coating of Organic Photovoltaics

4.1 Author Contributions

This chapter forms part of a collaborative project intended for submission as a paper and some experimental work was completed by other people. Specifically, Tom Catley performed AFM measurements. Dr Sam Burholt assisted in taking the GIWAXS measurements. Dr Joel Smith processed the GIWAXS data. Elena Cassella originated the use of the air-knife, assisted in optimising the spray coating process, performed LBIC measurements, assisted in GIWAXS processing, and advised on the direction of the project and manuscript. I wrote the manuscript, fabricated the devices, developed the spray coating process, performed device characterization, and analysed all the data. All interpretation of results is my own.

4.2 Abstract

The power conversion efficiencies (PCEs) of organic photovoltaics (OPVs) have risen dramatically since the introduction of the ‘Y-series’ of non-fullerene acceptors (NFAs). Scalable deposition of these systems has become increasingly important for commercialization but has been mostly restricted to meniscus-based techniques. Here, we demonstrate ultrasonic spray coating of a Y-series NFA based system. To overcome film reticulation due to prolonged drying times, we explore the use of an air-knife to rapidly remove the casting solvent. We show that this approach allows a control a control of drying dynamics without any solvent-additives, or heating of the substrate or casting ink and allows us to fabricate spray coated PM6:DTY6 devices with PCEs of up to 14.1%. Our work demonstrates the compatibility of ultrasonic spray coating with high-speed, roll-to-roll manufacturing techniques.

4.3 Introduction

The recent introduction of the “Y-series” of non-fullerene acceptors (NFAs)¹ has spurred renewed interest in the field of OPVs, leading to record PCEs approaching 19%.² This class of NFAs is particularly notable for enhanced absorption in the near infra-red region (leading to record short circuit current values),³ high electron mobility (promoting long diffusion lengths),⁴ and low voltage losses.

Whilst these efficiencies of such devices now approaching those required for commercialization,⁵ the best-performing Y-series cells are still created using spin coating; a wasteful process that is incompatible with high-speed and high-volume roll-to-roll (R2R) manufacturing. These cells are also typically fabricated using environmentally toxic, halogenated solvents – such as chloroform. To propel the transition from “lab-to-fab”, it is necessary to develop scalable deposition technologies that both retain the PCEs of lab-scale devices and employ green solvent formulations.⁶

Although there has been success in fabricating such devices using R2R-compatible methods, progress has been mostly limited to the use of meniscus-based techniques such as blade^{7–12} and slot-die coating.^{13–15} The adoption of non-halogenated solvents in film deposition has also been complicated by the poor solubility and aggregation tendency of many Y-series molecules.⁷ Various methods have been used to overcome this, including deposition from hot inks (so called “hot-casting”),^{10,13,16} the use of chemically modified acceptors such as DTY6,⁷ BTP-4F-12,¹⁷ BTP-BO-4Cl¹⁸ and BTP-eC9;¹⁹ and the addition of solvent additives.²⁰ Encouragingly, efficiencies from blade coated, non-halogenated systems now approach 17%.^{12,21}

We note that droplet-based scalable techniques, such as spray coating, offer several key advantages over meniscus-based methods. Firstly, non-contact deposition techniques unlocks opportunities to fabricate devices over non-planar surfaces;²² secondly, spray coating has been estimated to have a far lower initial investment cost than techniques such as blade coating.²³ Finally, spray coating has demonstrated at coating speeds as high as 12 m min⁻¹; a rate that far exceeds that of other common deposition techniques.²⁴ Critically, enhancing the speed of high-throughput processing has been demonstrated to be a major contributing factor to enable the sustainable growth of solar manufacturing techniques to limit climate-change targets.²⁵

Recently, a droplet-based aerosol “vibrating-mesh atomisation” method has been developed by Yang *et al.*¹⁶ This technique was used to deposit both the charge-transporting layers and active layer of PTQ10:Y6-BO devices, creating fully-printed devices with PCEs as high as 14.8 %. However, we note that the slow 3 mm s⁻¹ deposition speed of this technique, coupled with the requirement to heat the active layer solution to 80 °C, could lead to a process having relatively high manufacture-costs.

Ultrasonic spray coating is a droplet-based technique that has seen widespread use to fabricate both perovskite solar cells (PSCs)²⁶ and OPVs.^{27–29} Here, the ultrasonic vibration of a piezo ceramic tip is used to break up the ink into a fine mist that is directed to the surface of a substrate using a gas jet. Such droplets then coalesce and dry, forming a thin film. In this work we use ultrasonic spray coating with a Y-series acceptor to create an OPV device based on the polymer:NFA blend PM6:DTY6. Using the non-halogenated solvent *o*-Xylene, state-of-the-art PCEs of up to 14.1% are obtained. Importantly, this process does not require solvent additives nor the necessity to apply any heating processes to either the casting solution or substrate. Instead, we control the wet film drying dynamics using only an air-knife, which has been demonstrated to be an industrially-scalable technique used to “gas-quench” hybrid lead halide perovskite films spray-coated cells,²⁶ and to assist drying in blade coated OSCs.¹²

4.4 Results and Discussion

4.4.1 Methodology

Devices were fabricated on an indium-doped tin oxide (ITO) anode in “inverted” architecture format, with devices utilising a spin-coated zinc oxide (ZnO) electron-transporting layer and thermally evaporated molybdenum oxide (MoO_x) hole-transporting layer. The bulk heterojunction (BHJ) active layer was deposited by either spin coating or ultrasonic spray coating (referred to henceforth as “spray-coated devices”) from *o*-Xylene. The BHJ consisted of a DTY6 (**Figure 4.1a**) acceptor and a PM6 (**Figure 4.1b**) donor in a 1:1.2 blend. The absorption of the components and blend can be seen in **Figure 4.1c** and the complete device stack is shown in **Figure 4.1d**. Full details of all materials, fabrication techniques and processes used are described in the Experimental Methods.

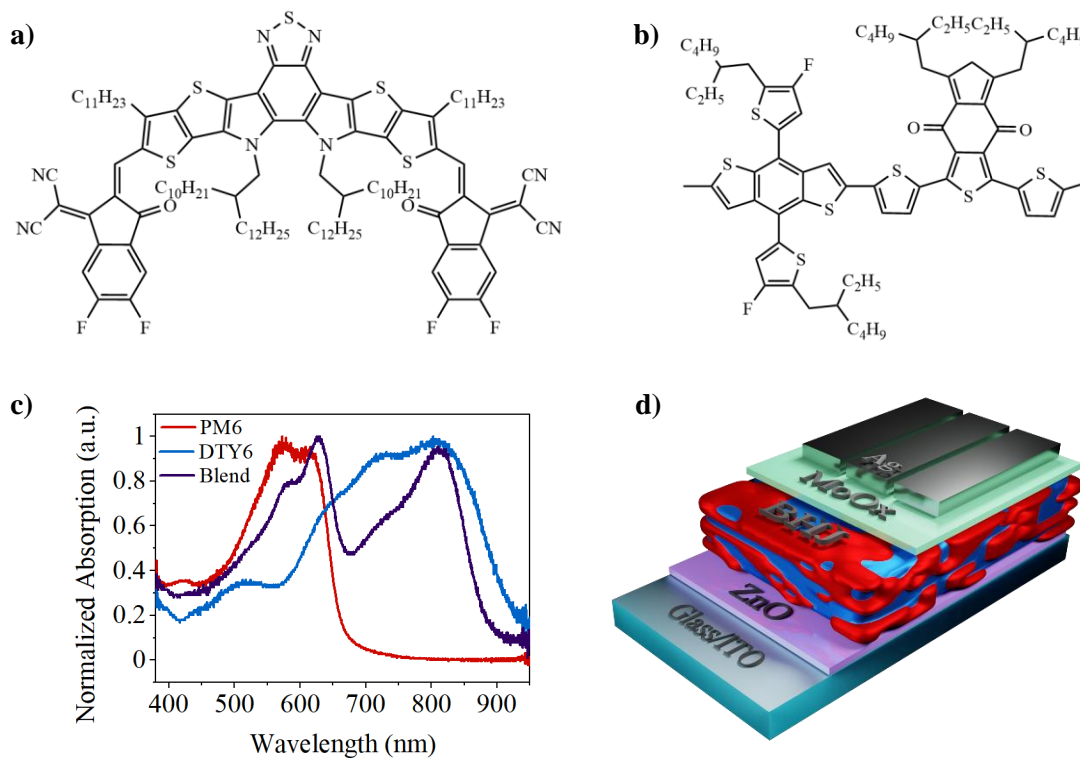


Figure 4.1: Chemical structure of **a)** DTY6, **b)** PM6. **c)** Thin film UV-Vis absorbance of PM6, DTY6, and a 1:1.2 blend. **d)** Schematic of the complete device architecture.

4.4.2 Device Fabrication and Performance

Spray-coated devices were fabricated using a Sonotek Exactacoat system housed within a nitrogen-filled glovebox. During the spray coating process, the casting solution was fed into the spray head at a predefined flow rate, with a piezoelectric transducer used to generate ultrasonic vibrations to break up the solution into a series of uniform droplets. A gas-jet is then used to guide the droplet mist towards the substrate surface. Following their arrival at the surface, the droplets coalesce to form a continuous wet film. It was found that optimisation of a series of parameters was necessary to deposit sufficient material to achieve formation of a high quality layer.³⁰ These parameters included head height, head speed, fluid flow rate, transducer driving power, substrate temperature, the pressure of the directing gas, and the nature of the casting solvent. In our optimised process, a motorized gantry was used to move the spray head linearly across the substrate surface at a speed of 20 mm s⁻¹, with a substrate-to-head separation maintained at around 10 cm. The active layer solution was spray-cast in a single pass at a flow rate of 1.5 mL min⁻¹ with the vibrating tip operating at a power of 1 W. This process is visualized in **Figure 4.2a**.

Although “Y-series” acceptors are typically deposited from chloroform, our initial experiments demonstrated that wet films spray-cast from chloroform did not undergo droplet

coalescence (see **Figure S4.1a & S4.1b**). Here, the low vapour pressure of chloroform (boiling point 61 °C), coupled with the reduced atmospheric pressure of the glovebox and the application of the directing gas caused the droplets to dry upon contact with the substrate before they were able to coalesce.

Previous studies have noted that the material Y6 tends to aggregate in high boiling point solvents.^{7,10} Modification of the chemical structure of Y6 can allow this to be overcome. For example, alkylated derivative DTY6 has been shown to produce high performance OPVs in both low and high boiling point solvents,⁷ including non-halogenated solvent *o*-Xylene. An *o*-Xylene solvent has also been used to fabricate high-efficiency Y-series based OPVs via blade coating,^{3,4,13} slot-die coating,¹³ and aerosol printing.¹⁶ It is therefore an excellent candidate for a higher boiling point solvent for spray coating. Inspired by these works, we therefore adapted the spray coating process to use a PM6:DTY6 blend in *o*-Xylene.

Here, it was found that if the deposition substrate was either heated or left at room-temperature, spray-cast films underwent significant reticulation (see **Figure 4.2b**). We note that solution de-wetting is not uncommon during spray-casting films due to the dilute nature of the casting ink even though *o*-Xylene has a low contact angle on ZnO (**Figure S4.2b**).²² This is less likely to occur in techniques such as spin coating and blade coating due to the additional forces present (centrifugal and meniscus dragging respectively). One strategy to overcome this issue is to deposit a moderately large amount of ink to form a continuous film, however, we found that the elevated drying times of high boiling point solvent such as *o*-Xylene together with surface tension effects still resulted in reticulation.

To mitigate this effect, we have explored the use of an air-knife which we pass over the film surface using a motorised gantry. We have developed a process in which the air-knife is moved linearly across the substrate surface at a separation of ~2 cm, blowing a jet of N₂ (at 20 psi) across the film surface shortly after the organic film has been spray-cast (see schematic in **Figure 4.2c**). We find that this process (which we call air-knife assisted solvent extraction [ASE]) encourages evaporation of the casting solvent and subsequently reduces the wet film drying time. Although the application of the air flow results in the loss of some of the spray-cast ink as it is “sheared off”, we find that the solution reticulation is largely overcome, with uniform films having a high degree of surface coverage realised (see **Figure 4.2d**).

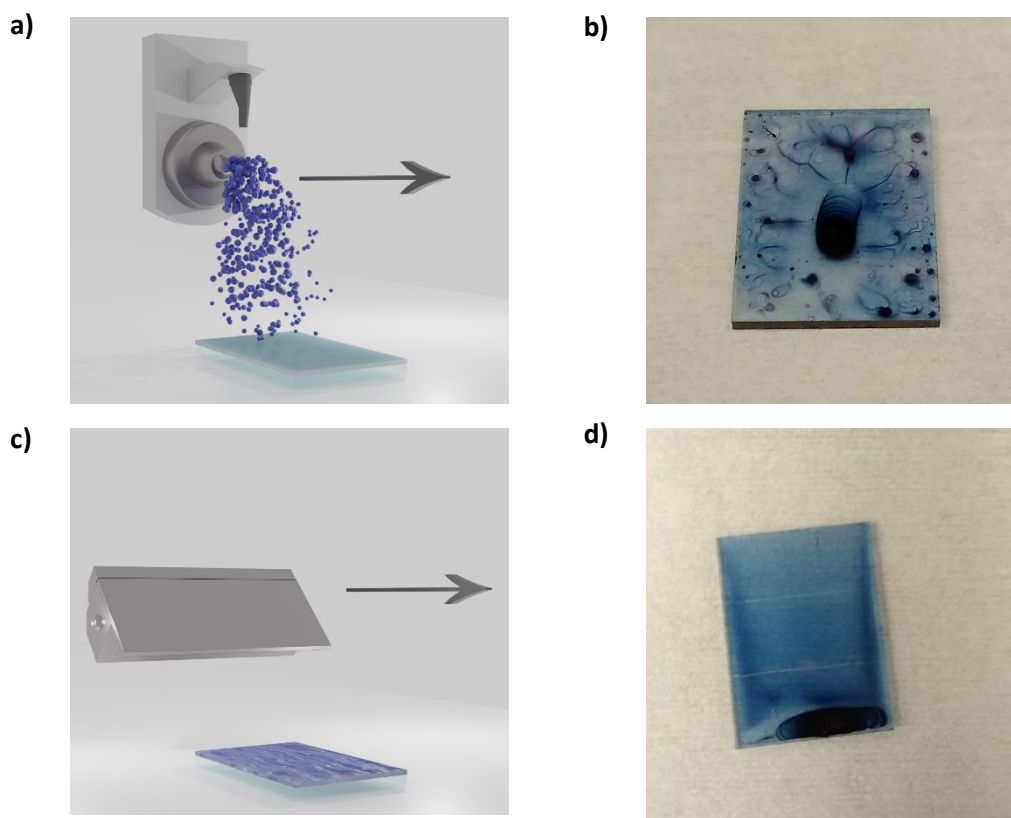


Figure 4.2: *a) Schematic of the spray coating head as it moves across the substrate. b) PM6:DTY6 film coated using o-Xylene, displaying significant reticulation. c) Schematic of the air-knife moving across the spray-cast film. d) PM6:DTY6 film coated using o-Xylene, showing superior coverage but some material accumulation at the edge.*

Our previously work on using an air-knife to control nucleation and crystallization of perovskite thin films indicated that the “delay time” between spray-casting the precursor solution and the application of the air-knife is a key optimisation parameter which we used to control the structure and morphology of the resultant perovskite films.²⁶ We use a similar approach here, and - guided by device performance - we have optimised this delay time and find that device PCE is maximised at a delay of 50 seconds (see **Figure 4.3a**).

Our measurements indicate that the air-knife delay time can be used to tune the thickness of the final film, with an extended delay time resulting in a film having enhanced thickness (see **Table S4.1**). We suspect that this effect most likely results from increased solvent evaporation before the application of the gas-jet, with the solution that is spread over the surface having enhanced solid concentration and viscosity. We find that this thickness increase is correlated with an increase in short-circuit current (J_{sc}), shown in **Figure S4.3a**, and Ultraviolet-Visible (UV-Vis) absorption intensity, shown in **Figure S4.3b**. Notably however, we find that device fill factor (FF) is reduced for extended delay times, a result explained by the creation of films that are too thick and result in devices with increased series resistance. Interestingly, we find that optimised devices based on spray-coated films generally utilise a slightly thinner (~ 90 nm) active layer than do those created by spin-coating (~ 140

nm); a result that we discuss further below. We therefore base our optimised spray-deposition process on a delay time of 50 seconds which is used in all device fabrication experiments detailed below.

We firstly compare the performance of optimised spin- and spray-cast devices using a box plot in **Figure 4.3b** and summarise device metrics in **Table 4.1**. The current-voltage (JV) curves for champion devices are also shown in **Figure 4.3c & 4.3d**. Encouragingly, we find that the champion performance of optimised spray- and spin-cast films is similar (see **Table 4.1**), with the highest achieved efficiencies 14.1 and 14.2% respectively.

Table 4.1: Device metrics for optimised spin-coated and optimised spray-coated devices. Results are presented as an average of 10 cells ± 1 standard deviation, with the champion cell efficiency shown in parenthesis. Forward and backward sweeps are treated separately but counted as 1 cell.

Deposition Method	PCE (%)	FF (%)	V_{oc} (V)	J_{sc} (mA cm ⁻²)
Spin	13.6 \pm 0.4 (14.2)	70.5 \pm 1.5 (73.4)	0.85 \pm 0.00 (0.85)	22.8 \pm 0.70 (24.0)
Spray	12.2 \pm 0.8 (14.1)	68.0 \pm 2.9 (71.8)	0.84 \pm 0.01 (0.85)	21.4 \pm 0.95 (23.1)

Despite the similar efficiency of champion devices prepared by spray- and spin-coating, we find a greater variation in performance for devices based on spray-cast films, (see the histogram of device efficiency shown in **Figure S4.4**). It is evident that this enhanced variation in efficiency principally occurs from greater spread in both V_{oc} and J_{sc} values. Furthermore, the device performance for spray-cast films did not improve consistently with increased thickness (i.e. extended delay time). These results indicate that the difference in average performance between the spin-coated and spray-coated films does not originate from thickness differences alone.

To understand the origin of the difference in efficiency of our spray- and spin-cast devices, we have characterised their external quantum efficiency (EQE), with the extracted integrated J_{sc} as shown in **Figure 4.3e**. We find that the integrated J_{sc} values determined from the EQE spectra match those determined using our solar simulator (see comparison detailed in **Table S4.2**), with any discrepancy between values being less than 10%.³¹ It is clear, however, that there are some differences between the EQE spectra for the spray- and spin-cast devices, with the EQE being relatively smaller around ~ 700 nm in the spray-coated devices. If we compare this spectral region with the absorption of the PM6 donor and DTY6 acceptor

(see **Figure 4.1c**) it appears that this reduction is due to reduced photocurrent generation by the DTY6.

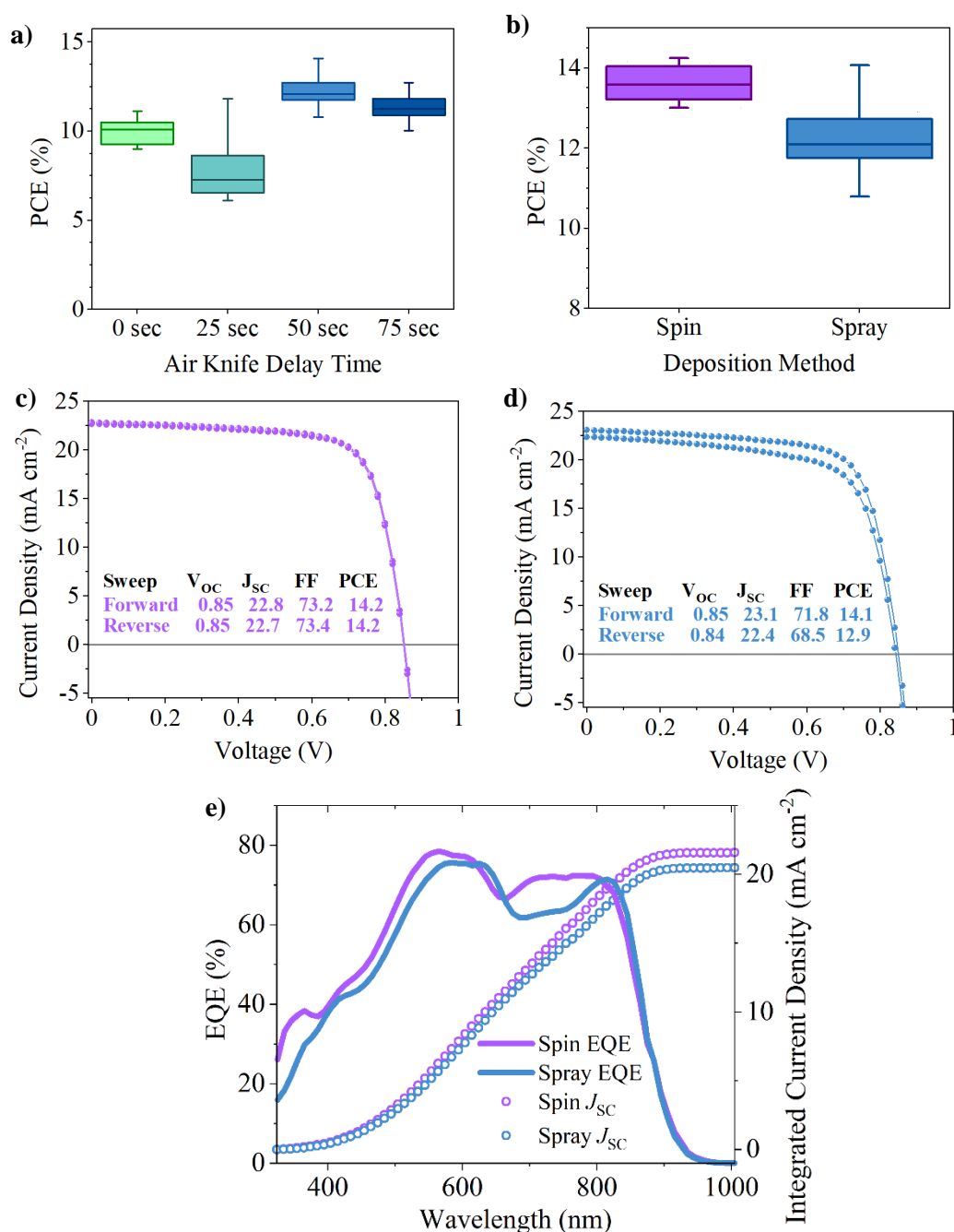


Figure 4.3: *a)* Box plot of PCE for varying air-knife delay time. *b)* Box plot of PCE for the optimised spray process compared to spin controls, *c)* Champion spin JV curve. *d)* Champion spray JV curve. *e)* EQE curves of representative spin and spray devices, with integrated J_{sc} values shown.

It is worth noting that photoluminescence (PL) emission spectra, shown in **Fig. S4.4**, undergo the same levels of quenching in all films prepared from the two process routes. This suggests either that exciton dissociation is similarly efficient in all cases, or that the differences cannot be distinguished with the resolution of the technique.

4.4.3 Optical Characteristics

To explore this difference in EQE, the thin film UV-Vis absorption was measured, and normalized (to the maximum of ~625 nm) to compare relative intensities, as shown in **Figure 4.4a**. Un-normalized data is shown in **Figure S4.3b**.

All spray films show red-shifted absorption for both the peak attributable to PM6 (~625 nm) and that attributable to DTY6 (~810 nm). These shifts are ~4 nm for the PM6 peak and ~20 nm for the DTY6 peak, both for a spin blend compared to a spray coated blend without air-knife delay time. Red-shifts in absorption are well-documented in organic semiconductors, and usually considered to be due to increases in crystallinity and ordering of the system.

There are also changes in the relative intensity of some absorption peaks with changing air-knife delay time of spray cast films. The shoulder peak of PM6 (~585 nm, marked as ‘*’) increases in intensity with increasing delay time, whilst the main DTY6 peak (~810 nm, marked as ‘o’) decreases. This can be seen more clearly in the relative intensities plotted in **Figure 4.4b**, where the corresponding peaks are clearly marked in **Figure 4.4a**.

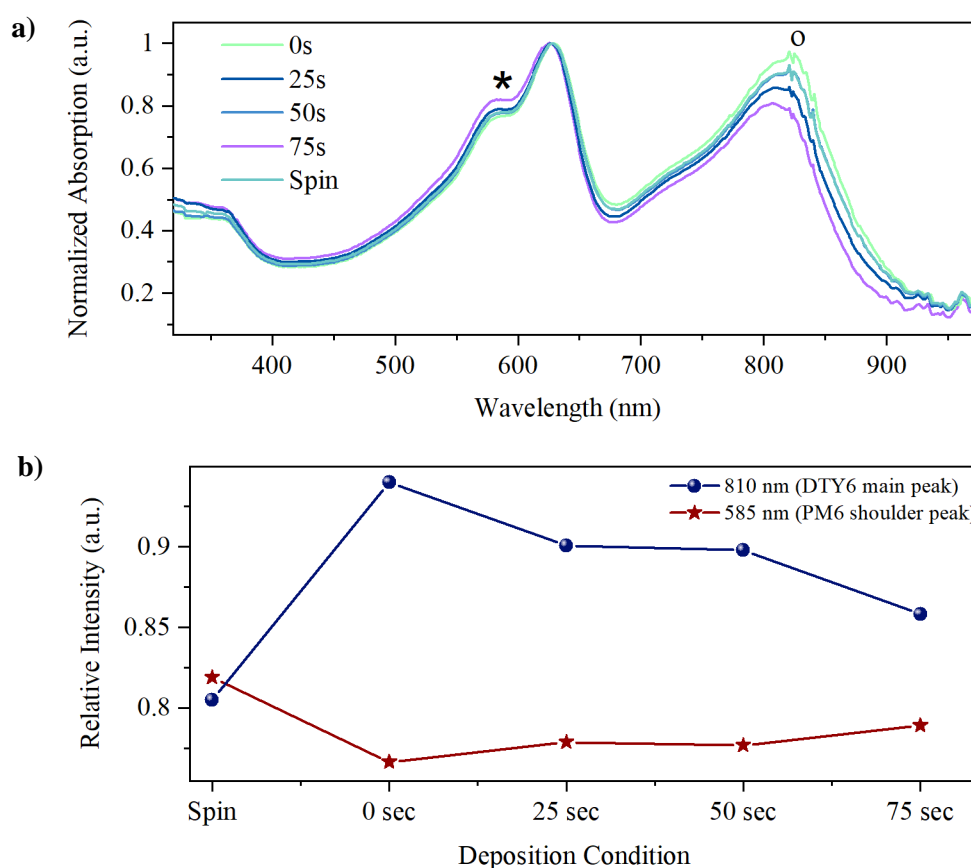


Figure 4.4: a) UV-Vis absorption spectrum for spin and spray coated films using varying air-knife delay time. b) Normalised intensities of the PM6 shoulder peak and DTY6 main peak, with deposition condition.

Changes in absorption intensity are often linked to levels of component aggregation and order.^{16,32} In 2020 Xu *et al.*¹⁸ reported improved molecular organization of PM6 led to increased intensity of absorption shoulder peaks. The same work also saw increased intensity in the Y-series acceptor absorption with increased aggregation. These results therefore suggest that spray cast films show increased DTY6 aggregation and decreased PM6 order compared to spin cast films. Increasing delay time before application of the air-knife yields spray cast films closer to spin coated films, with increasing PM6 ordering and decreased DTY6 aggregation.

To understand these differences in order and morphology more comprehensively, grazing incidence wide angle X-ray scattering (GIWAXS) was used to characterise blend films prepared under different conditions.

4.4.4 GIWAXS

The 2D GIWAXS patterns for pure, spin coated, DTY6 and PM6 are shown in **Figure 4.5a** and **4.5b** respectively. Patterns for PM6:DTY6 blend films coated via spin and optimised spray coating are shown in **Figure 4.5c** and **4.5e** respectively. Azimuthally integrated q -dependent 1D intensities for blends and components are shown in **Figure 4.5d**.

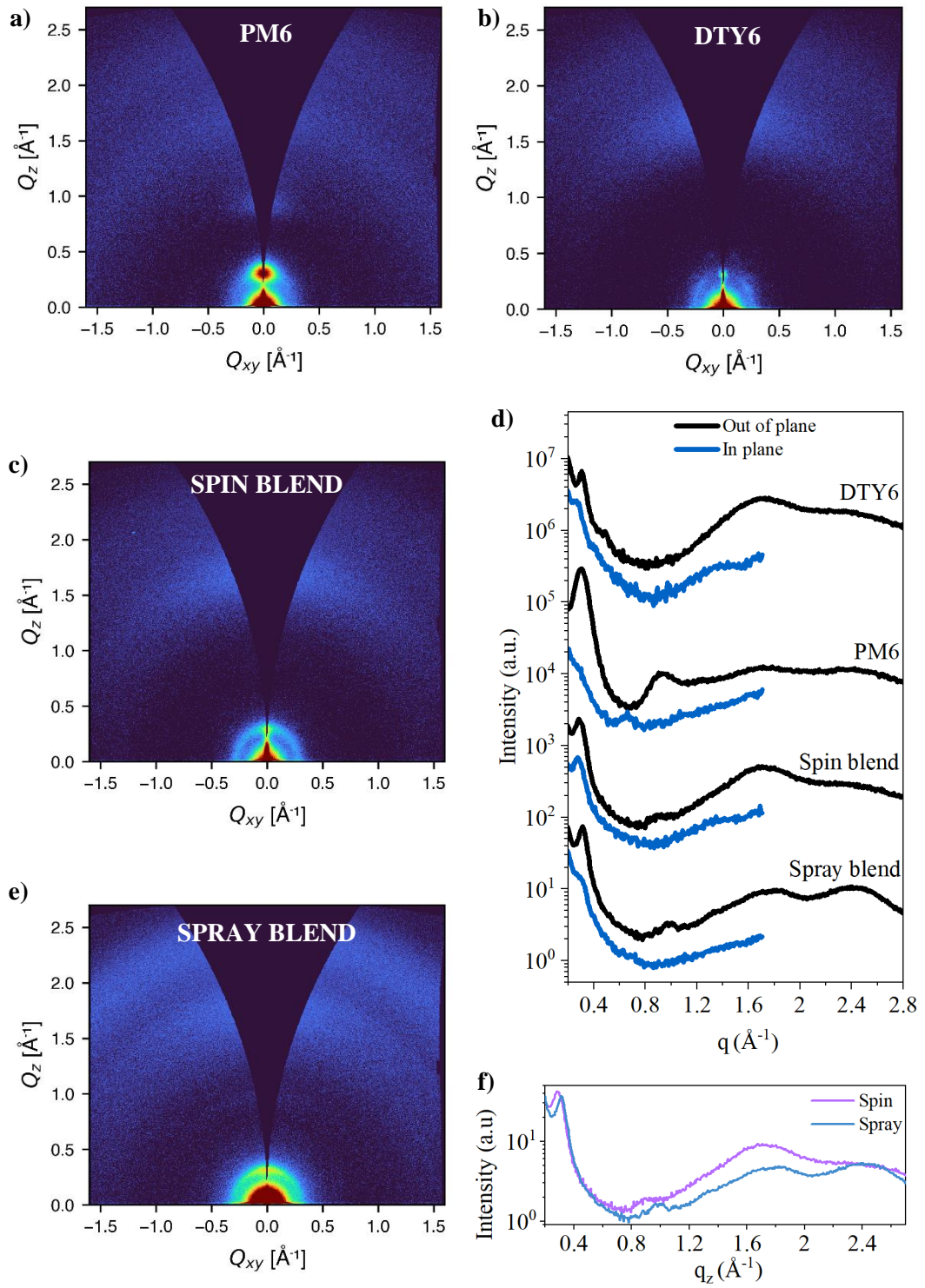


Figure 4.5: 2D GIWAXS patterns for films on ZnO. Spin coated **a)** PM6, **b)** DTY6, **c)** PM6:DTY6 blend, **e)** spray coated PM6:DTY6 blend. **d)** 1D linecuts for blends and components. **f)** 1D linecuts comparing out-of-plane intensity for spin and spray coated blends.

Details on the theory and analysis of GIWAXS scattering can be found in **Chapter 3**. We first consider the pure components alone. Here, we can see that the thin films of PM6 and DTY6 have several differences. In **Figure 4.5a** and **4.5d** it can be seen that PM6 shows prominent lamellar stacking in the out-of-plane direction ($q \sim 0.30 \text{ \AA}^{-1}$), with little in the in-plane direction. A higher order lamellar peak at $q \sim 0.92 \text{ \AA}^{-1}$ is also present in the out-of-plane direction. This implies preferential edge-on orientation, with a good level of order suggested by the strong diffraction spot in **Figure 4.5a**. Weak π - π stacking peaks can be seen in the out-of-plane direction at $q \sim 1.7 \text{ \AA}^{-1}$ and $q \sim 2.4 \text{ \AA}^{-1}$. In contrast, DTY6 shows lamellar stacking in both directions ($q \sim 0.31 \text{ \AA}^{-1}$), with the broader diffraction rings in **Figure 4.5b** suggesting a greater degree of disorder than PM6. Strong π - π stacking can be seen at $q \sim 1.7 \text{ \AA}^{-1}$, suggesting a face-on orientation dominates, alongside weak π - π stacking at $q \sim 2.4 \text{ \AA}^{-1}$.

The spin blend film shown in **Figure 4.5c** and **4.5d** displays similar scattering to that of pure DTY6, with a more even distribution of lamellar stacking both in and out-of-plane. Co-existence of face-on and edge-on orientations in PM6:DTY6 films has been shown in other works,⁷ and suggested to not negatively impact performance.³³ The strong out-of-plane π - π stacking peak at $q \sim 1.7 \text{ \AA}^{-1}$ cannot be attributed to either component, due to their overlapping nature.

The spray blend film shown in **Figure 4.5e** and **4.5d** displays some key differences to that of the spin blend. The in-plane lamellar peak at $q \sim 0.30 \text{ \AA}^{-1}$ is significantly broadened, with the crystal coherence length falling from $\sim 4.5 \text{ nm}$ to $\sim 4.1 \text{ nm}$, suggesting a reduction in the length scale of lamellar packing. For ease of comparison of the out-of-plane peaks, the 1D linecuts for the blends are displayed without offset in **Figure 4.5f**. From this figure, it is clear that the lamellar peaks are both shifted to higher q values in the spray coated film. The peak at $q \sim 0.30 \text{ \AA}^{-1}$ moves from 0.28 \AA^{-1} in the spin film to 0.31 \AA^{-1} in the spray film, corresponding to a decrease in d -spacing from $\sim 22.4 \text{ nm}$ to 20.3 nm . Similarly, the peak at $q \sim 0.90 \text{ \AA}^{-1}$ moves from 0.91 \AA^{-1} in the spin film to 0.99 \AA^{-1} in the spray film, corresponding to a decrease in d -spacing from $\sim 6.9 \text{ nm}$ to $\sim 6.3 \text{ nm}$. The π - π stacking peak at $q \sim 1.7 \text{ \AA}^{-1}$ is reduced to around half its original intensity, whilst that at $q \sim 2.4 \text{ \AA}^{-1}$ is marginally more prominent. This suggests a breakdown or change in the π - π stacking.

A reduction in the d -spacing of the out-of-plane lamellar peaks is consistent with closer packing, and aggregation of one or both of the components. This is likely because the spray film (before application of the air-knife) will contain a significant amount of solvent, meaning diffusion of the components will be facilitated compared to the spin film, in which solvent is rapidly removed. Whilst the exact nature of aggregation is difficult to establish as

the PM6 and DTY6 peaks overlap, our findings are consistent with the UV-Vis results that suggest enhanced DTY6 aggregation occurs.

Aggregation can lead to the formation of domains having sizes in excess of exciton diffusion lengths, thereby reducing exciton dissociation and efficiency of charge transport. To explore this further, exciton dissociation and recombination were explored using a range of device based optoelectronic measurements.

4.4.5 Optoelectronic Measurements

We then recorded light dependent JV curves, with **Figure 4.6a** plotting V_{oc} against the natural log of the light intensity [$\ln(P_{light})$]. Here, the gradient of V_{oc} vs $\ln(P_{light})$ is expected to be $\frac{nkT}{q}$, where n, k, T and q are the ideality factor, Boltzmann's constant, temperature and the elementary-charge respectively.³⁴ It been reported that as n approaches 2, trap-assisted recombination dominates over bimolecular recombination.¹⁶ Our data (shown in **Table 4.2**) indicates a value of $n = 1.37$ and 1.89 for the spin and spray-cast devices respectively, suggesting that spray-cast devices are dominated by trap-assisted recombination.

Figure 4.6b plots light dependent J_{sc} measurements on a double-logarithmic scale. Here, we expect a $J_{sc} \propto P_{light}^\alpha$ dependence, where α is known as the 'power factor'. Here values of $\alpha < 1$ indicate enhanced presence of bimolecular recombination.¹⁶ Our measurements suggest values of α of around unity for both types of device (see **Table 4.2**), indicating similar and low-levels of bimolecular recombination.

Finally, we plot the photocurrent density (J_{ph}) vs V_{eff} in **Figure 4.6c**. Here $J_{ph} = J_L - J_D$, was determined from the current recorded from dark (J_D) and light (J_L) JV sweeps. This is plotted against $V_{eff} = V_0 - V_{appl}$, where V_0 is the voltage at which $J_{ph} = 0$ and V_{appl} is the applied voltage. Here, the photocurrent density is expected to reach a saturation value of J_{sat} at large V_{eff} . This measurement is commonly used to determine the exciton dissociation efficiency ($P_{diss} = \frac{J_{ph}}{J_{sat}}$) at short circuit ($V_{appl} = 0$), and the exciton collection efficiency ($P_{coll} = \frac{J_{ph}}{J_{sat}}$) at the maximum power point.³⁵ From our measurements (see **Table 4.2**), it can be seen that both the P_{diss} and P_{coll} values of the spray coated devices are approximately 5% lower than that of spin coated controls.

Table 4.2: Optoelectronic properties compared for the two deposition conditions.

Deposition Condition	n	α	P_{diss}	P_{coll}
Spin Coated	1.37	1.02	94.9	75.6
Spray Coated	1.89	1.01	91.2	71.4

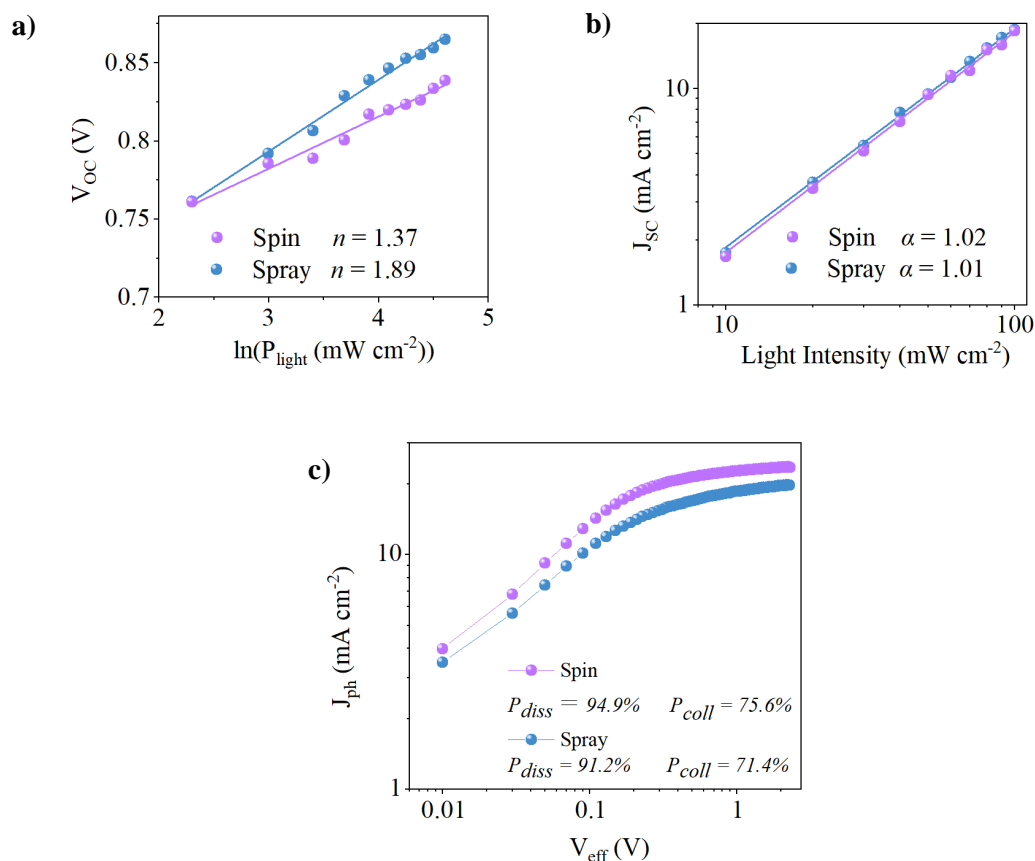


Figure 4.6: a) Light dependant V_{oc} measurements. b) Light dependant J_{sc} measurements. c) J_{ph} measurements.

Our measurements suggest therefore that devices containing spray-cast films have reduced levels of exciton dissociation and collection; a conclusion consistent with the reduced EQE (Figure 4.3e). As the levels of bimolecular recombination are similar between the deposition conditions, it seems likely that trap-assisted recombination is driving the reduction in charge generation. Structural defects, including those due to aggregation,³⁶ have been linked previously to traps. This means we can now link the DTY6 aggregation shown in the GIWAXS to enhanced trap-assisted recombination, leading to reduced charge generation, exciton dissociation, and exciton collection. As the degree aggregation may not be consistent between devices, this is also likely responsible for the greater variation seen in spray cast cells.

4.4.6 Larger Scale Morphology

Finally, to ensure larger scale defects and morphological differences were not responsible for the differences in device performance, uniformity was probed over wider areas. First, atomic force microscopy (AFM) was used to characterise films over a scan-area of $5\ \mu\text{m} \times 5\ \mu\text{m}$. Here, representative images are shown in **Figure 4.7a** and **4.7b** for optimised spin-cast and spray-coated films respectively, with films spray-cast using different air-knife delay times shown in **Figure S4.5**. Interestingly, we find no apparent change in film morphology or root-mean-square (RMS) roughness values (see **Table S4.3**), with film roughness in all cases being around 2.1 nm. Clearly any aggregation of DTY6 is not registered by this technique.

To explore film homogeneity over larger area, we then used laser beam-induced current (LBIC) mapping to characterise photocurrent emission from spin- and spray cast films over a scan area of $2\ \text{mm} \times 2\ \text{mm}$ area (see **Figure 4.7c** and **4.7d**). Whilst there is a surprising amount of non-uniformity for the spin coated film, this has clearly not severely impacted performance, and the spray coated film appears very uniform. We attribute the non-uniformity of the spin coated sample due to the time taken for the measurement (as this was taken after the spray film) and the high tendency for Y-series based systems to rapidly phase separate.³⁷

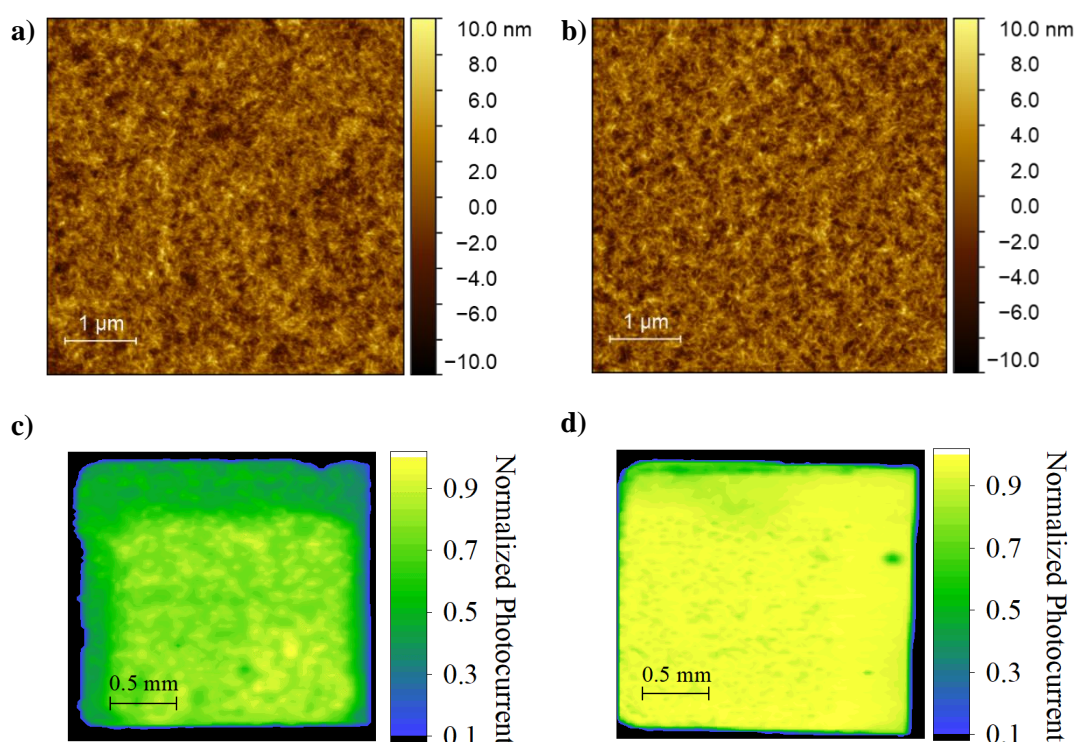


Figure 4.7: **a)** AFM of spin coated film. **b)** AFM of optimised spray-coated film. **c)** LBIC map of spin-coated device. **d)** LBIC map of spray-coated device.

4.5 Conclusions

We have used an air-knife assisted solvent extraction (ASE) protocol to fabricate spray-coated OSCs with champion PCEs comparable to spin-coated control devices. Here, the nitrogen gas-jet – applied by an air-knife moving linearly over the substrate surface – accelerates evaporation of the casting solvent, preventing film shrinkage or aggregation effects that occur due to prolonged drying times. We note increased variation in spray cast device performance, and a small reduction in mean efficiency. We attribute efficiency reductions to increases in trap-assisted recombination, as shown in the light dependent V_{OC} measurements. This trap-assisted recombination is likely due to the increased DTY6 aggregation shown in the GIWAXS patterns, leading to structural defects and sub-band gap states. It is suggested here that the increased drying time of the spray cast films leads to the aggregation. This also explains why increasing air-knife delay time improves performance (with increasing film thickness) only up to a certain point, beyond which performance decreases (caused by excessive molecular aggregation).

Despite this variation in performance, the champion spray value (14.1%) obtained was close to that of the spin coated control (14.2%). Importantly, the spray-casting protocol developed also does not require the use of additives to control solution rheology and is therefore ideal for low-cost, high-speed, roll-to-roll manufacturing. We believe that with modifications to the solvent system (for example using surfactants to improve wetting and reduce the wet film required for coalescence), this work marks an important first step towards developing a fully-sprayed organic non-fullerene based photovoltaic device.

4.6 Experimental Methods

Full details of device fabrication, GIWAXS, LBIC, and AFM can be found in **Chapter 3**. Details specific to this chapter are given here.

4.6.1 Device Fabrication

4.6.1.1 Materials

PM6 was purchased from 1-Material. 20 mm x 15 mm pre-patterned ITO glass ($\sim 20 \Omega/\square$) and DTY6 was purchased from Ossila. All solvents and remaining materials, including molybdenum (VI) oxide (99.97% trace metals basis), were purchased from Sigma Aldrich unless otherwise stated.

4.6.1.2 Initial Fabrication

Devices were made using ITO/ZnO/Active Layer/MoO₃/Ag.

Spin coating: Active layer solutions were made by dissolving 1:1.2 PM6:DTY6 (18 mg mL⁻¹ in *o*-xylene). Solutions were stirred at 80°C overnight before being cooled to room temperature before use. Solutions were formed by spin coating at 1500 rpm to create a film having a thickness of ~ 130 nm. All active-layer films were then annealed at 80°C for 10 minutes and then scratched using a razorblade to expose the underlying ITO contact.

Spray coating: Active layer solutions were prepared as above, but with solid concentration reduced to 10 mg mL⁻¹. Spray coating was performed using a Sonotek Exactacoat system using an Impact spray head. The piezo-electric tip was vibrated at 1 W and the solution delivered at a flow rate of 1.5 mL min⁻¹. The spray head was passed over the substrate at a speed of 20 mm s⁻¹ at a tip-surface separation of ~ 10 cm. After a short delay time, an automated gantry passed an air-knife (Meech A8 80 mm air knife, RS components) held at a distance of ~ 2 cm from the surface at a speed of 3 mm s⁻¹, delivering N₂ at a pressure of 20 psi. After the application of the air-knife, substrates were annealed at 80°C for 10 minutes.

4.6.2 UV-Vis absorption & photoluminescence measurements

Absorption samples were prepared using the coating conditions specified above onto quartz coated glass substrates. Spectra were recorded using a Fluoromax 4 fluorometer (Horiba) using a Xe lamp. Photoluminescence measurements were recorded on the same samples using the same machine with an excitation wavelength of 500 nm and the samples offset from the detector by 45°.

4.6.3 GIWAXS

GIWAXS measurements were performed on thin films prepared on ZnO coated ITO glass. Samples were prepared using the same coating conditions as in devices. Measurements were

taken on the DL-SAXS beamline at Diamond Light Source. Data was corrected, reduced and reshaped using a custom python code based on the PyFAI library.³⁸

4.6.4 Light dependent measurements

An Oriel LSH-7320 ABA LED solar simulator, with adjustable output power between 0.1 and 1.1 suns was used to perform light-intensity dependent current-voltage sweeps using the same sweep conditions as above.

4.6.5 Atomic Force Microscopy

Atomic Force Microscopy (Veeco Dimension 3100) samples were prepared using the same coating conditions specified above on ZnO coated un-patterned ITO. Each sample was scanned over three $5 \times 5 \mu\text{m}$ areas with a resolution of 512×512 pixels. Gwyddion software was used to step line correct the images and extract the root mean square roughness.

4.7 Supplementary Information

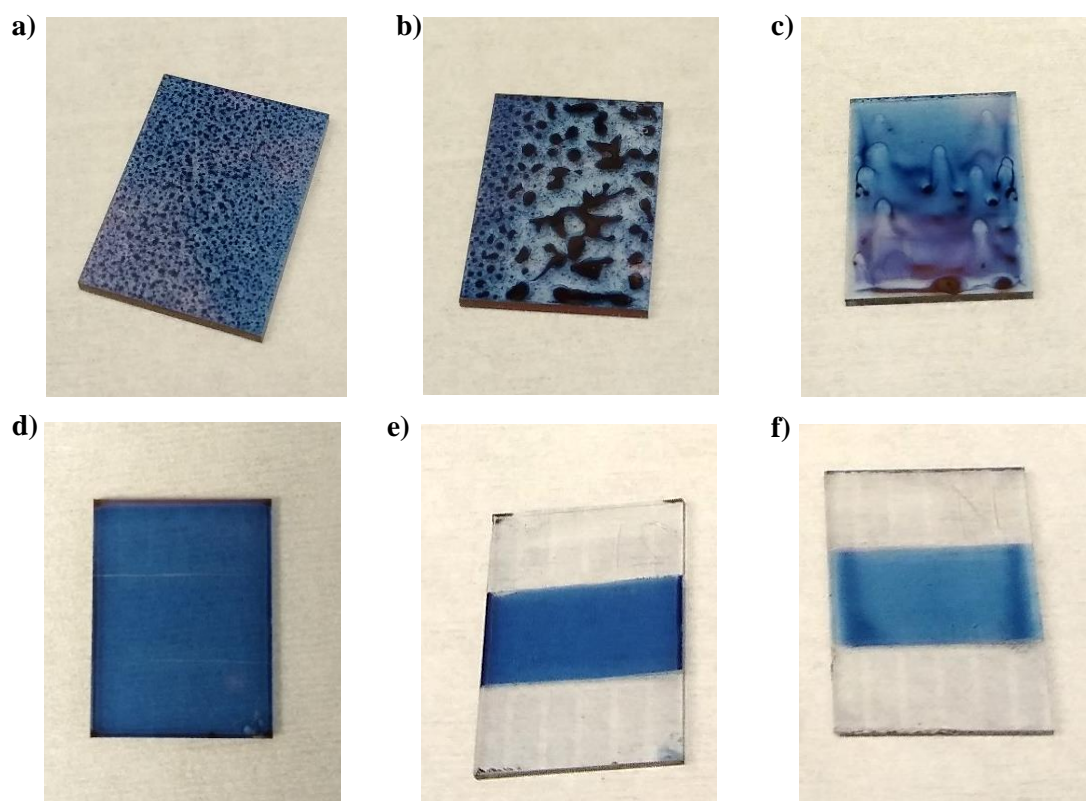


Figure S4.1: a) & b) PM6:Y6 films coated from chloroform, showing poor coalescence. c) PM6:DTY6 film coated from *o*-Xylene, with insufficient solution deposited leading to coalescence issues. A PM6:DTY6 film spin coated from *o*-Xylene d) before and e) after patterning. f) Optimised spray coated film after patterning

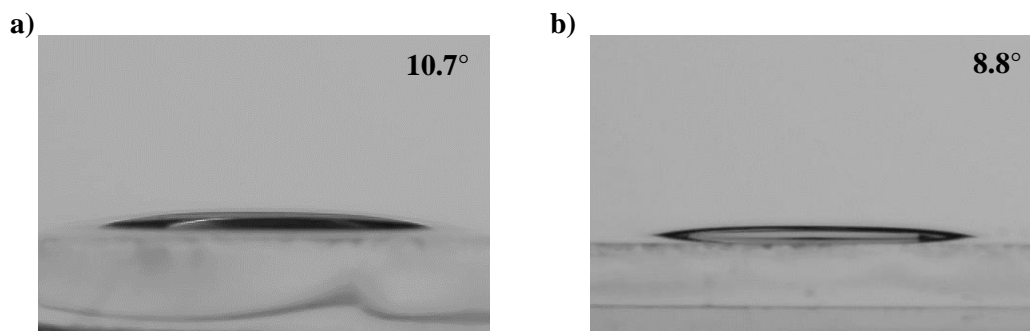


Figure S4.2: Contact angles of **a)** chloroform on ZnO, **b)** o-Xylene on ZnO.

Table S4.1: Thin film thickness and corresponding J_{SC} values for each deposition condition.

Deposition Method	Thickness of Film (nm)	J_{SC} (mA cm⁻²)
Optimised spin coated	139 ± 5.4	22.8 ± 0.7
Spray coated- 0 second air-knife delay	70 ± 2.1	20.1 ± 0.8
Spray coated- 25 second air-knife delay	84 ± 1.7	19.1 ± 0.4
Spray coated- 50 second air-knife delay	90 ± 4.4	21.4 ± 1.0
Spray coated- 75 second air-knife delay	114 ± 3.3	21.3 ± 0.5

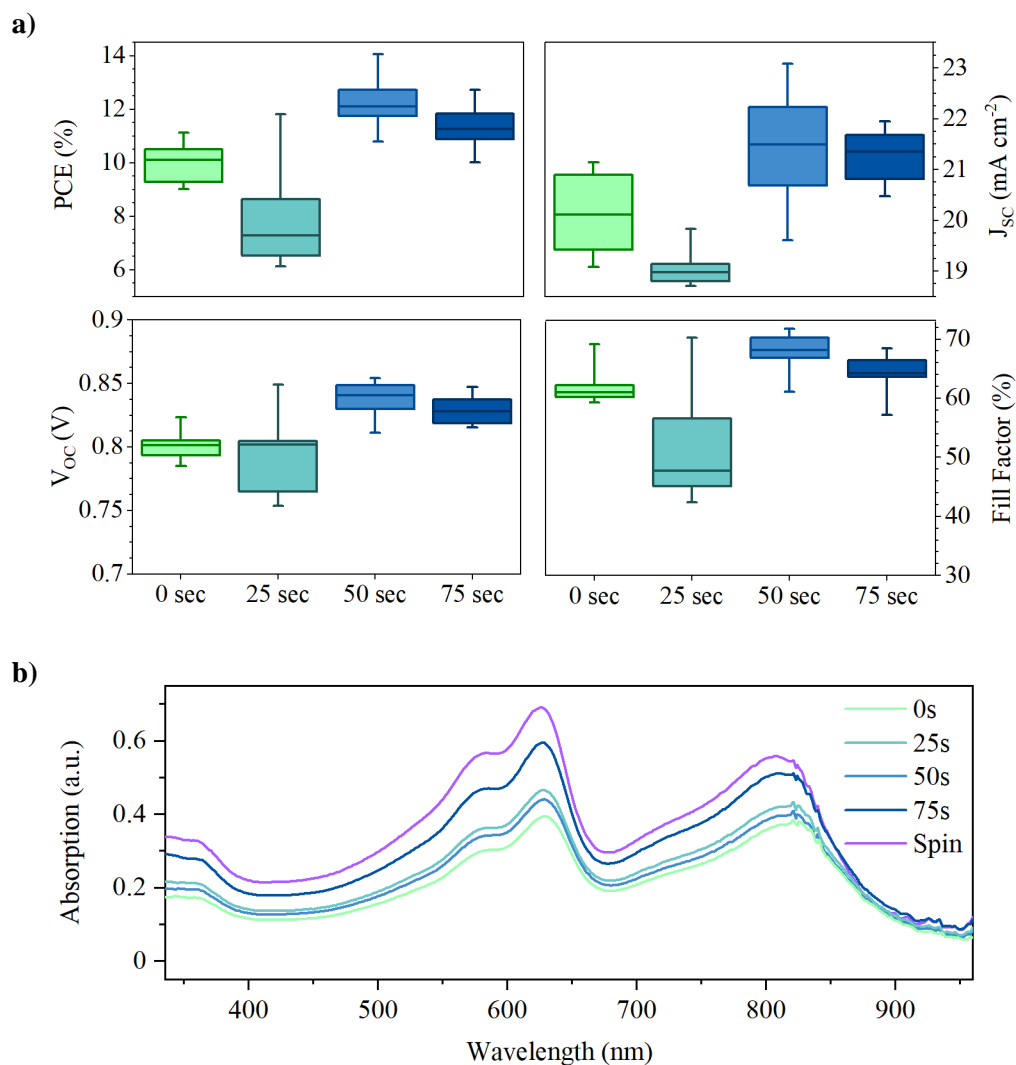


Figure S4.3: a) Box plots of device metrics for spray coated PM6:DTY6 devices with varying air-knife delay time. b) Absorption of PM6:DTY6 films with varying delay time, without normalization.

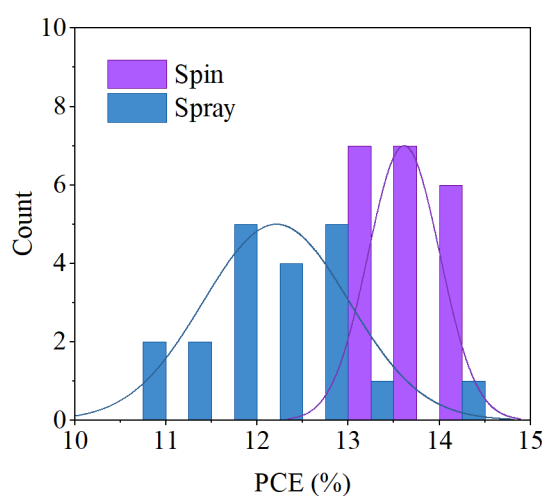


Figure S4.4: Histogram of spin and spray devices, with 10 separate devices shown for each, but forward and reverse sweeps treated separately.

Table S4.2: J_{SC} values for representative devices, compared to those achieved via integration of the EQE spectra.

Deposition Method	Measured J_{SC-JV} (mA cm ⁻²)	Calculated J_{SC-EQE} (mA cm ⁻²)	Discrepancy (%)
Spin	23.9	21.6	9.6
Spray	20.8	20.4	1.9

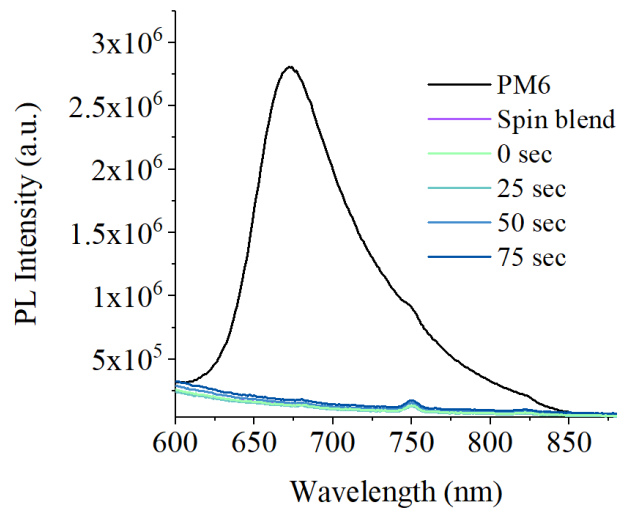


Figure S4.5: Photoluminescence intensity for spin and spray coated films. All films excited at 500 nm. The feature at 750 nm is attributed to an artifact of the diffraction grating.

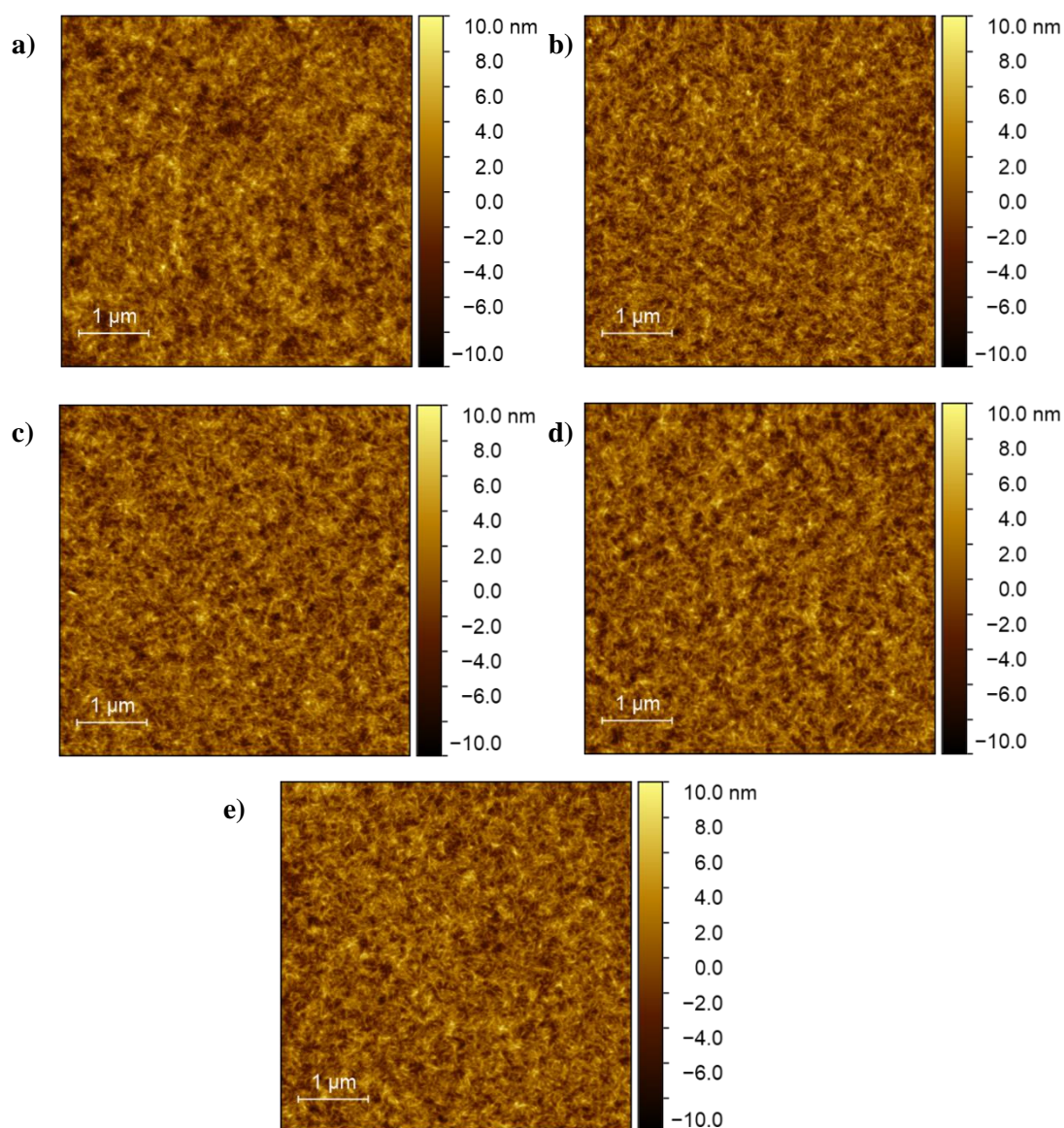


Figure S4.6: AFM images for **a)** Spin coated control. Spray coated films follow at **b)** 0 seconds air-knife delay time, **c)** 25 seconds, **d)** 50 seconds, **e)** 75 seconds.

Table S4.3: Root mean square (RMS) roughness values for each deposition condition. Values given as an average of 3 different measurements across one film, with the error ± 1 standard deviation.

Deposition Method	RMS Roughness (nm)
Spin coated	2.11 ± 0.10
Spray coated- 0 second air-knife delay	2.06 ± 0.01
Spray coated- 25 second air-knife delay	2.08 ± 0.06
Spray coated- 50 second air-knife delay	2.09 ± 0.02
Spray coated- 75 second air-knife delay	2.06 ± 0.03

4.8 References

1. Yuan, J. *et al.* Single-Junction Organic Solar Cell with over 15% Efficiency Using Fused-Ring Acceptor with Electron-Deficient Core. *Joule* **3**, 1140–1151 (2019).
2. Cui, Y. *et al.* Single-Junction Organic Photovoltaic Cell with 19% Efficiency. *Adv. Mater.* **33**, 2102420 (2021).
3. Li, S., Li, C., Shi, M. & Chen, H. New Phase for Organic Solar Cell Research: Emergence of Y-series electron acceptors and their perspectives *ACS Ener. Lett.* **5**, 1554–1567 (2020).
4. Tokmoldin, N. *et al.* Extraordinarily long diffusion length in PM6:Y6 organic solar cells. *J. Mater. Chem. A* **8**, 7854–7860 (2020).
5. Riede, M., Spoltore, D. & Leo, K. Organic Solar Cells—The Path to Commercial Success. *Adv. Energy Mater.* **11**, 1–10 (2021).
6. Ma, Z., Zhao, B., Gong, Y., Deng, J. & Tan, Z. Green-solvent-processable strategies for achieving large-scale manufacture of organic photovoltaics. *J. Mater. Chem. A* **7**, 22826–22847 (2019).
7. Dong, S., Jia, T., Zhang, K., Jing, J. & Huang, F. Single-Component Non-halogen Solvent-Processed High-Performance Organic Solar Cell Module with Efficiency over 14%. *Joule* **4**, 2004–2016 (2020).
8. Dong, S. *et al.* Suppressing the excessive aggregation of nonfullerene acceptor in blade-coated active layer by using n-type polymer additive to achieve large-area printed organic solar cells with efficiency over 15%. *EcoMat* **1**, 1–9 (2019).
9. Sun, R. *et al.* A Layer-by-Layer Architecture for Printable Organic Solar Cells Overcoming the Scaling Lag of Module Efficiency. *Joule* **4**, 407–419 (2020).
10. Li, Y. *et al.* Additive and High-Temperature Processing Boost the Photovoltaic Performance of Nonfullerene Organic Solar Cells Fabricated with Blade Coating and Nonhalogenated Solvents. *ACS Appl. Mater. Interfaces* **13**, 10239–10248 (2021).
11. Guan, W. *et al.* Blade-coated organic solar cells from non-halogenated solvent offer 17 % efficiency. *J. Semicond.* **42**, 030502 (2021)
12. Zhang, Y. *et al.* Graded bulk-heterojunction enables 17% binary organic solar cells via nonhalogenated open air coating. *Nat. Commun.* **12**, 1–13 (2021).
13. Zhao, H. *et al.* Hot Hydrocarbon-Solvent Slot-Die Coating Enables High-Efficiency Organic Solar Cells with Temperature-Dependent Aggregation Behavior. *Adv. Mater.* **32**, 1–10 (2020).
14. Yang, Y. *et al.* Layer-by-layer slot-die coated high-efficiency organic solar cells processed using twin boiling point solvents under ambient condition. *Nano Res.* **14**, 4236–4242 (2021).
15. Zhao, H. *et al.* Kinetics Manipulation Enables High-Performance Thick Ternary Organic Solar Cells via R2R-Compatible Slot-Die Coating *Adv. Mater.* **34**, 2105114 (2021).
16. Yang, P. *et al.* Toward all aerosol printing of high-efficiency organic solar cells using environmentally friendly solvents in ambient air. *J. Mater. Chem. A* **9**, 17198–17210 (2021).
17. Hong, L. *et al.* Eco-Compatible Solvent-Processed Organic Photovoltaic Cells with Over 16% Efficiency. *Adv. Mater.* **31**, 1–7 (2019).
18. Xu, X., Yu, L., Yan, H., Li, R. & Peng, Q. Highly efficient non-fullerene organic solar cells enabled by a delayed processing method using a non-halogenated solvent. *Energy Environ. Sci.* **13**, 4381–4388 (2020).
19. Zhang, Y. *et al.* Graded bulk-heterojunction enables 17% binary organic solar cells via nonhalogenated open air coating. *Nat. Commun.* **12**, 1–13 (2021).
20. Fo, W. Z. *et al.* Highly Efficient Binary Solvent Additive-Processed Organic Solar Cells by the Blade-Coating Method. *Macromol. Chem. Phys.* **222**, 1–7 (2021).
21. Guan, W. *et al.* Blade-coated organic solar cells from non-halogenated solvent offer 17% efficiency. *J. Semicond.* **42**, 030502 (2021).
22. Bishop, J. E., Routledge, T. J. & Lidzey, D. G. Advances in Spray-Cast Perovskite Solar Cells. *J. Phys. Chem. Lett.* **9**, 1977–1984 (2018).
23. Vohra, V., Tahirah, N., Wahi, R., Ganzer, L. & Virgili, T. Optical Materials : X A comparative study of low-cost coating processes for green & sustainable organic solar cell active layer manufacturing. *Opt. Mater. X* **13**, 100127 (2022).
24. Rolston, N. *et al.* Article Rapid Open-Air Fabrication of Perovskite Solar Modules Rapid Open-Air Fabrication of Perovskite Solar Modules. *Joule* **4**, 2675–2692 (2020).
25. Bruening, K. *et al.* Scalable Fabrication of Perovskite Solar Cells to Meet Climate Targets. *Joule* **2**, 2464–2476 (2018).
26. Cassella, E. J. *et al.* Gas-Assisted Spray Coating of Perovskite Solar Cells Incorporating Sprayed Self-Assembled Monolayers. *Adv. Sci.* **2104848**, 1–10 (2022).
27. Zhao, H. *et al.* Solvent-Vapor-Annealing-Induced Interfacial Self-Assembly for Simplified One-Step Spraying Organic Solar Cells. *ACS Appl. Energy Mater.* **4**, 7316–7326 (2021).
28. Cheng, J. *et al.* Intensification of Vertical Phase Separation for Efficient Polymer Solar Cell via Piecewise Spray Assisted by a Solvent Driving Force. *Sol. RRL* **4**, 1–11 (2020).
29. Zhang, Y., Griffin, J., Scarratt, N. W., Wang, T. & Lidzey, D. G. High efficiency arrays of polymer solar cells fabricated by spray-coating in air. *Prog. Photovoltaics Res. Appl.* **24**, 275–282 (2016).
30. Bishop, J. E., Smith, J. A. & Lidzey, D. G. Development of Spray-Coated Perovskite Solar Cells.

- ACS Appl. Mater. Interfaces* **12**, 48237–48245 (2020).
31. Almora, O. *et al.* Device Performance of Emerging Photovoltaic Materials (Version 1). *Adv. Energy Mater.* **11**, 2002774 (2021).
 32. Fu, H. *et al.* A Generally Applicable Approach Using Sequential Deposition to Enable Highly Efficient Organic Solar Cells. *Small Methods* **4**, 2000687 (2020).
 33. Tumbleston, J. R. *et al.* The influence of molecular orientation on organic bulk heterojunction solar cells. *Nat. Photonics* **8**, 385–391 (2014).
 34. Qi, B. & Wang, J. Open-circuit voltage in organic solar cells. *J. Mater. Chem.* **22**, 24315–24325 (2012).
 35. Li, W. *et al.* Molecular Order Control of Non-fullerene Acceptors for High-Efficiency Polymer Solar Cells. *Joule* **3**, 819–833 (2019).
 36. Du, X. *et al.* Unraveling the Microstructure-Related Device Stability for Polymer Solar Cells Based on Nonfullerene Small-Molecular Acceptors. *Adv. Mater.* **32**, 1908305 (2020).
 37. Qin, Y. *et al.* The performance-stability conundrum of BTP-based organic solar cells. *Joule* **5**, 2129–2147 (2021).
 38. Kieffer, J. & Karkoulis, D. PyFAI, a versatile library for azimuthal regrouping. *J. Phys. Conf. Ser.* **425**, 8–13 (2013).

Chapter 5 | Comparing the Influence of Solvent Additive Processing on Fullerene and Non-Fullerene Acceptors

5.1 Author Contributions

In this project the GIWAXS measurements, AFM measurements, and contact angle measurements were performed by Rachel Kilbride. GIWAXS and AFM data was also processed into the images presented below by Rachel. The samples for GIWAXS, AFM, absorbance and NMR were prepared by both Rachel and myself. The NMR measurements were taken by Dr Khalid Doudin and Dr Sandra van Meurs. The absorbance measurements and all device related preparation and characterization was carried out by me. All analysis is my own.

5.2 Abstract

With the advent of non-fullerene acceptors (NFAs), organic photovoltaic (OPV) efficiencies have dramatically increased in a matter of a few years. Long-term operational stability is now one of the most substantial obstacles to commercialisation. High boiling point solvent additives are a common method used to control efficiency in OPVs, but can impact both the performance and stability of NFA and fullerene-based systems in different, negative ways. Here, we explore the impact of the solvent additive 1,8-diiodooctane (DIO) on OPV devices using classic NFA ITIC, and traditional acceptor PC₇₀BM. We find that the NFA based system comparatively traps DIO more significantly, shows a greater degree of crystallization and aggregation upon DIO addition, and displays more severe vertical segregation at high DIO concentrations. These factors contribute to poorer morphological stability of the NFA based system upon addition of DIO, and significantly worse photo-stability, compared to that using the fullerene acceptor.

5.3 Introduction

Since the introduction of indacenodithienothiophene (IDTT) based acceptors in 2015¹ OPV record efficiencies have increased significantly, now reaching 19%.² Such advances have been driven by the superior absorption, tuneable energy levels and more significant crystallinity of NFAs³ over their fullerene-based counterparts. Despite this, long term operational stability remains an issue, especially for devices containing the highest performing^{4,5} benzothiadiazole (BT) based systems, which are prone to severe phase separation over time.⁶

Degradation of OPVs can occur through a host of different mechanisms, usually divided into intrinsic and extrinsic factors.⁷ Intrinsic degradation involves processes that occur without any additional driving forces, such as morphological changes or reactions at interfaces. Morphological instability can include phase separation, crystallization, and vertical segregation of components.⁸ Extrinsic degradation involves external factors such as light, heat, oxygen, or moisture, which will often exaggerate intrinsic pathways.⁹

An important factor that controls both efficiency and stability of OPVs is the use of solvent additives, such as DIO,¹⁰ 1-chloronaphthalene (CN)¹¹ and diphenyl ether (DPE).¹² Generally these additives have a high boiling point that extends the drying time of the film, facilitating phase separation and crystallinity. Some additive also have selective solubility for one of the components,¹³ which can likewise improve phase separation, and sometimes enhance vertical segregation.

Unfortunately, the presence of excess or residual additives (especially DIO) have been shown to severely impact OPV operational stability.¹⁴⁻¹⁶ The removal of DIO from a film after processing is still a topic under some debate, with many works noting residual material remains even after heating and vacuum processing. This occurs in part due to the high boiling point (~144°C).¹⁴ DIO has also been shown to impact both the performance¹³ and stability¹⁷ of NFA and fullerene-based systems differently, and as such remains an interesting area of exploration.

In this work we explore the differing impact of DIO on the device performance and stability of OPVs using fullerene acceptor PC₇₀BM and NFA ITIC. ITIC is an example of a IDTT based acceptor. Whilst the efficiencies of devices using this kind of NFA do not typically exceed 13%,¹⁸ IDTT based acceptors, and their indacenodithiophene (IDT) analogues, are notable for their excellent morphological, and sometimes photo-oxidative,¹⁹ stability in devices. However, DIO is often used to improve initial device performance, which can result in a variety of side-effects.

Significant among these is the enhancement of vertical segregation across the bulk heterojunction (BHJ), shown in **Figure 5.1c**, usually resulting in the lower surface energy donor diffusing to the air-interface of the film in order to minimize overall surface energy. DIO has been shown to facilitate this segregation in both ITIC²⁰ and PCBM²¹ based systems, although the impact of this varies on the degree of segregation and the final architecture of the cell. DIO has also been linked to changes in the orientation of the acceptor molecule, from a face-on to edge-on arrangement,²² an approximation of which can be seen in **Figure 5.1b**. A face-on arrangement is usually favoured for high OPV performance, as charge carrier mobility is much faster along the π - π stacking axis than through the side chains. DIO has also been shown to result in severe degradation under illumination for both PCBM and NFA systems. This is a consequence of the photo-induced formation of iodide radicals, as shown in **Figure 5.1a**, which can react and break down the active layer components.

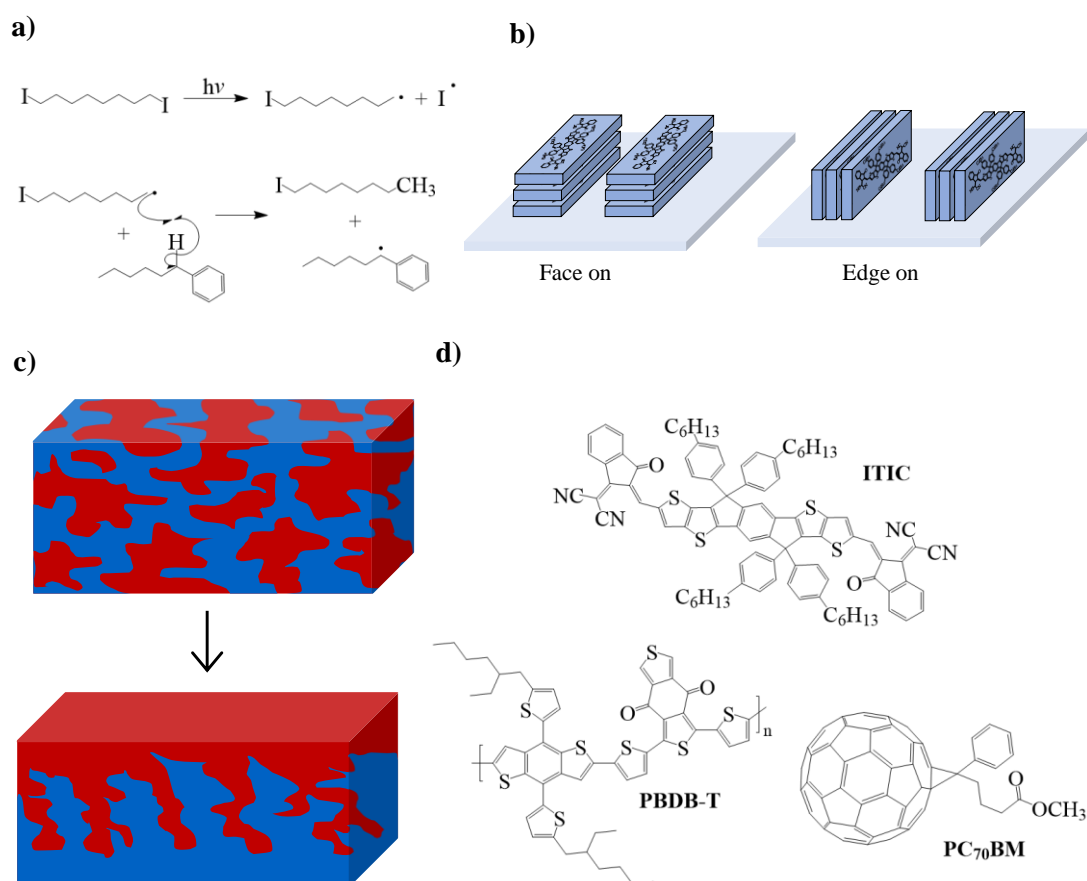


Figure 5.1: a) The reaction of DIO under illumination to produce an iodine and iodoheptane radical. These radicals can then go on to perform hydrogen abstraction on the acceptor or donor to produce more radicals. b) Possible orientations of ITIC: face-on and edge-on. c) Vertical segregation of the BHJ to form a donor rich air interface. d) Chemical structures of the materials used in this work.

In this work we explore the side effects listed above for a range of DIO loadings in both PBDB-T:PC₇₀BM and PBDB-T:ITIC OPVs. The chemical structures of our components are shown in **Figure 5.1d**. Here, our donor is fixed to ensure that differences are due to the acceptor alone. We confirm findings elsewhere¹³ that DIO impacts the morphology and performance of ITIC more significantly than that of PC₇₀BM. We also show that DIO reduces the dark and illuminated stability of ITIC based systems to a greater degree. We show here for the first time that ITIC films retain a larger amount of DIO than PC₇₀BM based films, and propose that the morphology induced by this is the leading factor behind the reduced performance and stability.

5.4 Results and Discussion

5.4.1 Initial Morphology

The morphology of the PBDB-T blend films was evaluated before any ageing, in order to assess the impact of the acceptor and DIO content. 2D grazing incidence wide-angle X-ray scattering (GIWAXS), atomic force microscopy (AFM) and ultraviolet-visible spectroscopy (UV-Vis) measurements were also carried out on blend films coated on PEDOT:PSS coated indium-doped tin oxide (ITO) substrates.

5.4.1.1 GIWAXS results

2D GIWAXS patterns for PBDB-T:ITIC are shown in **Figure 5.2**. Azimuthally integrated q -dependent 1D intensity profiles are shown in **Figure 5.3**, in both in-plane and out-of-plane directions. 2D component patterns are shown in **Figures S5.1** and **S5.2**.

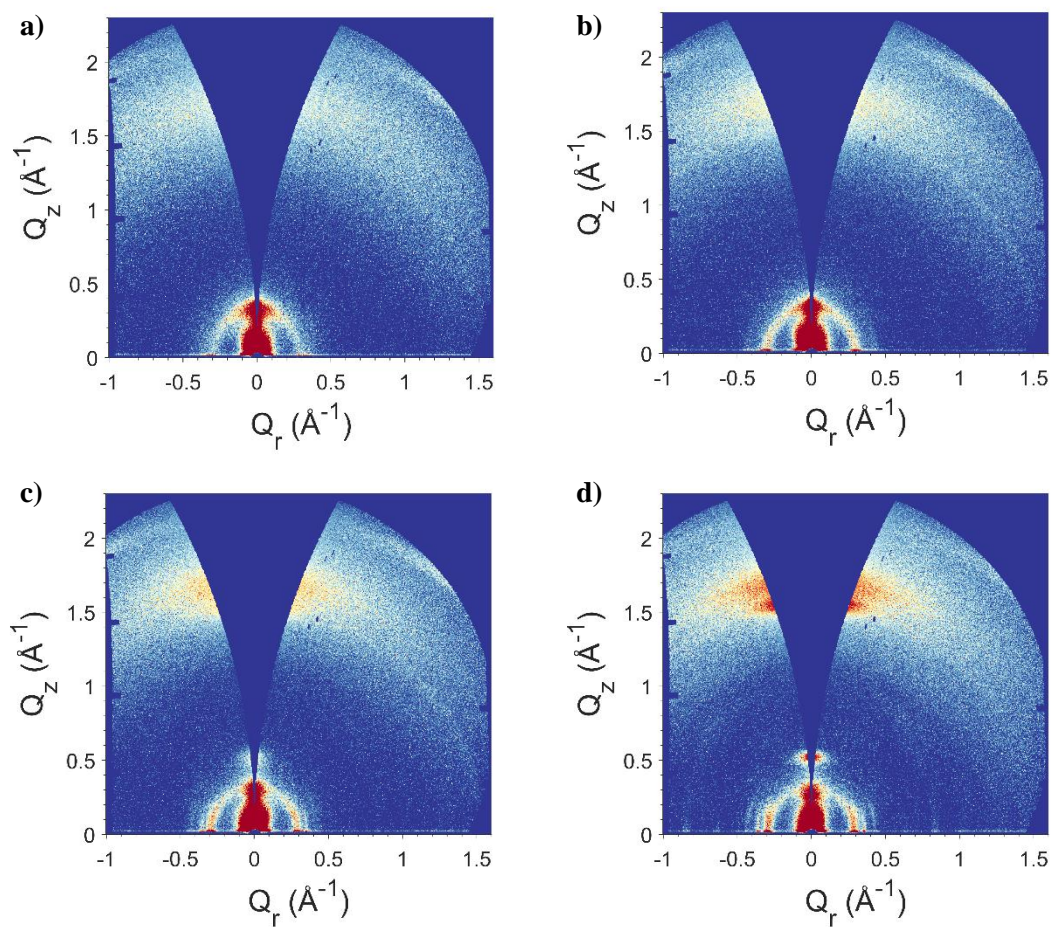


Figure 5.2: 2D GIWAXS patterns of PBDB-T:ITIC with **a)** no DIO, **b)** 0.5% DIO, **c)** 1% DIO and **d)** 3% DIO.

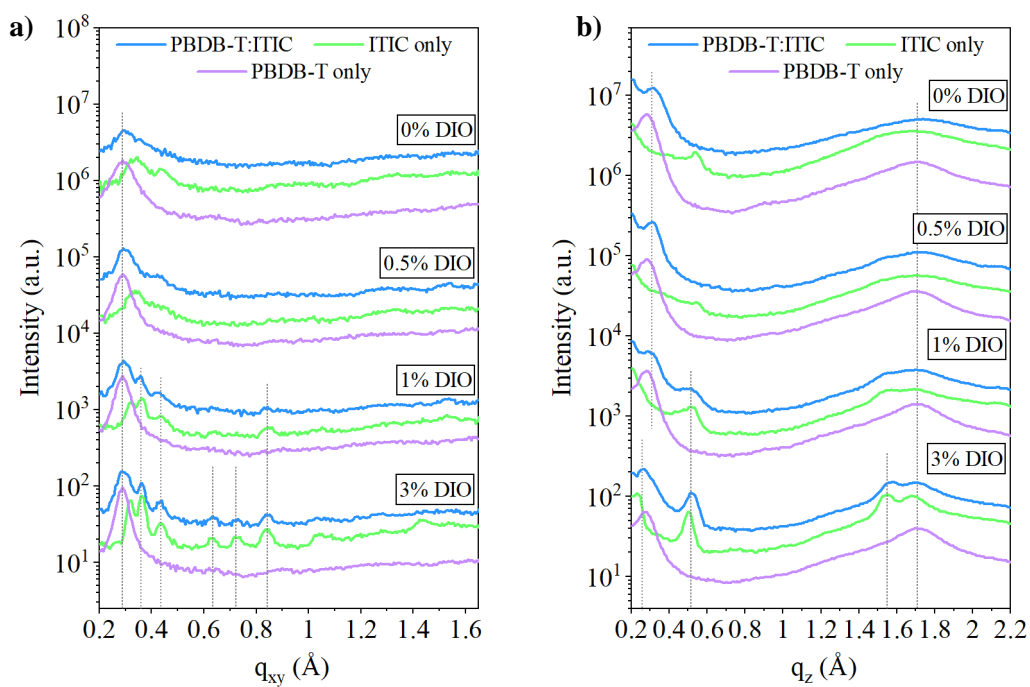


Figure 5.3: 1D GIWAXS linecuts of PBDB-T:ITIC, alongside pristine PBDB-T & ITIC. Linecuts are vertically offset for clarity, with the dotted lines acting as a guide for the eye. **a)** In-plane, **b)** Out-of-plane.

A summary of the q values, d -spacings, and crystal coherence lengths (CCLs) of the GIWAXS features in the blend can be found in **Table 5.1**. Details on these parameters, and their calculation, can be found in **Chapter 3**.

Table 1: GIWAXS features of the PBDB-T:ITIC blend. Features that could not be fit with a gaussian to extract their full width half maximum are marked as /.

DIO content	In-plane			Out-of-plane		
	q value (Å ⁻¹)	d -spacing (nm)	CCL (nm)	q value (Å ⁻¹)	d -spacing (nm)	CCL (nm)
0%	0.30	2.06	6.54	0.32	2.07	4.20
				1.70	0.36	0.89
0.5%	0.30	2.09	8.41	0.32	2.09	5.26
	0.42	1.45	/	1.69	0.36	1.00
1%	0.29	2.13	10.84	0.28	2.24	4.64
	0.36	1.75	22.20	0.50	1.26	4.25
	0.42	1.51	/	1.68	0.37	1.24
	0.84	0.75	/			
3%	0.29	2.34	10.80	0.26	2.40	4.81
	0.36	1.74	23.27	0.52	1.22	6.76
	0.43	1.46	/	1.57	0.40	/
	0.64	0.98	/	1.70	0.37	/
	0.72	0.87	/			
	0.84	0.75	/			

As q is inversely proportional to distance, we can attribute peaks at smaller q to larger scale features (usually lamellar stacks), and peaks at larger q to smaller scale features (usually π - π stacking). We first consider the in-plane scattering shown in **Figure 5.3a**. Considering pure components alone, we find that pristine PBDB-T undergoes minor increase in intensity of peaks with increased DIO concentration, suggesting marginally improved crystallinity. The changes in ITIC scattering are more dramatic, with an increasing number and intensity of reflection planes observed on increasing DIO concentration. This implies greater crystallinity and order. For both components, the presence of distinct lamellar peaks in the in-plane direction ($q \sim 0.30 \text{ \AA}^{-1}$) implies a favourable face-on orientation.

These features are reflected in the blend, where in films without DIO the scattering is initially dominated by the PBDB-T lamellar peak ($q \sim 0.30 \text{ \AA}^{-1}$). However, on increasing DIO concentration the ITIC scattering peaks become more obvious. Initial absence of ITIC peaks implies intimate mixing with PBDB-T, with increasing prominence suggesting greater phase separation.²³

Other work²⁴ has attributed scattering features at $q \sim 0.36 \text{ \AA}^{-1}$ and $q \sim 0.42 \text{ \AA}^{-1}$ to the ITIC backbone and lamellar stacking. While the d -spacing (representing the packing distance of the crystallites) remains relatively unchanged for these features with increasing DIO, the CCL does not. For most scattering peaks, increasing DIO content increases the CCL, implying the formation of larger aggregate structures.

The out-of-plane scattering is shown in **Figure 5.3b**. Again, pristine PBDB-T is only marginally affected by increasing DIO content. In contrast, the ITIC lamellar ($q \sim 0.52 \text{ \AA}^{-1}$) increases noticeably in intensity with increasing DIO concentration. Lamellar stacking in the out-of-plane direction suggests an edge-on orientation, meaning this intensity increase implies an increase in the edge-on orientation of the ITIC molecules, in coexistence with the usual face-on orientation. Bimodal ITIC stacking has been seen elsewhere, induced by both ageing²⁵ and the addition of DIO.²⁶ As charge carrier mobility has been shown to be fastest along the π - π stacking direction,²⁷ a face-on orientation has been shown to be superior to an edge-on orientation for enhancing OPV performance.²² As a result, increases in edge-on orientation will likely show a performance penalty.

The larger q ($\sim 1.7 \text{ \AA}^{-1}$) out-of-plane features observed here can be attributed to π - π stacking. As the pristine components show scattering peaks at a similar q value for this, their contributions are likely overlapping in the blend. For all out-of-plane scattering features in the blend, increasing DIO concentration again increases CCL, implying larger crystal structures.

From these patterns, it is clear that the morphology of ITIC is significantly more impacted by DIO content than that of PBDB-T, with increasing amounts of DIO inducing greater crystallinity and phase separation. Whilst crystallinity promotes higher mobility and phase purity can increase fill factor,²⁸ too much of both of these factors can be expected to decrease performance. This is due to a reduction of percolation pathways and enhanced roughness, especially coupled with reduced charge carrier mobility.

2D GIWAXS patterns for PBDB-T:PC₇₀BM, and its components, can be seen in **Figure 5.4**. Azimuthally integrated q -dependent 1D intensity profiles can be seen in **Figure 5.5**, in both in-plane and out-of-plane directions. 2D component patterns can be seen in **Figures S5.2** and **S5.3**.

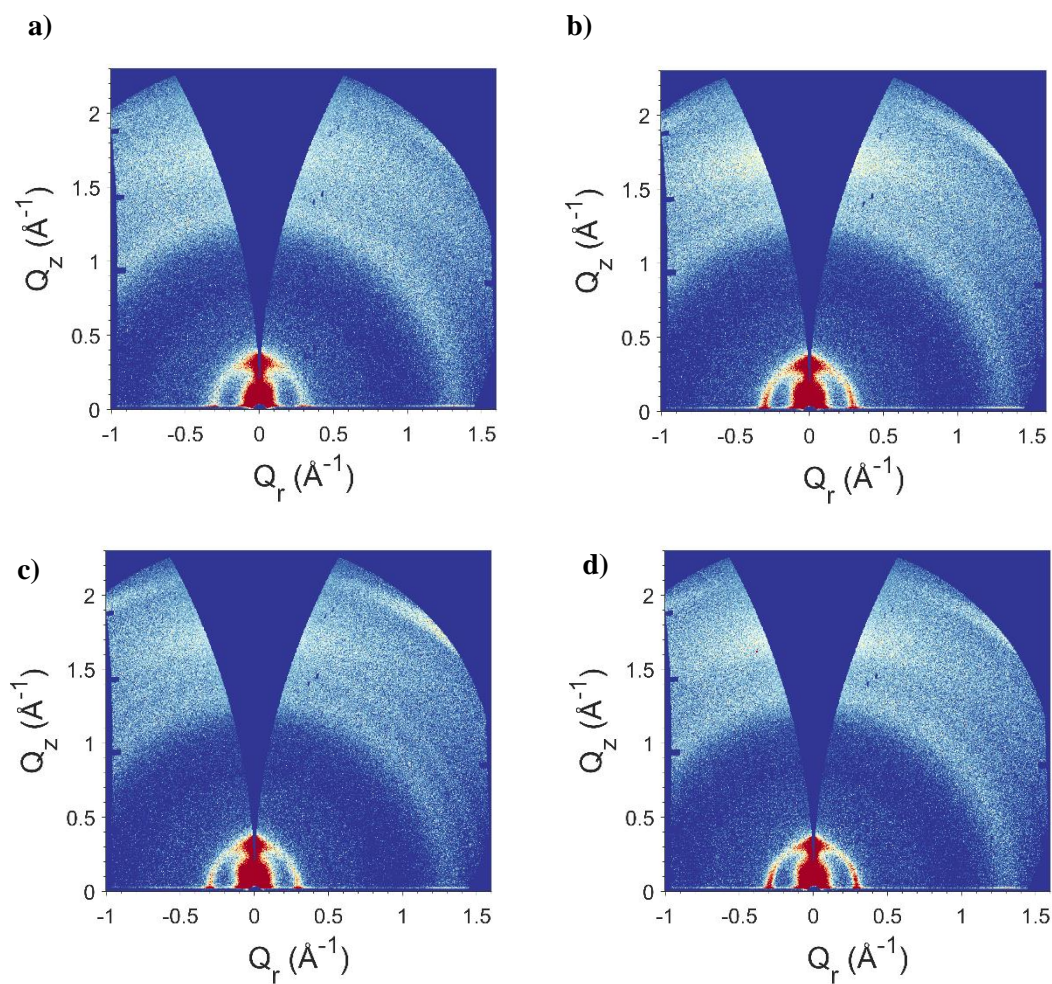


Figure 5.4: 2D GIWAXS patterns of PBDB-T:PC₇₀BM with **a)** no DIO, **b)** 0.5% DIO, **c)** 1% DIO and **d)** 3% DIO.

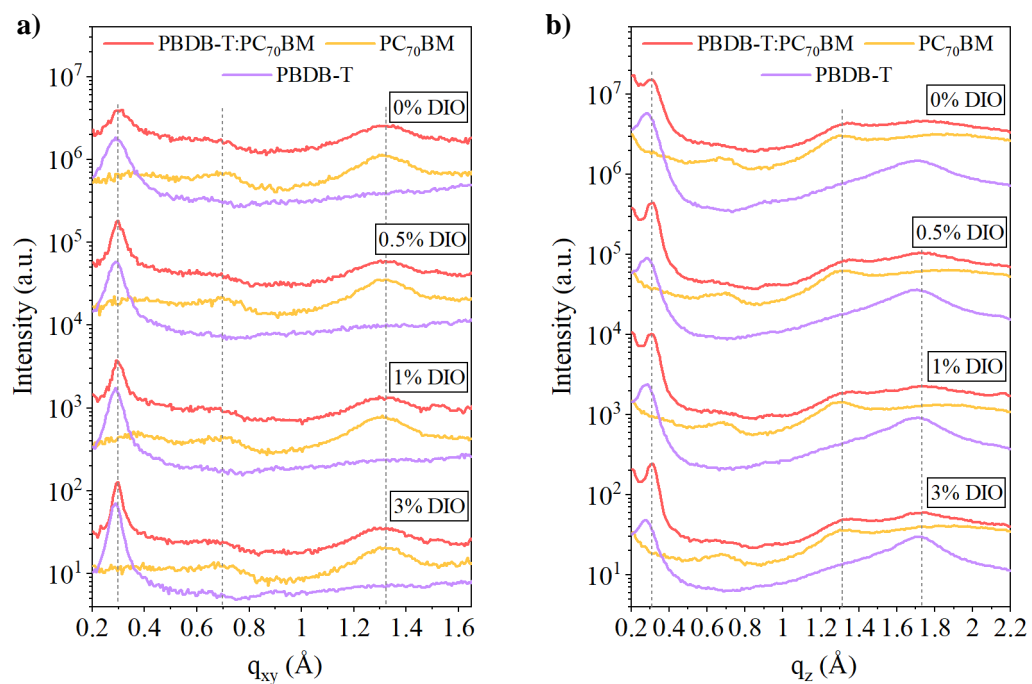


Figure 5.5: 1D GIWAXS linecuts of PBDB-T:PC₇₀BM, alongside pristine PBDB-T & PC₇₀BM. Linecuts are vertically offset for clarity, with the dotted lines acting as a guide for the eye. **a)** In-plane, **b)** Out-of-plane.

A summary of the extracted q values, d -spacings, and CCLs of the PBDB-T:PC₇₀BM blend is shown in **Table 5.2**.

Table 5.2: GIWAXS features of the PBDB-T:PC₇₀BM blend. In some cases, d -spacing values differ where a higher number of significant figures has been used in the calculation than quoted for q .

DIO content	In-plane			Out-of-plane		
	q value (Å ⁻¹)	d -spacing (nm)	CCL (nm)	q value (Å ⁻¹)	d -spacing (nm)	CCL (nm)
0%	0.30	2.06	6.89	0.31	2.04	5.11
	1.32	0.48	1.92	1.31	0.48	2.88
				1.75	0.36	0.76
0.5%	0.30	2.13	10.5	0.30	2.06	6.99
	1.33	0.48	2.08	1.30	0.48	2.97
				1.73	0.36	0.86
1%	0.30	2.13	11.2	0.30	2.09	6.59
	1.31	0.48	1.95	1.31	0.48	2.94
				1.75	0.36	0.82
3%	0.30	2.13	15.0	0.30	2.06	7.89
	1.31	0.48	2.15	1.30	0.48	2.95
				1.74	0.36	0.86

We first consider the in-plane scattering, as shown in **Figure 5.5a**. In the blend we find evidence of the PBDB-T lamellar peak, alongside the PC₇₀BM peaks at $q \sim 0.7 \text{ \AA}^{-1}$ and $\sim 1.3 \text{ \AA}^{-1}$. These PC₇₀BM features form broad ‘halos’, spanning the in-plane and out-of-plane directions, as shown in **Figure 5.4**. This type of feature is commonly seen in fullerene-based acceptors and implies a lack of directional packing.²⁹ For both components, no new reflection planes appear with increasing DIO concentration, and the various d -spacings also remain effectively constant. However, as shown in the ITIC blend, increased DIO concentration does induce larger CCLs for the PBDB-T lamellar peak ($q \sim 0.30 \text{ \AA}^{-1}$).

If we consider the out-of-plane scattering shown in **Figure 5.5b**, we find that the pristine PC₇₀BM film is characterised by similar peaks as observed in the in-plane direction, implying it has isotropic orientation. Again, no new peaks or changes in d -spacing are seen with increased DIO concentration, but small increases in CCLs are evident, specifically for the lamellar peak associated with PBDB-T.

In comparison to PBDB-T:ITIC, PBDB-T:PC₇₀BM patterns show much less dramatic changes with increasing DIO concentration. Here the changes in phase separation, acceptor molecule orientation, and acceptor aggregation shown for ITIC are not replicated using PC₇₀BM. This difference could be due to a number of factors, such as the miscibility of each acceptor with PBDB-T, and their tendency to aggregate. We note here that the relatively isotropic orientation of PC₇₀BM is different to the directional packing of ITIC, and as such changes in orientation with increased DIO concentration would be less apparent. The acceptors have similar reported solubilities in DIO¹³ and this is therefore unlikely to modify morphology. The relative tendencies of the acceptors to de-mix from PBDB-T are discussed in **Section 5.4.2.3**.

5.4.1.2 AFM

AFM scans are shown in **Figure 5.6** & **Figure 5.7**, with the corresponding root mean square (RMS) roughness values shown in **Table 5.4** & **Table 5.4**. For completeness, we also show AFM scans for pristine components in **Figure S5.4 – S5.6**.

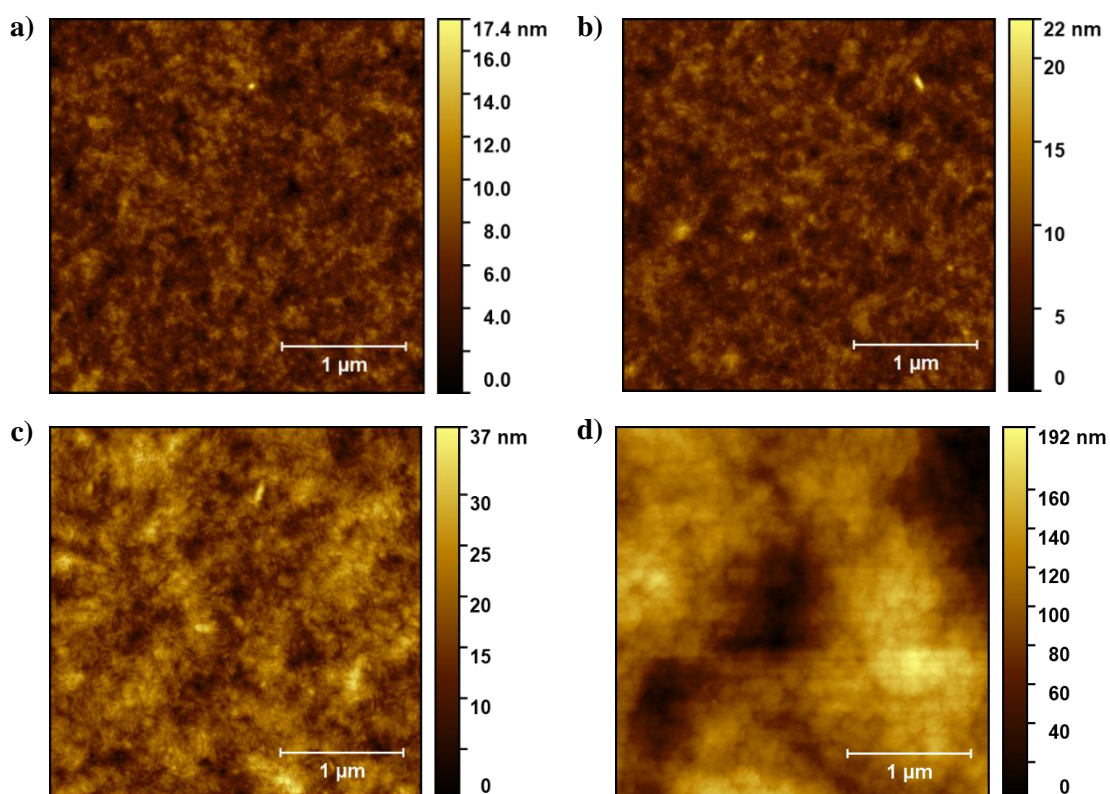


Figure 5.6: AFM scans of PBDB-T:ITIC blend films with **a)** no DIO, **b)** 0.5% DIO, **c)** 1% DIO and **d)** 3% DIO.

Table 5.3: Root mean square roughness values from the AFM of PBDB-T:ITIC films.

System	Root mean square roughness (nm)
PBDB-T:ITIC no DIO	1.60
PBDB-T:ITIC 0.5% DIO	1.80
PBDB-T:ITIC 1% DIO	4.27
PBDB-T:ITIC 3% DIO	30.6

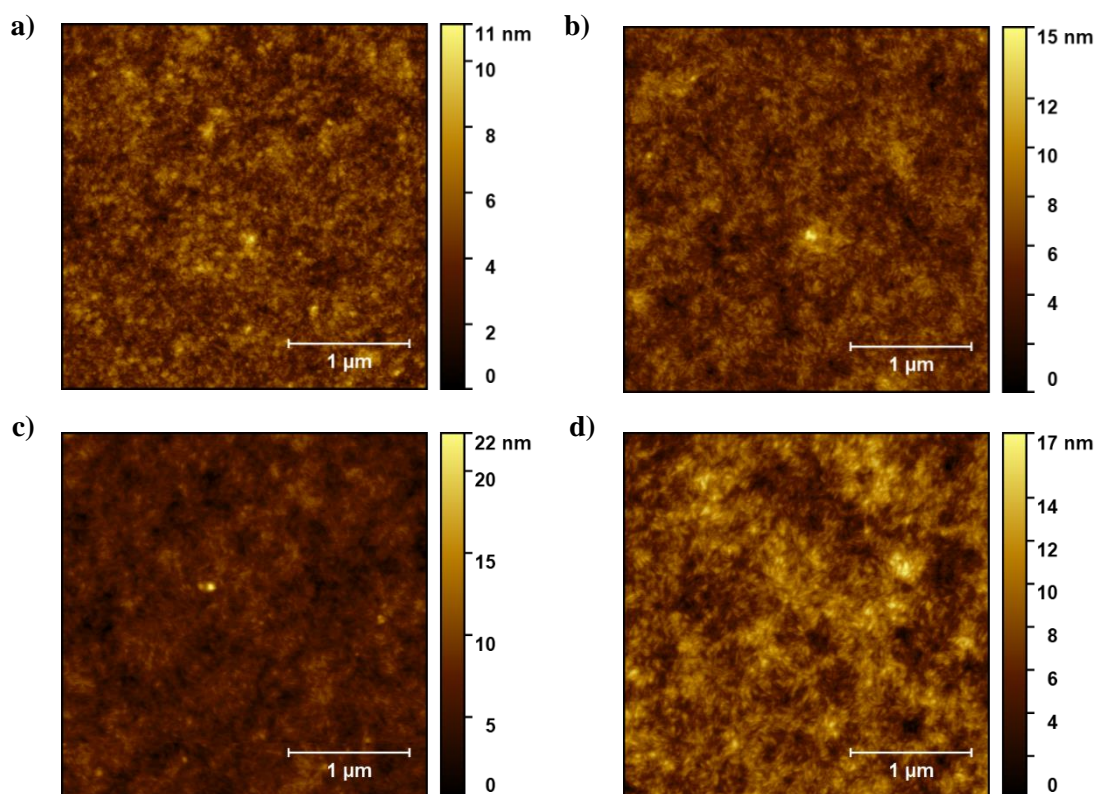


Figure 5.7: AFM scans of PBDB-T:PC₇₀BM blend films with a) no DIO, b) 0.5% DIO, c) 1% DIO and d) 3% DIO.

Table 5.4: Root mean square roughness values from the AFM of PBDB-T:PC₇₀BM films.

System	Root mean square roughness (nm)
PBDB-T:PC ₇₀ BM no DIO	1.00
PBDB-T:PC ₇₀ BM 0.5% DIO	1.32
PBDB-T:PC ₇₀ BM 1% DIO	1.53
PBDB-T:PC ₇₀ BM 3% DIO	2.44

As was found from GIWAXS measurements, the AFM scans indicate the addition of DIO has a much greater impact on the morphology of ITIC based systems than those based on PC₇₀BM. The appearance of large aggregates upon addition of DIO, leading to greatly increased roughness of films, can be seen in both pristine ITIC films (**Figure S5.4**) and PBDB-T:ITIC blend films (**Figure 5.6**). In contrast, PC₇₀BM, PBDB-T, and their corresponding blends, undergo only minor increases in roughness with increasing DIO content. This supports GIWAXS measurements that show that DIO induces de-mixing, crystallization, and aggregation of ITIC, but has much less of an effect on PC₇₀BM. In other work on these systems¹³ DIO has been shown to increase the phase separation of ITIC dramatically more than that of PC₇₀BM. This is linked to inducing increased trap assisted recombination and reduced charge carrier mobility.

Previous work has demonstrated that the increased aggregation of ITIC upon addition of DIO results from a greater tendency of ITIC to aggregate, compared to PC₇₀BM.³⁰ We note that aggregation is often used as a blanket term that refers to both de-mixing (and the formation of purer phases of material), and also the crystallization of a component. These processes are driven by different factors, however both will be dependent on the molecular diffusion rates, which are usually inversely correlated with T_g .³¹ Other works have determined T_g values of $\sim 180^\circ\text{C}$ ³² and $\sim 155^\circ\text{C}$ ³³ for ITIC and PC₇₀BM respectively, implying that PC₇₀BM should diffuse more rapidly. However, it has been shown recently that some NFAs do not follow this simple relation, and that ITIC can undergo a crystallization below its T_g .³² We speculate here that DIO is facilitating this low temperature crystallization, leading to the more significant aggregation seen for the NFA. In this case, both phase separation and crystallization are occurring.

5.4.1.3 Absorbance

UV-Vis absorption spectra of the PBDB-T:ITIC blend films are shown in **Figure 5.8a**, and that of PBDB-T:PC₇₀BM is shown in **Figure 5.8b**.

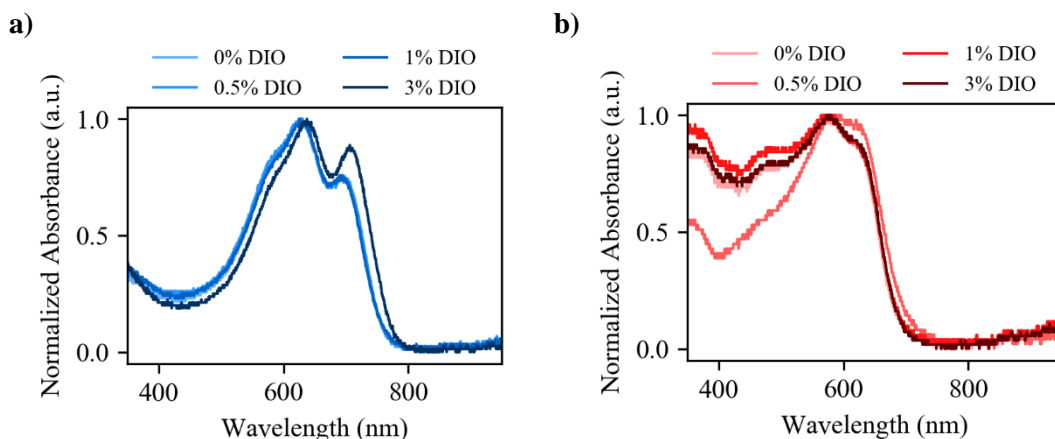


Figure 5.8: UV-Vis absorption of *a*) PBDB-T:ITIC, *b*) PBDB-T:PC₇₀BM.

Our results shown similar trends to the AFM and GIWAXS studies. With increasing DIO concentration, the absorption of the PBDB-T:PC₇₀BM blend films remains effectively constant. In contrast, the PBDB-T:ITIC blend films show an increase in the relative intensity of the ITIC absorption peak (~700 nm), and an observed red shift in the whole absorption. Both of these factors have been attributed in other works to improved crystallinity, in this case specifically of ITIC.³⁴ These results therefore support the conclusions of the GIWAXS and AFM measurements that increasing DIO concentration increases ITIC crystallinity.

5.4.2 Device Studies

5.4.2.1 Device Performance

To assess how the changes outlined above affected device performance, OPVs were fabricated using a conventional architecture. Here, a PEDOT:PSS hole transport layer and a PFN-Br electron transport layer were fabricated either side of the BHJ, with full experimental details given in the experimental methods. Unless specified, all devices were encapsulated to protect against the ingress of oxygen and moisture.

Initial device performance, external quantum efficiencies (EQEs) and current-voltage (*JV*) curves for the champion device run are shown in **Figure 5.9**. The devices are described in terms of their power conversion efficiency (PCE), open circuit voltage (V_{oc}), short circuit current density (J_{sc}) and fill factor (FF). Box plots are given for the PCE of the champion 10 devices, with further metrics shown in **Figure S5.8** and a summary of device metrics given in

Table 5.4. Figure S5.9 shows box plots across several device runs, approximately 150 devices per DIO concentration, to illustrate the trends over a larger data set.

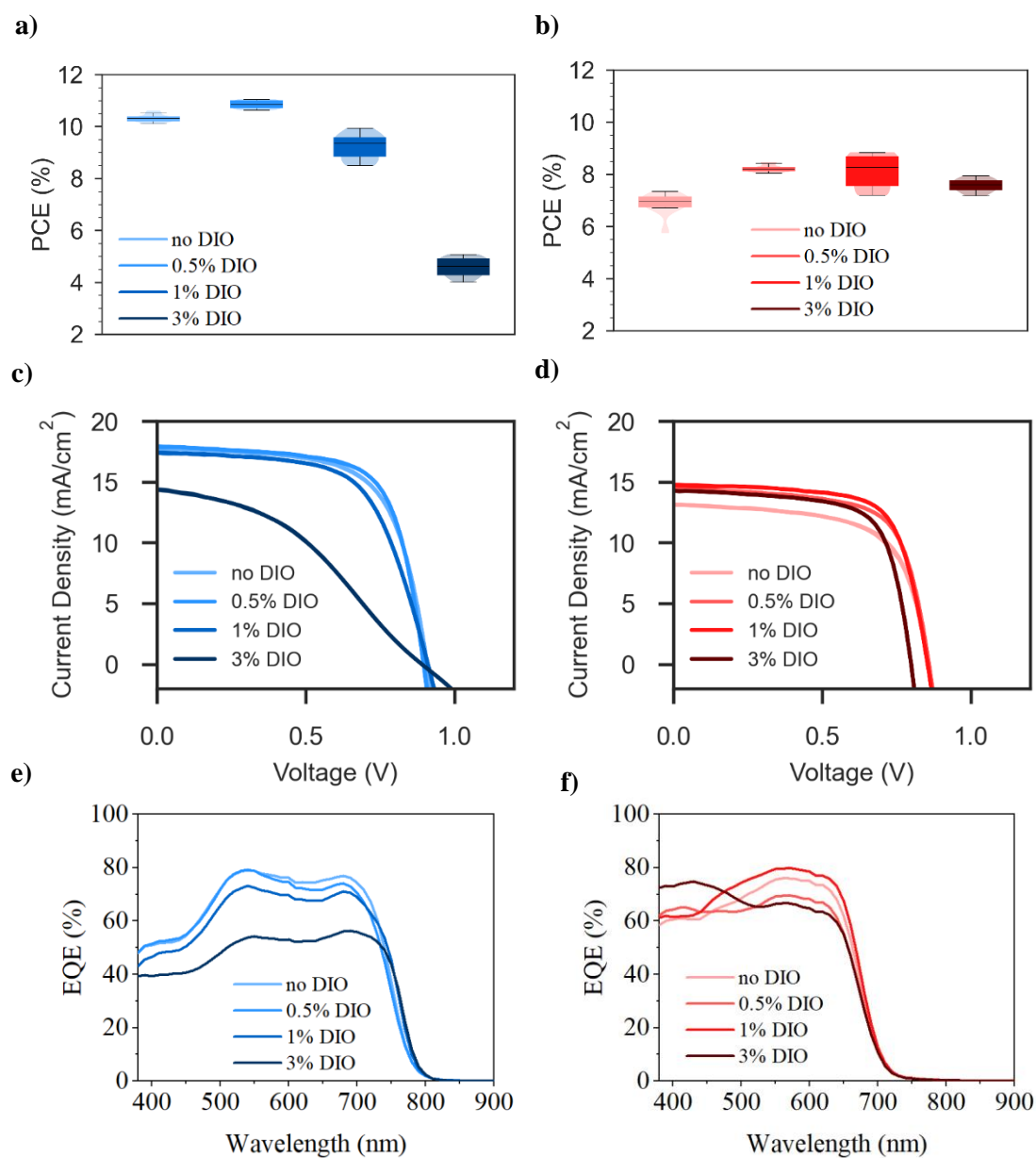


Figure 5.9: Box plots of the PCE values for a) PBDB-T:ITIC and b) PBDB-T:PC₇₀BM. 10 devices shown in each box plot. Champion JV curves for c) PBDB-T:ITIC and d) PBDB-T:PC₇₀BM. EQE curves for e) PBDB-T:ITIC and f) PBDB-T:PC₇₀BM.

Table 5.4: Device metrics for PBDB-T:ITIC and PBDB-T:PC₇₀BM for different DIO concentrations. An average is given for 10 devices ± 1 standard deviations, with the champion value given in brackets.

System	DIO Content (%)	PCE (%)	V _{OC} (V)	J _{sc} (mA/cm ²)	FF (%)
PBDB-T:ITIC	0	10.3 \pm 0.14 (10.6)	0.91 \pm 0.00 (0.91)	17.5 \pm 0.15 (17.8)	65.7 \pm 0.73 (67.0)
	0.5	10.8 \pm 0.14 (11.0)	0.89 \pm 0.00 (0.90)	17.7 \pm 0.18 (18.0)	69.1 \pm 0.33 (69.8)
	1	9.23 \pm 0.46 (9.94)	0.90 \pm 0.01 (0.91)	17.1 \pm 0.26 (17.5)	60.8 \pm 2.23 (63.1)
	3	4.60 \pm 0.32 (5.08)	0.87 \pm 0.01 (0.89)	14.2 \pm 0.87 (14.7)	37.6 \pm 1.32 (39.7)
PBDB-T:PC ₇₀ BM	0	6.86 \pm 0.40 (7.33)	0.86 \pm 0.02 (0.94)	12.7 \pm 0.24 (13.2)	63.5 \pm 2.88 (68.8)
	0.5	8.22 \pm 0.13 (8.48)	0.85 \pm 0.01 (0.86)	13.9 \pm 0.24 (14.4)	69.1 \pm 0.50 (70.2)
	1	8.12 \pm 0.59 (8.84)	0.85 \pm 0.00 (0.86)	14.2 \pm 0.35 (14.8)	67.8 \pm 2.99 (71.4)
	3	7.58 \pm 0.22 (7.94)	0.80 \pm 0.01 (0.81)	13.7 \pm 0.32 (14.3)	69.5 \pm 0.55 (70.2)

It is apparent from **Figure 5.9a** that the addition of 0.5% DIO to a blend film of PBDB-T:ITIC improves device performance, with this being driven by an increase in *FF*. This is expected due to the greater phase purity resulting from the addition of DIO. However, as DIO content is increased above 0.5%, device performance decreases, mostly driven by drops in *J_{sc}* and *FF*. Other work has attributed this to the excessive aggregation of ITIC³⁴ and exaggerated vertical segregation of the blend components.²⁰ Both of these effects are likely to degrade the optimised interpenetrating BHJ,³⁵ which will negatively impact charge carrier mobility and device performance. We note that the observed increase in edge-on orientation of ITIC may also play a role in reducing device efficiency. These trends are replicated in **Figure S5.9**.

For the PBDB-T:PC₇₀BM devices shown in **Figure 5.9b**, the addition of DIO initially appears to improve performance due to increased *J_{sc}* and *FF*. It appears that in contrast to the PBDB-T:ITIC devices, this trend was not replicated when considering multiple device runs, shown in **Figure S5.9**. Here, for a larger number of devices, the differences with

increased DIO content are marginal. Notably, the addition of 3% DIO does not significantly deteriorate device performance as is observed in the PBDB-T:ITIC cells.

Interestingly, a ‘kink’ is observed in the PBDB-T:ITIC *JV* curves containing 3% DIO. This is often referred to as an ‘s-shaped curve’. We note that whilst s-shape curves were common in most PBDB-T:ITIC devices containing 3% DIO, it did not always occur. S-shaped curves are not uncommon in literature, and are variably attributed to trap formation,³⁶ imbalanced charge carrier mobilities³⁷ and charge transport barriers.³⁸ However, these are not usually seen in high performance systems, such as those studied here. As the ‘kink’ was only present in devices containing a high concentration of DIO, and residual DIO content has been linked to a range of deleterious effects, we have used nuclear magnetic resonance (NMR) spectroscopy to characterise whether residual DIO is found within the different films.

5.4.2.2 NMR results

Other work has shown that DIO can be removed from OPV active layers by extended annealing, application of high vacuum, washes with a solvent such as methanol;¹⁶ or in some cases is disputed to not occur at all.¹⁴ To establish whether we are able to remove DIO, we used NMR to study thin films of our blends on PEDOT:PSS coated glass. These films were first exposed to various processing steps to mimic device preparation. They were then dissolved in chlorobenzene, with the resultant solution left to evaporate. Finally, the remaining solids were dissolved in *d*-chloroform for ¹H NMR characterization.

There are a number of processes during device fabrication that could remove DIO from our films. Firstly, films are exposed to a high temperature anneal (160°C for 10 minutes) after active layer deposition which could lead to DIO evaporation. Secondly, films are exposed to methanol via deposition of the PFN-Br solution, which could wash away DIO. Thirdly, films are exposed to a high vacuum during thermal evaporation of the electrode, which could also remove DIO. To establish if any of these steps successfully remove DIO, we prepared thin film samples that were exposed to each of these conditions. Films were also prepared without DIO and processed in the same way, to act as a control.

The results of this study are shown in **Figure 5.10**, with full NMR spectra shown in **Figure S5.10 – S5.12**. The presence of DIO is usually identified in ¹H NMR using its characteristic triplet peak at ~3.20 ppm.¹⁴ To examine this area **Figure 5.10a** shows the ¹H NMR spectrum for the PBDB-T:ITIC films over the chemical shift range 2.8 – 3.25 ppm. **Figure 5.10b** shows the spectrum of the PBDB-T:PC₇₀BM films over the same range.

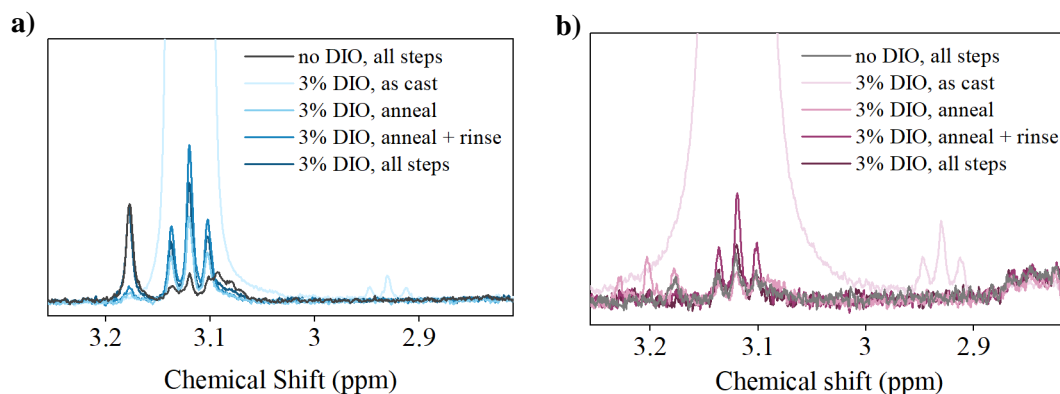


Figure 5.10: ^1H NMR signal of DIO from processed blend films of **a)** PBDB-T:ITIC and **b)** PBDB-T:PC₇₀BM. Here ‘all steps’ refers to films that have been treated with an anneal, methanol rinse and high vacuum step consecutively.

In **Figure 5.10a** we can immediately identify DIO by its triplet peak at ~ 3.1 ppm. It is clear in that DIO is present in all PBDB-T:ITIC samples, regardless of processing condition. It is worth noting that whilst the amount is dramatically decreased from the ‘3% DIO, as cast sample’ when any processing is applied, the difference between the various conditions is negligible. Rather surprisingly, we also detect small amounts of DIO in the PBDB-T:ITIC film that had 0% DIO initially.

If we now consider the PBDB-T:PC₇₀BM blend films, shown in **Figure 5.10b**, it is clear that residual DIO is also still present in these samples. It is worth noting here that the small triplet peaks seen at ~ 2.95 ppm in both ‘3% DIO, as cast’ samples is likely a satellite peak of the main DIO triplet. We note that residual concentrations of DIO after processing have been seen in other, similar studies,¹⁴ however some reports have shown complete DIO removal.¹⁶

As no internal standard was used in the measurements, we cannot state the absolute DIO concentration present. Elsewhere¹⁴ however, the ratio of DIO:acceptor peaks in ^1H NMR has been used to quantitatively compare the relative DIO concentration between samples. Here, molar concentration can be determined by peak area. In our work we therefore used the area of peaks at ~ 3.1 ppm, ~ 8.9 ppm, and ~ 7.6 ppm to identify the relative molar concentrations of DIO, ITIC, and PC₇₀BM. This was then used to calculate the ratio of molar concentration of DIO:acceptor, to allow the ITIC and PC₇₀BM based systems to be compared. Further details of the calculation are given in the supplementary information (**Section 5.7.4.2**), including a correction for the solid concentration and molecular weights of the acceptors. **Figure 5.11** plots the relative DIO:acceptor concentration for the different films. Here it can be seen that for films processed with 3% DIO, the ratio of DIO:acceptor is more than a

magnitude higher in ITIC based films than those based on a PC₇₀BM acceptor, after all processing steps.

It is clear that DIO is present in all films, even in those in which it was not initially added, suggesting some form of contamination. To investigate this further, the experiment was then partially repeated in a different lab (referred to as ‘lab 2’, with films prepared in the first lab referred to as ‘lab 1’). Here, non-DIO samples were carefully processed separately to avoid exposure to DIO, and fresh solvents were used. The results of this are also shown in **Figure 5.11**. Again, small amounts of DIO were present in all ‘lab 2’ samples, albeit at lower levels than PBDB-T:ITIC ‘lab 1’ samples for the same conditions. This suggests that the glovebox in lab 1, in which DIO was processed frequently, may have contained residual DIO in the atmosphere that then contaminated all samples. The origin of the DIO found in samples prepared in lab 2 is difficult to determine, but may be due to the fact that the solid materials (ITIC, PC₇₀BM, and PBDB-T) were stored in the lab 1 glovebox, and potentially absorbed DIO during storage. Clearly this will not be the case for all labs and groups, as has been shown in literature.³⁹ It does, however, imply that all devices manufactured in this study contain some residual DIO, regardless of processing, due to the same processing and storage conditions as the NMR samples.

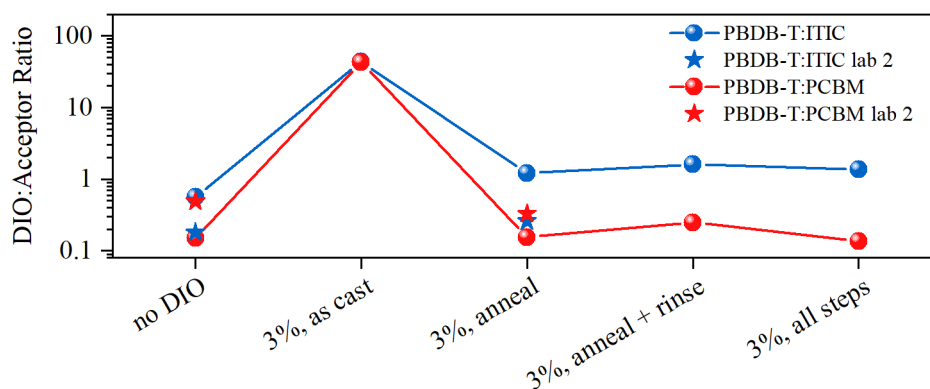


Figure 5.11: Molar concentration DIO:Acceptor ratios calculated from NMR peak integration.

The greater amounts of residual DIO in NFA based films compared with fullerene-based films has not been reported explicitly elsewhere, although is possibly implicated in works that have seen greater impact of DIO on NFA stability.¹⁷ The exact mechanism of this is difficult to understand, but we tentatively suggest that the planar, ordered packing of ITIC molecules effectively ‘traps’ the DIO to a greater degree than is possible in PC₇₀BM films.

As DIO has been linked to increased vertical segregation in both types of blend studied here,^{20,21} residual amounts of DIO is likely to play a role in determining device performance.

To study vertical segregation in our films they were characterised using contact angle measurements to calculate their surface energy. As the surface energy of each component differs, changes in blend surface energy can be used to track accumulation of one component at the film surface, giving a qualitative measure of vertical segregation.

5.4.2.3 Contact Angle Measurements

In this work the surface energy of the thin films of PBDB-T:ITIC and PBDB-T:PC₇₀BM was calculated using the contact angles of both water and hexadecane, using the Fowkes method.⁴⁰ The contact angles for the PBDB-T:ITIC and PBDB-T:PC₇₀BM blends, and their individual components, are shown in **Table S5.6**. Further details regarding the Fowkes method are given in **Section 5.7.5**. **Figure 5.12** plots the change in surface energy with increasing DIO content for each blend.

Noting that surface energy determination via contact angle has known inaccuracies,⁴¹ we find a trend of decreasing surface energy for the PBDB-T:ITIC surface with increasing DIO concentration. This is not unexpected as the component with the lowest surface energy will most likely segregate to the air interface in order to minimize film surface energy.⁴² Therefore this decrease in surface energy suggests an accumulation of PBDB-T at the surface of the BHJ, with an accumulation of ITIC therefore at the bottom of the BHJ.

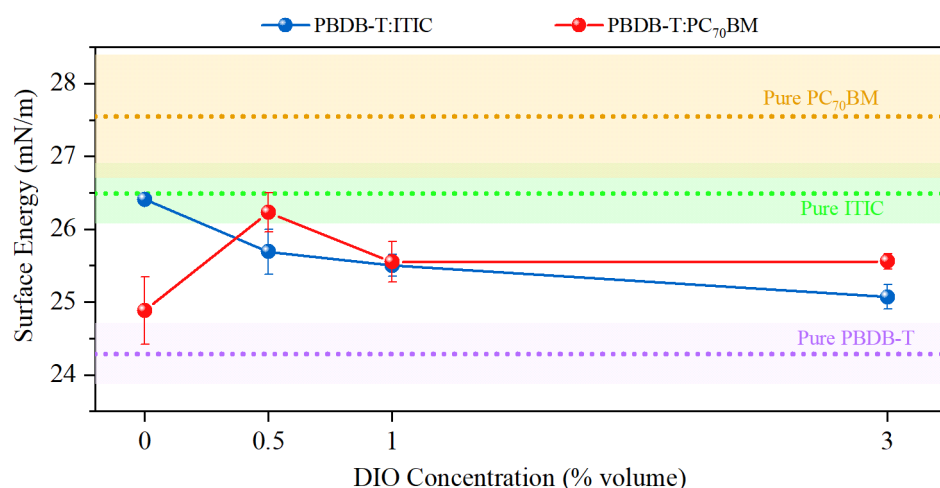


Figure 5.12: Change in surface energy with DIO content for PBDB-T:ITIC and PBDB-T:PC₇₀BM.

Here surface energy is calculated using both water and hexadecane, using the Fowkes method. Horizontal lines represent the surface energy of the pure components. Standard deviation is given by the error bars and shaded regions for two measurements for each data point.

In contrast, there is no clear trend in the surface energy of the PBDB-T:PC₇₀BM films. Therefore, unlike shown in other studies,²¹ increased segregation is not seen in the PBDB-

T:PC₇₀BM based system with increasing DIO concentration. Interestingly, both acceptors have similar surface energies. This suggests they should have very similar miscibilities with PBDB-T, as the Flory-Huggins interaction parameter is related to the difference in donor and acceptor surface energy.⁴³ This similar component miscibility suggests there is no significant thermodynamic difference driving an enhanced vertical segregation of PBDB-T:ITIC, or the aggregation seen previously. This therefore suggests that the greater DIO concentration evidenced from the NMR study may facilitate the altered morphology. This also explains why different levels of vertical segregation with DIO may be seen in different studies- as clearly laboratory and processing conditions will play a significant role in residual DIO content, and consequent segregation.

The driving force behind the segregation may be due to a greater concentration of residual DIO facilitating enhanced diffusion of components (i.e. acting as a plasticizer)⁴⁴ and/or due to differing solubilities of the PBDB-T or ITIC in DIO.²⁶ To further investigate this effect, devices were aged in the dark or under illumination.

5.4.3 Dark Stability

Devices were first stored in the dark, in an inert environment, and this efficiency characterised periodically over several months. The results of this can be seen in **Figure 5.13**, with other device metrics shown in **Figure S5.13 – S5.15**. *JV* curves and UV-Vis absorption for PBDB-T:ITIC blends over time are shown in **Figure 5.14** and **5.15** respectively with data for the PBDB-T:PC₇₁BM blends given in **Figure S5.16** and **S5.17**.

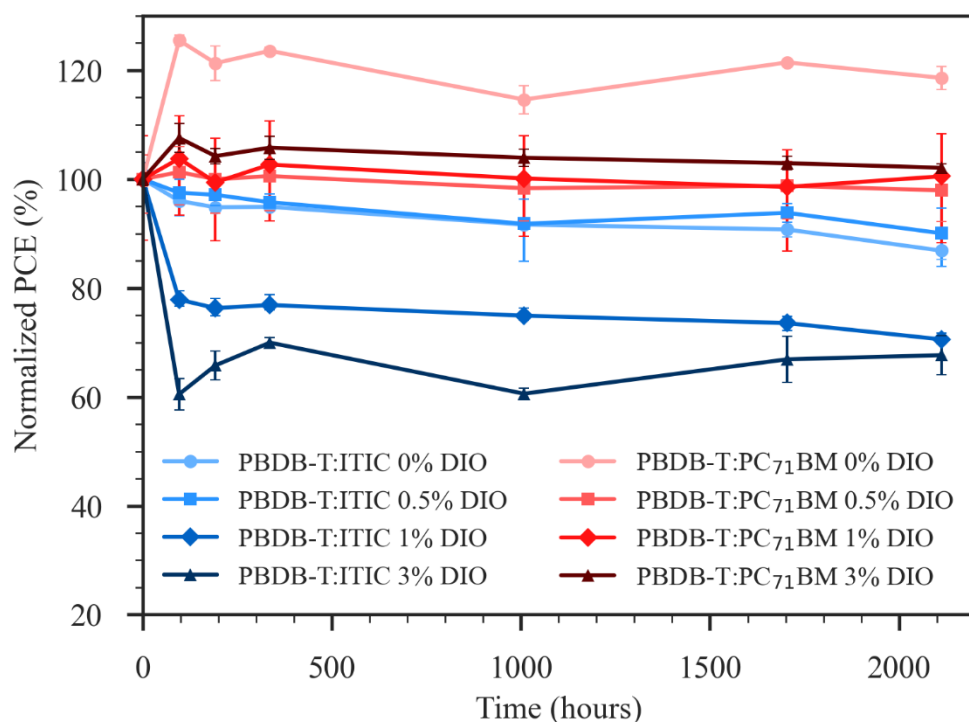


Figure 5.13: Power conversion efficiency over time for devices stored in the dark, in an inert environment. Markers represent the average of at least two pixels, with the error bars representing the minimum and maximum values.

Without the addition of DIO, both systems show a high degree of morphological stability, with relative PCE decreasing by less than 10% over 2000 hours. Here, an initial jump in performance of the PBDB-T:PC₇₁BM system results from increases in FF and J_{SC} , and is likely related to improved phase separation of the system. A detailed discussion of the origin of an increase in PCE over time ('positive burn-in') can be found in **Chapter 6**.

Upon addition of 1% DIO and above, the PBDB-T:ITIC based systems undergo a significant PCE burn in, whilst the PBDB-T:PC₇₁BM cells have a high degree of stability. In the PBDB-T:ITIC blend incorporating 3% DIO, the PCE loss is driven by decreases in J_{SC} and V_{OC} (shown in **Figure S5.14** & **S5.15**). In contrast, in the blend incorporating 1% DIO, the decrease is almost entirely due to a loss in FF (**Figure S5.13**), as a result of the emergence of an s-shaped *JV* curve, as can be seen in **Figure 5.14**.

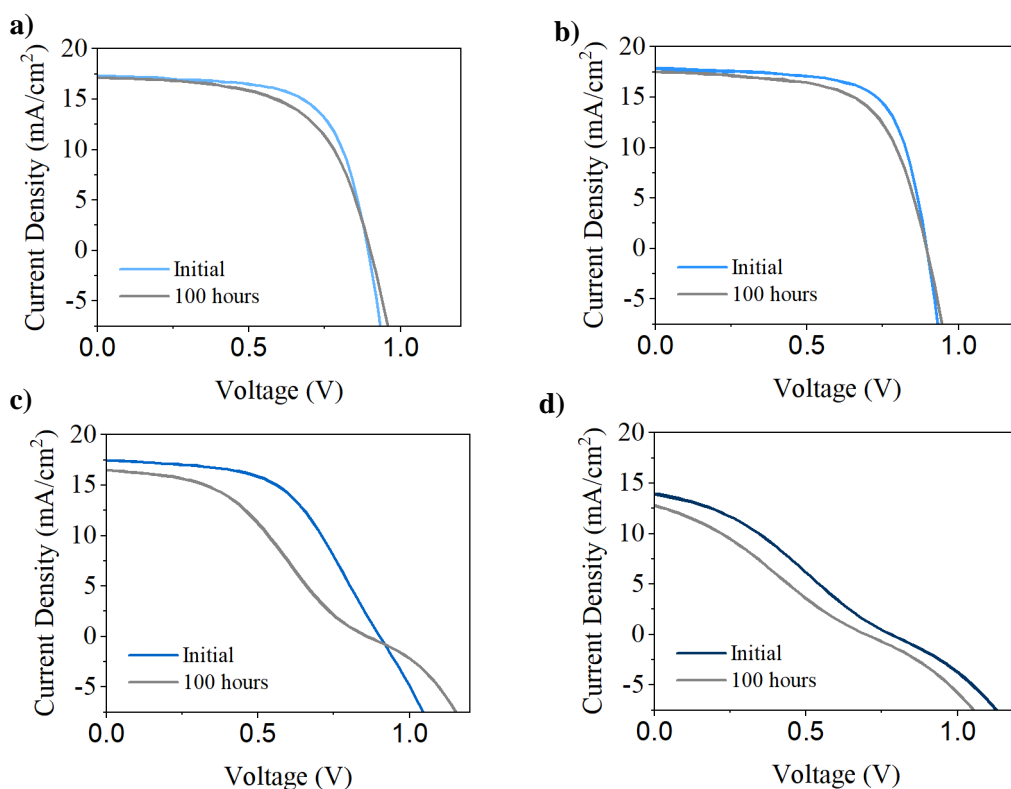


Figure 5.14: *JV curves for PBDB-T:ITIC. a) no DIO, b) 0.5% DIO, c) 1% DIO, d) 3% DIO. Data recorded after approximately 100 hours of storage, to illustrate the speed at which s-shaped curves emerge in the 1% DIO sample. Data for PCBM based devices shown in the supplementary information.*

As we have shown that DIO remains most significantly in the PBDB-T:ITIC films, and degradation is most extreme for these, we can assume that the DIO is, in part, driving the degradation. Here, loss in J_{SC} and V_{OC} can both imply a breakdown in charge generation and extraction.

Whilst ITIC has been shown to undergo several reactions with both PEDOT:PSS⁴⁵ and DIO,¹⁷ we see no changes in the UV-Vis spectra of the blends over 24 hours (**Figure 5.15**). Any reactions of active layer components would likely be accompanied by decreases in absorption, suggesting this is not taking place. Instead it seems possible DIO is altering the morphology of the BHJ over time, especially as DIO has been linked to gradual morphology changes in other work.⁴⁶ To investigate this further, the cells were then aged under harsher conditions, where they were exposed to light and held at a temperature of $\sim 43^{\circ}\text{C}$.

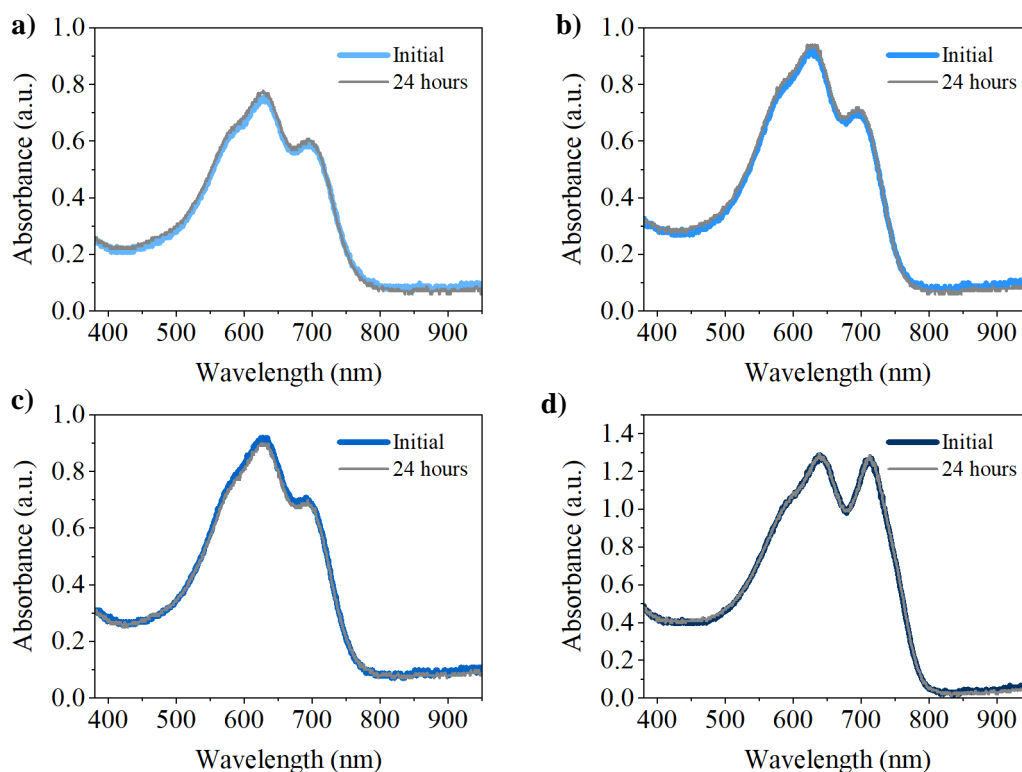


Figure 5.15: UV-Vis absorption of PBDB-T:ITIC films before and after storage in a dark, inert atmosphere for 24 hours. **a)** no DIO, **b)** 0.5% DIO, **c)** 1% DIO, **d)** 3% DIO.

5.4.4 Illuminated Stability

Encapsulated devices were held at open circuit under approximately 1 sun, in air, using an Atlas CPS+ lifetime tester. The efficiency over time is shown in **Figure 5.16**, with further device metrics shown in **Figure S5.18 – S5.20**.

It is clear that whilst the PBDB-T:PC₇₀BM devices have excellent photostability, all PBDB-T:ITIC devices (regardless of DIO content) undergo a dramatic burn-in. To examine if oxygen and moisture were playing a role, this experiment was repeated using un-encapsulated devices, shown in **Figure S5.26 – S5.29**. These measurements confirm the effectiveness of the encapsulation, as the PBDB-T:PC₇₀BM cells degrade dramatically without it, likely due to well established photo-oxidation reactions.^{9,47} For this reason we largely ignore the impact of oxygen and moisture as being causes of degradation in the encapsulated cells.

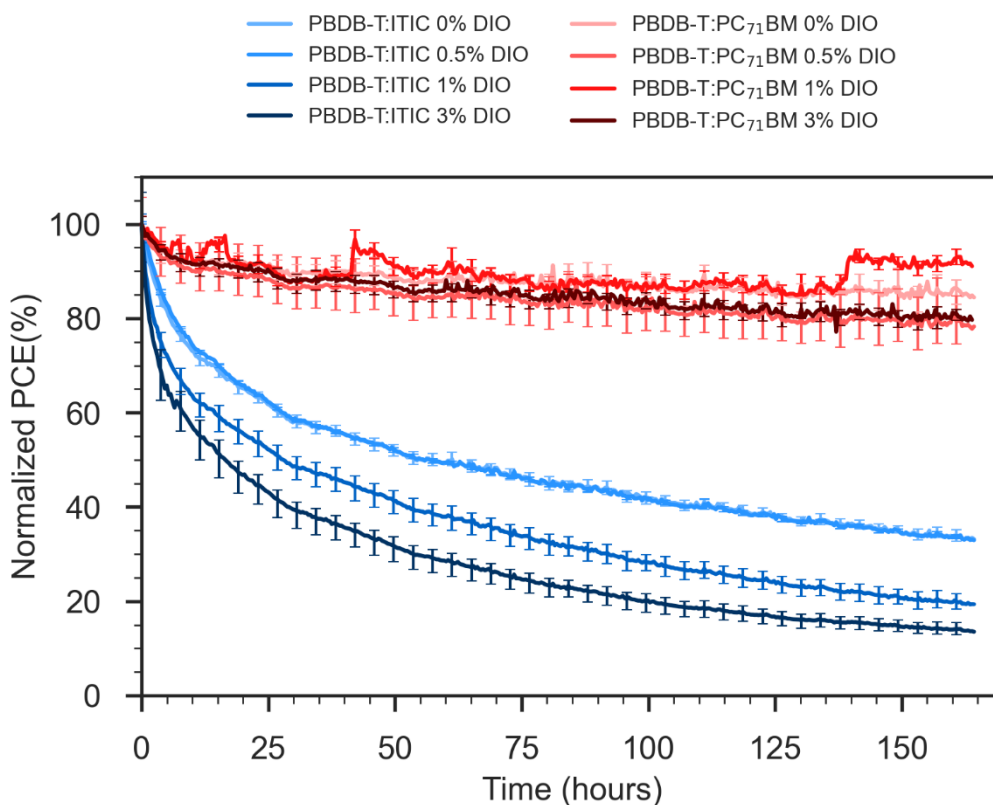


Figure 5.16: PCE of encapsulated devices illuminated in air as a function of time. Data is the average of at least two pixels, with the error bars representing the minimum and maximum values.

Due to the slightly elevated temperature in the Atlas CPS+ system during testing we have also heated devices to $\sim 43^{\circ}\text{C}$ (see **Figure S5.21**) without illumination to examine the impact of temperature. The results of this are shown in **Figure S5.22 – S5.25**. Here, PBDB-T:ITIC devices with 3% DIO undergo a significant burn-in, driven by a loss in all metrics. However, all other devices show little change in performance. This measurement implies that whilst elevated temperature is likely playing some role in the PBDB-T:ITIC blend with 3% DIO, exposure to light appears to be the main driving factor of degradation in most devices. It is noted that in addition to moisture, oxygen, heat, and light, extended periods of time under bias may also cause loss in performance,¹⁷ but this was not considered here.

A difference in photo-stability of PC₇₀BM and ITIC has been seen elsewhere,⁴⁸ and has been attributed to the susceptibility of the INCN end-groups to bond twisting and breakage.⁴⁹ ITIC has also been shown to form electronic traps upon ageing,²⁵ which lowers charge carrier mobility and leads to the decrease in J_{SC} and FF , as we see here. It is worth noting that the relatively low DIO concentration found in the PC₇₀BM blends does not appear to cause catastrophic radical induced breakdown. This suggests that whilst photo-induced DIO reactions may play a role, the intrinsic photo-instability of ITIC seems to be the dominating factor behind device burn-in.

JV curves for PBDB-T:ITIC blends are shown in **Figure 5.17**, with those of PBDB-T:PC₇₀BM based devices shown in **Figure S5.30**. Interestingly, s-shaped curves were apparent in all PBDB-T:ITIC devices following illumination regardless of DIO content, but were not evident in devices after heating (**Figure S5.32**). These instead show similar trends to that of devices left in dark storage.

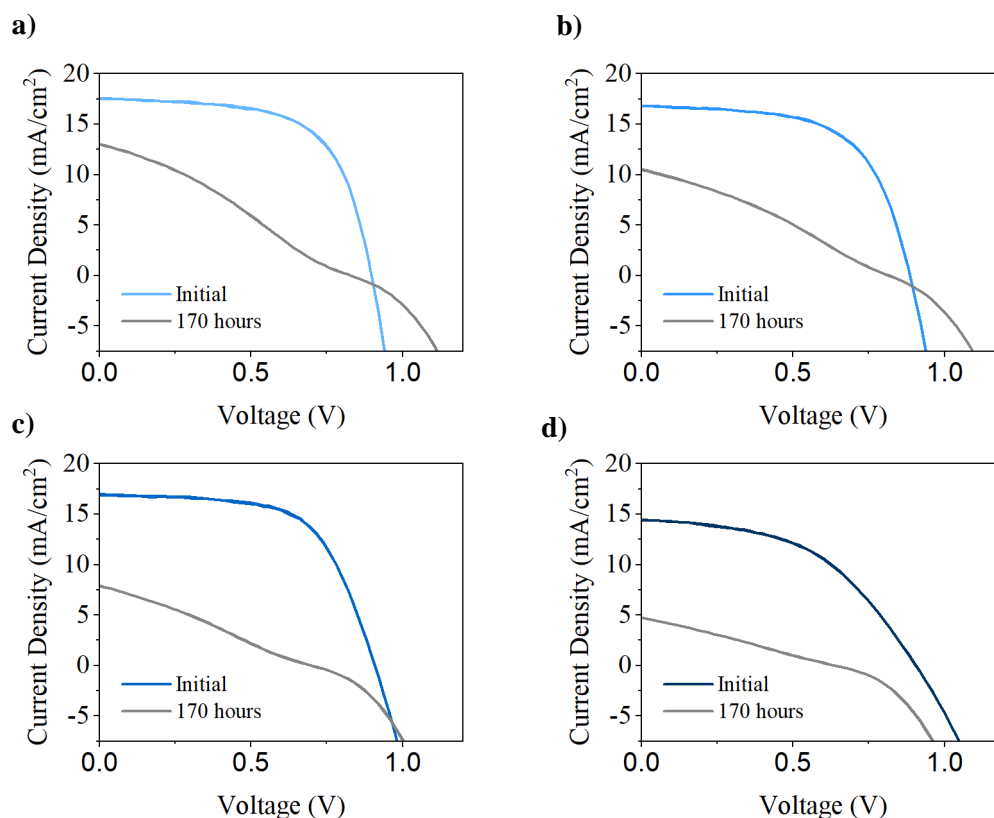


Figure 5.17: Example *JV* curves over time for PBDB-T:ITIC. *JV* curves for the PCBM blends can be seen in the supplementary information. The curves given here are after the full 170 hours of illumination. **a)** no DIO, **b)** 0.5% DIO, **c)** 1% DIO, **d)** 3% DIO. This particular set of devices are an example of the rare occasion when an explicit s-shape curve was not shown for the initial PBDB-T:ITIC 3% devices.

5.4.4.1 S-Shaped Curves

We can now consider all of the conditions where s-shaped *JV* curves are observed, and what may cause them. We observe s-shaped curves in freshly made PBDB-T:ITIC devices containing 3% DIO, and in devices containing 1% and 3% DIO cells after storage in the dark, or upon heating. Upon illumination all PBDB-T:ITIC cells have s-shaped curves, however they are not seen in PBDB-T:PC₇₀BM based devices under any conditions.

Possible reasons for the s-shaped curves include vertical segregation, aggregation and an orientation switch of the ITIC, with such side effects being enhanced by DIO content. Whilst

representative UV-Vis measurements could not be taken after illumination to assess photo-induced absorption changes, meaning reaction induced changes in absorption could not be quantified, some reactions can be disregarded as causing the s-shaped curves. In studies⁴⁵ examining the common reaction between ITIC and PEDOT:PSS, a dramatic loss in V_{OC} normally accompanies the reaction, which we do not see here.

Some experiments were also conducted with a sample of PBDB-T polymer having a lower molecular weight (~80,000 g/mol compared to the original 90,311 g/mol). Here, when manufactured in devices, s-shaped curves were consistently no longer observed upon addition of 3% DIO in PBDB-T:ITIC devices, as shown in **Figure 5.18**.

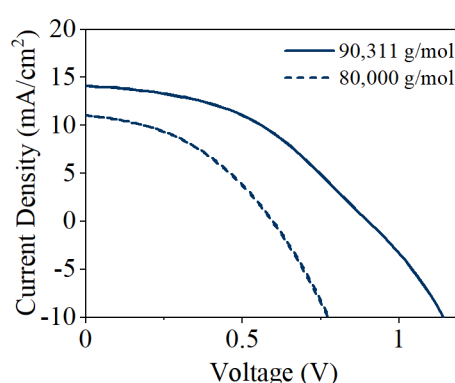


Figure 5.18: *JV curve comparing PBDB-T:ITIC cells with 3% DIO and PBDB-T of either 80,000 or 90,311 g/mol molecular weight.*

The differences in molecular weight of these polymers are likely too close to lead to any considerable impact upon morphological changes. Instead, we suggest that differences in impurities between the two materials may be linked to the appearance or disappearance of s-shaped curves. Impurities or impurity related reactions may lead to the formation of traps and restricted charge transport. Furthermore, the photo-degradation of ITIC molecules would likely reduce electron transport even more, enhancing charge build-up in the device, resulting in s-shaped *JV* curves. It is noted that reactions between ITIC and DIO cannot be discounted as playing a role, due to the residual DIO most likely present in all devices.

5.5 Conclusions

Our work confirms conclusions shown in other studies^{13,17} that large amounts (>1%) of the additive DIO impacts the performance and stability of non-fullerene systems more than it does fullerene based OPVs. Whilst the greater tendency of ITIC to aggregate has been cited as the origin of this effect for this in literature,³⁰ we suggest that enhanced residual DIO in ITIC based devices may also drive increased aggregation. We also observed s-shaped *JV* curves of fresh ITIC based devices containing 3% DIO, with such effects later emerging in 1% DIO cells on dark storage, and in all ITIC based devices under illumination. We attribute these s-shaped curves to a breakdown in electron transport due to the aggregation of ITIC in devices with a large concentration of DIO. Photo-degradation leading to a breakdown in electron transport is proposed to yield a similar effect for all ITIC containing devices upon illumination. This study provides an important rationale for the different behaviour of NFA and PCBM based systems with DIO, and suggests that solvent additives cannot be used in both types of system to achieve high performance and operational stability.

5.6 Experimental

Full details of device fabrication and film characterization can be found in **Chapter 3**. Details specific to this chapter can be found here. PBDB-T (M1003), ITIC and PC₇₀BM purchased from Ossila. Lower molecular weight PBDB-T (used only for **Figure 5.18**) purchased from 1-Material. Unless specified all other solvents and materials purchased from Sigma Aldrich.

5.6.1 GIWAXS

GIWAXS measurements were performed on thin films prepared on PEDOT:PSS coated ITO glass. Samples were prepared using the same coating conditions as used for devices. Data was corrected, reduced and reshaped using GIXSGUI MatLab toolkit.

5.6.2 AFM

Atomic Force Microscopy samples were prepared using the same coating conditions as in devices, on PEDOT:PSS coated ITO glass. Each sample was scanned over a $5 \times 5 \mu\text{m}$ area, with a resolution of 512×512 pixels. Gwyddion 2.56 was used to step line correct the images and extract the root mean square roughness.

5.6.3 UV-Vis Absorption

Samples were prepared using the same conditions as in devices, on PEDOT:PSS coated ITO glass. UV-Vis absorption measured using an Ocean Insight light source (DH-2000-BAL) and spectrometer (HR2000+ES).

5.6.4 Device Fabrication

Devices were fabricated in the form ITO/PEDOT:PSS/Active Layer/PFN-Br/Ag. Active layer solutions were made at either 15 mg/mL (PBDB-T:PC₇₀BM) or 18 mg/mL (PBDB-T:ITIC), at a ratio of 1:1 in chlorobenzene, and stirred overnight at 60°C before use. After cleaning and PEDOT:PSS deposition, PBDB-T:PC₇₀BM films were spin coated dynamically at 1000rpm for 40 seconds, and PBDB-T:ITIC films were spin coated dynamically at 2000rpm for 40 seconds. In both cases film thickness was ~100 nm. All films were annealed at 160°C for 10 minutes. Following electrode deposition, some devices were encapsulated using a UV curable epoxy (purchased from Ossila), which was dropped onto the substrate, topped with a glass slide and cured using a UV lamp (~365 nm) for 15 minutes.

5.6.5 NMR

NMR samples were prepared in the same manner as devices on ITO coated glass. ‘As cast’ samples had no further processing and ‘annealed’ samples were annealed for 160°C for 10 minutes. ‘Annealed + rinse’ samples were rinsed via dynamic deposition of methanol at 3000rpm following the anneal. ‘All steps’ samples were placed inside the evaporator (following an anneal and rinse), and subjected to the same pump down and vacuum time as devices during a Ag evaporation. After processing approximately ~10 films per condition were dissolved in chloroform with the solution then left to evaporate over ~24 hours. Following this, the solid was re-dissolved in *d*-chloroform, with solution characterised via ¹H NMR.

5.6.6 Contact Angle

Contact angle measurements were performed and processed using an Ossila contact angle goniometer, using both water and hexadecane for each film. Samples were prepared in the same manner as devices on PEDOT coated ITO glass.

5.6.7 Dark Stability

Devices aged under dark inert conditions were kept in a N₂ filled glovebox maintained at ~23°C and >0.1ppm H₂O and tested periodically.

5.6.8 Illuminated Stability

Devices illuminated in air were kept inside an Atlas Suntest CPS+ tester, which was maintained at a temperature of 41-44°C and a relative humidity of 23-27%. Devices were kept at open circuit voltage and tested approximately every 20 minutes automatically, without an aperture mask. Devices were mounted inside the Atlas using an Ossila test board and were illuminated through the ITO contact.

5.7 Supplementary Information

5.7.1 Component GIWAXS

5.7.1.1 ITIC

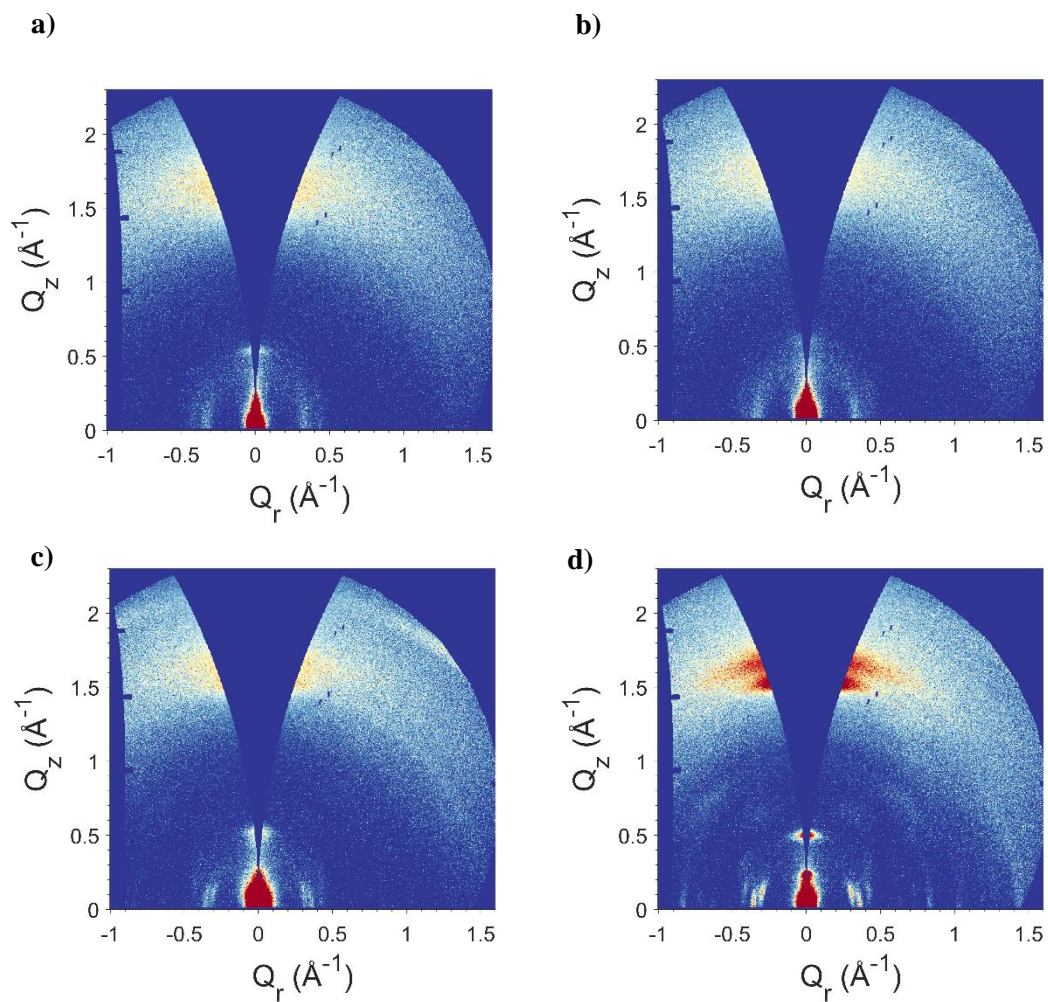


Figure S5.1: 2D GIWAXS patterns of ITIC with **a)** no DIO, **b)** 0.5% DIO, **c)** 1% DIO and **d)** 3% DIO.

5.7.1.2 PBDB-T

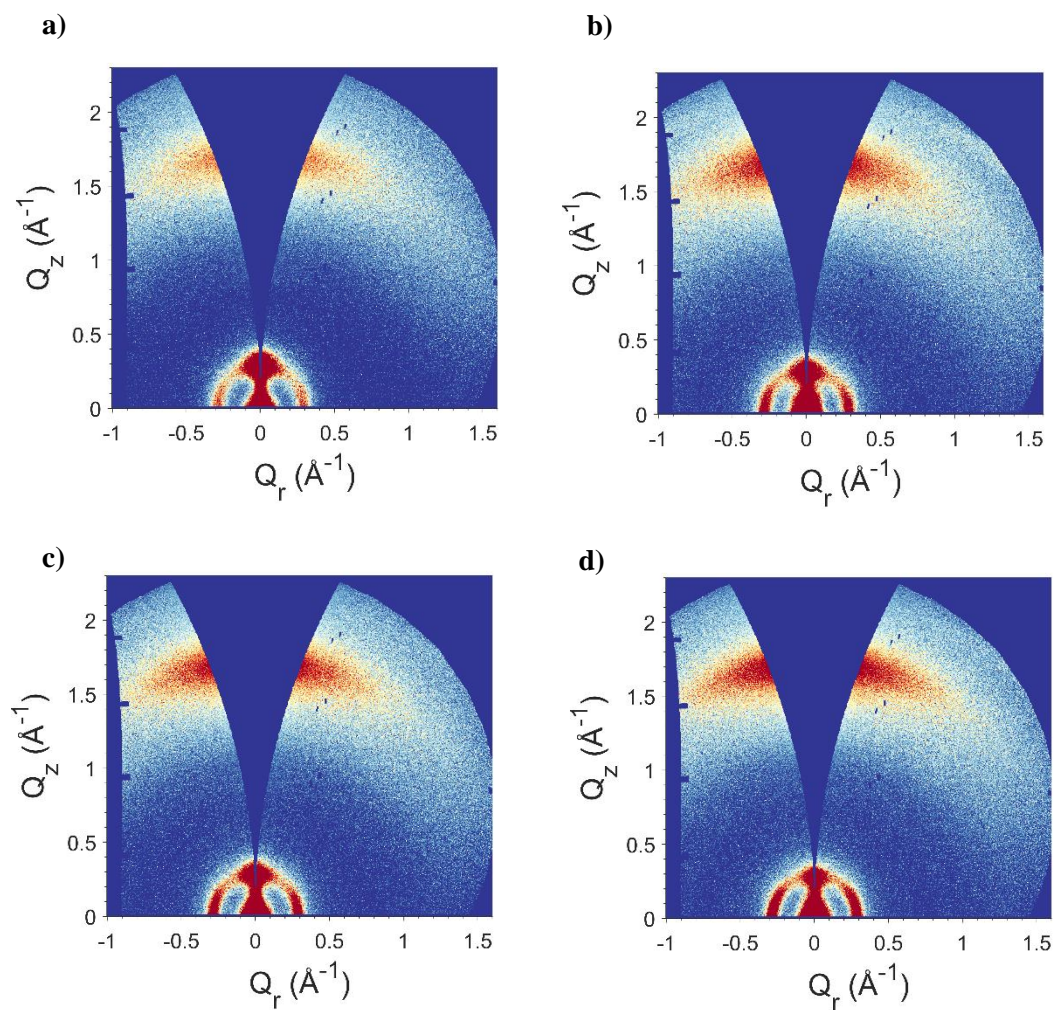


Figure S5.2: 2D GIWAXS patterns of PBDB-T with **a)** no DIO, **b)** 0.5% DIO, **c)** 1% DIO and **d)** 3% DIO.

5.7.1.3 PC₇₀BM

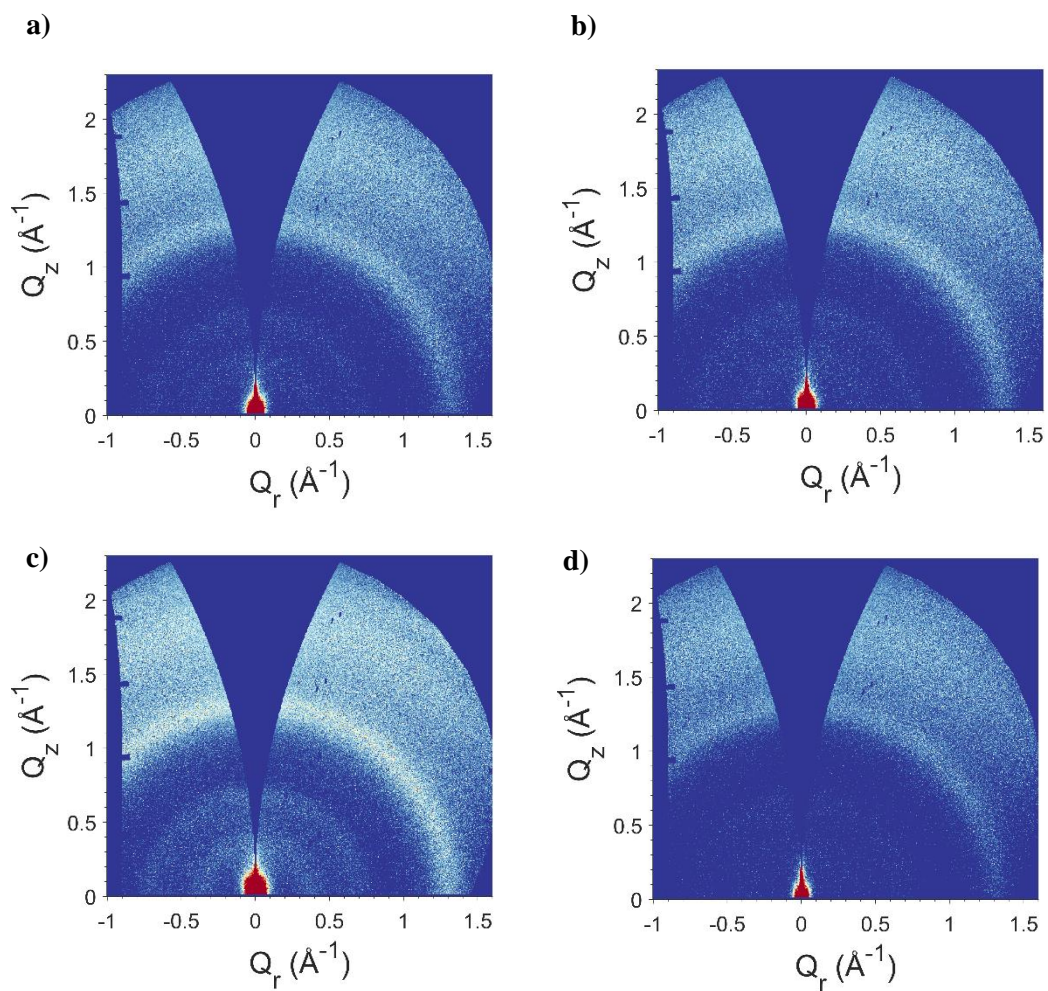


Figure S5.3: 2D GIWAXS patterns of PC₇₀BM with **a)** no DIO, **b)** 0.5% DIO, **c)** 1% DIO and **d)** 3% DIO.

5.7.2 Component AFM

5.7.2.1 ITIC

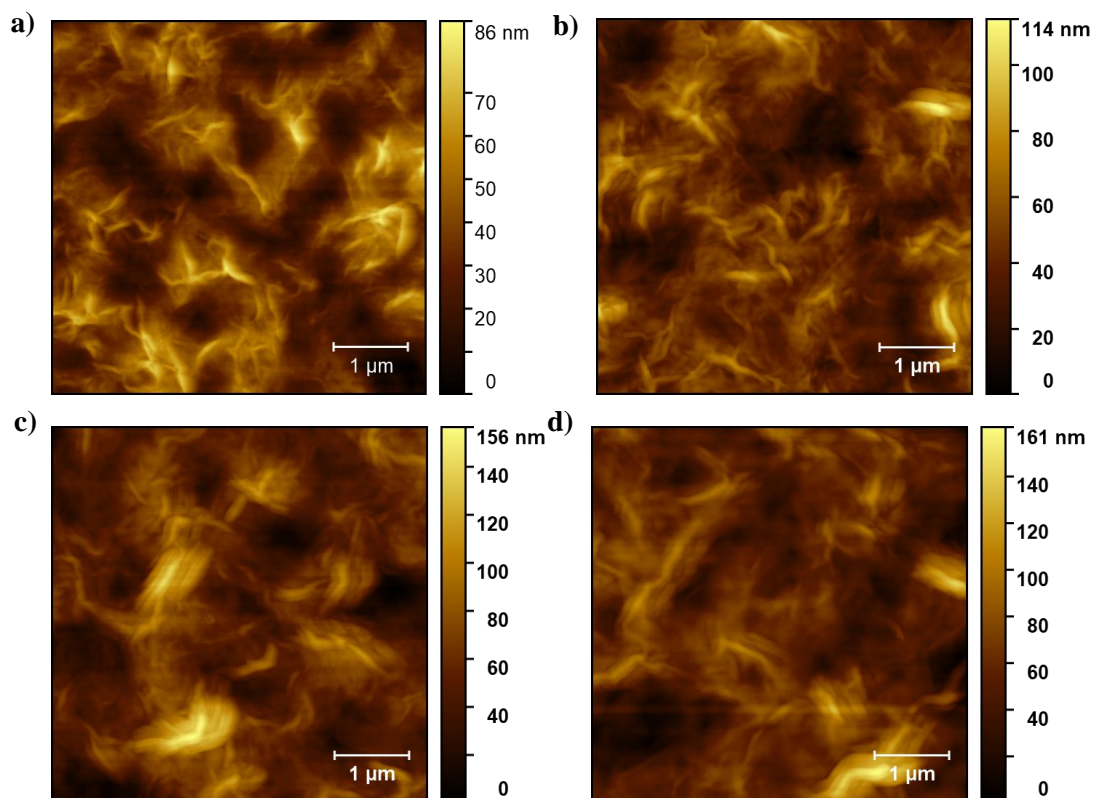


Figure S5.4: AFM scans of pristine ITIC films, a) no DIO, b) 0.5% DIO, c) 1% DIO and d) 3% DIO.

Table S5.1: Root mean square roughness values from the AFM of pristine ITIC films.

System	Root mean square roughness (nm)
ITIC no DIO	13.17
ITIC 0.5% DIO	14.71
ITIC 1% DIO	21.38
ITIC 3% DIO	20.65

5.7.2.2 PBDB-T

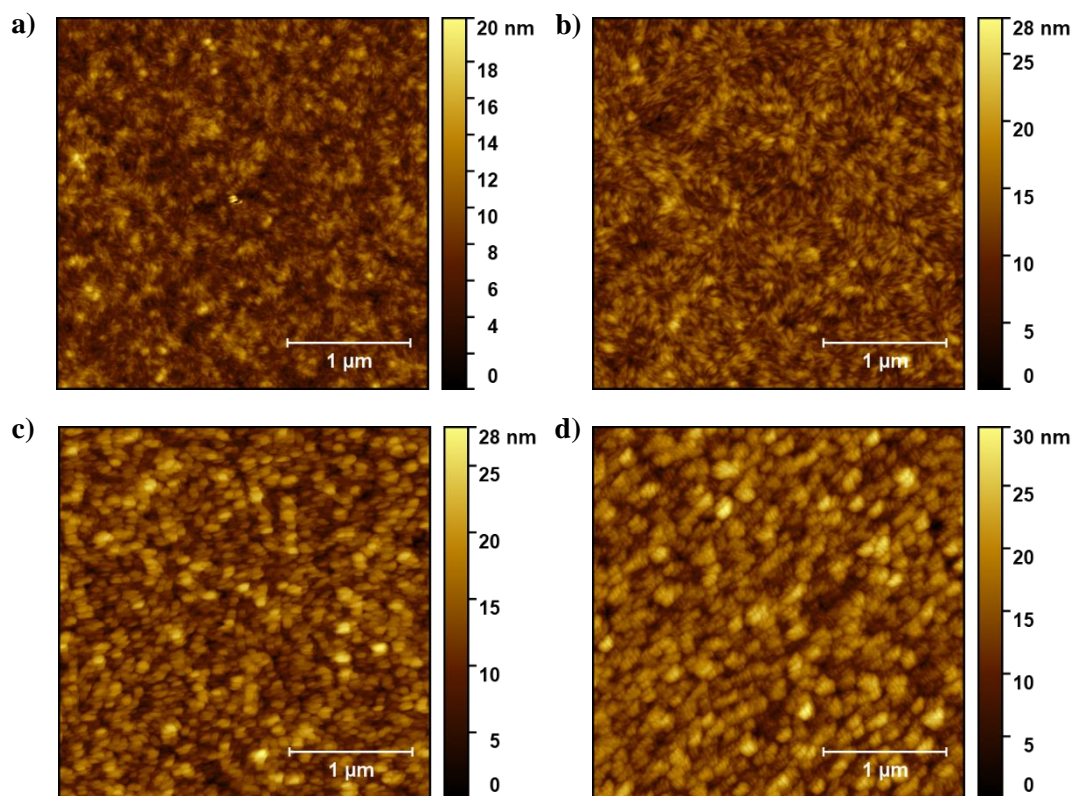


Figure S5.5: AFM scans of pristine PBDB-T films with a) no DIO, b) 0.5% DIO, c) 1% DIO and d) 3% DIO.

Table S5.2: Root mean square roughness values from the AFM of pristine PBDB-T films.

System	Root mean square roughness (nm)
PBDB-T no DIO	2.04
PBDB-T 0.5% DIO	2.80
PBDB-T 1% DIO	3.50
PBDB-T 3% DIO	3.84

5.7.2.3 PC₇₀BM

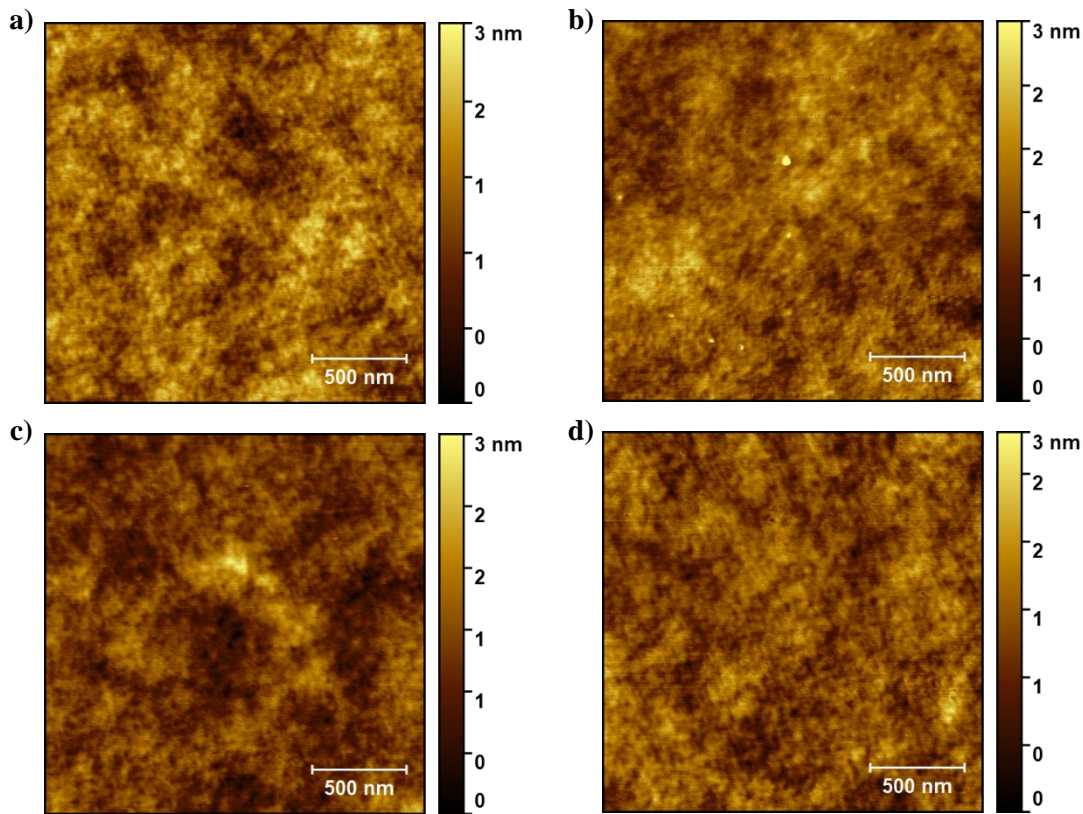


Figure S5.6: AFM scans of pristine PC₇₀BM films with **a)** no DIO, **b)** 0.5% DIO, **c)** 1% DIO and **d)** 3% DIO.

Table S5.3: Root mean square roughness values from the AFM of pristine PC₇₀BM films.

System	Root mean square roughness (nm)
PC ₇₀ BM no DIO	0.32
PC ₇₀ BM 0.5% DIO	0.34
PC ₇₀ BM 1% DIO	0.35
PC ₇₀ BM 3% DIO	0.31

5.7.3 Device Performance

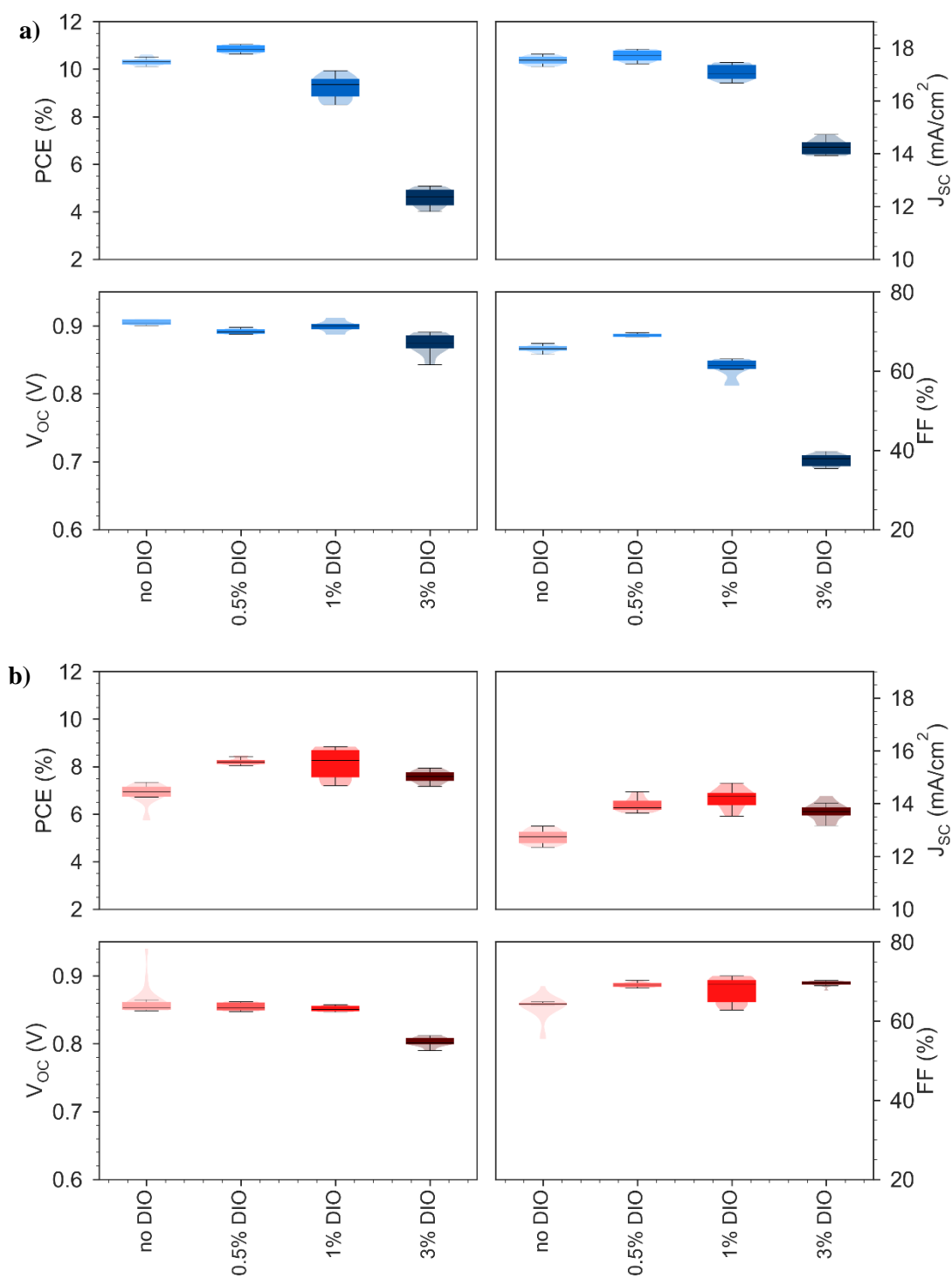


Figure S5.7: Full box plots for the champion device run given in the main text. Each box represents 10 devices. **a)** PBDB-T:ITIC, **b)** PBDB-T:PC₇₀BM.

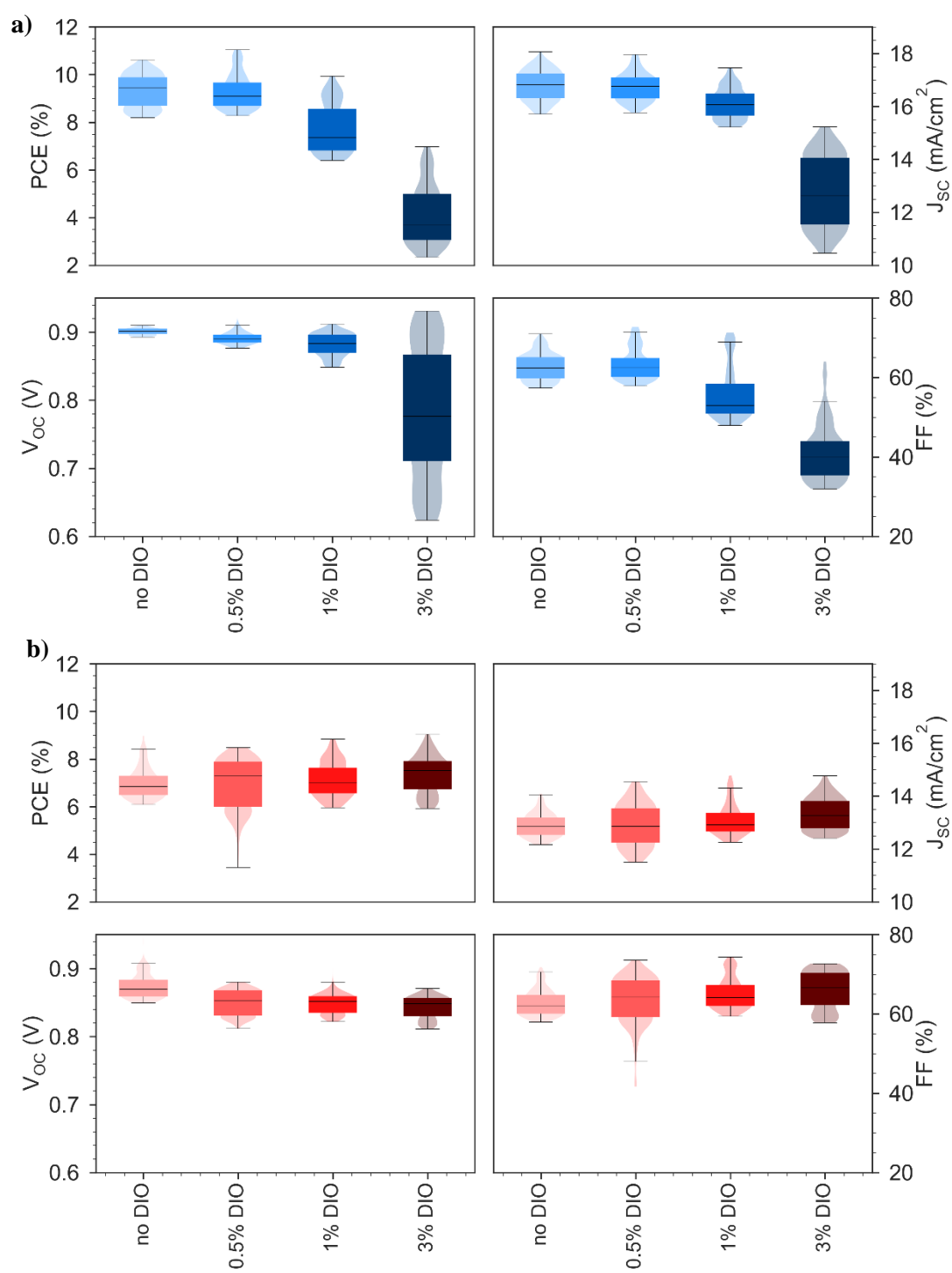


Figure S5.8: Full box plots for all device runs, representing 150 devices for each box. **a)** PBDB-T:ITIC, **b)** PBDB-T:PC₇₀BM.

Table S5.4: Integrated EQE values for the EQE graphs shown in the main text.

System	Initially tested J_{SC} (mA cm^{-2})	Integrated J_{SC} from EQE (mA cm^{-2})
PBDB-T:ITIC no DIO	17.1	16.5
PBDB-T:ITIC + 0.5% DIO	17.1	16.0
PBDB-T:ITIC + 1% DIO	16.2	15.4
PBDB-T:ITIC + 3% DIO	12.5	12.3
PBDB-T:PC ₇₀ BM no DIO	13.5	12.6
PBDB-T:PC ₇₀ BM + 0.5% DIO	12.8	11.8
PBDB-T:PC ₇₀ BM + 1% DIO	13.5	13.3
PBDB-T:PC ₇₀ BM + 3% DIO	13.0	12.0

5.7.4 NMR

5.7.4.1 Supporting ^1H NMR spectra

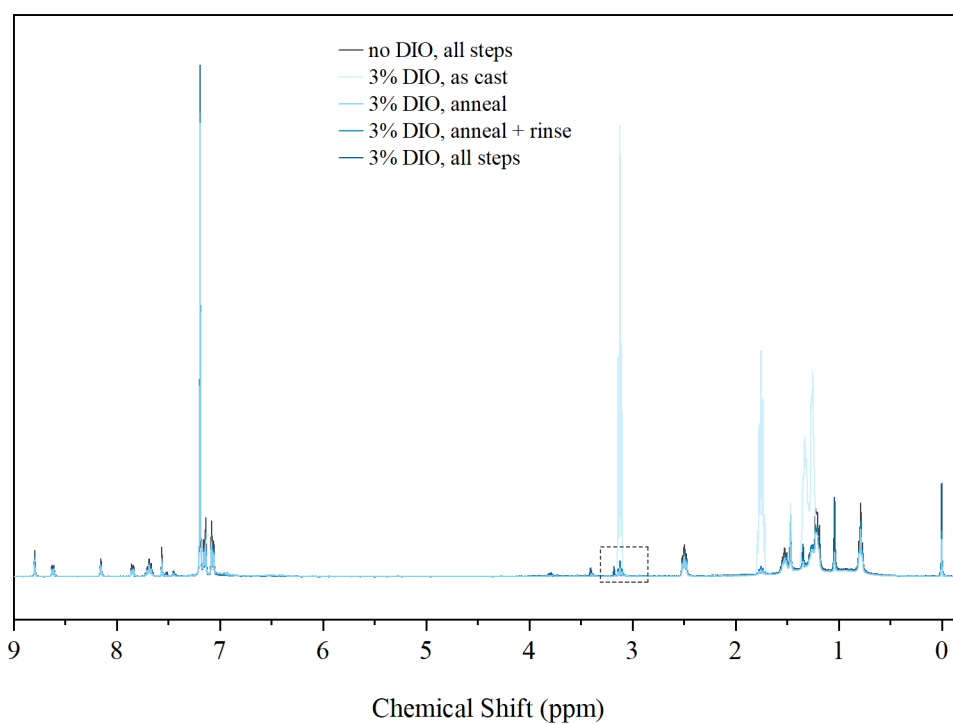


Figure S5.9: ^1H NMR spectra of PBDB-T:ITIC films after various processing steps. Here 'all steps' refers to films that have been treated with an anneal, methanol rinse and high vacuum step. Box represents the area shown in zoomed in main text figures.

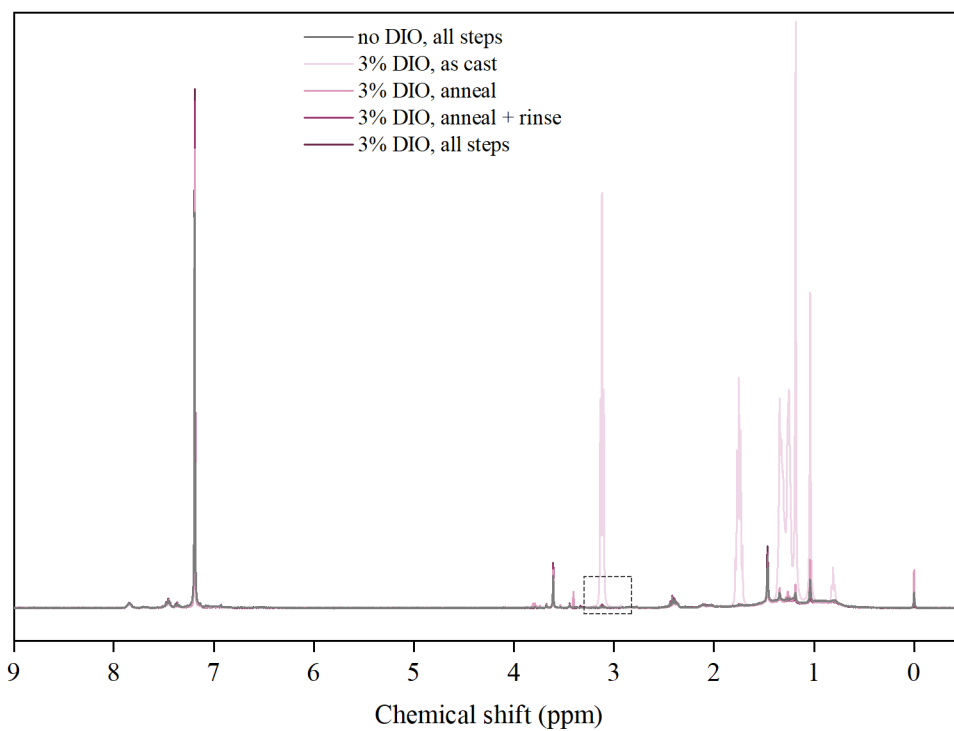


Figure S5.10: Spectra of PBDB-T:PC₇₀BM films after various processing steps. Here ‘all steps’ refers to films that have been treated with an anneal, methanol rinse and high vacuum step. Box represents the area shown in zoomed in main text figures.

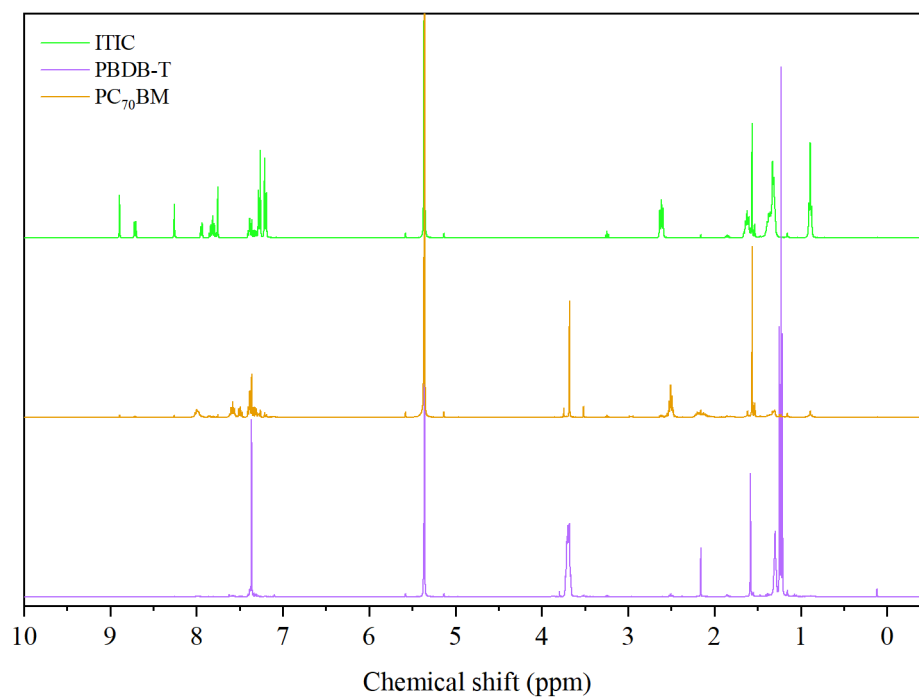


Figure S5.11: Component ^1H NMR spectra. Curves vertically offset for clarity.

5.7.4.2 Ratio Calculation Details

Work by Jacobs *et al.*¹⁴ used the ratio of peak integration areas of shifts belonging to DIO and the acceptor to compare DIO content between samples. In our work, PBDB-T does not have any peaks that are well-separated enough from the acceptor molecules in order to use this, so ITIC and PC₇₀BM are used in their respective blends. The peaks that were integrated for these ratios can be seen below. Jacobs' work notes that any well-separated, unique peak can be used, and the ratio will be the same:

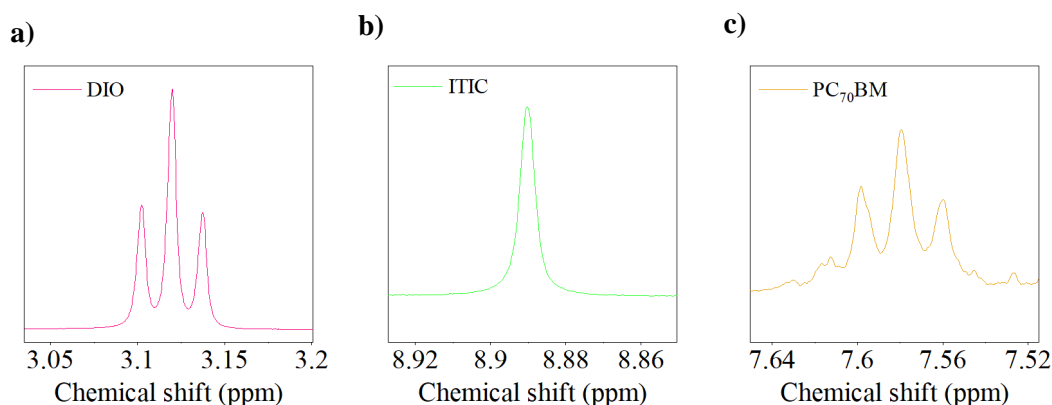


Figure S5.12: Peaks integrated to compare DIO contents.

As peak integration area is considered proportional to molar concentration, we therefore must consider the differences between ITIC and PC₇₀BM. The PBDB-T:PC₇₀BM films are prepared at a lower solid concentration than that of PBDB-T:ITIC (15 mg/mL compared to 18 mg/mL), as this is optimised for device performance. This means the films will contain less mass of PC₇₀BM, if it is assumed that the same volume of ink forms the wet film. The molecular weights of ITIC and PC₇₀BM are also different (1423 g/mol compared to 1031 g/mol), and as a result their moles from equivalent mass. These differences in molar concentration can be summarised as:

$$\frac{ITIC \frac{\text{mol}}{\text{mL}}}{PCBM \frac{\text{mol}}{\text{mL}}} = \frac{\left(\frac{0.009 \frac{\text{g}}{\text{mL}}}{1423 \frac{\text{g}}{\text{mol}}} \right)}{\left(\frac{0.0075 \frac{\text{g}}{\text{mL}}}{1031 \frac{\text{g}}{\text{mol}}} \right)} = 0.87 \quad (\text{Eq. S5.1})$$

Here, the mass concentration used is half that of the solution as all inks are made in a 1:1 donor:acceptor ratio. From this relation, we know in a given volume there are less moles of ITIC than PC₇₀BM. This means that the same moles of DIO in a solution will yield a higher DIO:Acceptor ratio for ITIC than PC₇₀BM. As a result, all ratios obtained for PC₇₀BM films are corrected to obtain moles of DIO that can be compared to the ITIC films:

$$\text{moles DIO:ITIC} = \frac{\text{moles DIO:PCBM}}{0.87} \quad (\text{Eq. S5.2})$$

The results of the corrected integrations can be seen in the main text, and are summarised below.

Table S5.5: Corrected DIO:Acceptor molar concentration

Conditions	DIO:Acceptor for PBDB-T:ITIC	DIO:Acceptor for PBDB-T:PC ₇₀ BM
No DIO, all steps	0.57	0.15
3% DIO, as cast	43.5	43.0
3% DIO, annealed	1.22	0.16
3% DIO, annealed + rinse	1.61	0.25
3% DIO, all steps	1.37	0.14

Support for the validity of this method can be found in the very similar ratios for the two blends with 3% DIO and no other processing steps. Here an identical volume will have been used to form each film, and the same number of films used to fabricate the NMR solution, and as such the moles of DIO should be identical.

5.7.5 Contact Angle Data

Contact angles of water and hexadecane on the blends, and their components, can be found in **Table S5.6**.

Table S5.6: Contact angle measurements, and their corresponding surface energy values. Values given ± 1 standard deviation for two measurements.

System	DIO Content	Water contact angle (°)	Hexadecane contact angle (°)	Surface Energy, γ (mN m ⁻¹)
PBDB-T	/	103 \pm 3.6	31 \pm 1.1	24.3 \pm 0.4
ITIC	/	99 \pm 2.7	23 \pm 0.7	26.5 \pm 0.4
PC ₇₀ BM	/	97 \pm 5.0	19 \pm 1.1	27.5 \pm 0.8
PBDB-T:ITIC	0	101 \pm 0.2	20 \pm 0.0	26.4 \pm 0.0
	0.5	102 \pm 2.5	25 \pm 1.0	25.7 \pm 0.3
	1	109 \pm 2.0	22 \pm 1.0	25.5 \pm 0.1
	3	112 \pm 1.5	25 \pm 1.0	25.1 \pm 0.2
PBDB-T:PC ₇₀ BM	0	104 \pm 1.4	28 \pm 2.8	24.9 \pm 0.5
	0.5	105 \pm 2.3	19 \pm 2.1	26.2 \pm 0.3
	1	106 \pm 4.8	23 \pm 0.7	25.6 \pm 0.3
	3	106 \pm 1.5	23 \pm 0.4	25.6 \pm 0.1

Here, surface energy was calculated via Fowkes' equation:⁴⁰

$$\sqrt{\sigma_l^D \sigma_s^D} + \sqrt{\sigma_l^P \sigma_s^P} = \frac{\sigma_l(1 + \cos\theta)}{2} \quad (\text{Eq. S5.3})$$

Where σ^D and σ^P are the dispersive and polar components of the surface energy, and σ_l and σ_s represent the liquid and solid respectively, with θ being the contact angle of the liquid on the solid (in radians). The values for our liquids can be seen in **Table S5.7**.

Table S5.7: Surface tension components for the liquids used.

Liquid	σ_l^D (mN m ⁻¹)	σ_l^P (mN m ⁻¹)	Total σ_l (mN m ⁻¹)
Water	21.8	51	72.8
Hexadecane	27.5	0	27.5

By using a liquid with a purely dispersive component, such as hexadecane, Fowkes' equation can be reduced to:

$$\sigma_s^D = \frac{\sigma_l(1 + \cos\theta)^2}{4} \quad (\text{Eq. S5.4})$$

Following the calculation of the dispersive component of the test solid using the contact angle of hexadecane, the contact angle and known surface tensions of water can be inserted into **Eq. S5.3**, to obtain the polar component. The total surface energy of the film is then:

$$\sigma_s = \sigma_s^D + \sigma_s^P \quad (\text{Eq. S5.5})$$

5.7.6 Dark Device Stability

5.7.6.1 Device parameters

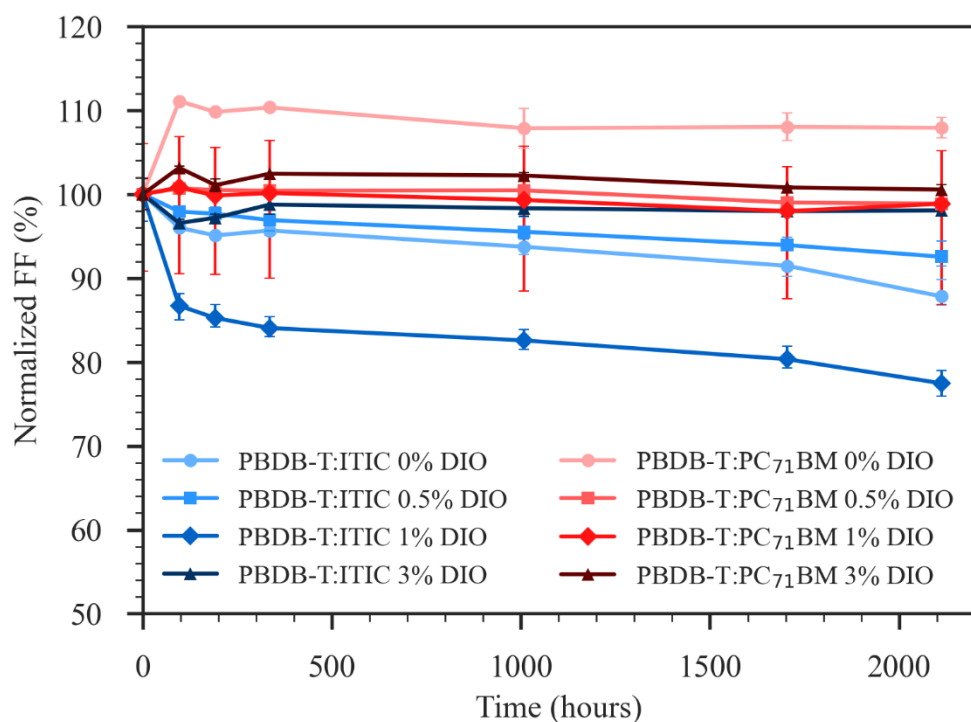


Figure S5.13: Fill factor over time for devices stored in the dark in an inert atmosphere. Markers represent the average of at least two devices, with minimum and maximum values given by the error bars.

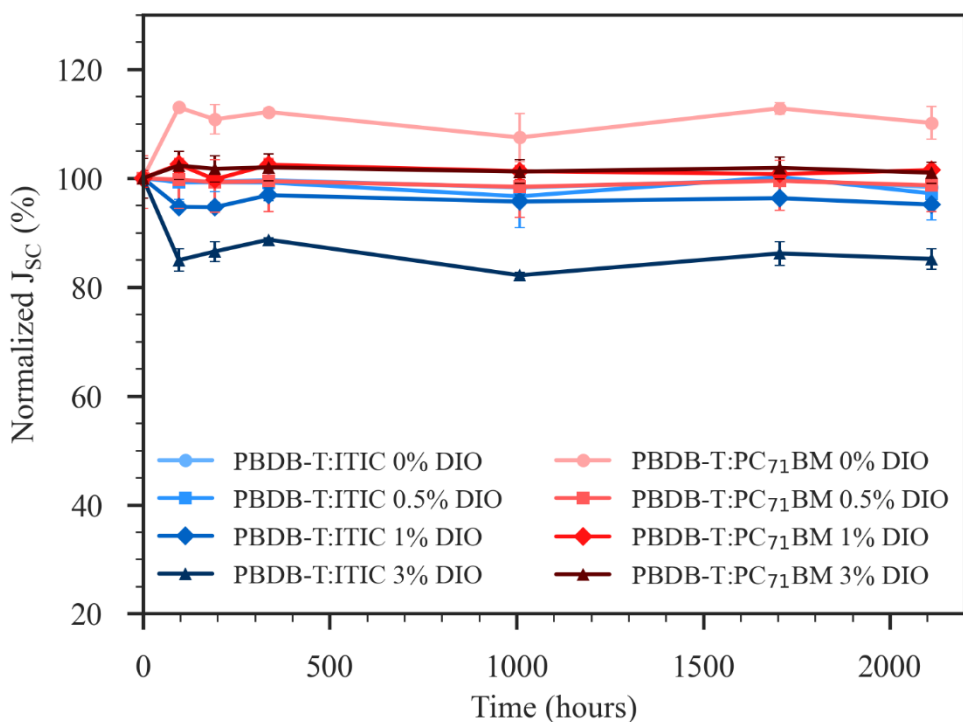


Figure S5.14: Short circuit current density over time for devices stored in the dark in an inert atmosphere. Markers represent the average of at least two devices, with minimum and maximum values given by the error bars.

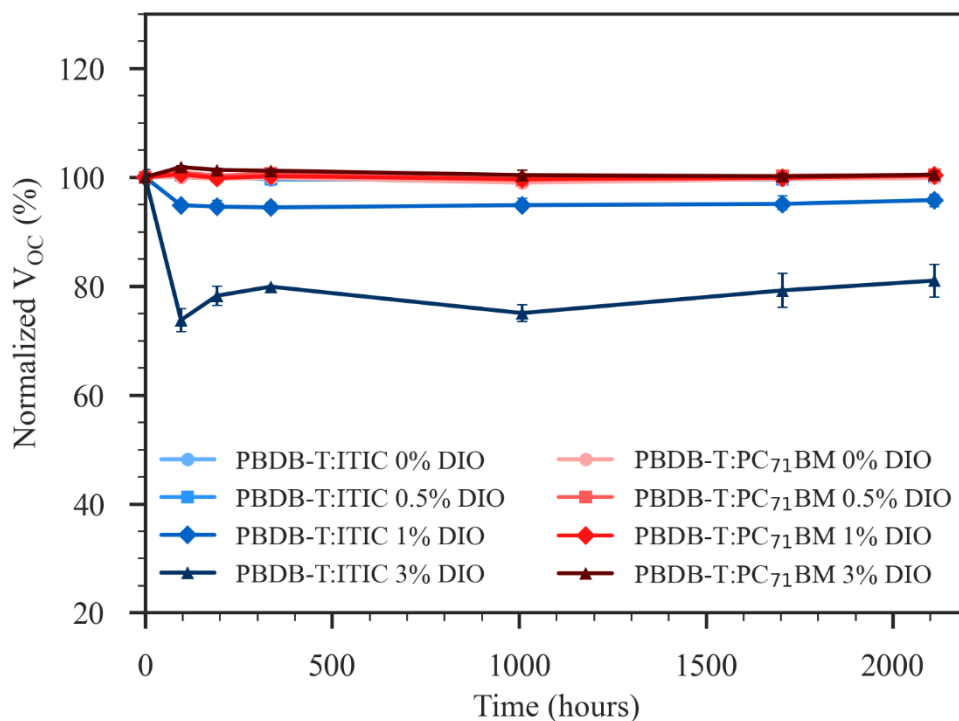


Figure S5.15: Open circuit voltage over time for devices stored in the dark in an inert atmosphere. Markers represent the average of at least two devices, with minimum and maximum values given by the error bars.

5.7.6.2 JV curves over time for PCBM blends

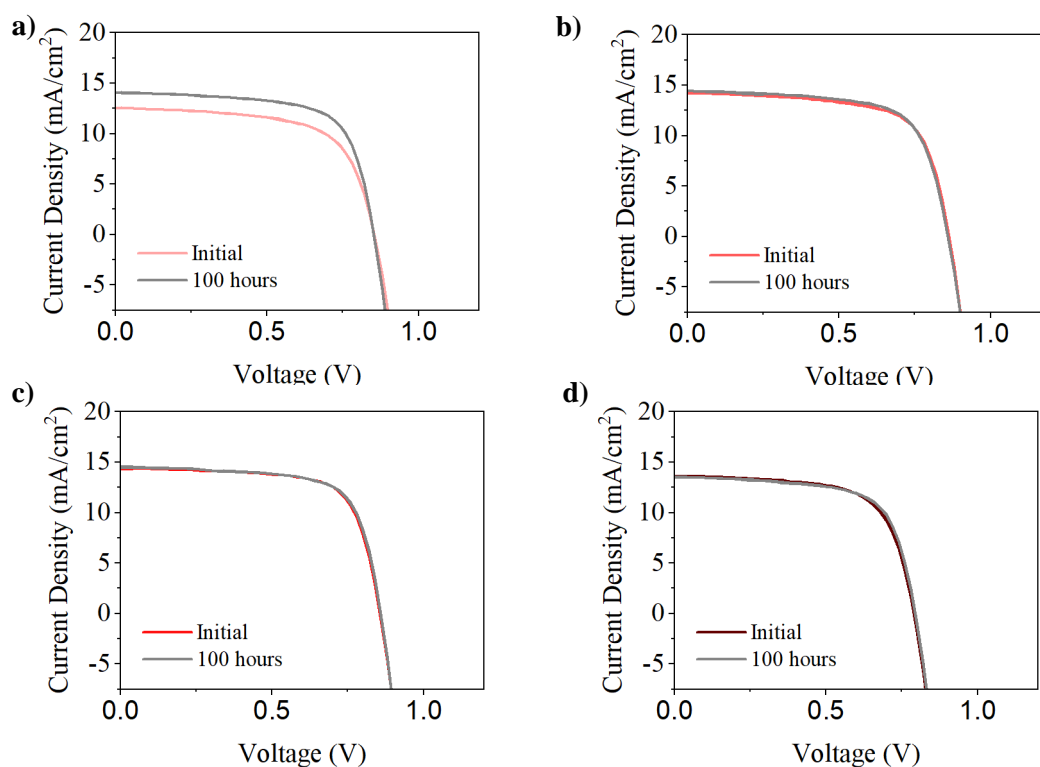


Figure S5.16: JV curves over time for PBDB-T:PC₇₀BM devices, stored in the dark in an inert atmosphere. **a)** no DIO, **b)** 0.5% DIO, **c)** 1% DIO, **d)** 3% DIO.

5.7.6.3 Absorption over time

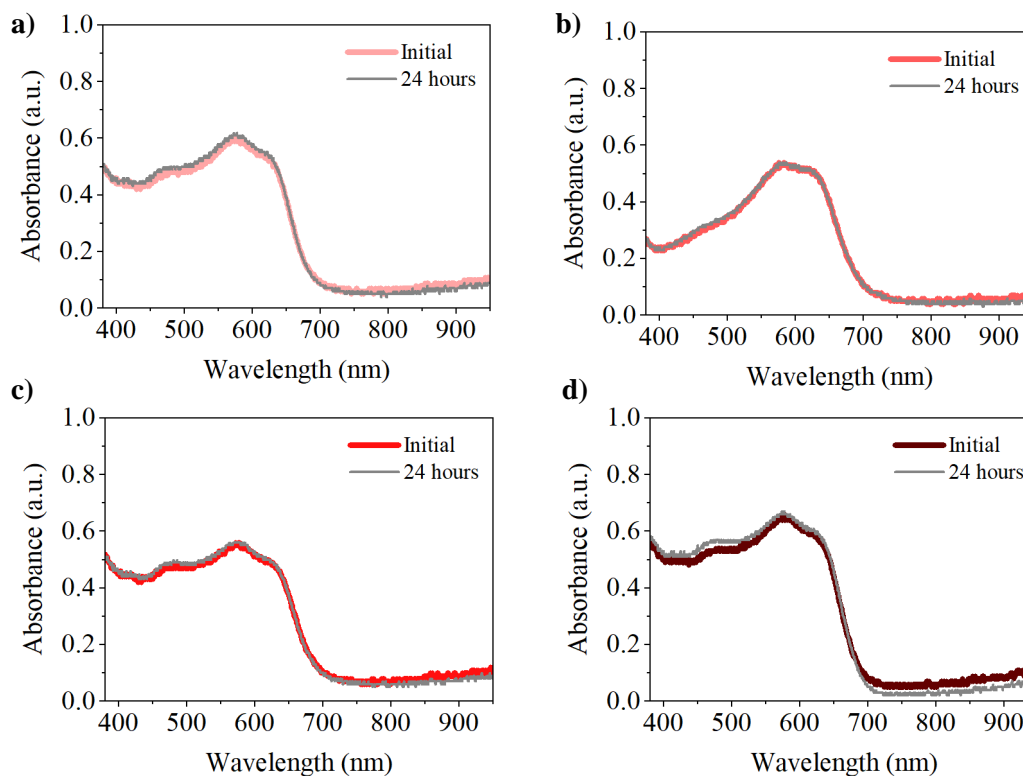


Figure S5.17: UV-Vis absorption of PBDB-T:PC₇₀BM films, before and after storage in the dark, in an inert atmosphere. **a)** no DIO, **b)** 0.5% DIO, **c)** 1% DIO, **d)** 3% DIO.

5.7.7 Illuminated Device Stability

5.7.7.1 Device Parameters

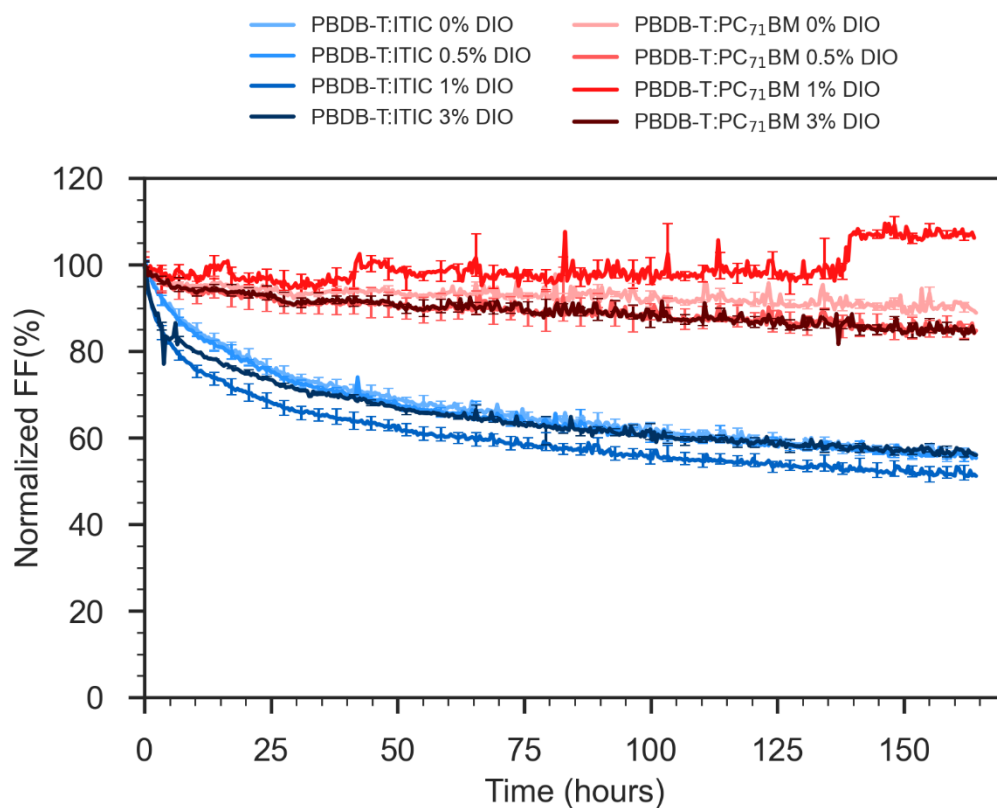


Figure S5.18: Fill factor over time for encapsulated devices illuminated in air. Line represents the average of at least two pixels, with the error bars representing the minimum and maximum values, displayed every 10 points.

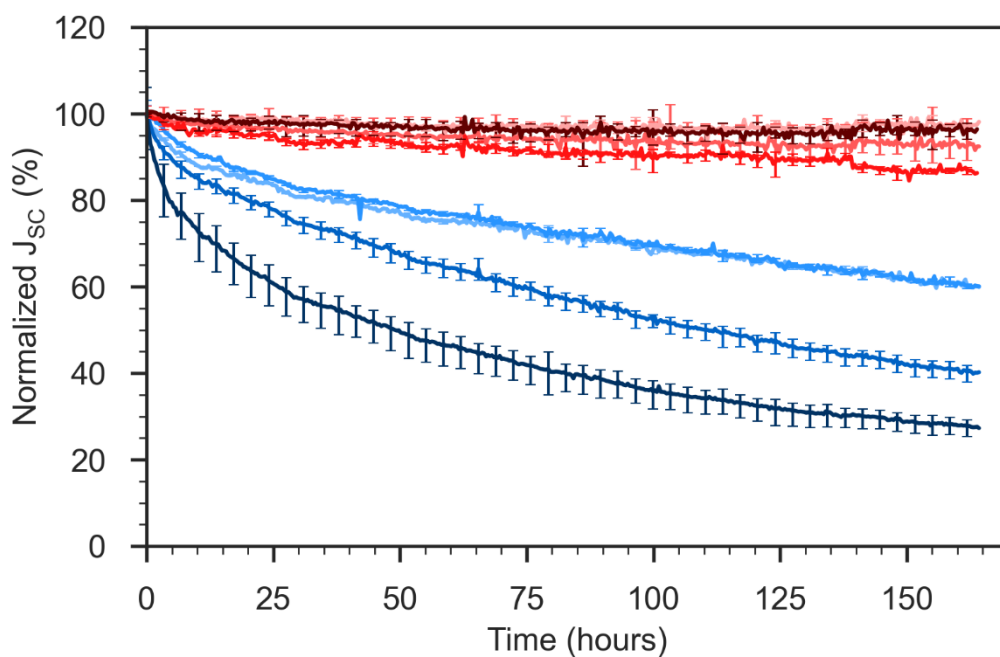


Figure S5.19: Short circuit current density over time for encapsulated devices illuminated in air. Line represents the average of at least two pixels, with the error bars representing the minimum and maximum values, displayed every 10 points. Legend as above.

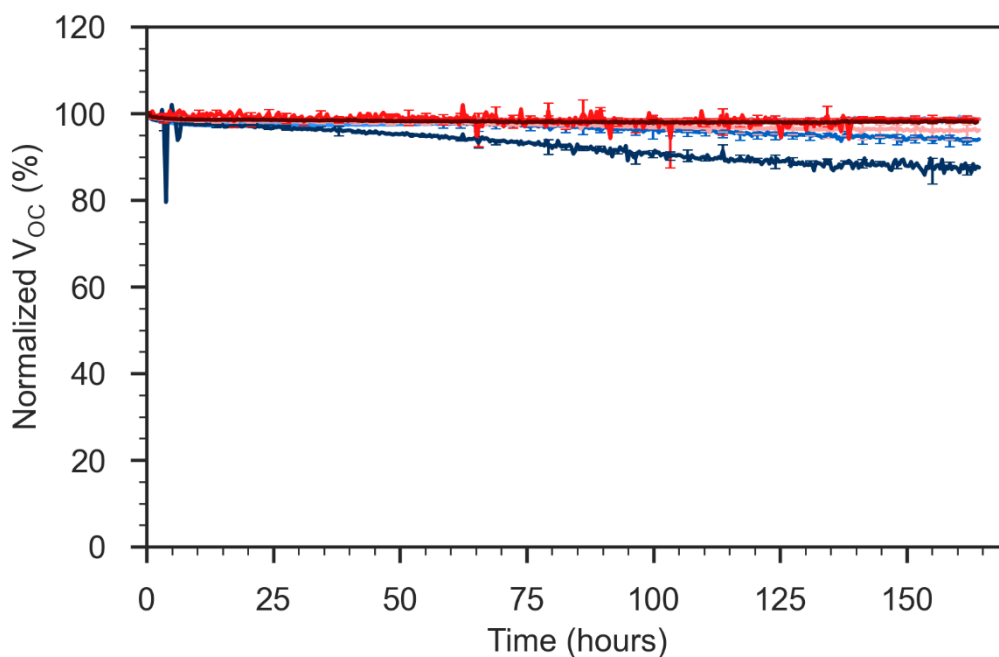


Figure S5.20: Open circuit voltage over time for encapsulated devices illuminated in air. Line represents the average of at least two pixels, with the error bars representing the minimum and maximum values, displayed every 10 points. Legend as above.

5.7.7.2 Heated devices

In order to replicate the heat under illumination, the temperature inside our lifetime tester was tracked using an Arduino temperature sensor, shown in **Figure S5.21**. An average temperature of 43°C was then used to heat devices without illumination.

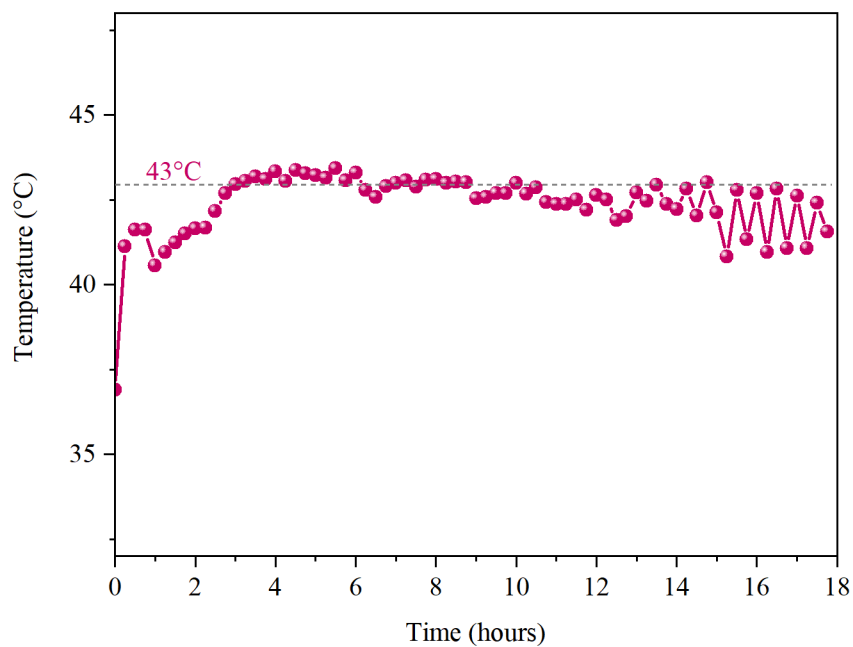


Figure S5.21: Temperature over time inside the lifetime tester used for illuminated measurements, tracked using an arduino and temperature sensor.

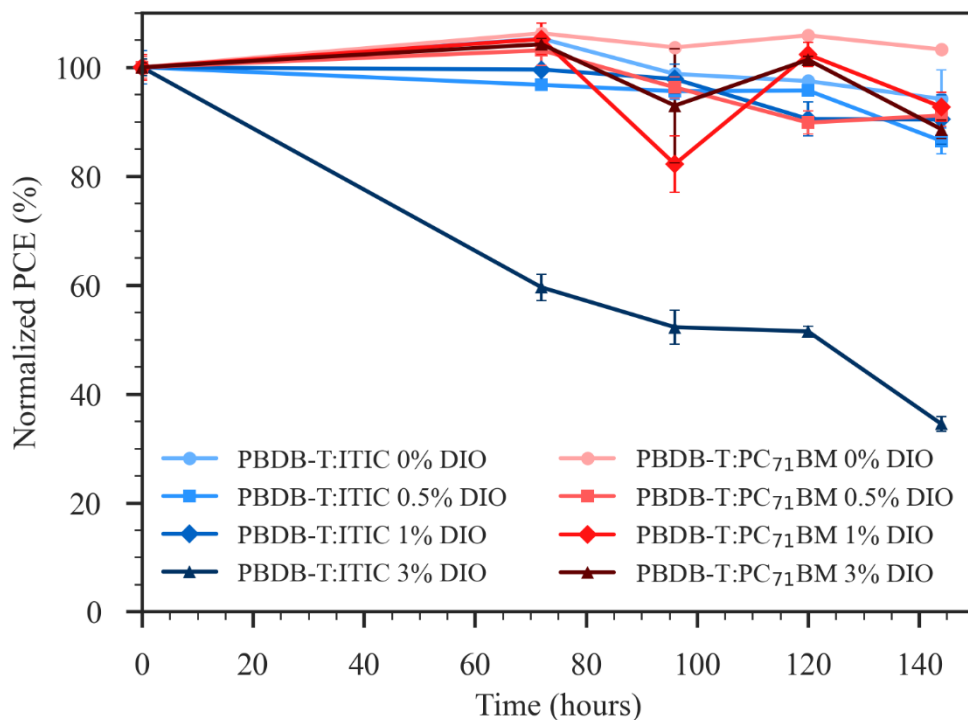


Figure S5.22: Power conversion efficiency over time for encapsulated devices heated in the dark in air. Markers represent the average of at least two pixels, with the error bars representing the minimum and maximum values.

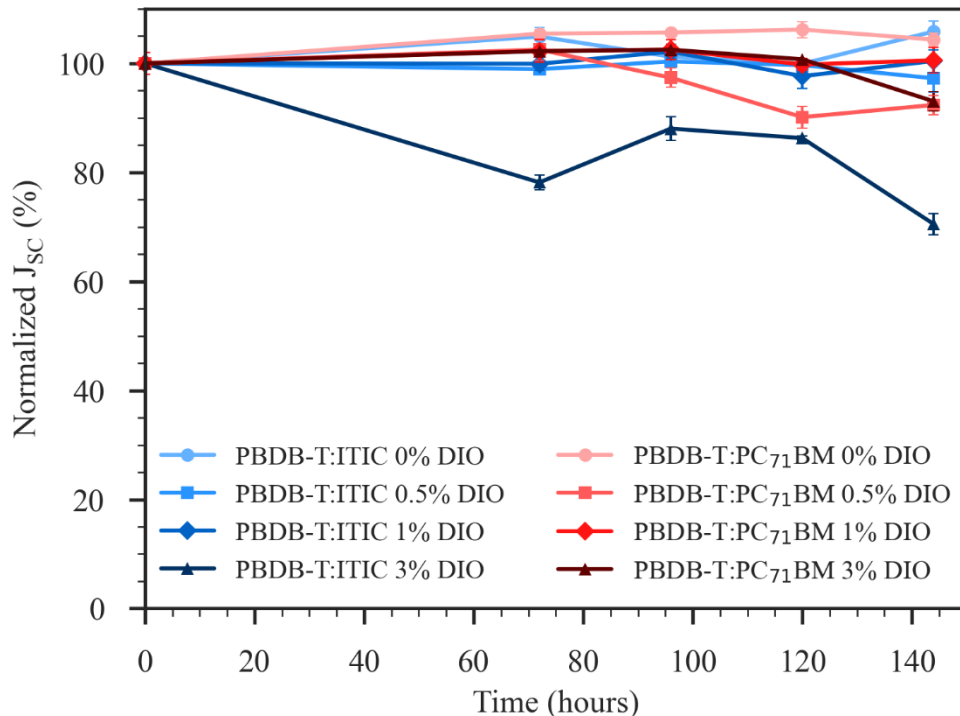


Figure S5.23: Short circuit current density over time for encapsulated devices heated in the dark in air. Markers represent the average of at least two pixels, with the error bars representing the minimum and maximum values.

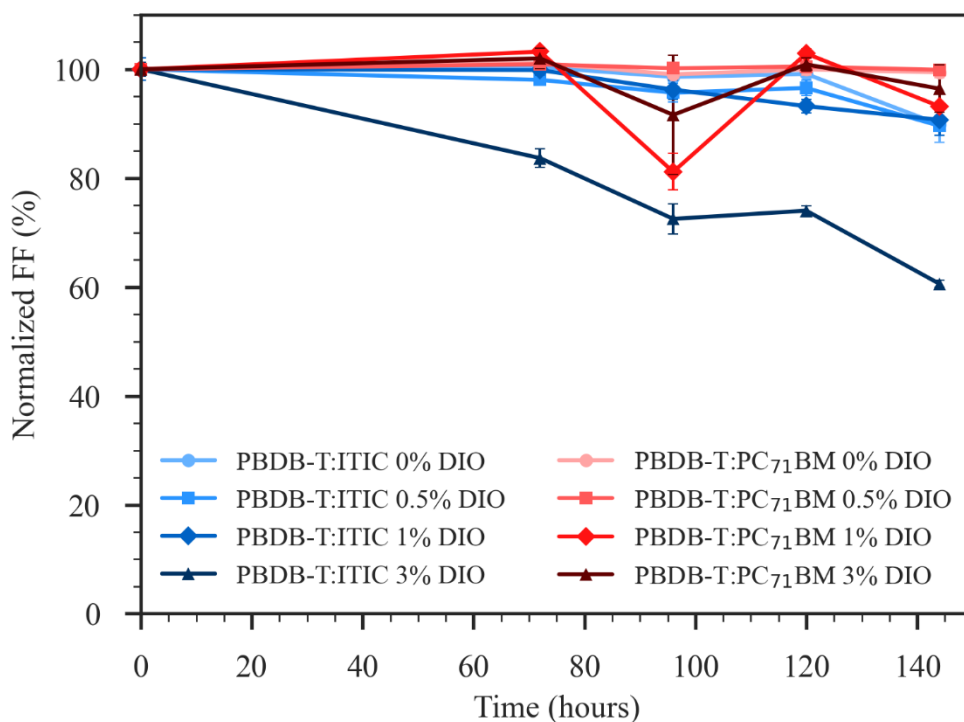


Figure S5.24: Fill factor over time for encapsulated devices heated in the dark in air. Markers represent the average of at least two pixels, with the error bars representing the minimum and maximum values.

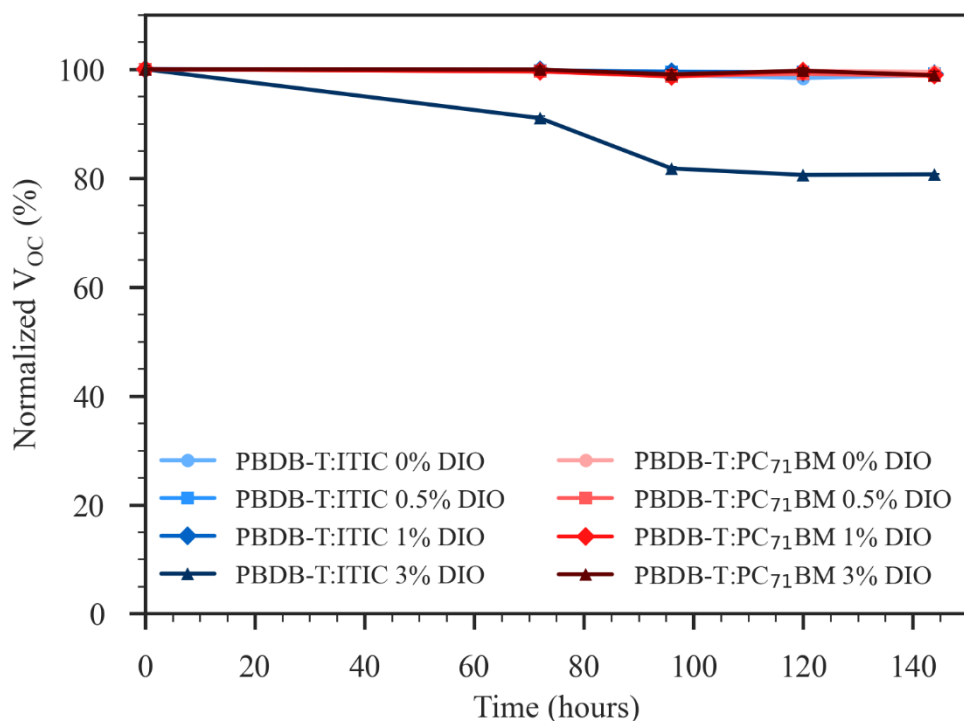


Figure S5.25: Open circuit voltage over time for encapsulated devices heated in the dark in air. Markers represent the average of at least two pixels, with the error bars representing the minimum and maximum values.

5.7.7.3 Un-encapsulated devices

Un-encapsulated devices were manufactured and illuminated in the same manner as the encapsulated devices shown in the main text. Here the rapid and severe degradation leads to relatively noisy data.

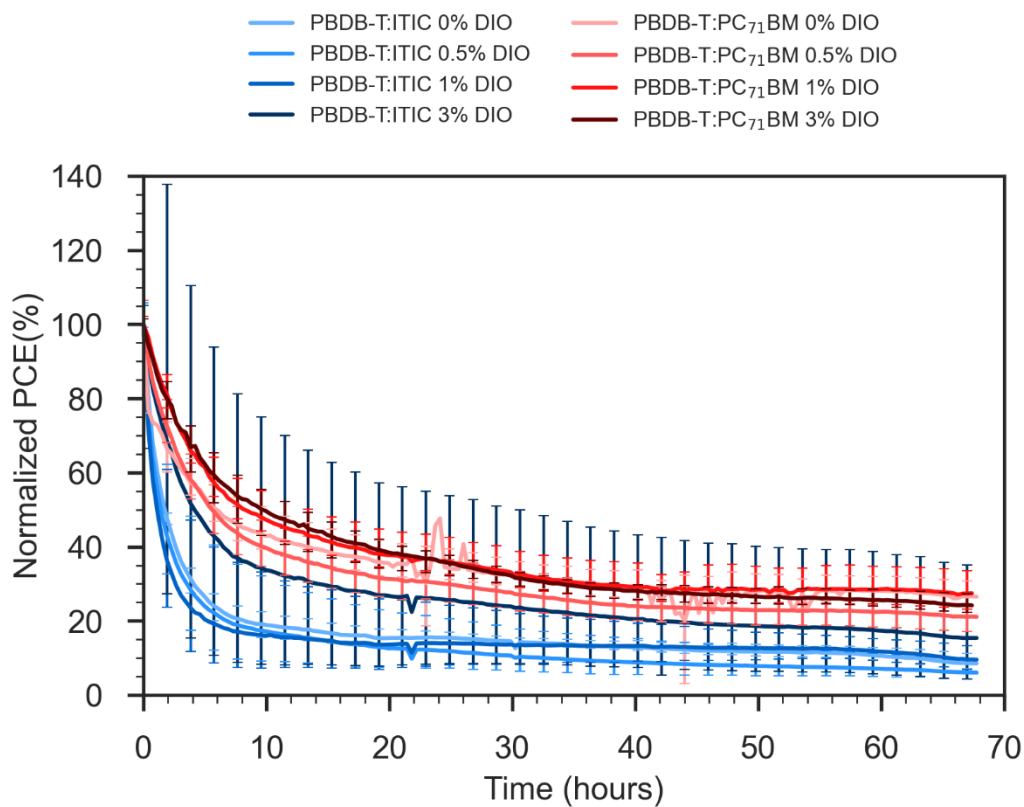


Figure S5.26: Power conversion efficiency over time for un-encapsulated devices illuminated in air. Line represents the average of at least two pixels, with the error bars representing the minimum and maximum values, displayed every 5 points.

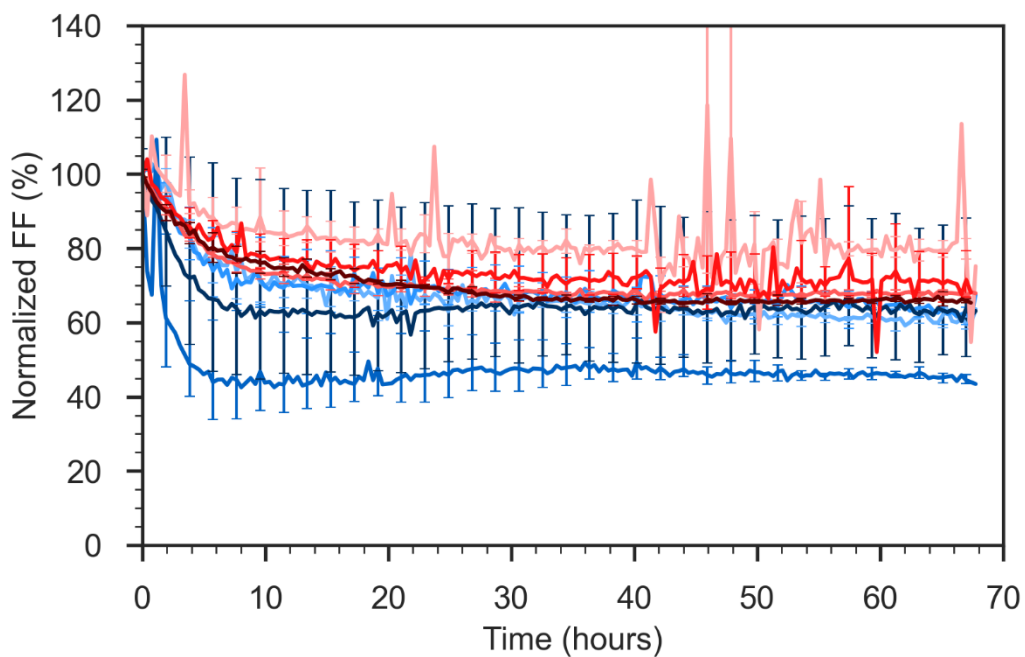


Figure S5.27: Fill factor over time for un-encapsulated devices illuminated in air. Line represents the average of at least two pixels, with the error bars representing the minimum and maximum values, displayed every 5 points. Legend as above.

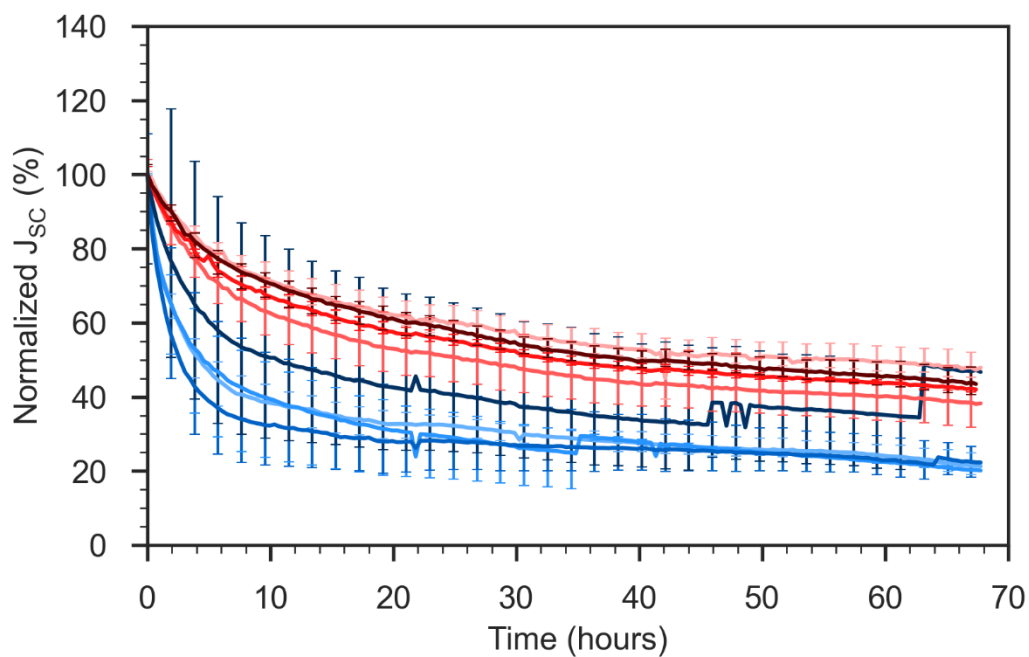


Figure S5.28: Short circuit density over time for un-encapsulated devices illuminated in air. Line represents the average of at least two pixels, with the error bars representing the minimum and maximum values, displayed every 5 points. Legend as above.

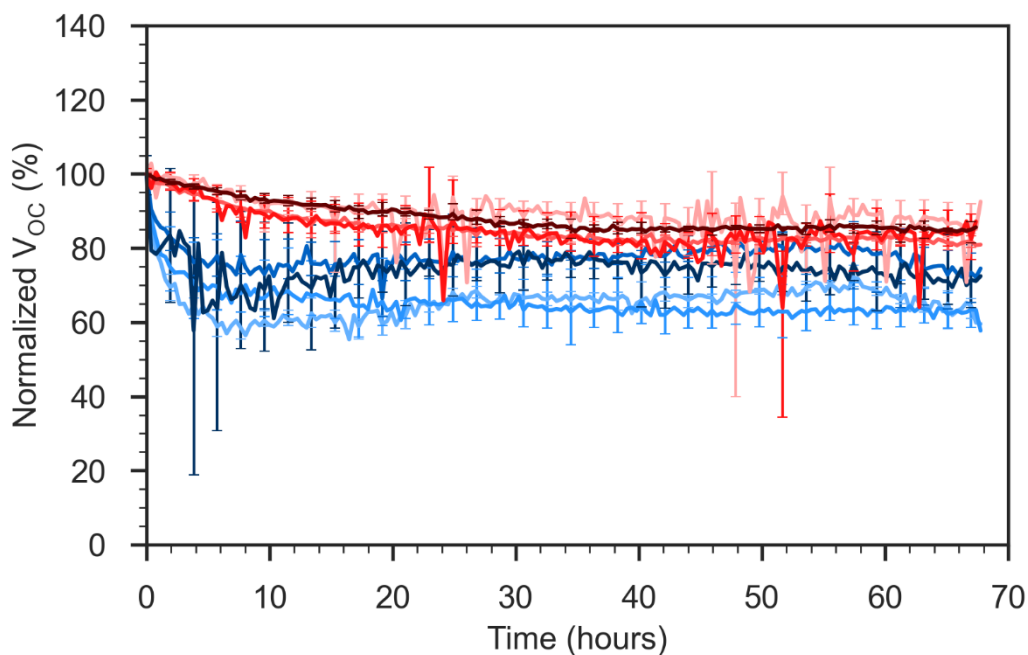


Figure S5.29: Open circuit voltage over time for un-encapsulated devices illuminated in air. Line represents the average of at least two pixels, with the error bars representing the minimum and maximum values, displayed every 5 points. Legend as above.

5.7.7.4 JV Curves over time

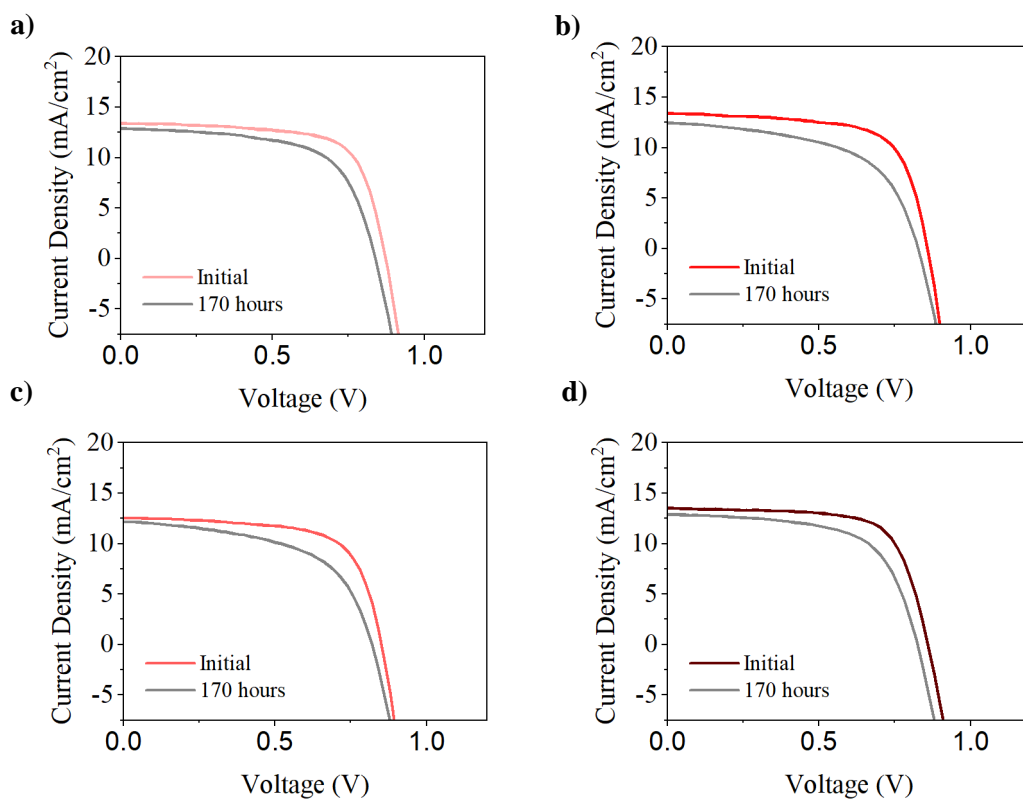


Figure S5.30: JV curves over time for encapsulated, illuminated devices. PBDB-T:PC₇₀BM with a) no DIO, b) 0.5% DIO, c) 1% DIO, d) 3% DIO. Before and after the illumination period.

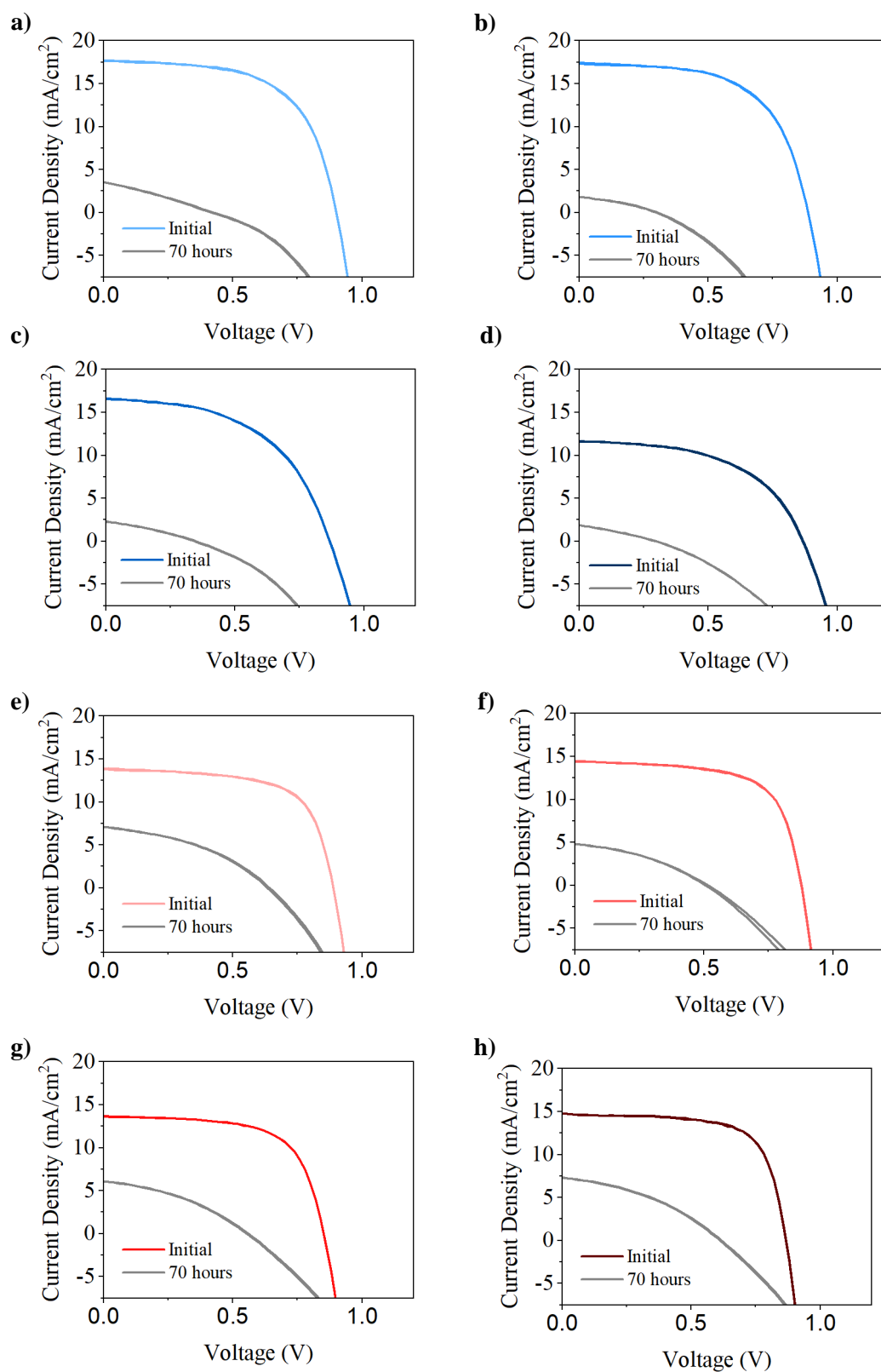


Figure S5.31 JV curves over time for un- encapsulated devices heated in air. PBDB-T:ITIC with **a)** no DIO, **b)** 0.5% DIO, **c)** 1% DIO, **d)** 3% DIO. PBDB-T:PC₇₀BM with **a)** no DIO, **b)** 1% DIO, **c)** 1% DIO, **d)** 3% DIO. Before and after the illumination period.

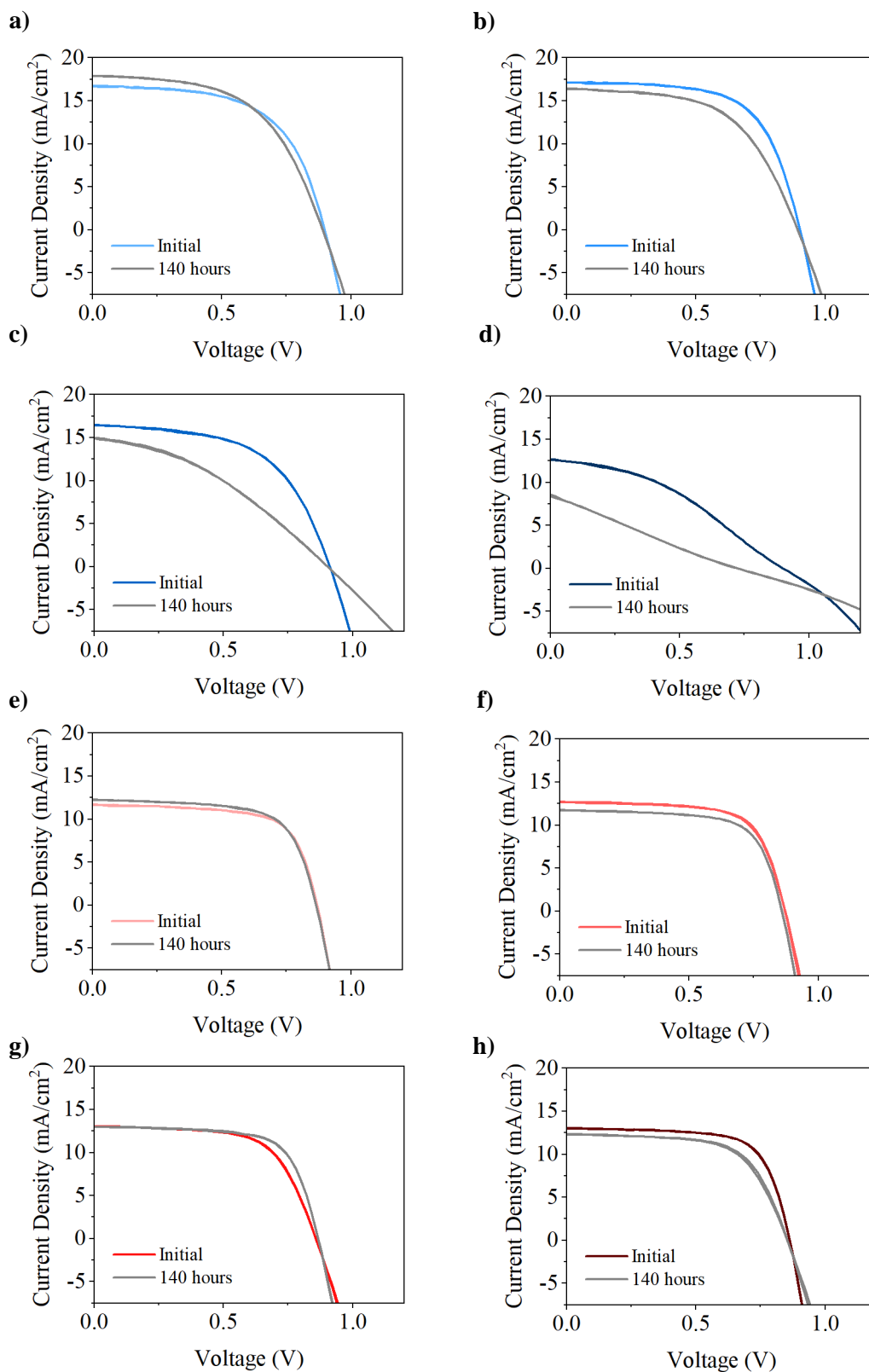


Figure S5.32: *JV curves over time for encapsulated devices heated in the dark, in air. PBDB-T:ITIC with a) no DIO, b) 0.5% DIO, c) 1% DIO, d) 3% DIO. PBDB-T:PC₇₀BM with a) no DIO, b) 1% DIO, c) 1% DIO, d) 3% DIO. Before and after the heating period.*

5.8 References

1. Lin, Y. *et al.* An electron acceptor challenging fullerenes for efficient polymer solar cells. *Adv Mater* **27**, 1170–1174 (2015).
2. Cui, Y. *et al.* Single-Junction Organic Photovoltaic Cell with 19% Efficiency. *Adv. Mater.* **33**, 2102420 (2021).
3. Hou, J., Inganäs, O., Friend, R. H. & Gao, F. Organic solar cells based on non-fullerene acceptors. *Nat. Mater.* **17**, 119–128 (2018).
4. Yuan, J. *et al.* Single-Junction Organic Solar Cell with over 15% Efficiency Using Fused-Ring Acceptor with Electron-Deficient Core. *Joule* **3**, 1140–1151 (2019).
5. Zeng, Y. *et al.* Exploring the Charge Dynamics and Energy Loss in Ternary Organic Solar Cells with a Fill Factor Exceeding 80%. *Adv. Energy Mater.* **11**, 2101338 (2021).
6. Qin, Y. *et al.* The performance-stability conundrum of BTP-based organic solar cells. *Joule* **5**, 2129–2147 (2021).
7. Duan, L. & Uddin, A. Progress in Stability of Organic Solar Cells. *Adv. Sci.* **7**, 1903259 (2020).
8. Ghasemi, M. *et al.* Delineation of Thermodynamic and Kinetic Factors that Control Stability in Non-fullerene Organic Solar Cells. *Joule* **3**, 1328–1348 (2019).
9. Guo, J. *et al.* Suppressing photo-oxidation of non-fullerene acceptors and their blends in organic solar cells by exploring material design and employing friendly stabilizers. *J. Mater. Chem. A* **7**, 25088–25101 (2019).
10. Zhang, Y. *et al.* Understanding and controlling morphology evolution via DIO plasticization in PffBT4T-2OD/PC 71 BM devices. *Sci. Rep.* **7**, 1–12 (2017).
11. Song, X. *et al.* Controlling Blend Morphology for Ultrahigh Current Density in Nonfullerene Acceptor-Based Organic Solar Cells. *ACS Energy Lett.* **3**, 669–676 (2018).
12. Zhao, W., Zhang, S. & Hou, J. Realizing 11.3% efficiency in fullerene-free polymer solar cells by device optimization. *Sci. China Chem.* **59**, 1574–1582 (2016).
13. Song, X., Gasparini, N. & Baran, D. The Influence of Solvent Additive on Polymer Solar Cells Employing Fullerene and Non-Fullerene Acceptors. *Adv. Electron. Mater.* **4**, 1–7 (2018).
14. Jacobs, I. E. *et al.* Photoinduced degradation from trace 1,8-diiodooctane in organic photovoltaics. *J. Mater. Chem. C* **6**, 219–225 (2018).
15. Doumon, N. Y. *et al.* 1,8-Diiodooctane Acts As a Photo-Acid in Organic Solar Cells. *Sci. Rep.* **9**, 1–14 (2019).
16. Tremolet De Villers, B. J. *et al.* Removal of Residual Diiodooctane Improves Photostability of High-Performance Organic Solar Cell Polymers. *Chem. Mater.* **28**, 876–884 (2016).
17. Classen, A. *et al.* Revealing Hidden UV Instabilities in Organic Solar Cells by Correlating Device and Material Stability. *Adv. Energy Mater.* **9**, 1–11 (2019).
18. Zhao, W. *et al.* Molecular Optimization Enables over 13% Efficiency in Organic Solar Cells. *J. Am. Chem. Soc.* **139**, 7148–7151 (2017).
19. Clarke, A. J. *et al.* Non-fullerene acceptor photostability and its impact on organic solar cell lifetime. *Cell Reports Phys. Sci.* **2**, 100498 (2021).
20. Wang, L. M. *et al.* Quantitative Determination of the Vertical Segregation and Molecular Ordering of PBDB-T/ITIC Blend Films with Solvent Additives. *ACS Appl. Mater. Interfaces* **12**, 24165–24173 (2020).
21. Li, Q. *et al.* Impact of Donor-Acceptor Interaction and Solvent Additive on the Vertical Composition Distribution of Bulk Heterojunction Polymer Solar Cells. *ACS Appl. Mater. Interfaces* **11**, 45979–45990 (2019).
22. Yang, L. *et al.* Modulating Molecular Orientation Enables Efficient Nonfullerene Small-Molecule Organic Solar Cells. *Chem. Mater.* **30**, 2129–2134 (2018).
23. Xin, Y., Zeng, G., Ouyang, J. Y., Zhao, X. & Yang, X. Enhancing thermal stability of nonfullerene organic solar cells: Via fluoro-side-chain engineering. *J. Mater. Chem. C* **7**, 9513–9522 (2019).
24. Mai, J. *et al.* Hidden structure ordering along backbone of fused-ring electron acceptors enhanced by ternary bulk heterojunction. *Adv. Mater.* **30**, 1–8 (2018).
25. Du, X. *et al.* Efficient Polymer Solar Cells Based on Non-fullerene Acceptors with Potential Device Lifetime Approaching 10 Years. *Joule* **3**, 215–226 (2019).
26. Wang, L. M. *et al.* Quantitative Determination of the Vertical Segregation and Molecular Ordering of PBDB-T/ITIC Blend Films with Solvent Additives. *ACS Appl. Mater. Interfaces* **12**, 24165–24173 (2020).
27. Printz, A. D. & Lipomi, D. J. Competition between deformability and charge transport in semiconducting polymers for flexible and stretchable electronics. *Appl. Phys. Rev.* **3**, 021302 (2016).
28. Ye, L. *et al.* Quantitative relations between interaction parameter, miscibility and function in organic solar cells. *Nat. Mater.* **17**, 253–260 (2018).
29. Peng, Z., Ye, L. & Ade, H. Understanding, quantifying, and controlling the molecular ordering of semiconducting polymers: from novices to experts and amorphous to perfect crystals. *Mater. Horizons* **9**, 577–606 (2022).
30. Zhang, T., Zhao, X., Yang, D., Tian, Y. & Yang, X. Ternary Organic Solar Cells with >11% Efficiency Incorporating Thick Photoactive Layer and Nonfullerene Small Molecule Acceptor.

- Adv. Energy Mater.* **8**, 1–9 (2018).
31. Ghasemi, M. *et al.* Delineation of Thermodynamic and Kinetic Factors that Control Stability in Non-fullerene Organic Solar Cells. *Joule* **3**, 1328–1348 (2019).
 32. Yu, L. *et al.* Diffusion-Limited Crystallization: A Rationale for the Thermal Stability of Non-Fullerene Solar Cells. *ACS Appl. Mater. Interfaces* **11**, 21766–21774 (2019).
 33. Wang, T. *et al.* Correlating structure with function in thermally annealed PCDTBT:PC 70BM photovoltaic blends. *Adv. Funct. Mater.* **22**, 1399–1408 (2012).
 34. Yu, Y. Y., Tsai, T. W. & Chen, C. P. Efficient Ternary Organic Photovoltaics Using Two Conjugated Polymers and a Nonfullerene Acceptor with Complementary Absorption and Cascade Energy-Level Alignment. *J. Phys. Chem. C* **122**, 24585–24591 (2018).
 35. Jiang, X. *et al.* Internal nanoscale architecture and charge carrier dynamics of wide bandgap non-fullerene bulk heterojunction active layers in organic solar cells. *J. Mat. Chem. A* **8**, 23628–23636 (2020).
 36. Kumar, A., Sista, S. & Yang, Y. Dipole induced anomalous S-shape I-V curves in polymer solar cells. *J. Appl. Phys.* **105**, 094512 (2009).
 37. Tress, W. *et al.* Imbalanced mobilities causing S-shaped IV curves in planar heterojunction organic solar cells. *Appl. Phys. Lett.* **98**, 8–11 (2011).
 38. Tress, W. & Inganäs, O. Simple experimental test to distinguish extraction and injection barriers at the electrodes of (organic) solar cells with S-shaped current-voltage characteristics. *Sol. Energy Mater. Sol. Cells* **117**, 599–603 (2013).
 39. Jacobs, I. E. *et al.* Photoinduced degradation from trace 1,8-diiodooctane in organic photovoltaics. *J. Mater. Chem. C* **6**, 219–225 (2018).
 40. Fowkes, F. M. ATTRACTIVE FORCES AT INTERFACES. *Ind. Eng. Chem.* **56**, 40–52 (1964).
 41. Vuckovac, M., Latikka, M., Liu, K., Huhtamäki, T. & Ras, R. H. A. Uncertainties in contact angle goniometry. *Soft Matter* **15**, 7089–7096 (2019).
 42. Cao, B. *et al.* Role of Interfacial Layers in Organic Solar Cells: Energy Level Pinning versus Phase Segregation. *ACS Appl. Mater. Interfaces* **8**, 18238–18248 (2016).
 43. Xiao, J. *et al.* An Operando Study on the Photostability of Nonfullerene Organic Solar Cells. *Sol. RRL* **3**, 1900077 (2019).
 44. Zhang, Y. *et al.* Understanding and controlling morphology evolution via DIO plasticization in PffBT4T-2OD/PC 71 BM devices. *Sci. Rep.* **7**, 1–12 (2017).
 45. Wang, Y. *et al.* Stability of Nonfullerene Organic Solar Cells: from Built-in Potential and Interfacial Passivation Perspectives. *Adv. Energy Mater.* **9**, 1–9 (2019).
 46. Zhang, Y. *et al.* Thermally Stable All-Polymer Solar Cells with High Tolerance on Blend Ratios. *Adv. Ener. Mater.* **8**, 1800029 (2018).
 47. Lee, H. K. H. *et al.* The role of fullerenes in the environmental stability of polymer:fullerene solar cells. *Energy Environ. Sci.* **11**, 417–428 (2018).
 48. Doumon, N. Y. *et al.* Photostability of Fullerene and Non-Fullerene Polymer Solar Cells: The Role of the Acceptor. *ACS Appl. Mater. Interfaces* **11**, 8310–8318 (2019).
 49. Clarke, A. J. *et al.* Non-fullerene acceptor photostability and its impact on organic solar cell lifetime. *Cell Reports Phys. Sci.* **2**, 100498 (2021).

Chapter 6 | Examining the Driving Factors of Positive Burn-in in Organic Photovoltaics

6.1 Author Contributions

In this chapter the grazing incidence wide angle X-ray scattering was carried out and processed by Rachel Kilbride. The differential scanning calorimetry was carried out by Joe Gaunt. Elena Cassella advised on the interpretation of Flory-Huggins parameter results. All other experimental work and interpretation is my own.

6.2 Abstract

As organic photovoltaics efficiencies rise, their operational stability is becoming increasingly important. It is well established that the morphological stability of a bulk heterojunction is influenced by both thermodynamic factors, such as donor acceptor miscibility, together with kinetic factors, such as the glass transition temperature of components. Whilst many high performing systems exhibit poor morphological stability, some systems increase in performance over time, known as ‘positive burn-in’. Here, the factors driving this positive burn-in are examined for a range of PTB7-Th based systems and explained in terms of miscibility and crystallization temperature. Several methods are used to study the characteristics of the acceptors, and it is shown that interactions between donor and acceptor can differ for even closely structurally related analogues.

6.3 Introduction

As OPV efficiencies continue to improve, issues with long-term stability remain a key obstacle to large-scale commercialisation.¹ A number of factors can contribute to degradation, but those that occur without extrinsic drivers are the most important to eliminate. Morphological degradation is the foremost of these intrinsic pathways, and includes unfavourable vertical segregation, de-mixing of donor and acceptor leading to over-purification of domains, and deleterious crystallization.

The drivers of morphological degradation can be broadly divided into kinetic and thermodynamic factors.² Kinetically, the rate of diffusion of components will dictate the speed of de-mixing and crystallization, where diffusion coefficients have been recently inversely

correlated with acceptor glass transition temperature (T_g) and donor elastic modulus (E_F).³ This means the greater the T_g or E_F of a material, the slower it will diffuse and the more stable it will be against de-mixing or crystallization.

Thermodynamically, the miscibility between components will dictate their tendency to de-mix, which can be quantified by their temperature dependent Flory-Huggins interaction parameter: $\chi(T)$. This interaction parameter describes the net enthalpic interaction energy between two environments,⁴ and is described in more detail in **Section 2.8.2.1**. Typically, high performance systems have poor miscibility, meaning their $\chi(T)$ is high. As a consequence, they have a high thermodynamic tendency to de-mix. In the case of a small molecule acceptor and an amorphous polymer donor, the BHJ formed will comprise of almost pure, acceptor-rich domains and donor-rich, mixed amorphous domains.² This is shown in **Figure 6.1c**. It is the de-mixing in these mixed domains that drives degradation. De-mixing will drive the mixed regime towards the binodal composition, which is often expressed as the volume fraction of one component, for example $\phi_{acceptor}$.

As is discussed in **Section 2.3.2**, to generate charge transfer pathways sufficient acceptor content is required in the mixed domains. The minimum required acceptor content to create charge conduction pathways which result in efficient device performance is known as the ‘percolation threshold’. As a result, films which combine photovoltaic performance and stability should be kinetically stabilised (‘quenched’) at a morphology close to the percolation threshold.⁵ This is realised at around 20 - 30% acceptor volume fraction. Such quenching is usually obtained by annealing a film to rapidly remove solvent and freeze its composition. Kinetic hinderance can also be obtained by using components with high T_g values, resulting in slow diffusion. Due to the typical immiscibility of donor acceptor combinations, it is uncommon, but not impossible, for systems to have a percolation threshold (ideal, minimum acceptor content) close to the binodal composition (equilibrium ratio).³

The relationship between χ (at a given temperature and material combination) and the binodal composition can be described by a Flory-Huggins phase diagram, as shown in **Figure 6.1a**. The curve on the phase diagram is known as the ‘binodal curve’, where points are at thermodynamic equilibrium. Interpolating this curve for a χ value at a certain temperature therefore gives $\phi_{acceptor}$ when the system is at equilibrium.

Here, the curve has been simulated based on Flory-Huggins theory, using freely available resources detailed in the experimental methods. This binodal curve applies for the combination of a polymer and small molecule, at a certain degree of polymerisation. **Figure 6.1a** illustrates that for χ values below ~ 0.6 , components are miscible and will form a single phase, whereas above this two phases will form. The ideal χ value of ~ 1.2 (marked by ‘o’)

would give a binodal composition at the percolation threshold (20 – 30% acceptor)- which is thought to be perfect for both efficiency and stability.

To illustrate how de-mixing reduces performance, we can visualize changes on the phase diagram. **Figure 6.1b** and **6.1c** shows a system just after coating, with a χ value of 2 at room temperature. Rapidly removing solvent freezes the donor:acceptor composition close to the percolation threshold, meaning there are good pathways for electron transport and the system will act as an efficient OPV. However, as the BHJ is not yet at equilibrium, it does not yet lie on the binodal curve. **Figure 6.1d** and **6.1e** show this system after de-mixing. The high χ value means as it approaches the binodal curve, the acceptor content will drop below the percolation threshold, reducing performance and causing degradation. The χ value of the system will not change (as long as it is kept at the same temperature), so movement will only occur along the x axis of the phase diagram.

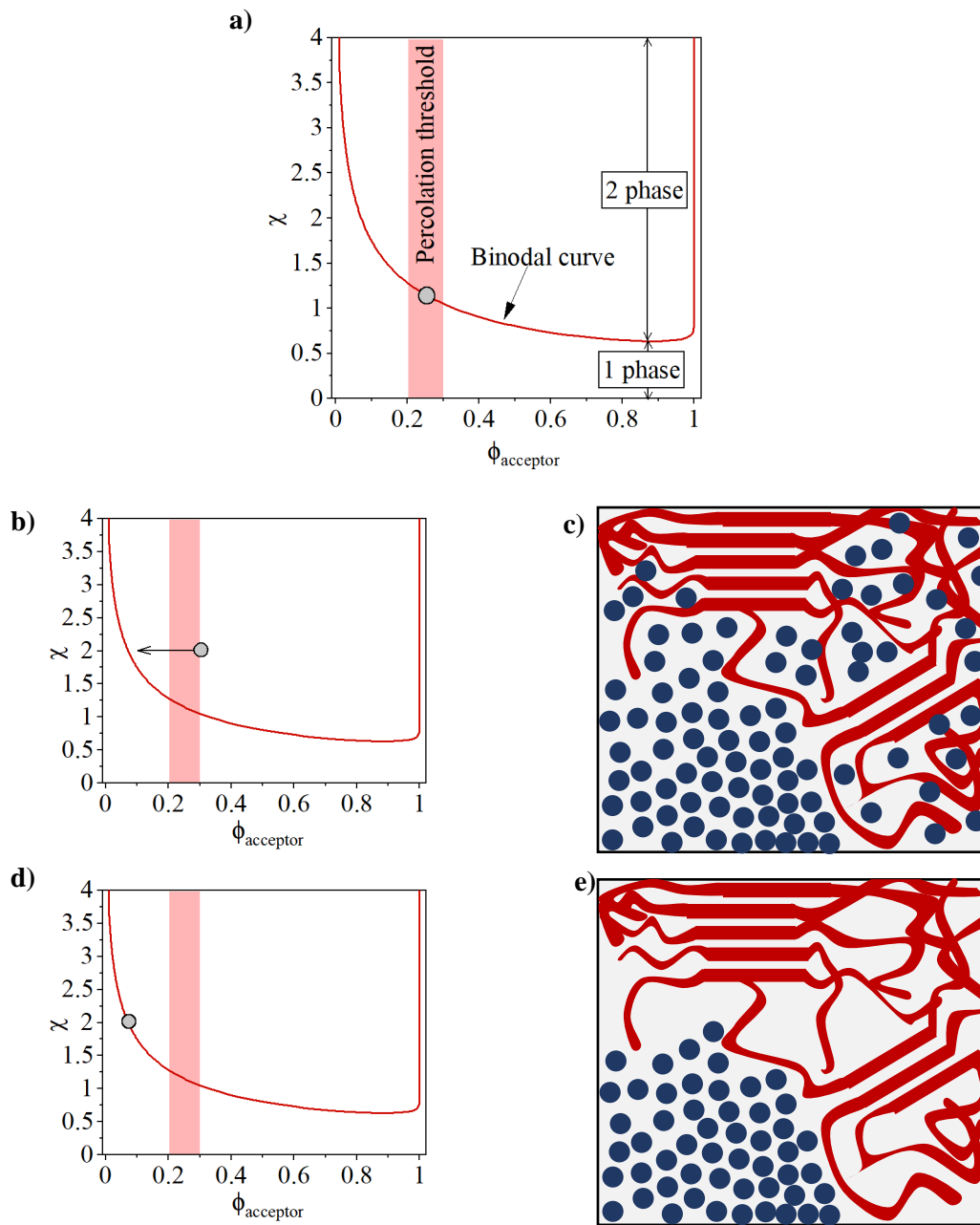


Figure 6.1: *a)* A Flory-Huggins phase diagram. The binodal curve shows the relationship between χ and acceptor content (represented by volume fraction, ϕ) at equilibrium. This applies for a given temperature and material combination. *b)* & *c)* A system straight after fabrication, where it is quenched close to the percolation threshold and performs well. *d)* & *e)* The system after de-mixing to the binodal composition, showing loss of percolation and poor performance.

While most high performing OPV systems exhibit χ values above the ideal – meaning that they tend to demix – several have been shown to have exemplary morphological stability. An intriguing example of this is the ‘positive burn-in’ seen recently in PTB7-Th:EH-IDTBR devices, where their PCE initially sharply increased before levelling out.² This phenomenon was attributed to de-mixing placing the system closer to the percolation threshold, however this effect was not investigated in depth.

In this work we explore the kinetic and thermodynamic driving factors for the positive burn-in seen in PTB7-Th:EH-IDTBR OPVs and compare the system with a range of other PTB7-Th-based devices. EH-IDTBR is assessed against other closely related structural analogues: O-IDTBR and O-IDTBCN, both of which are also high performing⁶ and stable⁷ non-fullerene acceptors (NFAs) based on an indacenodithiophene (IDT) core. This choice of acceptor allows the impact of the branched side-chains of EH-IDTBR to be compared to the linear groups on O-IDTBR and O-IDTBCN. The impact of the differing end-group of O-IDTBCN, compared to the other acceptors, can also be established. Finally, these NFAs are also compared to ubiquitous acceptor PC₇₀BM.

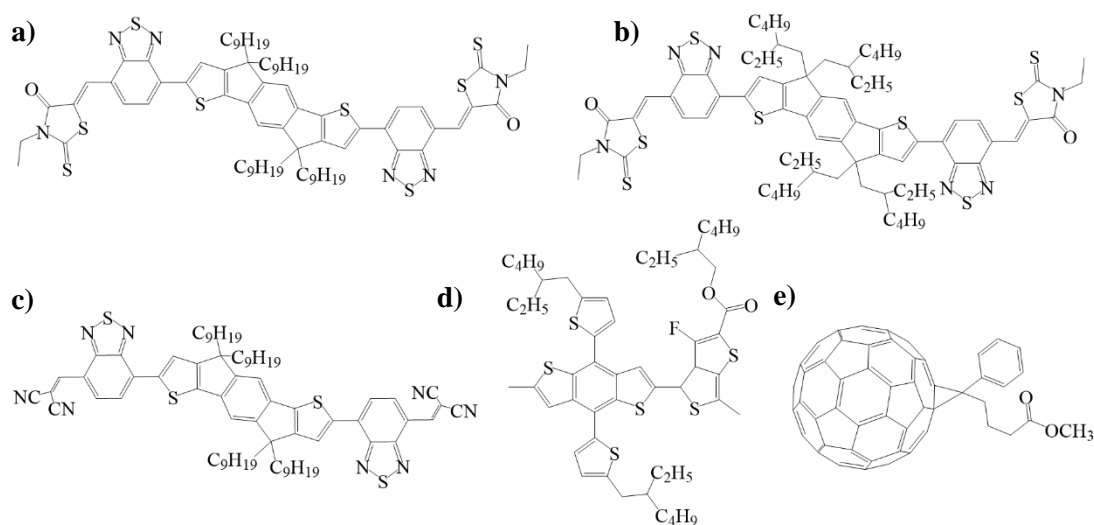


Figure 6.2: Chemical structures of **a)** O-IDTBR, **b)** EH-IDTBR, **c)** O-IDTBCN, **d)** PTB7-Th and **e)** PC₇₀BM.

We first test devices over an extended period of time in dark, under inert conditions, observing a positive burn-in for only EH-IDTBR and O-IDTBR. We then use differential scanning calorimetry (DSC) and grazing incidence wide angle x-ray scattering (GIWAXS) to evaluate T_g and the tendency of the various systems to crystallize. To compare the miscibilities of the acceptors with PTB7-Th, a dual approach is applied. $\chi(T_m)$ is first determined at the

melting temperature of the acceptors using DSC and melting point depressions. A novel method introduced in 2018 by Peng *et al.*,⁸ using ultraviolet-visible (UV-Vis) absorption and visible light microscopy (VLM) is then applied to establish $\chi(T)$ and the miscibility at room temperature.

It is found that the miscibility of acceptors with PTB7-Th differs dramatically depending on the structure of the acceptor, and that this plays a significant role in the appearance of a positive burn-in. Such effects occur despite the high crystallization temperatures (and kinetic hindrance) of the acceptors. This work is the first comprehensive study of both kinetic and thermodynamic factors driving morphological changes in OPVs using only instrumentation that is available at most research institutions (“accessible” techniques), and the first application of Peng’s method to a range of NFAs. Importantly, we provide evidence that positive burn-in occurs in kinetically hindered systems having a strong tendency to de-mix, meaning slow diffusion constants alone cannot prevent phase separation.

6.4 Results and Discussion

6.4.1 Device Fabrication & Morphological Stability

6.4.1.1 Initial Performance

Devices were fabricated in inverted architecture, using a ZnO electron transport layer and a MoO₃ hole transport layer, with full details given in the Experimental Methods. Initial device performance is shown in **Figure 6.3**, with device metrics summarised in **Table 6.1**.

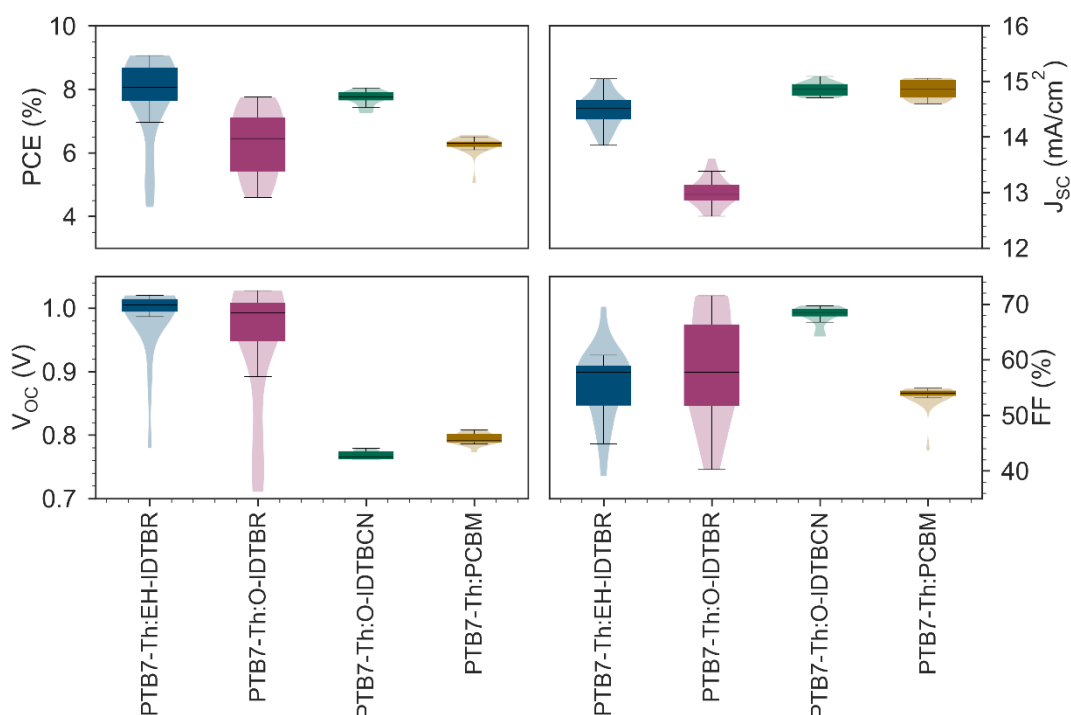


Figure 6.3: Box plot showing device performance for 10 devices for each system, with each box representing the interquartile range and each violin plot representing the entire distribution.

These values are comparable to those obtained in literature,⁶ with significant differences in open circuit voltage (V_{oc}) occurring as a result of differing energy alignments with PTB7-Th.⁶

Table 6.1: Operational metrics of freshly prepared devices, where an average is given for 10 devices ± 1 standard deviation, and the champion value is given in brackets.

System	PCE (%)	V _{oc} (V)	J _{sc} (mA/cm ²)	FF (%)
PTB7-Th:EH-IDTBR	7.8 \pm 1.3 (9.1)	0.99 \pm 0.06 (1.02)	14.5 \pm 0.3 (15.0)	55.4 \pm 6.5 (69.5)
PTB7-Th:O-IDTBR	5.9 \pm 1.6 (7.8)	0.92 \pm 0.12 (1.03)	13.0 \pm 0.3 (13.6)	53.0 \pm 10.3 (69.6)
PTB7-Th:O-IDTBCN	7.7 \pm 0.2 (8.1)	0.77 \pm 0.01 (0.78)	14.9 \pm 0.1 (15.1)	68.0 \pm 1.7 (69.7)
PTB7-Th:PC ₇₀ BM	6.3 \pm 0.3 (6.6)	0.79 \pm 0.01 (0.81)	14.9 \pm 0.2 (15.1)	53.4 \pm 2.3 (54.9)

6.4.1.2 Dark Stability

In order to assess morphological stability the devices were kept in the dark in a inert atmosphere and tested periodically. The results of this study in terms of efficiency are shown in **Figure 6.4**, with other parameters plotted over time shown in **Figures S6.1– 6.3**.

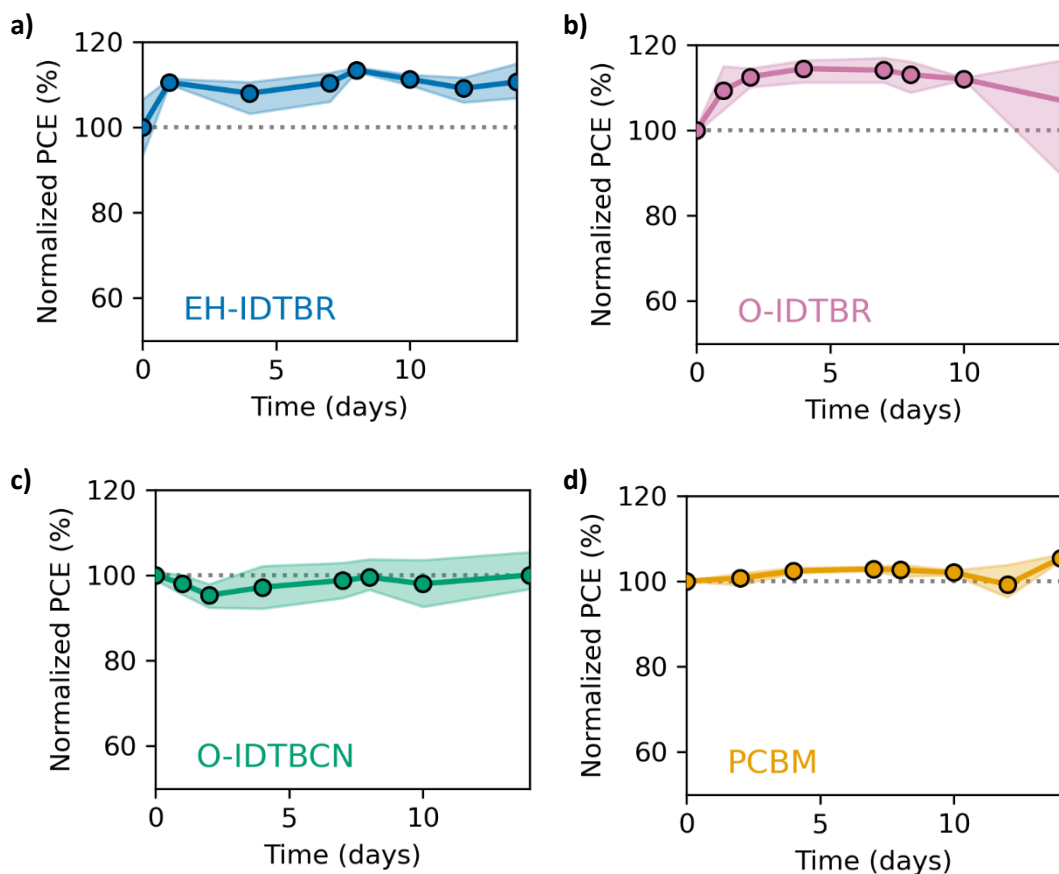


Figure 6.4: PCE over time for cells kept in the dark in an inert atmosphere. Each point represents an average of 3 devices, with the minimum and maximum values covered by the error bar. Annealed samples treated at 80°C for 10 minutes. **a)** PTB7-Th:EH-IDTBR, **b)** PTB7-Th:O-IDTBR, **c)** PTB7-Th:O-IDTBCN, **d)** PTB7-Th:PC₇₀BM. Horizontal line at 100% acts as a guide for the eye.

Here, a ‘positive burn-in’ in device efficiency can be seen for PTB7-Th based devices using O-IDTBR and EH-IDTBR, both exhibiting a fill factor (FF) driven increase in PCE. This is expected for domain purification, as (up to a certain point), purer domains will show less recombination. Interestingly, no positive burn-in is seen for the similar O-IDTBCN based system, nor in the system using a PC₇₀BM acceptor.

To investigate these observations further, the kinetic and thermodynamic differences between the systems were explored.

6.4.2 Kinetic Factors: Exploration of Thermal Characteristics

6.4.2.1 Differential Scanning Calorimetry Measurements

As a link between kinetic morphological stability of OPV systems and the T_g of the materials used has previously been well-established,³ this is an important baseline measurement. As discussed in **Section 3.8.1**, thermal transitions can be identified in DSC measurements according to the direction of the peak. The curves shown here are in the form of ‘exotherm up’, meaning exothermic transitions (such as crystallization) are in the form of positive peaks. Endothermic transitions (such as glass transition and melting) are in the form of troughs. The DSC curves of each pure acceptor material with their melting point, T_m , indicated are shown in **Figure 6.5a**. **Figure 6.5b** highlights the regions of the DSC curves corresponding to the T_g and T_c of the systems.

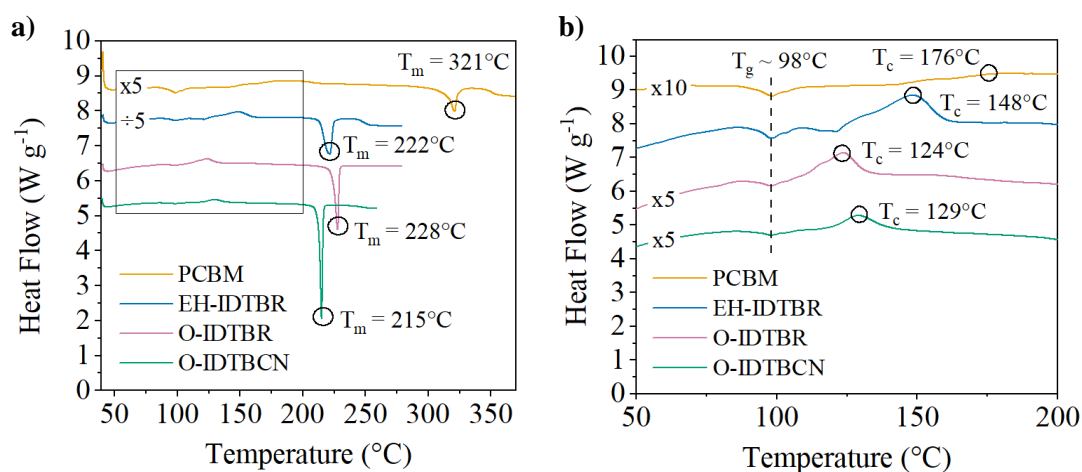


Figure 6.5: DSC curves of each acceptor, collected from the first heat cycle at a $10^\circ\text{C min}^{-1}$ heating rate, exotherm up. Curves vertically shifted for clarity and multiplied as specified to exaggerate features. **a)** Full spectra, with melting point (T_m) highlighted. Box highlights area shown in part **b)**. This highlights the glass transition (T_g) and cold crystallization (T_c) features.

As has been previously reported,² the T_g values for each acceptor lie at a similar temperature. The cold crystallization temperature, T_c , does however differ between each acceptor, as highlighted in **Figure 6.5b**. Therefore, the T_c can instead be used as an assessment of relative kinetic hinderance. A summary of the T_c and T_m values determined from the DSC curves are shown in **Table 6.2**, with such findings in good agreement with reports in the literature.^{2,6}

Table 6.2: A summary of the features seen in the DSC curves of the pure acceptors.

Acceptor	T_c	T_m
EH-IDTBR	148°C	222°C
O-IDTBR	124°C	228°C
O-IDTBCN	129°C	215°C
PC ₇₀ BM	176°C (broad)	321°C

The cold crystallization peak of PC₇₀BM is broad and indistinct, possibly indicating a large range of different crystallite sizes.⁵ Moreover, T_g has been shown to be inversely correlated with diffusion constant,³ i.e. a higher transition temperature implies slower diffusion. The higher T_c values therefore suggest that the greatest kinetic hindrance will exist for PC₇₀BM with PTB7-Th, followed by EH-IDTBR. The non-branched analogues, O-IDTBR and O-IDTBCN exhibit very similar, but lower temperature transitions.

6.4.2.2 Grazing Incidence Wide Angle X-ray Scattering

To gain more information about the relative crystallinity of the materials, GIWAXS measurements were performed on pristine components after annealing at 80°C (the temperature used in device fabrication). Details on the methods and parameters of GIWAXS can be found in **Chapter 3**. 2D GIWAXS patterns are shown in **Figure 6.6a-e** with 1D linecuts in-plane and out-of-plane shown in **Figure 6.6f** and **Figure 6.6g**, respectively.

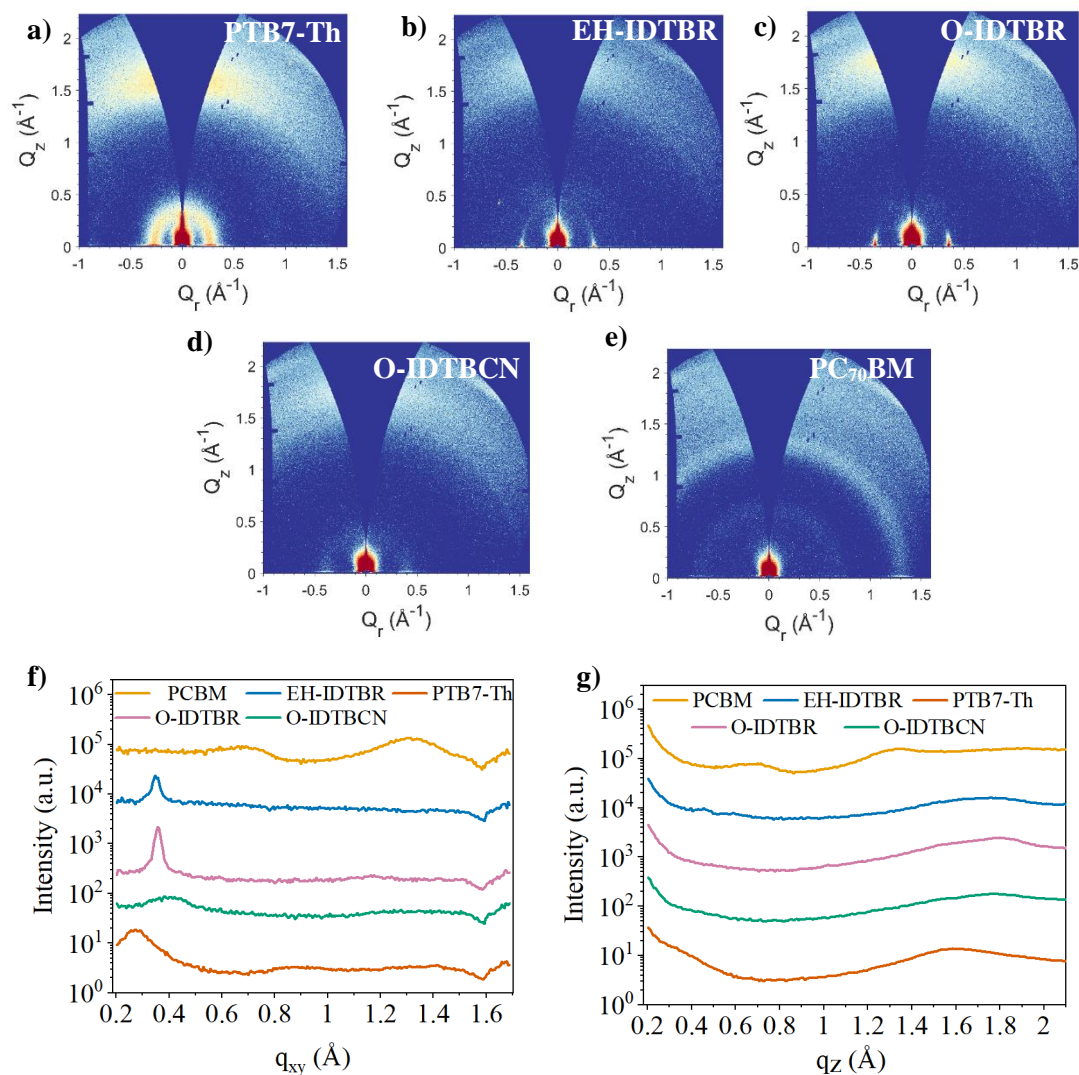


Figure 6.6: 2D GIWAXS patterns of pristine components after annealing at 80°C for 10 minutes. **a)** PTB7-Th, **b)** EH-IDTBR, **c)** O-IDTBR, **d)** O-IDTBCN, **e)** PC₇₀BM. 1D linecuts, vertically offset for clarity in the **f)** in-plane, **g)** out-of-plane direction.

2D GIWAXS patterns upon blending with PTB7-Th are shown in **Figure 6.7a-d**, with 1D linecuts shown in **Figure 6.7e** and **6.7f** for the in-plane and out-of-plane directions respectively.

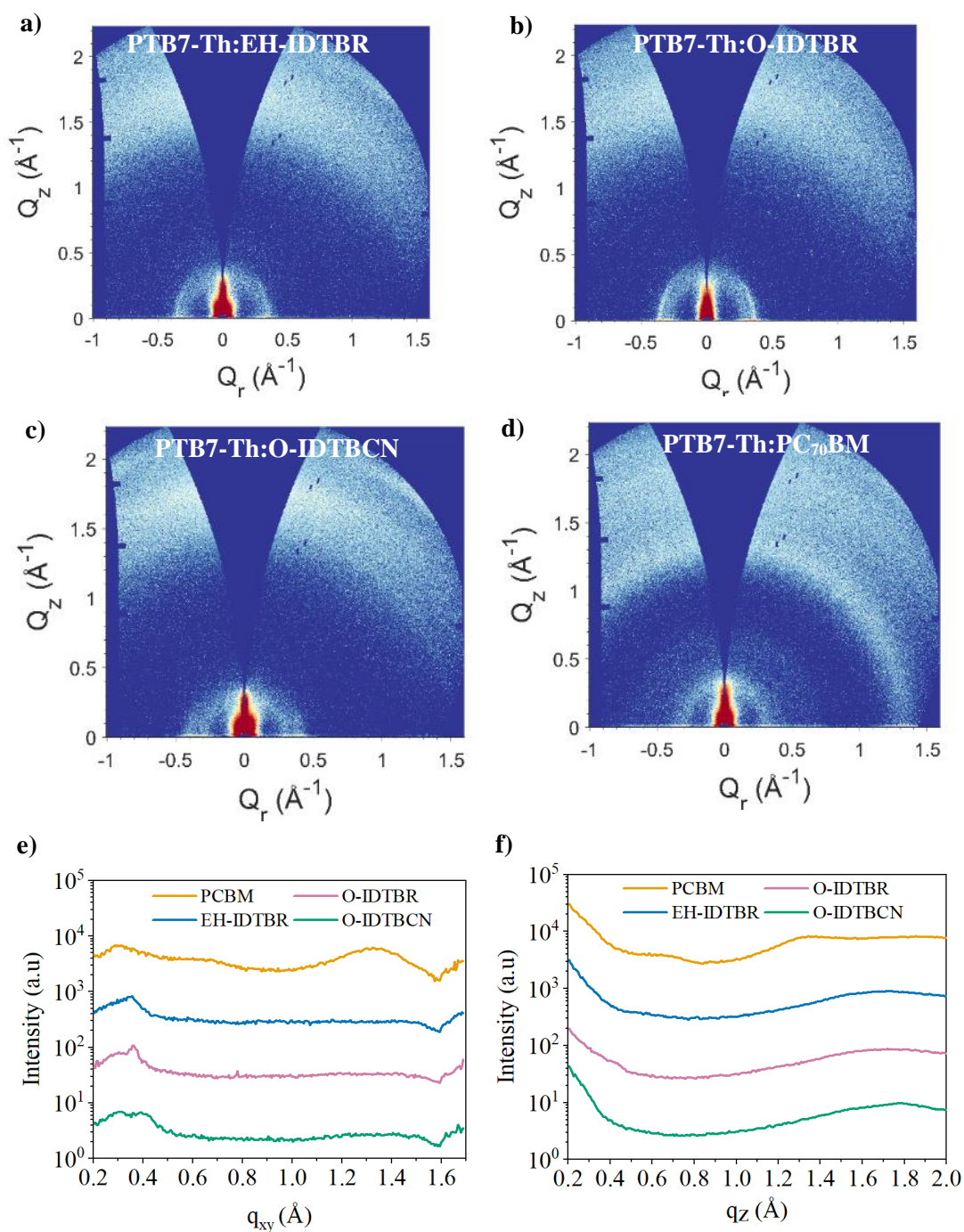


Figure 6.7: 2D GIWAXS patterns for blends of PTB7-Th with a) EH-IDTBR, b) O-IDTBR, c) O-IDTBCN, d) PC₇₀BM. 1D linecuts, vertically offset for clarity in the e) in-plane, f) out-of-plane direction.

Details of the calculation of crystal coherence length (CCL) and d -spacing can be found in **Chapter 3**. These values were calculated for all components, and their corresponding blends, and are summarised in **Table 6.3**.

Table 6.3: Parameters extracted from the GIWAXS measurements. Higher q in-plane PTB7-Th and lower q PC₇₀BM features not considered here. Red font dictates peaks attributed to donor; blue font dictates peaks attributed to acceptor. Table rows corresponding to pristine components are shaded grey, to distinguish from the 1:1 blend films (unshaded).

Film	In-plane (Q_r)			Out-of-plane (Q_z)		
	q (\AA^{-1})	d -spacing (nm)	CCL (nm)	q (\AA^{-1})	d -spacing (nm)	CCL (nm)
PTB7-Th	0.27	2.32	8.43	1.59	0.40	1.02
PC ₇₀ BM	1.31	0.48	2.27	1.33	0.47	2.26
PTB7-Th:PC ₇₀ BM	0.30	2.12	3.88	1.35	0.47	2.01
	1.31	0.48	2.51			
EH-IDTBR	0.35	1.80	16.40	1.74	0.36	0.99
PTB7-Th:EH-IDTBR	0.36	1.77	3.19	1.73	0.36	0.86
O-IDTBR	0.36	1.75	20.36	1.79	0.35	0.92
PTB7-Th:O-IDTBR	0.30	2.07	3.01	1.75	0.36	0.78
	0.36	1.74	21.08			
O-IDTBCN	0.40	1.57	3.69	1.78	0.35	0.82
PTB7-Th:O-IDTBCN	0.30	2.07	1.40	1.76	0.36	0.84
	0.40	1.59	5.32			

In their pristine form, all three NFAs and PTB7-Th exhibit a diffraction peak in the in-plane direction (q_{xy}) at $\sim 0.3 - 0.4 \text{ \AA}^{-1}$ (**Figures 6.6a-d**). As established in literature,⁹ this (100) plane is attributable to the lamellar stacking of the molecules. Similarly, an (010) diffraction peak is present in the out-of-plane direction (q_z) at $\sim 1.6 - 1.7 \text{ \AA}^{-1}$, arising from π - π stacking. Here, π - π stacking occurs at higher q values due to the smaller d -spacing between conjugated groups, than occurs for lamellar stacking between the side chains. As shown in **Section 3.7.5**, prominent in-plane lamellar stacking and out-of-plane π - π stacking suggests a favourable face-on orientation for all of the NFAs, and PTB7-Th.

The well-defined in-plane diffraction spot observed for all three NFA species indicates a strong degree of preferential orientation for the lamellar packing. Contrastingly, the broad halo at low q for PTB7-Th (**Figure 6.6a**) indicates a degree of random orientation, as reported

elsewhere⁹ and expected due to its mostly amorphous nature. Similarly, the amorphous halos at higher q values in the GIWAXS pattern for PC₇₀BM (**Figure 6.6e**) are indicative of disordered crystallites.¹⁰ The NFAs exhibit slightly different in-plane d -spacing values, being 1.57 nm for O-IDTBCN, 1.75 nm for O-IDTBR, and 1.80 nm for EH-IDTBR. We suspect that the largest d -spacing occurs in EH-IDTBR due to its branched structure, that results in steric hinderance. The corresponding CCLs of O-IDTBCN, O-IDTBR, and EH-IDTBR also differ substantially (being 3.69 nm, 20.36 nm, and 16.40 nm respectively). This possible implies different packing modes during crystallization, or may be due to differing tendencies to crystallize at 80 °C.

In all blends, the CCL of the acceptor π - π stacks (out-of-plane) is within 20% of the CCL of the pristine film for all NFAs. However, the behaviour of the (100) peak is more complex. The in-plane lamellar stacking of PTB7-Th at $q = 0.30 \text{ \AA}^{-1}$ is observed in all blend films except those containing EH-IDBTR. Furthermore, the PTB7-Th: EH-IDTBR blend is the only acceptor to show a significantly reduced lamellar (in-plane) CCL, going from 16.40 nm in the pure material to 3.19 nm in the blend. Whilst this result is difficult to explain from GIWAXS alone, reduced CCL values and the absence of both donor and acceptor lamellar peaks have been attributed to poorer donor: acceptor miscibility.^{11,12} These results may imply that EH-IDTBR has worse miscibility with PTB7-Th, than does O-IDTBR or O-ITBCN.

To explore the impact of such effects on device stability, we now attempt to further characterize the relative miscibilities of the acceptors with PTB7-Th.

6.4.3 Thermodynamic Factors: Assessment of the Flory-Huggins Interaction Parameter

The determination of $\chi(T)$ for a donor acceptor combination is not straightforward, and can require the use of advanced techniques such as scanning transmission X-ray microscopy (STXM)¹³ and dynamic secondary ion mass spectrometry (DSIMS).² Alternative techniques include contact angle¹⁴ and differential-scanning calorimetry measurements (DSC),¹⁵ although these are considered to be inaccurate as they only determine χ at a single temperature. There is also often a high degree of measurement error associated with contact angle measurements. Here, we first use the DSC approach to determine the interaction parameter at the melting point of the acceptor, $\chi(T_m)$. We then use a method first proposed in 2018⁸ by Peng *et al.* that uses extended annealing and UV-visible spectroscopy (UV-Vis) to determine χ across a range of temperatures. Based on these values, a model is applied to extrapolate the room temperature interaction parameter, $\chi(25^\circ\text{C})$. Peng's approach is considered to be more accessible due to the wide accessibility of UV-Vis equipment in most

research institutes, the easy operation of such instruments, applicability to most systems, and reliability of the results in comparison to the advanced techniques mentioned above.

6.4.3.1 Determination of $\chi(T_m)$ via Melting Point Depression

DSC can be used to assess miscibility by monitoring the changes in melting point of a material upon mixing with a different material, a process known as melting point depression. The ‘depression’ of a melting point refers to the shifting of the melting point of a material to a lower temperature as a result of mixing with another material (with lower melting point). The greater the mixing (and therefore miscibility), the greater the depression of the melting point. The Flory-Huggins interaction parameter $\chi(T_m)$ – the tendency of a system to de-mix at the melting point of the acceptor – can be estimated from melting point depression using the Nishi and Wang equation, where the system is modelled as a miscible diluent (the polymer) in a solvent (the small molecule acceptor):¹⁶

$$\frac{1}{T_m} - \frac{1}{T_m^0} = \frac{R}{\Delta H_f} \frac{v_a}{v_d} (\phi - \chi\phi^2) \quad (\text{Eq. 6.1})$$

Where T_m^0 is the melting point of the acceptor, T_m is the melting point of the acceptor upon addition of the donor, R is the ideal gas constant ($8.314 \text{ J K}^{-1} \text{ mol}^{-1}$), ΔH_f is the enthalpy of fusion of the acceptor melt (J g^{-1}), v_a and v_d are the molar volume of the acceptor and donor respectively ($\text{cm}^3 \text{ mol}^{-1}$), χ is the Flory-Huggins interaction parameter between the acceptor and donor, and ϕ is the volume fraction of the polymer. The molar volume can be calculated from:

$$v = \frac{M_w}{\rho} \quad (\text{Eq. 6.2})$$

Here, M_w is the monomer molecular weight (893 g mol^{-1} for PTB7-Th, 1326 g mol^{-1} for EH-IDTBR, 1382 g mol^{-1} for O-IDTBR, 1192 g mol^{-1} for O-IDTBCN and 1031 g mol^{-1} for PC₇₀BM) and ρ is the material density (1.17 g mol^{-1} for PTB7-Th,¹⁷ 1.15 g mol^{-1} for the NFAs² and 1.5 g mol^{-1} for PC₇₀BM¹⁸).

DSC curves were collected for each of the acceptors blended with the donor. Here, thin films were prepared by drop casting at various donor:acceptor ratios, before being scraped into aluminium pans for DSC analysis. The donor:acceptor blend ratios investigated were 0:100, 20:80, 30:70, and 40:60. The DSC curves for each system are shown in **Figure 6.8a-d**. Here, analysis was complicated by the melting point of the pure acceptor (indicated by a vertical, dashed line) alongside the depressed melting point (circled). This effect most likely results from the fact that the blend was not completely intermixed before drop casting; an

issue that may result in corresponding inaccuracies in the estimation of $\chi(T_m)$. It is noted that these smaller, new endothermic peaks may also be related to liquid crystal transitions, and that more information could be gained by studying the corresponding cooling curves.

Assuming that the peaks are indeed depressed melting points, we start the analysis by rearranging **Equation 6.1** to form:¹⁵

$$\frac{1}{T_m} - \frac{1}{T_m^0} = \frac{R}{\Delta H_f} \frac{v_a}{v_d} \phi - \frac{R}{\Delta H_f} \frac{v_a}{v_d} \phi^2 \chi \quad (\text{Eq. 6.3})$$

Using this, the melting point depression from a range of polymer volume contents can be plotted in the form $\frac{1}{T_m} - \frac{1}{T_m^0}$ vs ϕ , and fitted using:

$$y = a\phi - b\phi^2 \quad (\text{Eq. 6.4})$$

where the interaction parameter can then be obtained using:

$$\chi = \frac{b}{a} \quad (\text{Eq. 6.5})$$

The $\chi(T_m)$ values calculated using this method can be found in **Table 6.4**, with an example calculation given in supplementary **Section 6.7.2**. The melting point enthalpy in **Table 6.4** is calculated via integration of the melting peak (indicated on each graph in **Figure 6.8**). An example melting point depression is given at the 40:60 blend ratio. $\phi_{acceptor}$ at the binodal is calculated from the simulated binodal curve for PTB7-Th, as discussed below.

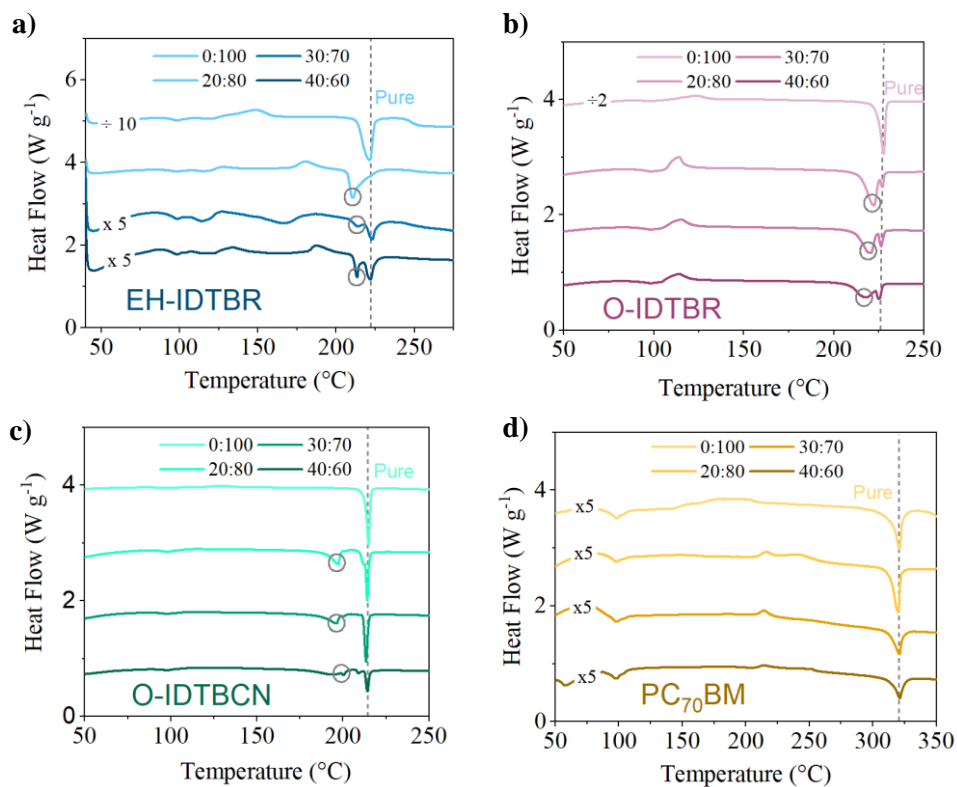


Figure 6.8: DSC curves collected from the first heat cycle, with a $10^{\circ}\text{C min}^{-1}$ heating rate, exotherm up. Curves shifted vertically for clarity and multiplied as specified to enhance features. In each case volume ratio given is donor:acceptor. Blends of PTB7-Th with **a)** EH-IDBTR, **b)** O-IDTBR, **c)** O-IDTBCN and **d)** PC₇₀BM. A vertical, dashed line indicates the melting point of the pure acceptor, whilst the “depressed” melting point is circled.

Table 6.4: Flory-Huggins interaction parameters obtained via analysis of melting point depression.

Acceptor	Melting Enthalpy (J g^{-1})	Melting point depression at $\phi_{\text{polymer}} = 0.4$ ($^{\circ}\text{C}$)	$\chi(T_m)$	ϕ_{acceptor} at binodal
EH-IDTBR	453	8.0	1.91	0.08
O-IDTBR	43	10.4	1.34	0.18
O-IDTBCN	51	22.1	1.25	0.21
PC ₇₀ BM	7	0	2.66	0.03

The greatest melting point depression is found in the O-IDTBCN blend (**Figure 6.8c**), followed by the O-IDTBR (**Figure 6.8b**), and EH-IDTBR blend (**Figure 6.8a**). In contrast, a negligible depression is seen in PC₇₀BM (**Figure 6.8d**). In general, a greater decrease in melting temperature implies a greater miscibility, as reflected in the $\chi(T_m)$ values, with an absence of melting point depression implying very poor miscibility. DSC $\chi(T_m)$ values should be interpreted with caution, considering they only apply at the melting temperature of the acceptor, and therefore these trends may not apply at room temperature (which is clearly more applicable to devices). Nevertheless, these calculations suggest that miscibility with PTB7-Th does differ significantly depending on the exact acceptor. The equilibrium acceptor content ($\phi_{acceptor}$ at the binodal) in the mixed regimes can be interpolated from the simulated binodal curve for PTB7-Th (discussed in **Section 6.3**, plotted in **Figure 6.1**), with the results shown below.

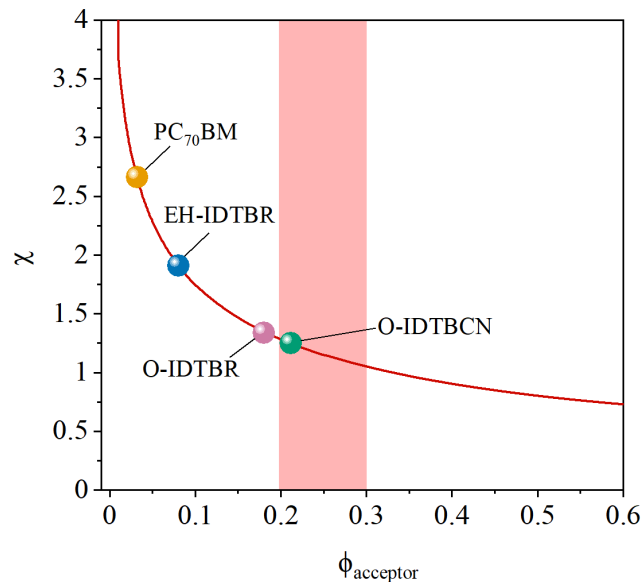


Figure 6.9: The simulated binodal curve for PTB7-Th with a small molecule acceptor, where the plotted data represents the interaction parameter obtained from DSC melting point measurements, and its corresponding acceptor content at equilibrium. The shaded region represents the average percolation threshold for a polymer-small molecule system.

Here, we have calculated values for $\chi(T_m)$ at the melting temperature of each acceptor. However, before interpreting these results with regards to the device stability, the value of $\chi(25^\circ\text{C})$ must be determined. This is to ensure that the miscibility trends obtained via the melting point depression method can be applied to understand the burn-in effects observed for devices that are aged at room temperature.

6.4.3.2 Determination of $\chi(T)$ via UV-Vis Spectroscopy

In 2018 a new method of establishing $\chi(T)$ was proposed by Peng *et al.*⁸ Thin film blends of donor and acceptor were annealed at high temperatures for extended periods of time until a thermodynamic equilibrium was reached. This was tracked via observation of crystal formation in visible-light microscopy (VLM) images. The UV-Vis absorption of the equilibrated blend films was measured and fitted by a linear combination of the component spectra. Using these fitting coefficients, the volume fraction of the acceptor at equilibrium is established, and this value is used to determine a corresponding χ value at the range of elevated temperatures investigated. The room temperature interaction parameter $\chi(T)$ is then modelled. As discussed earlier, this method uses only widely accessible techniques to determine $\chi(T)$, combining ease of operation, general applicability, and reportedly high reliability.

We followed this approach and heated the four blend systems discussed above at 140 °C, 160 °C, 180 °C and 200 °C for 216 hours, 96 hours, 48 hours, and 48 hours respectively, with these values loosely based on those used by Peng. Whilst these temperatures are high, establishing χ over several different temperature values allows a model to be generated, and χ at room temperature to be later established. High temperatures are also required in order for thermodynamic equilibrium to be obtained on a reasonable time scale (e.g. a few days).

Example VLM images of each system after heating at 200°C can be seen in **Figure 6.10**, with the full set of images shown in **Figure S6.5 – S6.20**. It is clear that even the closely structurally related acceptors have very different crystalline structures, as suggested by the differences discussed in the GIWAXS patterns in **Section 6.4.2.2**. A full set of images tracking the formation of crystals over time in each system is shown in the Supplementary Information.

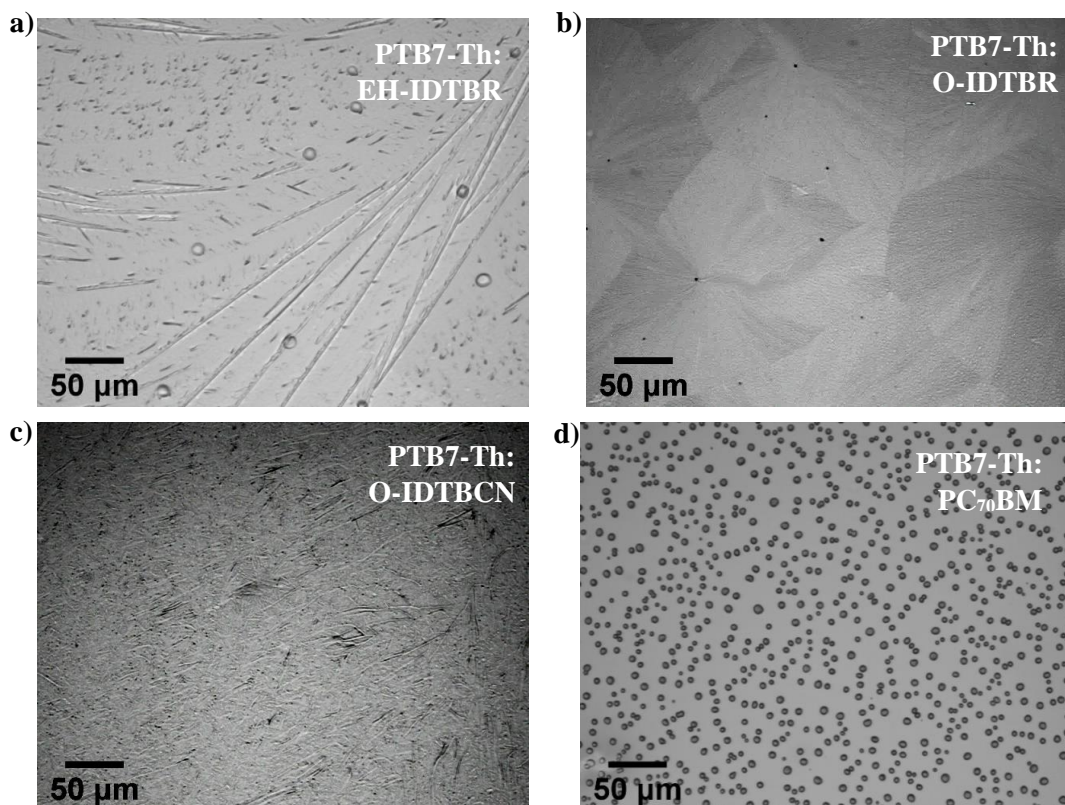


Figure 6.10: Thin films annealed at 200°C for 48 hours. Blends are a) PTB7-Th:EH-IDTBR, b) PTB7-Th:O-IDTBR, c) PTB7-Th:O-IDTBCN, d) PTB7-Th:PC₇₀BM.

Although Peng *et al.*'s original paper tracked the approach to local equilibrium via formation and disappearance of depletion fronts (characterised by the appearance or disappearance of lighter regions surrounding acceptor crystallites in their VLM images), these regions were not always visible in our images. Where depletion regions could not be observed, equilibrium was instead considered to have been reached after the formation of visible large crystals which did not continue to significantly change. The time frame for these processes were verified by comparison to the annealing times used in Peng's work for similar systems where available. The time frame for this equilibrium process varied depending on acceptor and annealing temperature, as expected from the variation in the crystallization temperatures determined from the DSC measurements in **Section 6.4.2.1**. For example, the EH-IDTBR displayed the highest T_c of all of the NFAs studied, and also demonstrated the longest annealing time required (168 hours) to show visible crystals at 140 °C.

During the heating process, the UV-Vis of each film was measured periodically to characterise changes. After equilibrium was determined to have been reached, the UV-Vis absorption of the blend was fitted with a linear combination of its component acceptor and donor spectra. The ratio of acceptor and donor spectra that provided the best fit was assumed to correspond to the ratio of donor:acceptor in the mixed regime. This method assumes that

acceptor molecules that have formed crystals are so opaque and thick that they do not contribute to absorption spectra determined via transmission.⁸ As such, the blend absorption spectra only accounts for the donor and acceptor components within the mixed regime, validating the fitting of the donor and acceptor components. In order to minimize parasitic scattering effects of the acceptor crystals, a majority donor blend (7:3 donor: acceptor) is used throughout. The donor and acceptor component spectra were normalized according to thickness and material density to yield the mass-absorption coefficient, and then used to fit the blend absorbance.

An example of the fitting procedure is shown in **Figure 6.12**, with full fits shown in **Figure S6.20 – S6.24**. In **Figure 6.12a**, the normalised absorbance of a 7:3 blend of PTB7-Th: EH-IDTBR after heating at 140°C for 216 hours is shown alongside the normalised absorbance of the PTB7-Th and EH-IDTBR component films. **Figure 6.12b** shows the evolution of the blend absorbance spectra over each of the timepoints collected, from 24 hours to 216 hours. The timepoint spectra corresponding to the local equilibrium are fitted with a linear combination of the donor and acceptor absorption spectra, as demonstrated for timepoint 216 hours in **Figure 6.12c**. The volume fraction of the polymer (donor), $\phi_{polymer}$, is extracted from the coefficient of the donor component in this fit. In **Figure 6.12d**, the value of $\phi_{polymer}$ at each annealing temperature is plotted.

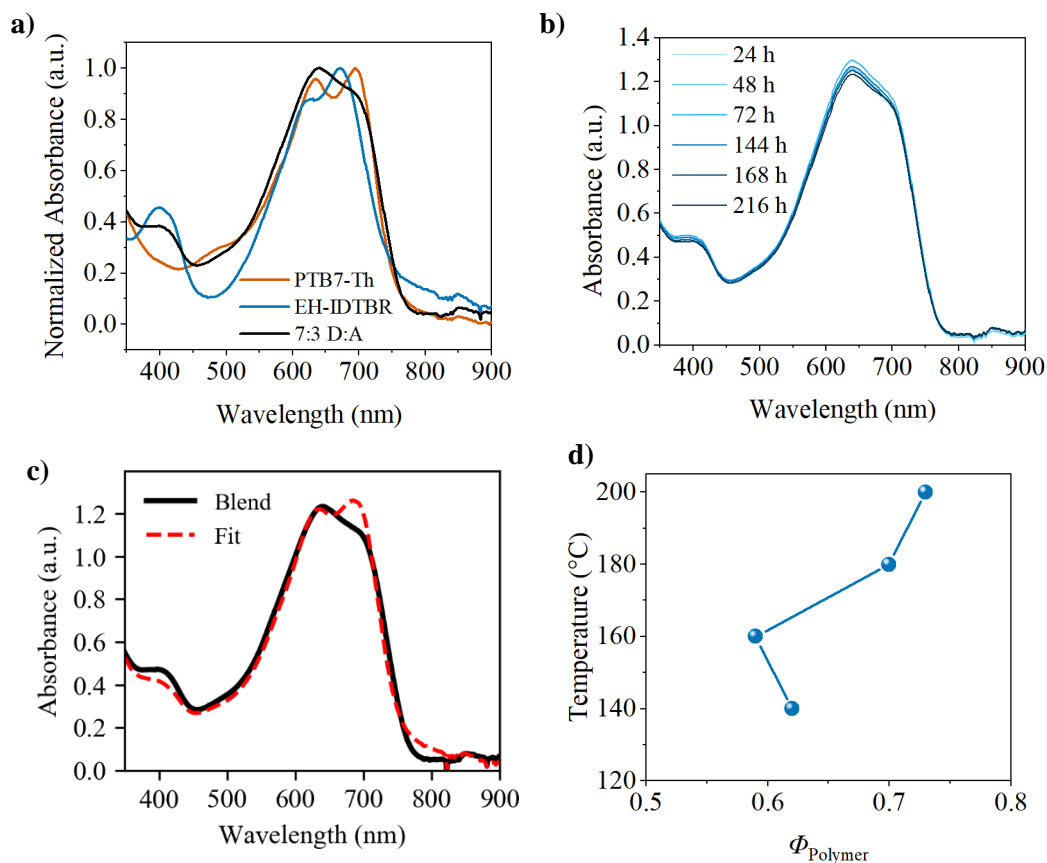


Figure 6.12: *a)* Normalized absorbance of single component films and the 7:3 PTB7-Th:EH-IDTBR blend after annealing at 140°C for 216 hours. *b)* Evolution of the blend spectrum over time, upon heating at 140°C. *c)* Fit of the mass-absorption coefficients of the component films to the blend spectrum after heating for 216 hours. *d)* Plot of the PTB7-Th content obtained from fitting PTB7-Th:EH-IDTBR films across all temperatures.

It can be seen that the fit shown in **Figure 6.12c** does not fully describe the measured absorption spectrum. This is because fitting was complicated by wavelength shifts and shape changes of the absorption spectra upon heating. We attribute this partially to thermal transitions and formations of aggregates in the NFAs. This can be seen in the spectra of pure films annealed for a short time at the relevant temperatures as shown in **Figure 6.13a-e**. Further, suppression of the aggregation-induced shoulder peaks in the 650 to 750 nm region in the blend absorption spectra (shown in **Figure 6.12c**) also obfuscates the fit. Evolution of NFA absorption spectra with heating, due to thermal morphological changes, has been reported elsewhere, and used to evaluate T_g .³ The drastic change of the O-IDTBCN spectrum at 200 °C (**Figure 6.13c**) can be attributed to the approach towards its melting temperature (215°C), which is the lowest melting temperature of the NFAs used in this work.

Crystallization of the pristine component films at high temperature was expected to severely reduce the accuracy of the fit, and therefore the heated component spectra were not used to fit the blend spectra. Instead, all the blend absorption spectra were fitted with the same component spectra, which were only heated briefly at 80°C to remove solvent. Although (as discussed) this method introduces some inaccuracies we expect a reduced degree of inaccuracy than if fitting with component films having a high degree of crystallization.

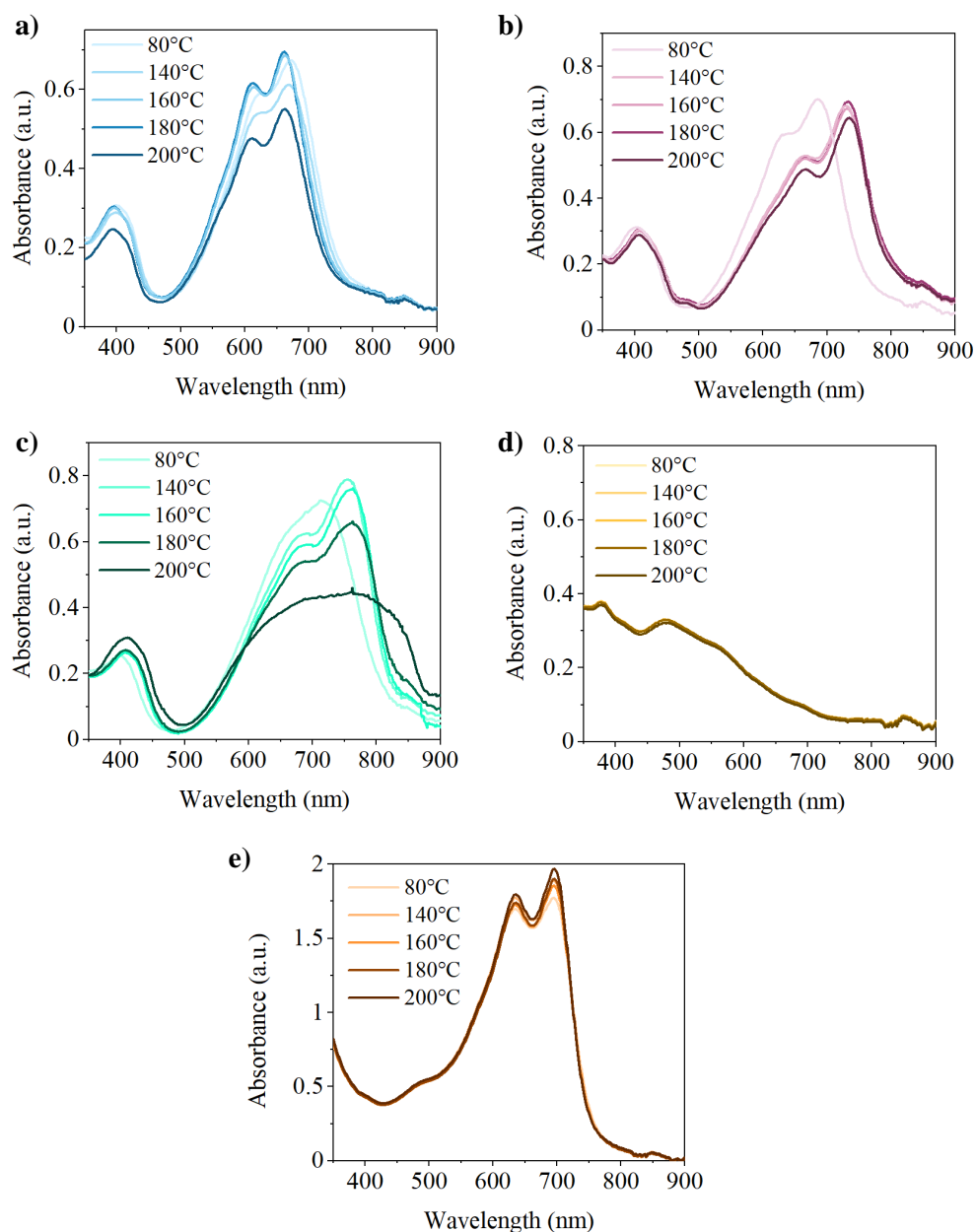


Figure 6.13: Absorbance of single component thin films heated for 5 minutes at various temperatures, with the NFAs showing changes in shape and position of absorption. **a)** EH-IDTBR, **b)** O-IDTBR, **c)** O-IDTBCN, **d)** PC₇₀BM, **e)** PTB7-Th.

The $\phi_{polymer}$ values at each annealing temperature for each acceptor blend are plotted in **Figure 6.14a**. After determining $\phi_{polymer}$ from the fitting coefficient, the corresponding χ value is determined for each annealing temperature investigated. The volume fraction of the acceptor, $\phi_{acceptor}$, is calculated from $1 - \phi_{polymer}$. Again, this value is applied to the simulated binodal curve for PTB7-Th as shown in **Figure 6.1a** and **Figure 6.9**. The relevant χ value is extracted from the corresponding $\phi_{acceptor}$ value along the binodal curve. The values of χ for each acceptor blend at each temperature investigated are shown in **Figure 6.14b**.

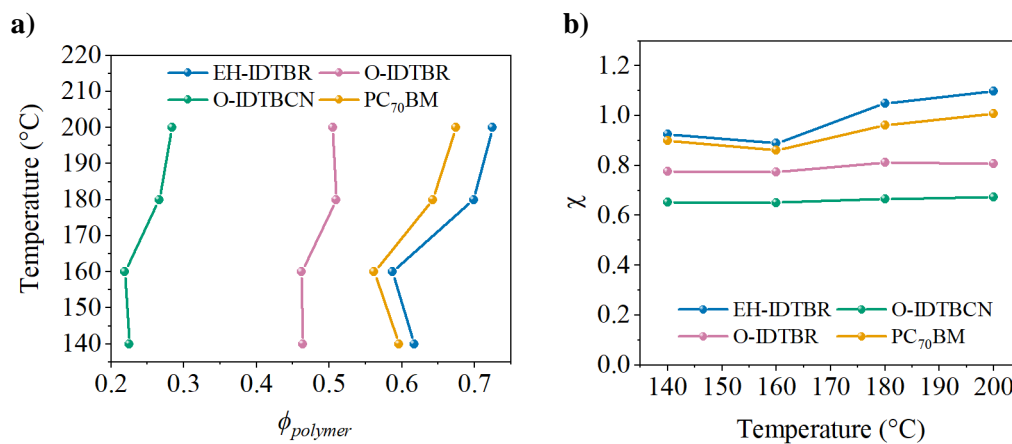


Figure 6.14: a) Polymer content in the mixed regimes of each system, obtained from fits of the UV-Vis spectra. Key refers to acceptor within a 7:3 blend with PTB7-Th. b) Corresponding Flory-Huggins interaction parameters, obtained from interpolation of the binodal curve.

6.4.3.3 Determination of Miscibility at Room Temperature

The $\chi(T_m)$ values calculated from the melting point depression DSC data implied increasing miscibility with the polymeric donor in the order: PC₇₀BM, EH-IDTBR, O-IDTBR, O-IDTBCN. The χ values obtained from Peng's UV-Vis method produced similar results, but with EH-IDTBR predicted to be very slightly less miscible than PC₇₀BM at the high temperatures investigated. However, in order to quantify the relative tendencies to de-mix at room temperature and apply these insights to real-world device stability data, we must establish χ at room temperature: $\chi(25^\circ\text{C})$.

The interaction parameter, χ , is usually fitted according to the simple equation:⁴

$$\chi = A + \frac{B}{T} \quad (\text{Eq. 6.6})$$

where A and B are constants. Commonly, binary organic mixtures are expected to exhibit lower critical solution temperature (LCST) behaviour, meaning they become more miscible with increasing temperature. Upper critical solution temperature (UCST) refers to mixtures that become less miscible with increased temperature. Recent work in 2021 by Peng *et al.*¹⁹, however, saw both LCST *and* UCST behaviour in several systems. Peng reported shifts between the types of behaviour at or above the T_c of the acceptor. We observe a similar behaviour, demonstrated by the 'kinks' in the χ values calculated for the four acceptors shown above in **Figure 6.14b**.

In order to account for both LCST and UCST behaviour within one system, **Eq. 6.6** can be modified to form:

$$\chi = A + \frac{B}{T} + C \ln(T) \quad (\text{Eq. 6.7})$$

As we observe both UCST and LCST behaviour in our systems, we therefore fit our data with this modified equation. Here, temperature is fitted in Kelvin, but is plotted in Celsius in **Figure 6.15** to allow it to be compared with other figures. The fitting parameters and resulting calculated $\chi(25^\circ\text{C})$ values are shown in **Table 6.5**. $\chi(T_m)$ values calculated via DSC measurements in **Section 6.4.3.1** are included for a comparison of the two techniques to evaluate the interaction parameter.

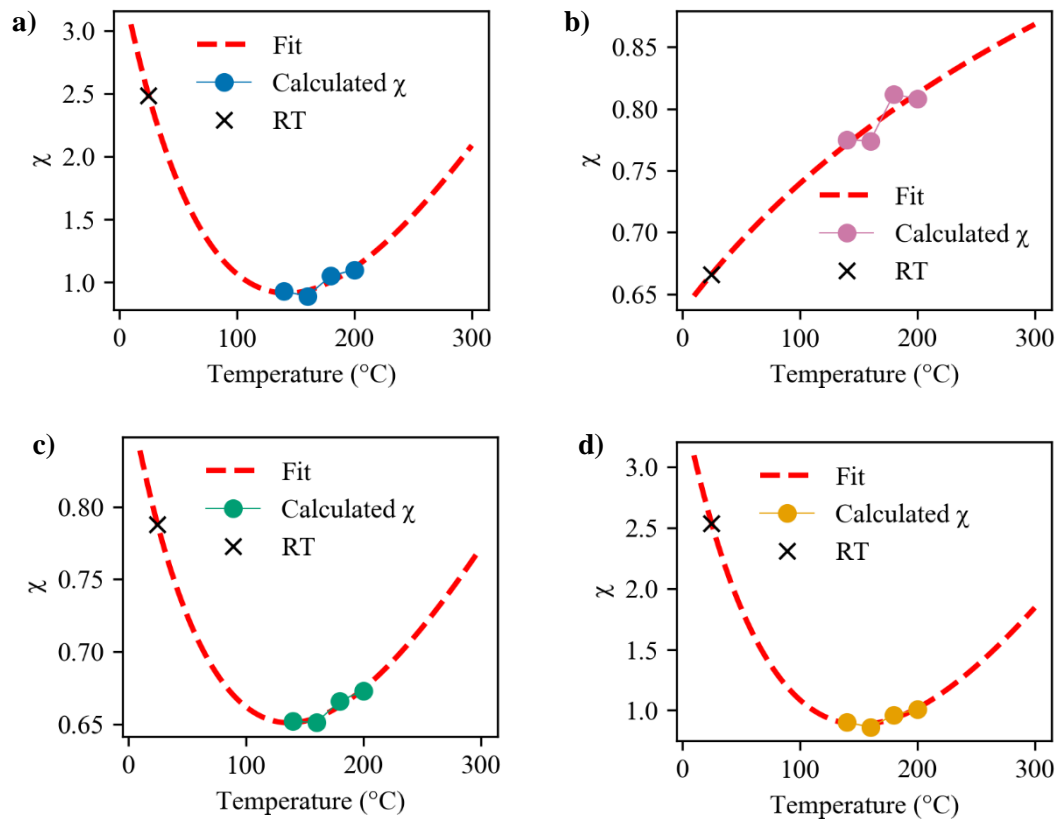


Figure 6.15: Fits of χ values according to modified Flory-Huggins theory to obtain $\chi(25^\circ\text{C})$, and to determine the relative tendency to de-mix at room-temperature. Curves are for PTB7-Th with a) EH-IDTBR, b) O-IDTBR, c) O-IDTBCN, d) PC₇₀BM. RT refers to the χ value at room temperature, i.e. 25°C.

Table 6.5: Estimated Flory-Huggins interaction parameters at room temperature, their fitting constants, and the corresponding volume fraction of the acceptor (ϕ_{acceptor}) at equilibrium (obtained by interpolation of the binodal curve).

Acceptor	A	B	C	$\chi_{\text{PTB7-Th:A}}$ (25°C)	ϕ_{acceptor} at 25°C	$\chi_{\text{PTB7-Th:A}}$ (T_m) (DSC)
EH-IDTBR	-177	1.05×10^4	25	2.49	0.04	1.91
O-IDTBR	-0.54	-32.2	0.23	0.67	0.74	1.34
O-IDTBCN	-16.2	987	2.41	0.79	0.52	1.25
PC ₇₀ BM	-164	9.95×10^3	23.5	2.54	0.04	2.66

Whilst $\chi(T)$ is rarely calculated in literature, there have been a few studies on some of the systems used here. Ghasemi *et al.*³ determined $\chi(25^\circ\text{C})$ for PTB7-Th:EH-IDTBR to be ~ 2.3 ; very similar to the value that we calculate (2.49). Likewise, the χ value of PTB7 (closely related to our donor PTB7-Th) with PCBM has been calculated as ~ 1.1 at 180°C ;²⁰ again, similar to the value of 0.96 obtained using the UV-Vis method. The similarity of these literature values to our data gives us some confidence in the accuracy of the fitting parameters used here.

As discussed above, the $\chi(T_m)$ values calculated in **Section 6.4.3.1** indicated increasing miscibility (lower $\chi(T_m)$ values) with PTB7-Th in the order of PC₇₀BM, EH-IDTBR, O-IDTBR, and O-IDTBCN. Here, the $\chi(25^\circ\text{C})$ values extracted from the extended Flory-Huggins model corroborate this trend. The highest $\chi(25^\circ\text{C})$ value is obtained for PC₇₀BM, at 2.54, with a similar value for EH-IDTBR (2.49). Both O-IDTBR and O-IDTBCN are expected to have a much lower tendency to demix from the donor at room temperature, with calculated $\chi(25^\circ\text{C})$ values of only 0.67 and 0.79, respectively. These $\chi(25^\circ\text{C})$ values now indicate greater miscibility with PTB7-Th for O-IDTBR than for O-IDTBCN. This is the opposite of the trend predicated from the $\chi(T_m)$ values (1.34 and 1.25) respectively. The validity of this is, however, questionable, as the fit of our calculated $\chi(25^\circ\text{C})$ values for O-IDTBR is the poorest (**Figure 6.15b**), O-IDTBCN showed a more significant melting point depression with PTB7-Th, and elsewhere O-IDTBCN has been reported to be more miscible with PTB7-Th than O-IDTBR.⁶ Nevertheless, both methods predict that EH-IDTBR and PC₇₀BM have much worse miscibility with PTB7-Th than O-IDTBR or O-IDTBCN.

6.4.4 Relation of Kinetic and Thermodynamic Factors to Stability

The relation of the Flory-Huggins interaction parameter, device stability, and the percolation threshold (optimum acceptor content for efficient PV devices) can be understood more clearly with reference to the simulated binodal curve for PTB7-Th, shown in **Figure 6.16**. Each acceptor and its calculated $\chi(25^\circ\text{C})$ values are plotted at the corresponding point on the binodal curve (the simulated equilibrium composition). The initial ratio of donor: acceptor before de-mixing will depend on the system and deposition conditions but can be assumed to be higher than the percolation threshold. This is because if the mixed regimes form in the same ratio as the blend solution that is deposited, we would expect ~ 0.7 acceptor content (ϕ_{acceptor}) for the NFAs and ~ 0.6 ϕ_{acceptor} for PTB7-Th:PC₇₀BM. These blend solutions are described in detail in the Experimental Methods. Therefore, de-mixing of these systems towards the equilibrium point (meeting the binodal curve) shifts these points left along the x-axis, at a constant χ value on the y-axis. This migration means that some systems will move to pass through the percolation threshold (the optimum composition).

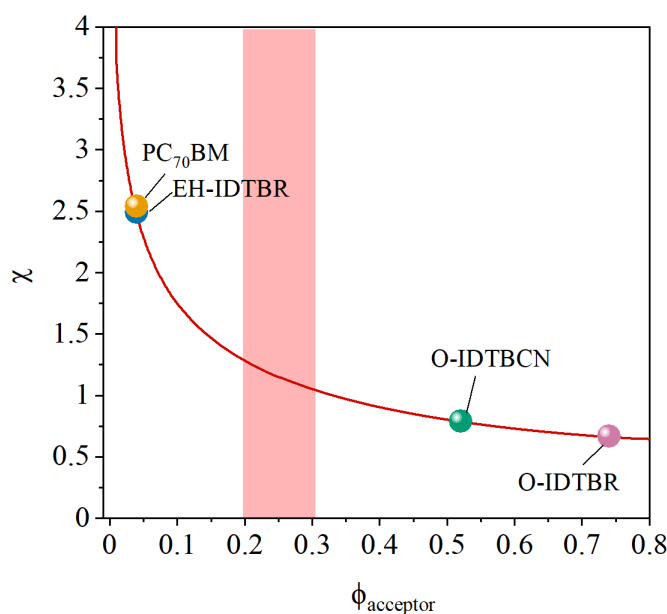


Figure 6.16: The simulated binodal curve for PTB7-Th with a small molecule acceptor, where the plotted data represents the room temperature interaction parameter obtained from UV-Vis measurements and its corresponding acceptor content at equilibrium. The shaded region represents the average percolation threshold for a polymer-small molecule system.

Here, we consider each system in turn. In our initial stability measurements (**Section 6.4.1.2**), a positive device efficiency burn-in – driven by an FF increase – was seen in EH-IDTBR. Both the DSC and UV-Vis techniques showed the PTB7-Th: EH-IDTBR system to have high χ values ($\chi(25^\circ\text{C})$ of 2.49 and $\chi(T_m)$ of 1.91). These high χ values lead to a binodal equilibrium content significantly below the percolation threshold. Accordingly, as the devices

age, the mixed regime in the BHJ moves towards, and eventually passes through, the percolation threshold (optimum composition). This results in a ~10% increase in the normalised device PCE, as the optimum film composition for performance is realised. This supports theories described by Ghasemi *et al.*³ that the positive burn-in is driven by de-mixing to the percolation threshold.

Interestingly, the same device efficiency burn-in is not seen for PC₇₀BM, predicted to be equally as immiscible with PTB7-Th ($\chi(25^\circ\text{C})$ of 2.54 and $\chi(T_m)$ of 2.66). PC₇₀BM demonstrated the highest T_c value of the systems considered here (176 °C, **Figure 6.5b**). T_c can be considered as an effective T_g , with T_g being correlated with the diffusion constant. Therefore, a possible reason for the absence of any burn-in effect is that the kinetic hindrance is significant, such that the timescale of de-mixing is too slow to have been observed here for the PTB7-Th:PC₇₀BM system. This result implies, as suggested recently,³ that T_c plays a significant role in morphological stability for highly hypo-miscible systems. It does, however, indicate that although EH-IDTBR has a relatively high T_c (~148 °C), is not high enough to prevent phase separation. Although this phase separation is favourable for device performance on the timescales investigated here, the system is not expected to be stable long term.

O-IDTBCN and O-IDTBR have significantly lower T_c values (129 °C and 124 °C, respectively) than either EH-IDTBR or PC₇₀BM. These systems might therefore be expected to demonstrate significant phase separation. The performance of O-IDTBCN does not change over the timescale of the experiment. We have calculated that O-IDTBCN has amongst the highest miscibility with PTB7-Th ($\chi(25^\circ\text{C})$ of 0.79 and $\chi(T_m)$ of 1.25) of the systems studied here. At these χ values, the initial composition is expected to lie close to the equilibrium composition on the binodal curve. Therefore, it is proposed here that the tendency to de-mix from the initial ratio is low, and so the system is relatively thermodynamically stable.

Contrastingly, the positive burn-in for O-IDTBR implies that the $\chi(T_m)$ value of 1.34 obtained via DSC may be more accurate than the $\chi(25^\circ\text{C})$ value of 0.79 obtained by UV-Vis. At a χ value of 1.34, the system is again expected to move towards the percolation threshold, resulting in an increase in device efficiency as the devices age towards the equilibrium composition. As mentioned previously, the fit for O-IDTBR and therefore the $\chi(25^\circ\text{C})$ is expected to be inaccurate.

As O-IDTBCN has the same core group as O-IDTBR (see **Figure 6.2** for the chemical structures), it might be expected to undergo a similar interdigitated packing process with PTB7-Th. These interdigitated, layered packing structures are likely due to moderately good miscibility with the donor. Comparatively, the packing of O-IDTBR and EH-IDTBR with PTB7-Th has been shown to differ²¹ due to the steric hindrance of the branched chains in EH-

ODTBR. The poor miscibility calculated here for EH-IDTBR with PTB7-Th may therefore be due to the steric hindrance of the branched side-chains preventing close packing.

In summary, despite very similar chemical structures, the side chains of NFAs play a significant role in dictating miscibility and therefore the stability of OPV devices.

6.5 Conclusions

In this work we use a combination of kinetic and thermodynamic properties to understand the morphological stability of a range of systems based on a PTB7-Th donor. Kinetic hindrance for each system is assessed using DSC. Thermodynamic miscibility is evaluated using the Flory-Huggins interaction parameter, χ . Here, we have calculated χ using two methods. First, χ at the melting temperature of each acceptor is calculated using DSC. Next, χ is evaluated over a range of temperatures using a combination of VLM and UV-Vis, as first reported by Peng *et al.* in 2018.⁸ Compared to the usual, advanced techniques of evaluating χ (such as STXM and TOF-SIMS), DSC, VLM, and UV-Vis are all much more likely to be available to the average lab user. Therefore, this work provides a template for comprehensive exploration of morphological degradation factors using simple, widespread techniques.

We have used the calculated χ values to understand how each system will evolve over time, and how this relates to morphological stability. Our results show that the systems that display positive burn-in (PTB7-Th:EH-IDTBR and PTB7-Th:O-IDTBR) both likely have high χ values. This means they will have a tendency to de-mix, moving through the percolation threshold, which will result in a brief rise in efficiency. The relatively high T_c values of the acceptor means this diffusion happens slow enough to observe positive burn-in over a few days. Although PTB7-Th:PC₇₀BM has a similarly high χ value, it has a higher T_c , which is suggested to hinder diffusion to a greater degree. This means any positive burn-in is likely too slow to observe on the timescale of our experiment. Lastly, no positive burn-in is seen for PTB7-Th:O-IDTBCN. We suggest this is due to the high miscibility between PTB7-Th and O-IDTBCN leading to a lower thermodynamic tendency to de-mix.

Our results indicate that the chemical structure of both side chains and end-groups of acceptors play a significant role in miscibility with donor polymers. This is an important finding, and one that has not been explored comprehensively in other works. We also find that whilst χ can be easily calculated using the methods above, different techniques can yield different trends. Ideally multiple methodologies should be used for accurate results.

We believe reporting of $\chi(T)$ values is a vital step towards identifying OPV blends that are both efficient and stable. This work demonstrates how commonplace techniques can be used to find $\chi(T)$, and that this result can be used to understand morphological stability (and how to improve it).

6.6 Experimental

Full details of device fabrication, DSC, GIWAXS, and UV-Vis measurement techniques can be found in **Chapter 3**. Details specific to this chapter are given here.

6.6.1 Flory Huggins Binodal Curve

The binodal curve shown in **Figure 6.1** describes PTB7-Th with any small molecule acceptor. It was produced from a modified version of the Flory-Huggins code available here: https://github.com/laphysique/FH_LLPS_simple_system, and relies on a root finding algorithm. The degree of polymerisation of PTB7-Th was calculated using the ratio of the M_w of the full polymer (57, 183 g mol⁻¹) and that of the repeat unit (893 g mol⁻¹), to yield 64.01. The degree of polymerisation of the small molecule acceptor was 1, meaning the Flory-Huggins theory describing a polymer in a solvent could be used.²² Interpolation of the binodal was done using the `scipy curve_fit` module in python.

6.6.2 Devices

6.6.2.1 Initial Fabrication

Devices were made using ITO/ZnO/Active Layer/MoO₃/Ag. Active layer solutions were made up at 1:2.5 for PTB7-Th:NFA and 1:1.5 PTB7-Th:PC₇₀BM, all in chlorobenzene. Solid concentrations were 16 mg mL⁻¹, 18 mg mL⁻¹, 20 mg mL⁻¹ and 17 mg mL⁻¹ for PTB7-Th with EH-IDTBR, O-IDTBR, O-IDTBCN and PC₇₀BM respectively. All solutions stirred overnight at 60°C to dissolve. After cleaning and deposition of ZnO, active layers were fabricated via static spin coating at 1500 rpm, 2500 rpm, 3000 rpm and 3000 rpm to achieve layer thicknesses of ~70 nm, 80 nm, 70 nm and 70 nm for PTB7-Th with EH-IDTBR, O-IDTBR, O-IDTBCN and PC₇₀BM respectively. All active layers deposited in air, but annealed in a glovebox at 80°C for 10 minutes after deposition.

6.6.2.2 Stability

For stability measurements devices were kept in the dark, in a temperature controlled, N₂ filled glovebox and tested periodically in the manner described above. Results given as an average of the top three initial performing devices. In this chapter stability results given as averages of the forward (0 to 1.2 V) *JV* sweeps due to device contacting issues with our equipment at the time.

6.6.3 Differential Scanning Calorimetry

DSC samples prepared from solutions at the appropriate volume ratio of the sample (e.g. 0.2:0.8 PTB7-Th:Acceptor), were weighed at a solid concentration of 33 mg mL⁻¹, to ensure a final weight of 5 mg per sample. All solutions were stirred overnight in chlorobenzene at 60°C before drop casting onto ITO coated substrates that were then left under vacuum for 2 days to remove solvent. After drying the films were scraped into new vials for DSC analysis. Heating was carried out at a rate of 10°C min⁻¹, with all curves given as exotherm up. Melting enthalpies were obtained via integration of the melt peak in the Trios software package.

6.6.4 Grazing Incidence Wide Angle X-Ray Scattering

GIWAXS measurements were performed on thin films prepared on ZnO coated ITO glass. Substrates cleaned in the manner described above. FWHM values obtained via gaussian fitting using the `scipy curve_fit` module in python.

6.6.5 Determination of $\chi(T)$ via UV-Vis

Samples for UV-Vis were prepared at a donor: acceptor ratio of 7:3 and a solid concentration of 15 mg mL⁻¹ in chlorobenzene. Components also prepared at 15 mg mL⁻¹. All films were spun statically at 1000 rpm onto ITO coated glass. Components heated at 80°C for 5 minutes to remove solvent, as without annealing peaks were poorly resolved and this temperature was considered sufficiently below the crystallization temperature to avoid altering the accuracy of the results.

6.6.5.1 UV-Vis Spectroscopy

UV-Vis spectroscopy measurements were taken on a Fluoromax 4 fluorometer (Horiba) using a Xe lamp. Samples were left to cool for 5 minutes before removal into air, to

avoid reactions. All figures use optical density ($-\log_{10} \left(\frac{\text{transmitted signal}}{\text{incident signal}} \right)$), referred to as absorbance throughout. Where spectra are normalized, this is labelled as normalized absorbance. The only place where spectra are converted to mass absorption coefficient, and normalized by thickness and density, is the reference spectra for fitting. Here, the densities used were 1.17 g cm^{-3} for PTB7-Th, 1.15 g cm^{-3} for the NFAs and 1.5 g cm^{-3} for PC₇₀BM. Samples were fitted with the form Blend = A*donor + B*acceptor.

6.7 Supplementary Information

6.7.1 Device Stability

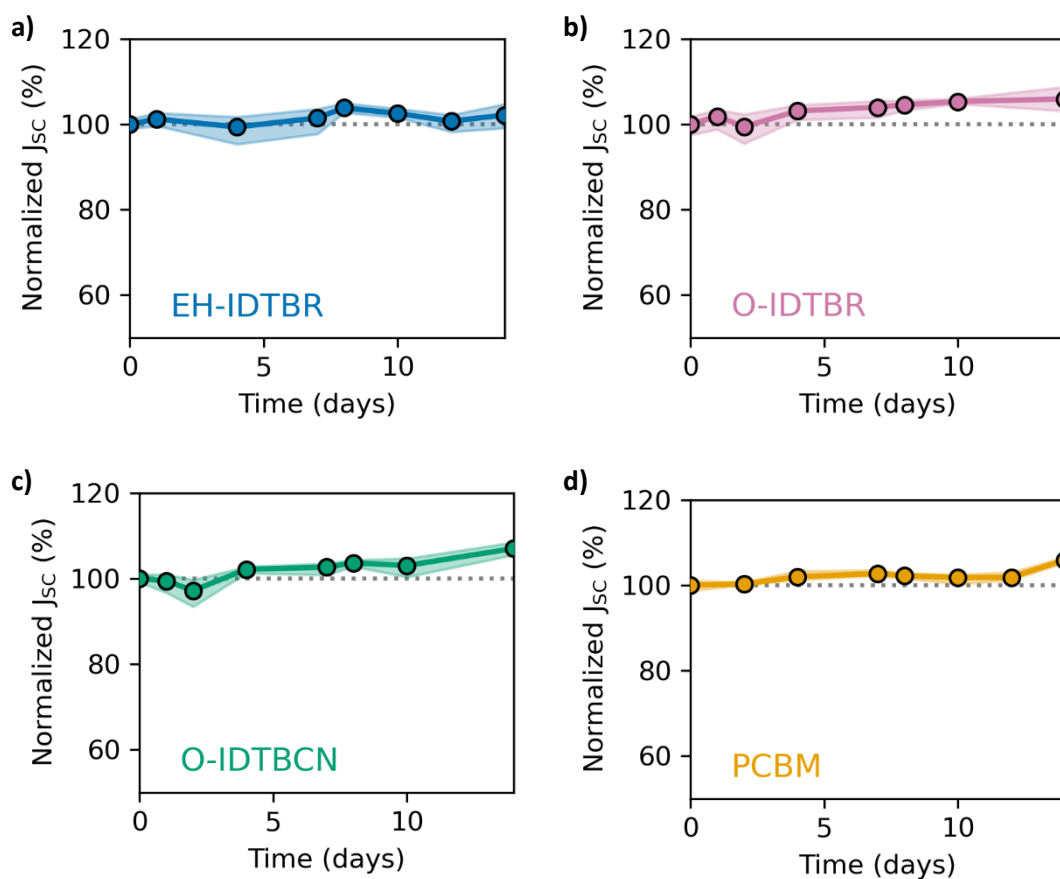


Figure S6.1: J_{sc} over time for cells kept in the dark in an inert atmosphere. Each point represents an average of 3 devices, with the minimum and maximum values covered by the error bar. **a)** PTB7-Th:EH-IDTBR, **b)** PTB7-Th:O-IDTBR, **c)** PTB7-Th:O-IDTBCN, **d)** PTB7-Th:PC₇₀BM.

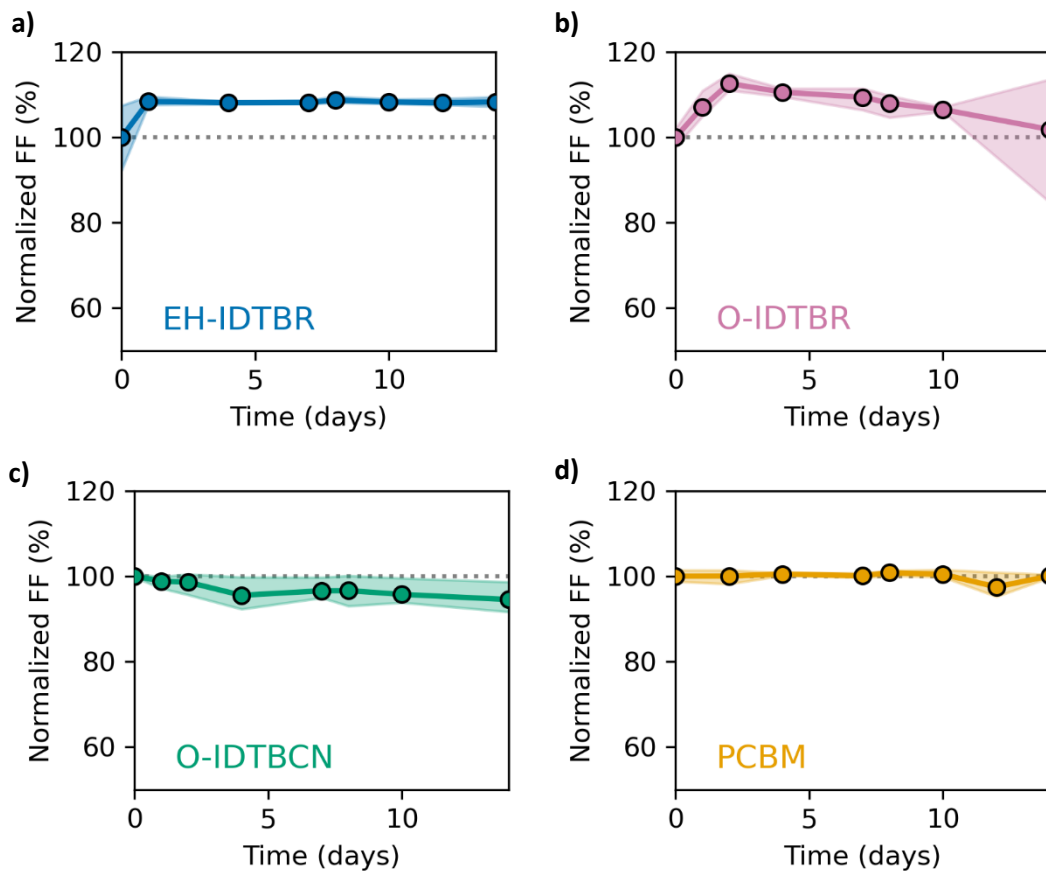


Figure S6.2: FF over time for cells kept in the dark in an inert atmosphere. Each point represents an average of 3 devices, with the minimum and maximum values covered by the error bar. Annealed samples treated at 80°C for 10 minutes. **a)** PTB7-Th:EH-IDTBR, **b)** PTB7-Th:O-IDTBR, **c)** PTB7-Th:O-IDTBCN, **d)** PTB7-Th:PC₇₀BM.

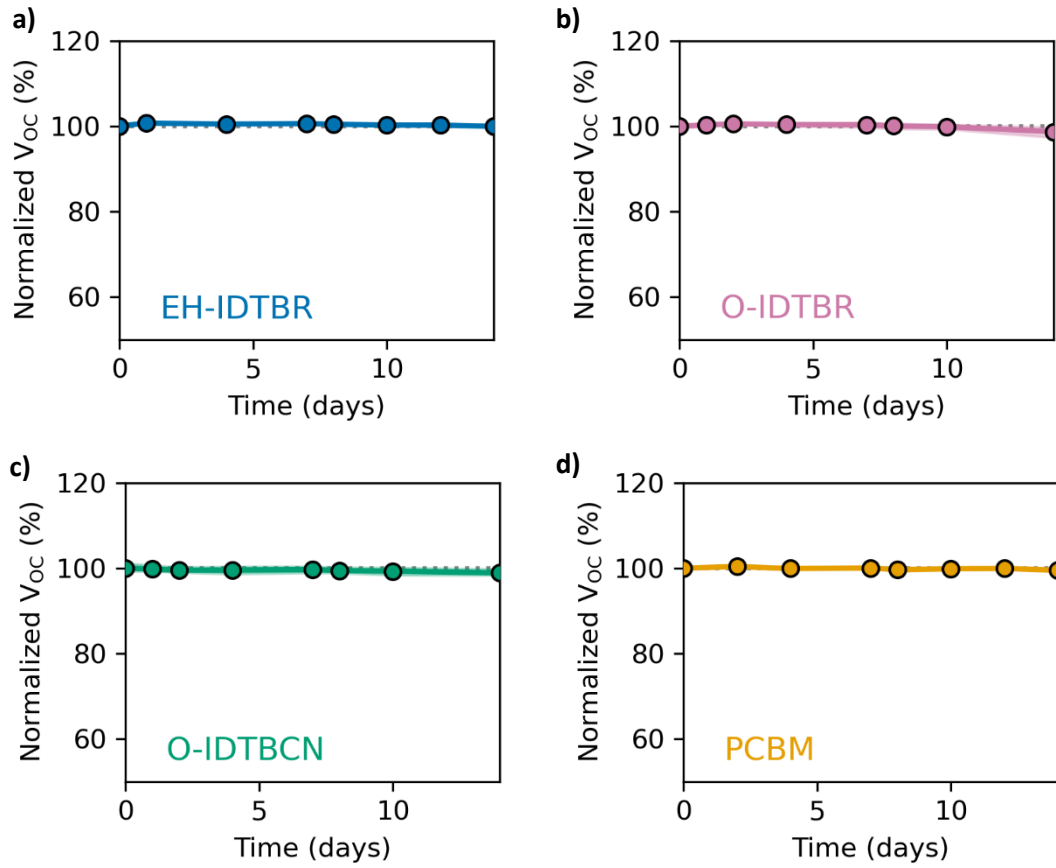


Figure S6.3: V_{oc} over time for cells kept in the dark in an inert atmosphere. Each point represents an average of 3 devices, with the minimum and maximum values covered by the error bar. Annealed samples treated at 80°C for 10 minutes. **a)** PTB7-Th:EH-IDTBR, **b)** PTB7-Th:O-IDTBR, **c)** PTB7-Th:O-IDTBCN, **d)** PTB7-Th:PC₇₀BM.

6.7.2 Example Calculation of χ via Melting Point Depression

The melting point depression of O-IDTBCN is summarised in **Table S6.1**.

Table S6.1: Melting point depression data for addition of PTB7-Th into O-IDTBCN,

$\phi_{polymer}$	Melting point of O-IDTBCN (°C)	$\frac{1}{T_m} - \frac{1}{T_m^0}$ (10^{-4})
0	215	0
0.2	197	4.19
0.3	196	4.42
0.4	193	5.32

This data can then be plotted in the form of **Equation 6.3**, as shown below:

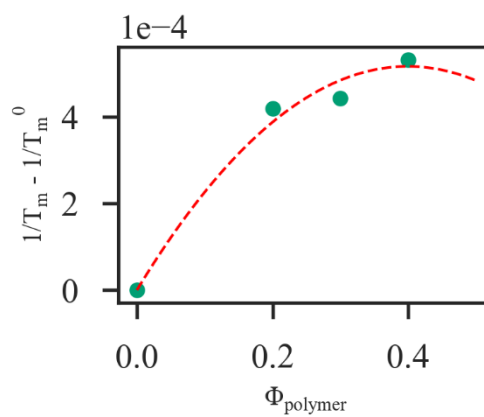


Figure S6.4: Fit of the melting point depression of O-IDTBCN to $y = ax - bx^2$.

From this fit, $a = 2.6 \times 10^{-3}$ and $b = 3.2 \times 10^{-3}$, meaning using **Equation 6.4** yields a χ value of ~ 1.25 .

6.7.3 VLM images

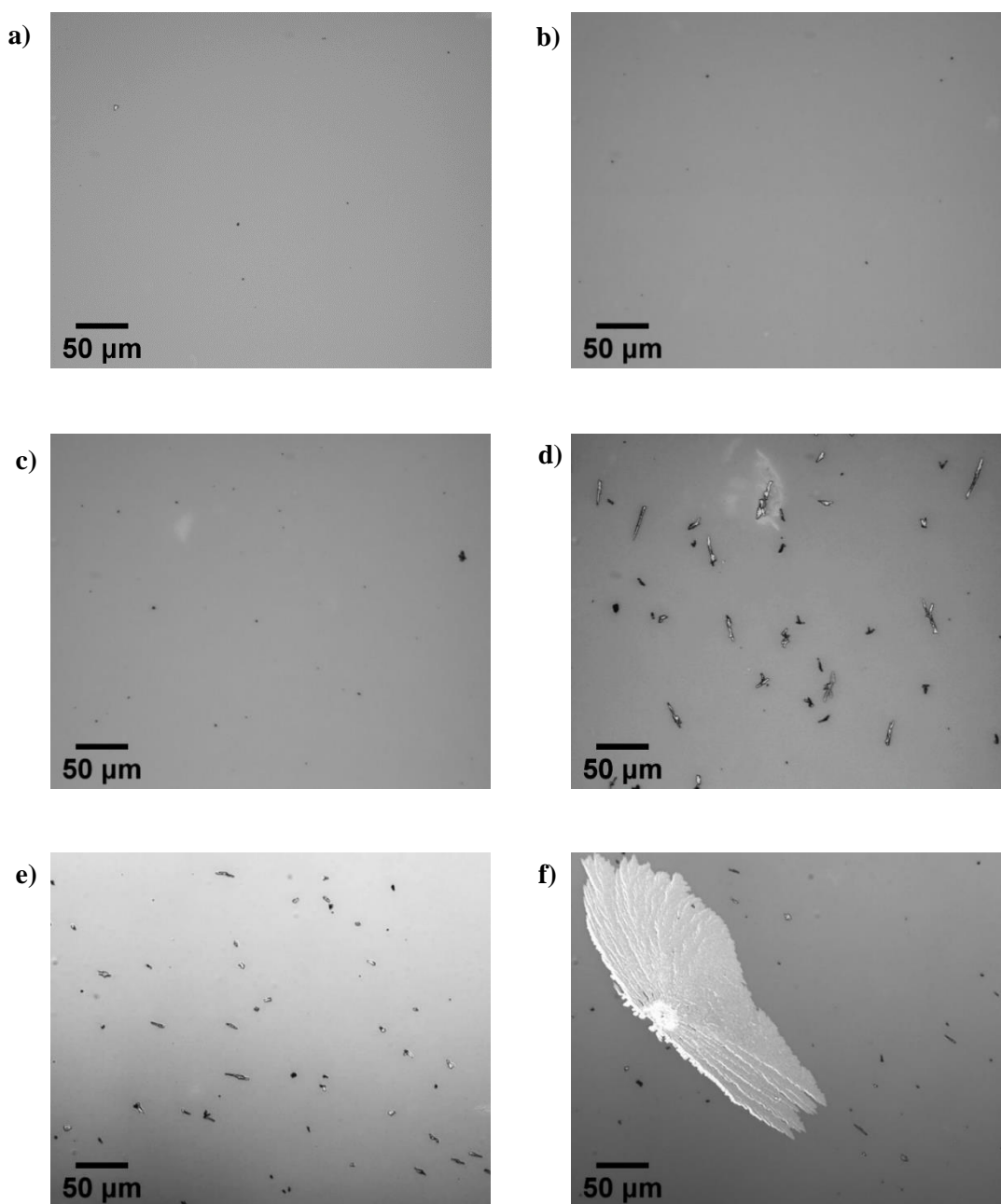


Figure S6.5: *PTB7-Th:EH-IDTBR* films annealed at 140°C for **a)** 48 hours, **b)** 72 hours, **c)** 144 hours, **d)** 168 hours, **e)** 216 hours, **f)** 216 hours, depicting a one of a few large crystals formed.

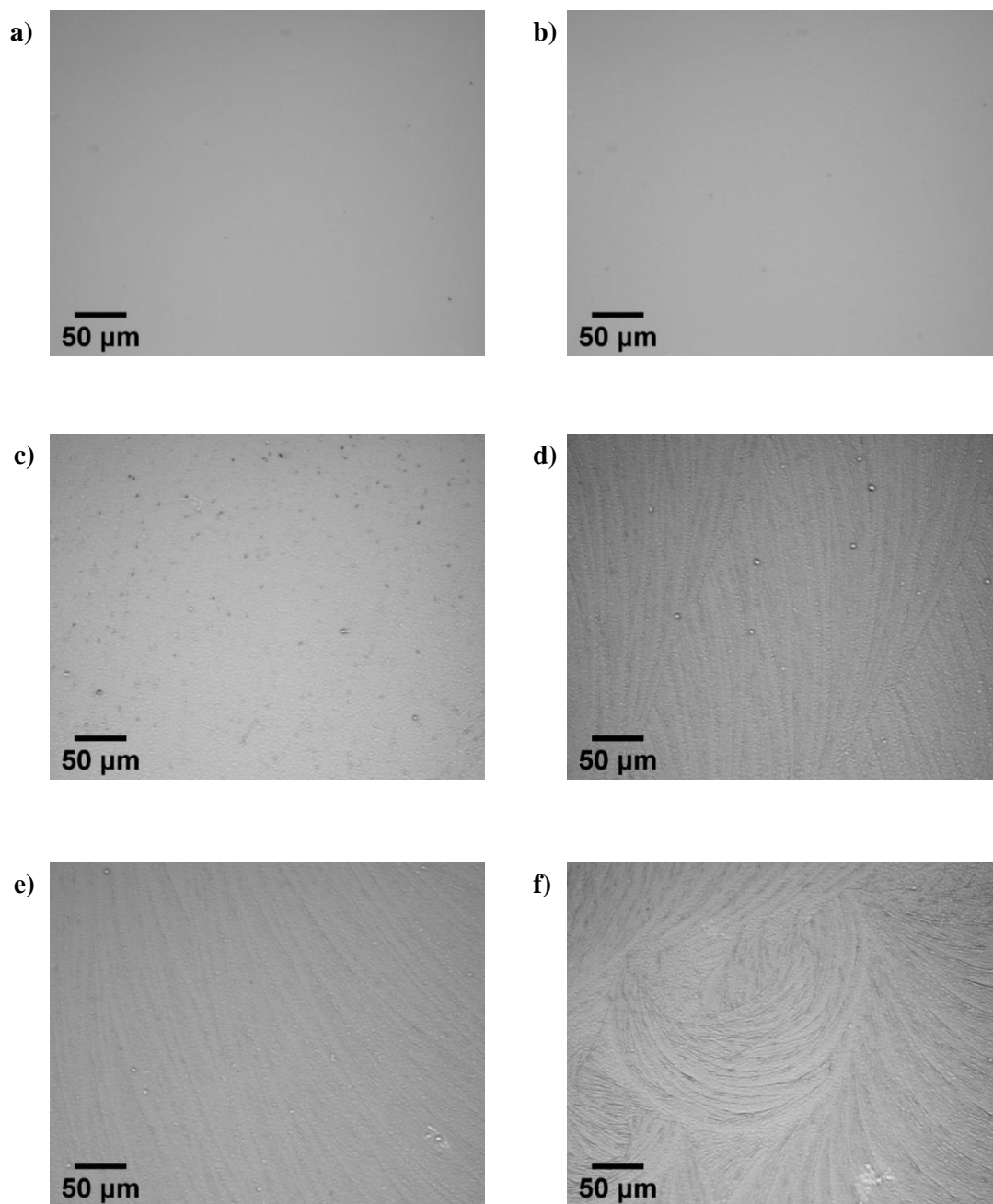


Figure S6.6: *PTB7-Th:EH-IDTBR* films annealed at 160°C for **a)** 5 minutes, **b)** 90 minutes, **c)** 24 hours, **d)** 48 hours, **e)** 72 hours, **f)** 96 hours.

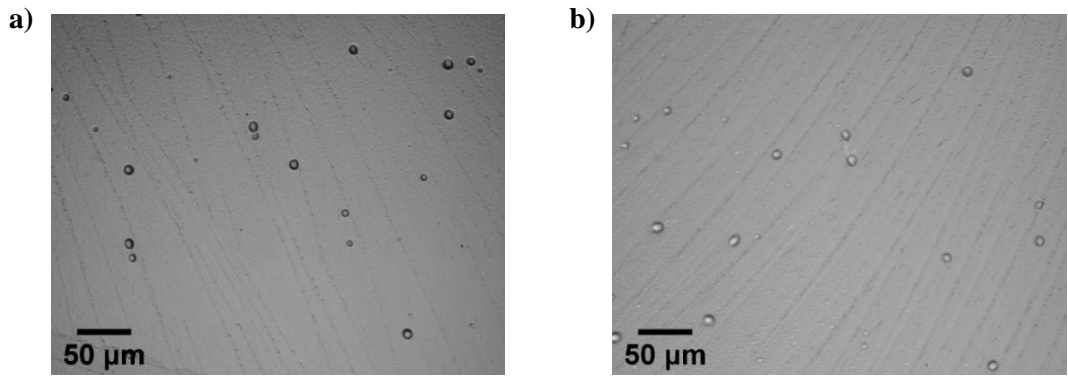


Figure S6.7: PTB7-Th:EH-IDTBR films annealed at 180°C for a) 24 hours, b) 48 hours.

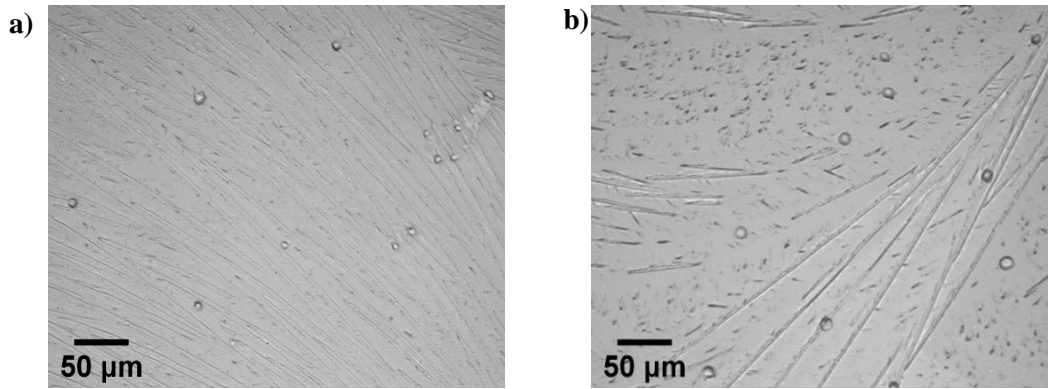


Figure S6.8: PTB7-Th:EH-IDTBR films annealed at 200°C for a) 24 hours, b) 48 hours.

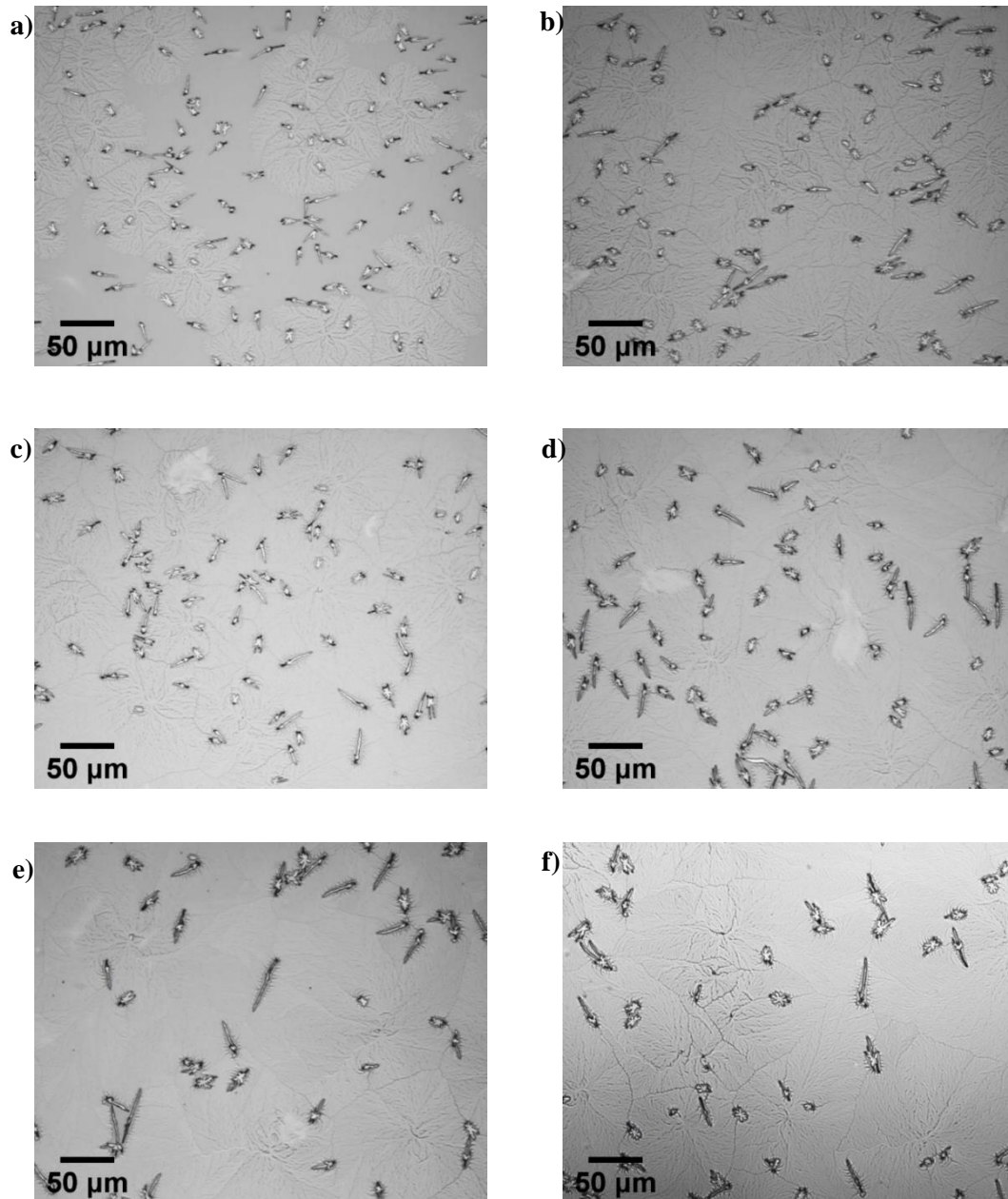


Figure S6.9: PTB7-Th:O-IDTBR films annealed at 140°C for a) 24 hours, b) 48 hours, c) 72 hours, d) 144 hours, e) 168 hours, f) 216 hours.

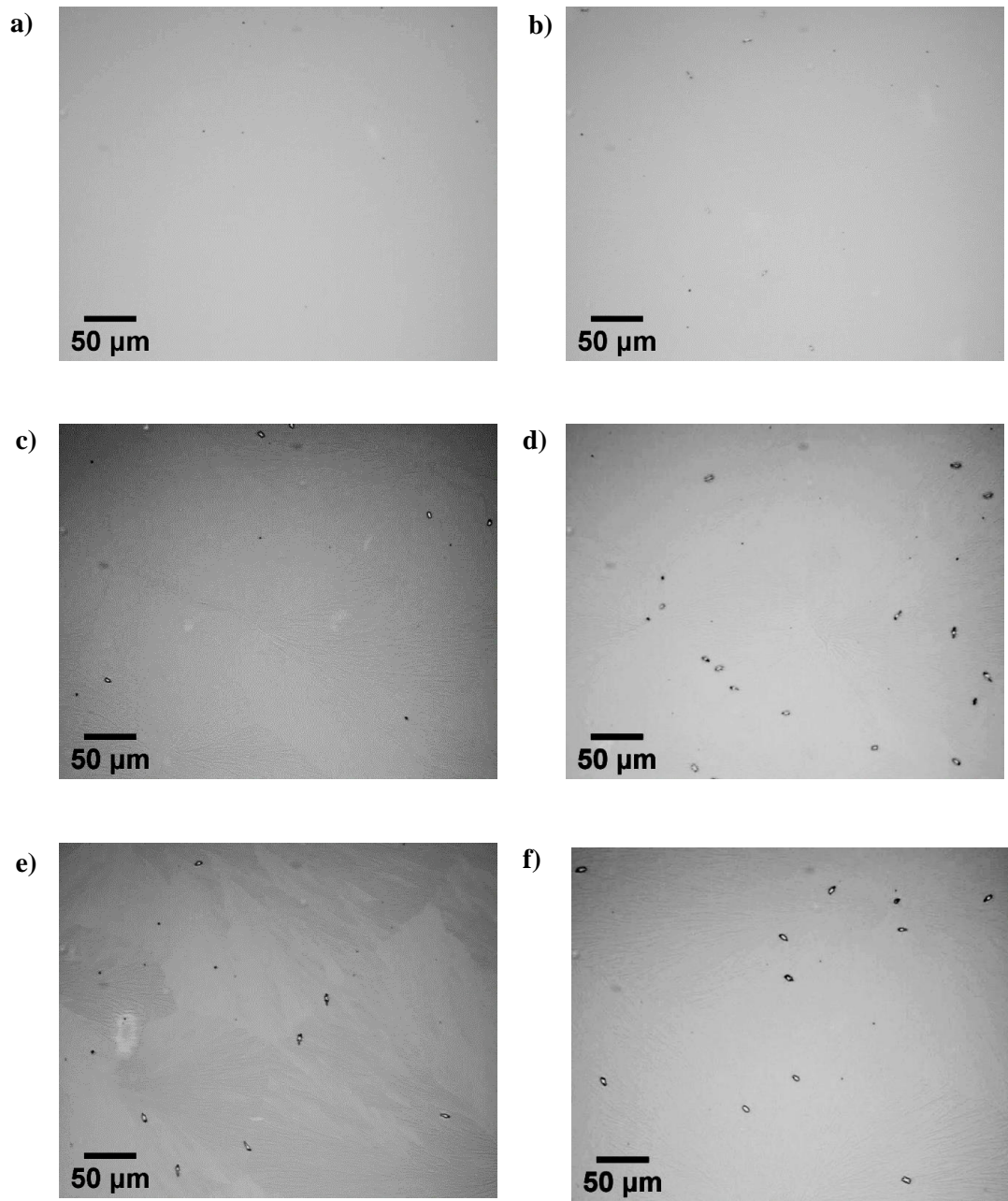


Figure S6.10: PTB7-Th:O-IDTBR films annealed at 160°C for a) 5 minutes, b) 90 minutes, c) 24 hours, d) 48 hours, e) 72 hours, f) 96 hours.

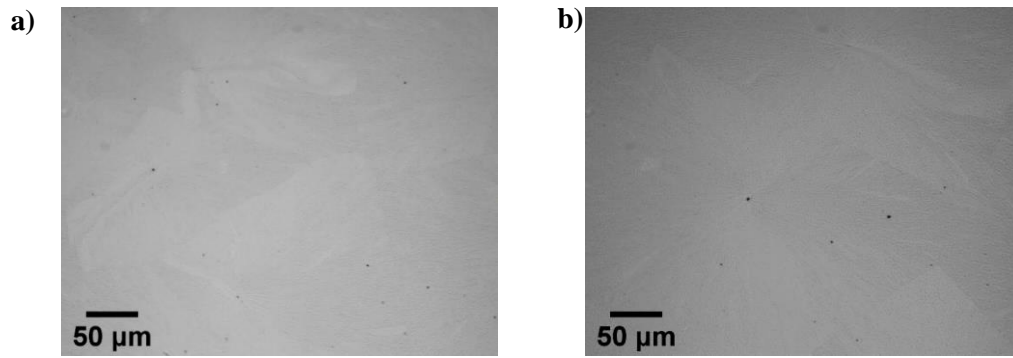


Figure S6.11: PTB7-Th:O-IDTBR films annealed at 180°C for a) 24 hours, b) 48 hours.

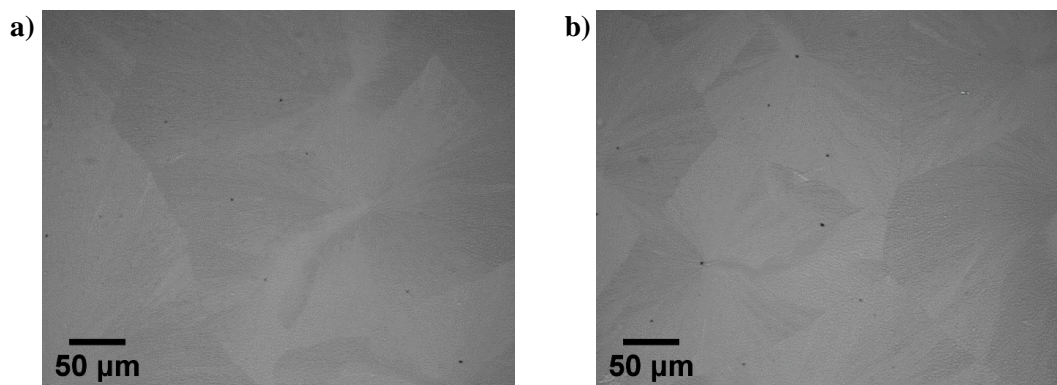


Figure S6.12: PTB7-Th:O-IDTBR films annealed at 200°C for a) 24 hours, b) 48 hours.

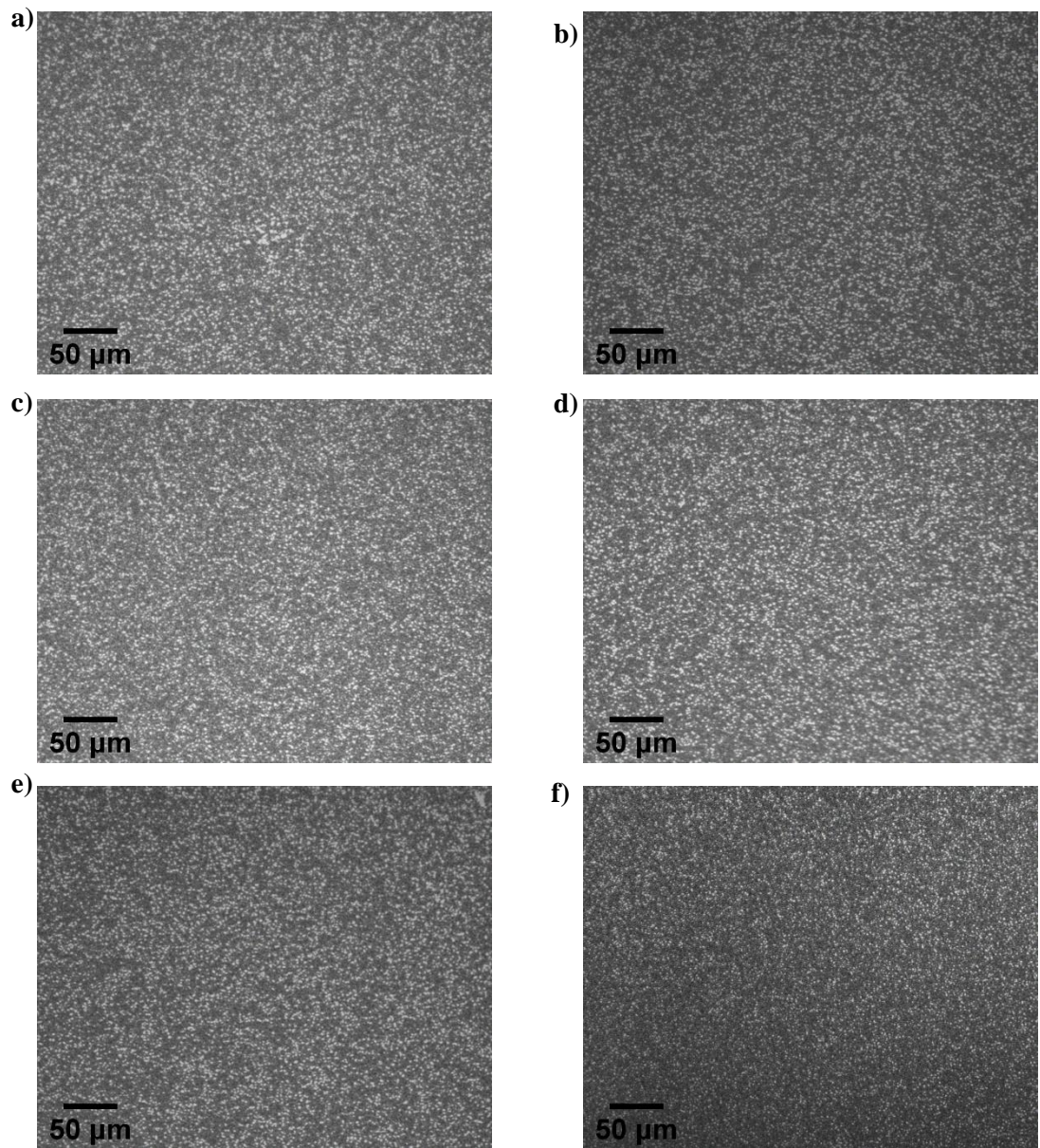


Figure S6.13: PTB7-Th:O-IDTBCN films annealed at 140°C for a) 24 hours, b) 48 hours, c) 72 hours, d) 144 hours, e) 168 hours, f) 216 hours.

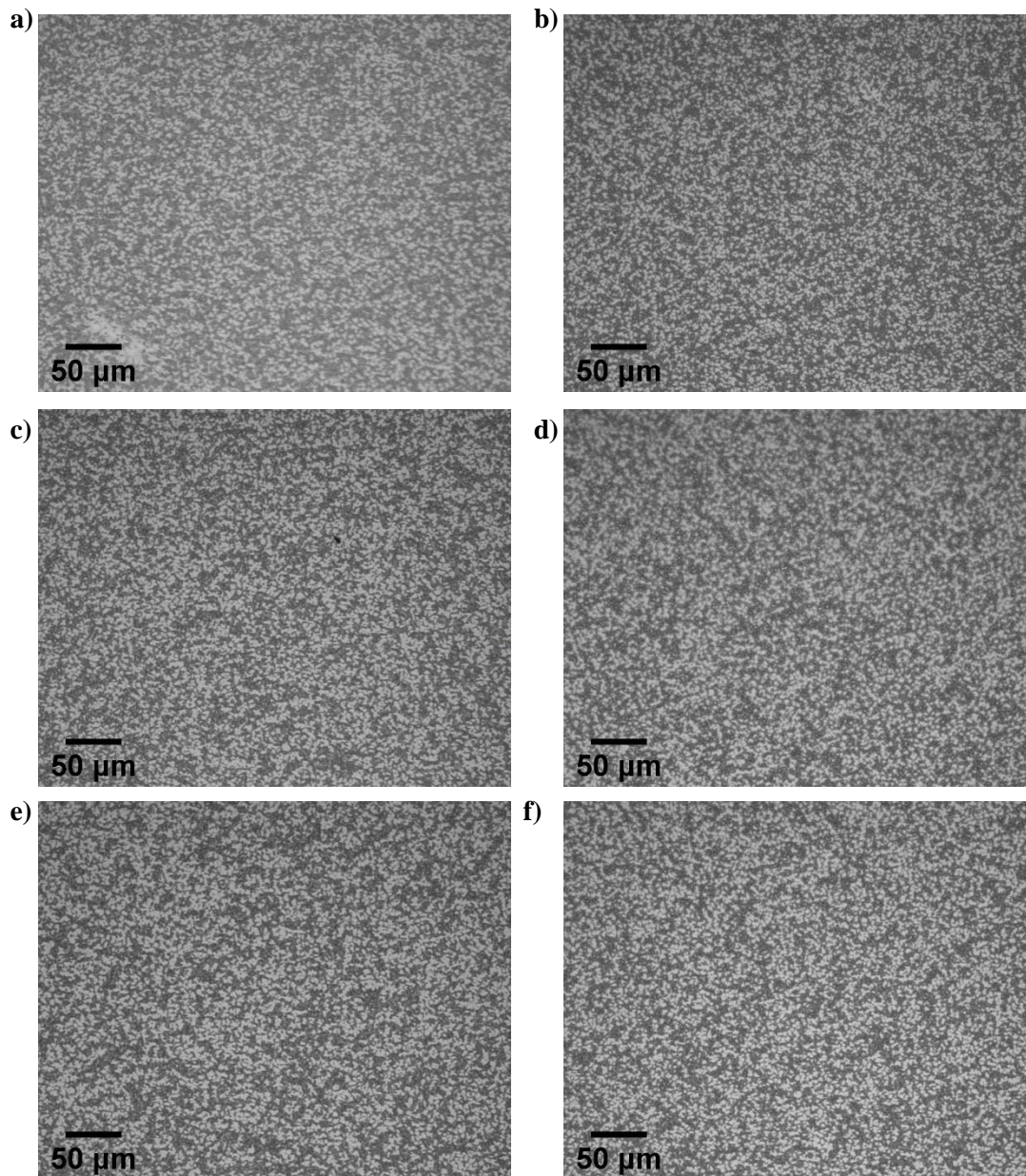


Figure S6.14: PTB7-Th:O-IDTBCN films annealed at 160°C for a) 5 minutes, b) 90 minutes, c) 24 hours, d) 48 hours, e) 72 hours, f) 96 hours.

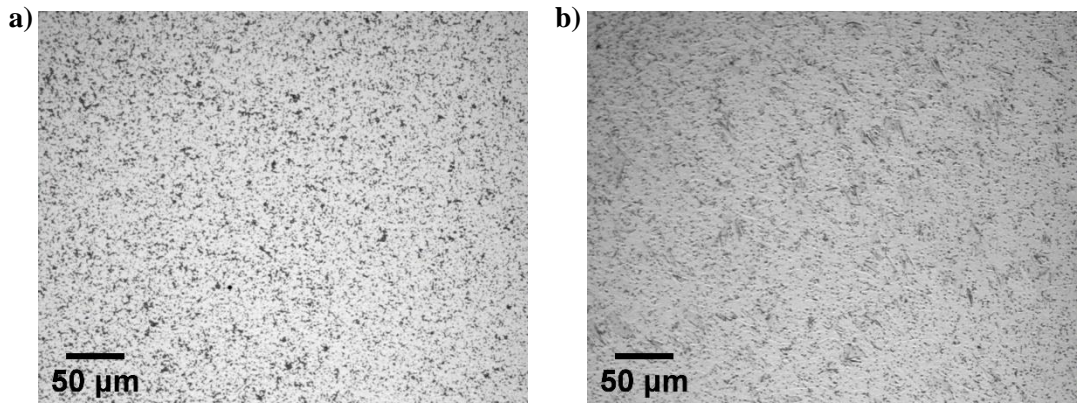


Figure S6.15: PTB7-Th:O-IDTBCN films annealed at 180°C for a) 24 hours, b) 48 hours.

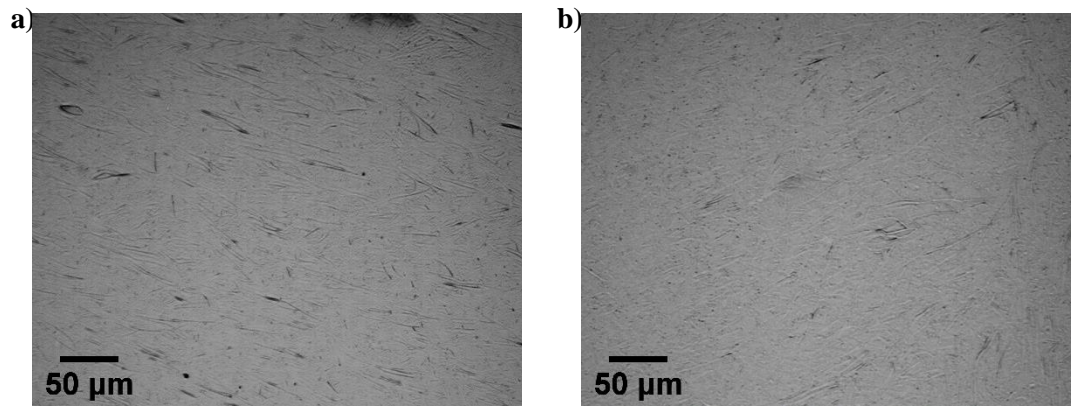


Figure S6.16: PTB7-Th:O-IDTBCN films annealed at 200°C for a) 24 hours, b) 48 hours.

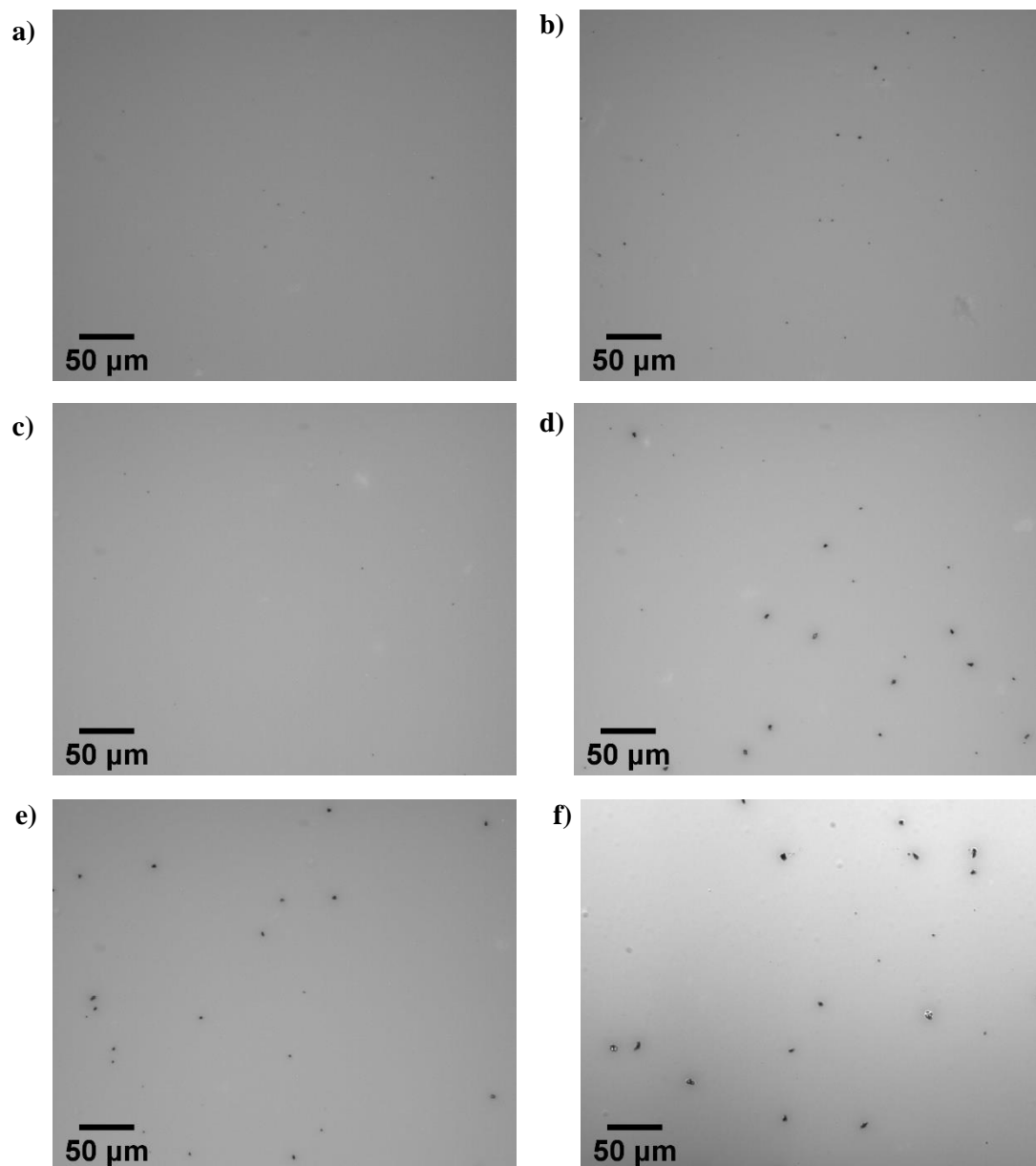


Figure S6.17: PTB7-Th:PCBM films annealed at 140°C for **a)** 24 hours, **b)** 48 hours, **c)** 72 hours, **d)** 144 hours, **e)** 168 hours, **f)** 216 hours.

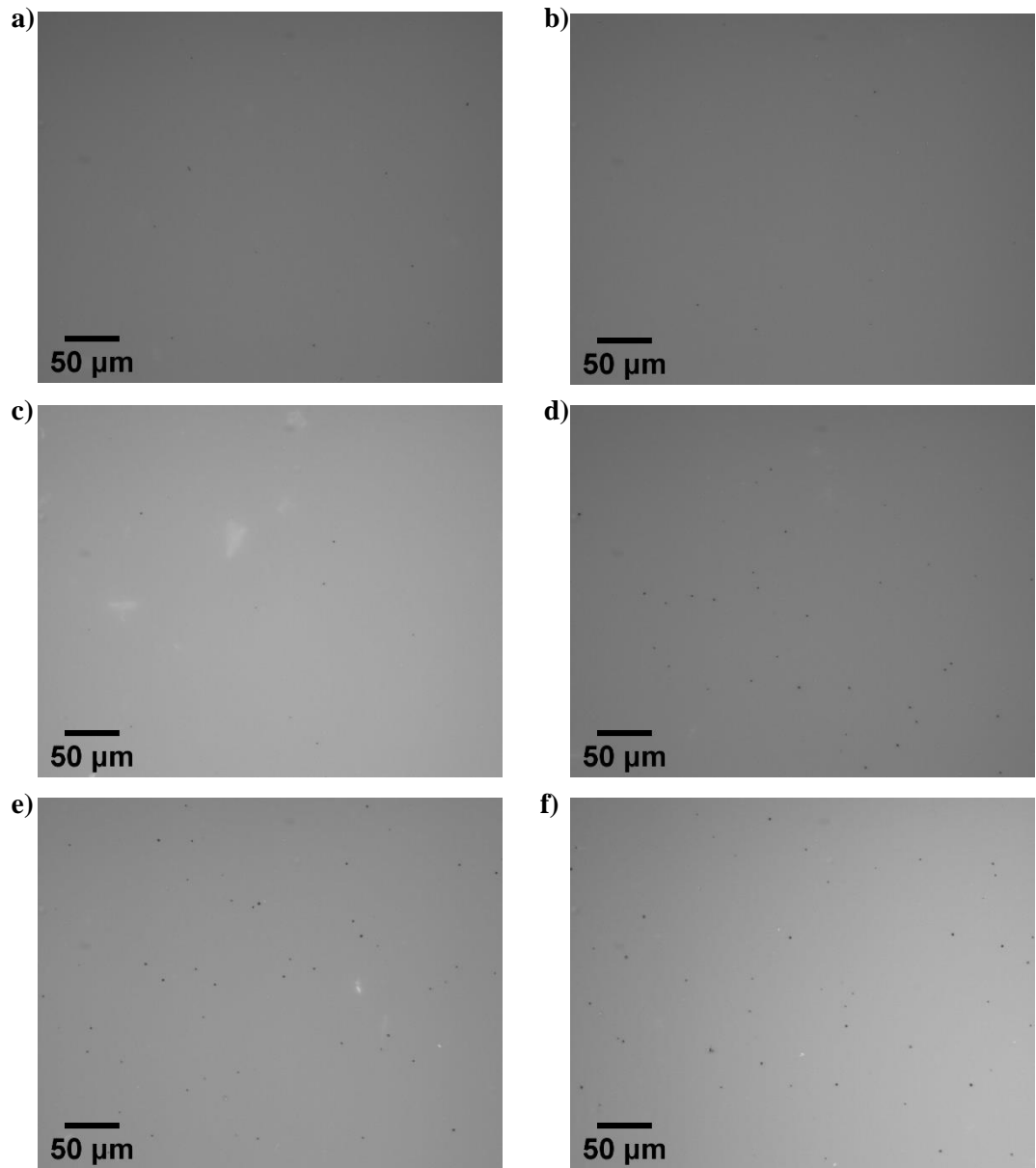


Figure S6.18: *PTB7-Th:PCBM* films annealed at 160°C for **a)** 5 minutes, **b)** 90 minutes, **c)** 24 hours, **d)** 48 hours, **e)** 72 hours, **f)** 96 hours.

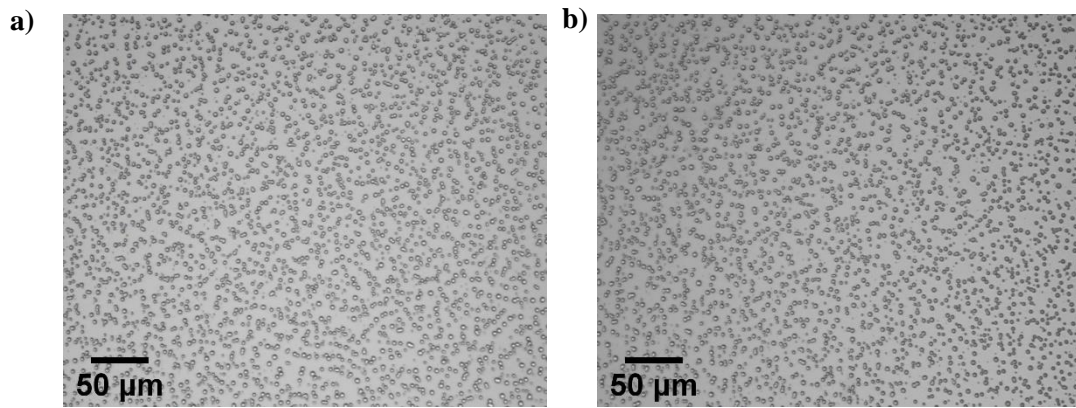


Figure S6.19: PTB7-Th:PCBM films annealed at 180°C for a) 24 hours, b) 48 hours.

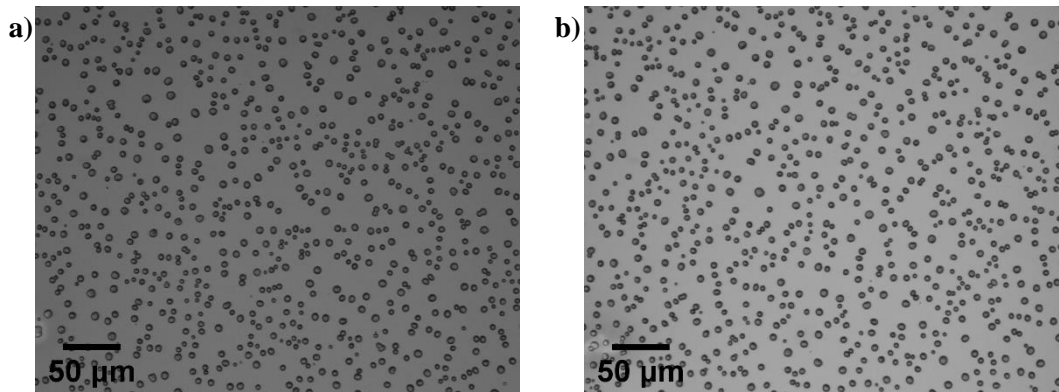


Figure S6.20: PTB7-Th:PCBM films annealed at 200°C for a) 24 hours, b) 48 hours.

6.7.4 Fitting of UV-Vis Spectra

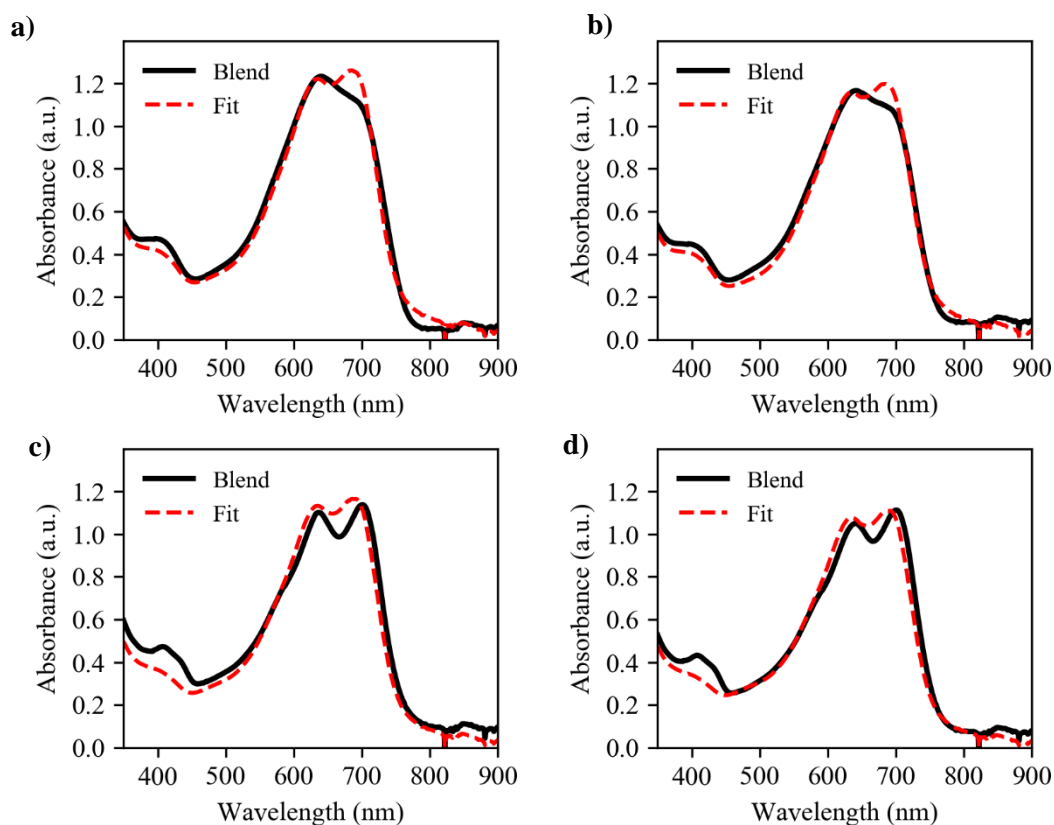


Figure S6.21: Post annealing blends fitted with reference spectra for PTB7-Th:EH-IDTBR blends at **a)** 140°C, **b)** 160°C, **c)** 180°C, **d)** 200°C.

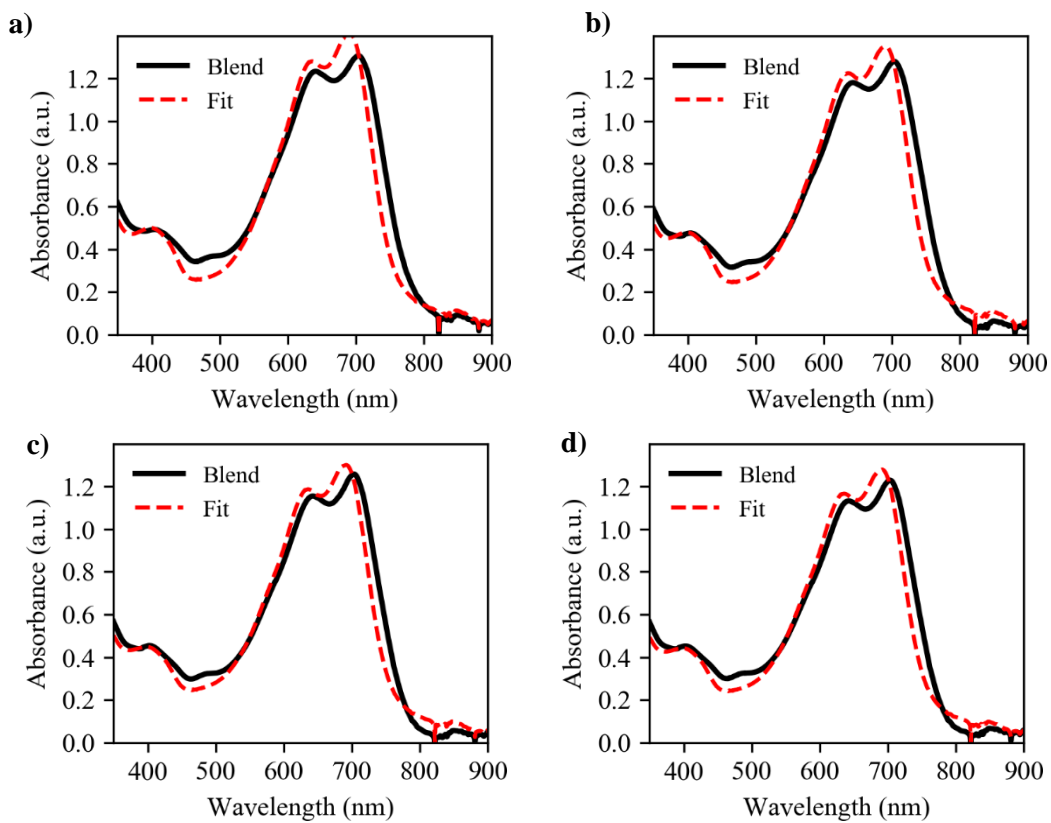


Figure S6.22: Post annealing blends fitted with reference spectra for PTB7-Th:O-IDTBR blends at **a)** 140°C, **b)** 160°C, **c)** 180°C, **d)** 200°C.

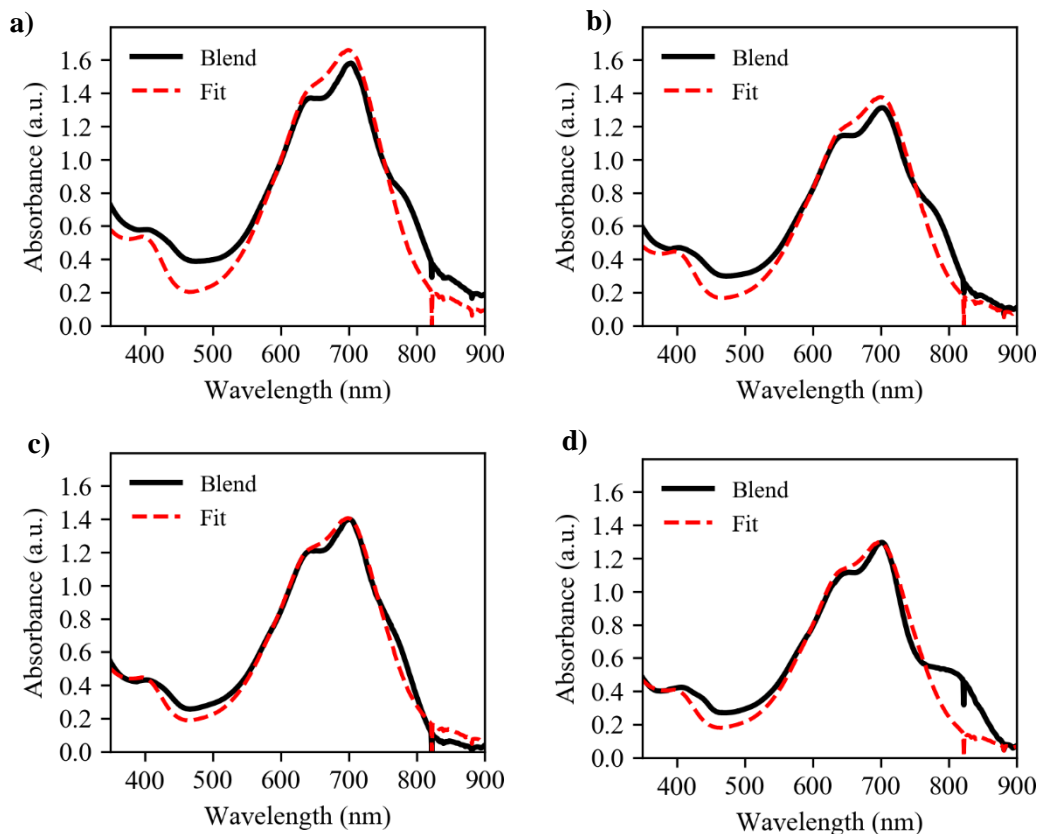


Figure S6.23: Post annealing blends fitted with reference spectra for PTB7-Th:O-IDTBCN blends at **a)** 140°C, **b)** 160°C, **c)** 180°C, **d)** 200°C.

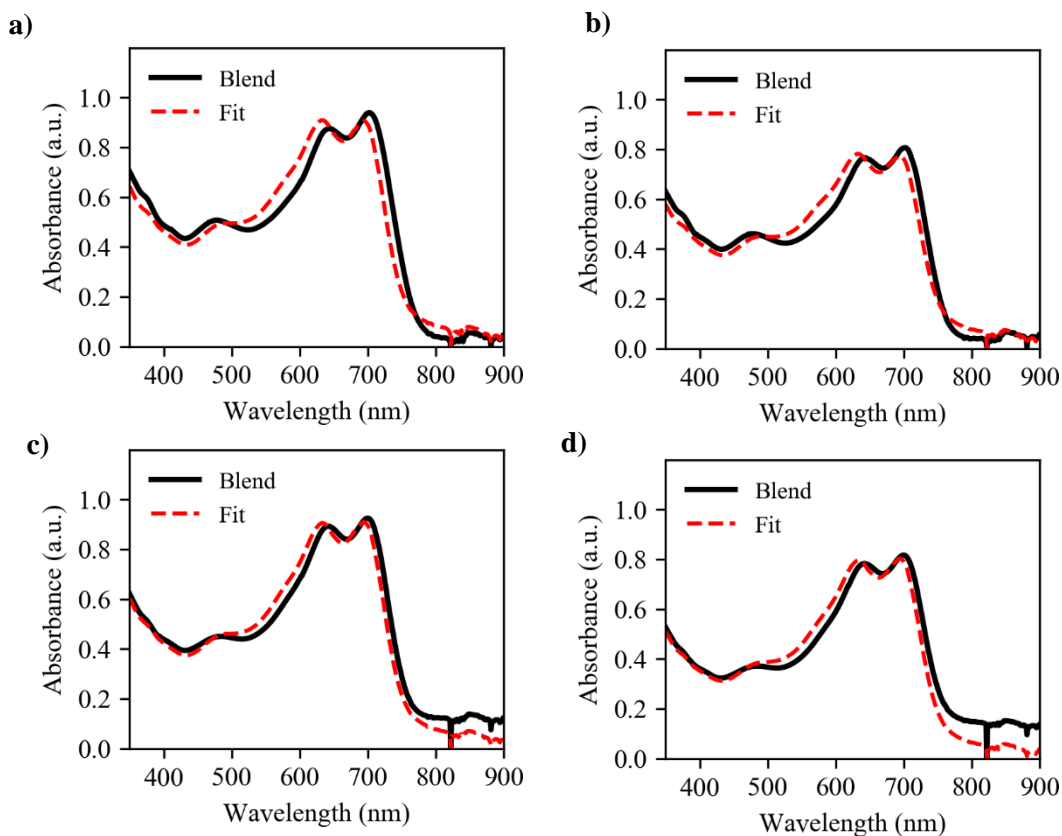


Figure S6.24: Post annealing blends fitted with reference spectra for PTB7-Th:PC₇₀BM blends at **a)** 140°C, **b)** 160°C, **c)** 180°C, **d)** 200°C.

6.8 References

1. Qin, Y. *et al.* The performance-stability conundrum of BTP-based organic solar cells. *Joule* **5**, 2129–2147 (2021).
2. Ghasemi, M. *et al.* Delineation of Thermodynamic and Kinetic Factors that Control Stability in Non-fullerene Organic Solar Cells. *Joule* **3**, 1328–1348 (2019).
3. Ghasemi, M. *et al.* A molecular interaction–diffusion framework for predicting organic solar cell stability. *Nat. Mater.* **20**, 525–532 (2021).
4. Ye, L. *et al.* Miscibility–Function Relations in Organic Solar Cells: Significance of Optimal Miscibility in Relation to Percolation. *Adv. Energy Mater.* **8**, 1–15 (2018).
5. Ye, L. *et al.* Quenching to the Percolation Threshold in Organic Solar Cells. *Joule* **3**, 443–458 (2019).
6. Wadsworth, A. *et al.* End Group Tuning in Acceptor–Donor–Acceptor Nonfullerene Small Molecules for High Fill Factor Organic Solar Cells. *Adv. Funct. Mater.* **29**, 1–8 (2019).
7. Clarke, A. J. *et al.* Non-fullerene acceptor photostability and its impact on organic solar cell lifetime. *Cell Reports Phys. Sci.* **2**, 100498 (2021).
8. Peng, Z. *et al.* Measuring temperature-dependent miscibility for polymer solar cell blends: An easily accessible optical method reveals complex behavior. *Chem. Mater.* **30**, 3943–3951 (2018).
9. Oh, S. *et al.* Enhanced efficiency and stability of PTB7-Th-based multi-non-fullerene solar cells enabled by the structure and energy transfer model. *J. Mat. Chem. A* **7**, 22044–22053 (2019).
10. Pan, L. *et al.* Efficient Organic Ternary Solar Cells Employing Narrow Band Gap Diketopyrrolopyrrole Polymers and Nonfullerene Acceptors. *Chem. Mat.* **32**, 7309–7317 (2020).
11. Zhang, L. *et al.* High Miscibility Compatible with Ordered Molecular Packing Enables an Excellent Efficiency of 16.2% in All-Small-Molecule Organic Solar Cells. *Adv. Mater.* **34**, 2106316 (2022).
12. Li, S. *et al.* Energy-Level Modulation of Small-Molecule Electron Acceptors to Achieve over 12% Efficiency in Polymer Solar Cells. *Adv Mater* **28**, 9423–9429 (2016).
13. Ye, L. *et al.* Quantitative relations between interaction parameter, miscibility and function in organic solar cells. *Nat. Mater.* **17**, 253–260 (2018).
14. Li, Q. *et al.* Impact of Donor–Acceptor Interaction and Solvent Additive on the Vertical Composition Distribution of Bulk Heterojunction Polymer Solar Cells. *ACS Appl. Mater. Interfaces* **11**, 45979–45990 (2019).
15. Dowland, S. A. *et al.* Suppression of Thermally Induced Fullerene Aggregation in Polyfullerene-Based Multiacceptor Organic Solar Cells. *ACS Appl. Mater. Interfaces* **9**, 10971–10982 (2017).
16. Nishi, T. & Wang, T. T. Melting Point Depression and Kinetic Effects of Cooling on Crystallization in Poly(vinylidene fluoride)-Poly(methyl methacrylate) Mixtures. *Macromolecules* **8**, 909–915 (1975).
17. Dyck, O. *et al.* Quantitative phase fraction detection in organic photovoltaic materials through EELS imaging. *Polymers (Basel)*. **7**, 2446–2460 (2015).
18. Hansson, R. *et al.* Vertical and lateral morphology effects on solar cell performance for a thiophene-quinoxaline copolymer:PC70BM blend. *J. Mater. Chem. A* **3**, 6970–6979 (2015).
19. Peng, Z., Balar, N., Ghasemi, M. & Ade, H. Upper and Apparent Lower Critical Solution Temperature Branches in the Phase Diagram of Polymer:Small Molecule Semiconducting Systems. *J. Phys. Chem. Lett.* **12**, 10845–10853 (2021).
20. Liu, F. *et al.* Understanding the morphology of PTB7:PCBM blends in organic photovoltaics. *Adv. Energy Mater.* **4**, 1–9 (2014).
21. Bristow, H. *et al.* Impact of Nonfullerene Acceptor Side Chain Variation on Transistor Mobility. *Adv. Electron. Mater.* **5**, 1–11 (2019).
22. Orwoll, R. A. & Arnold, P. A. Polymer–Solvent Interaction Parameter χ . in *Physical Properties of Polymers Handbook* (ed. Mark, J. E.) 233–257 (Springer New York, 2007).

Chapter 7 | Conclusions and Future Work

7.1 Discussion of Conclusions

In this chapter the previous results chapters are discussed individually. Their conclusions, and how they relate to the aims of this thesis and the wider research field, are examined.

In **Chapter 4**, a method is developed to fabricate a high efficiency OPV using ultrasonic spray coating. Here, an air-knife was used to rapidly dry the film, negating the use of heat or solvent additives. As both of these factors will influence the industrial relevance of a technique, a process without heat or solvent additives is particularly attractive. This work marks a record for spray coated OPV efficiencies, in part due to careful control of the film morphology via use of the air-knife and choice of delay time, solvent identity, and acceptor molecule. Therefore, it fulfils the initial aims set out in the introduction of this thesis to contribute towards improving scalable efficiencies via morphology control.

This work does have several potential areas of improvement. Firstly, the final optimised spray process is far from a perfect recipe. A very specific combination of experimental conditions were required to form efficient devices, and for this process to be commercially viable it would need to be more universally applicable to a range of material and solvent systems. The ‘shearing’ of solution by the air-knife also leads to associated solution loss. Most critically, the final devices showed much greater device variability than spin coated controls. As this variability was attributed to aggregation of the donor polymer, and corresponding trap formation, minimizing air-knife delay time to reduce aggregation would be an important next step. In order for this to still produce high efficiency devices, the solution would have to be optimised for better wetting, potentially using a surfactant, to induce faster coalescence. This faster coalescence would reduce the air-knife delay time required, and also allow less solution to be initially deposited, reducing wastage. Ideally with a better wetting solution the parameter space for good performance would also be wider, making this a truly scalable process.

In the research field as a whole, scalable techniques are most relevant when considering larger areas of coating, as would be required for commercialisation. Therefore, ideally the techniques outlined in this chapter would be applied to larger device areas, for example 1 cm² and over. Currently, research values for large area efficiencies lag behind those of small-scale devices, usually attributed to non-ideal film quality and sheet resistance of electrodes. However, this is a key area of growing research, with recent works showing efficiencies exceeding 13% across a module area over 50 cm².¹ One particular obstacle to

OPV scale up is its typical thickness intolerance, meaning very careful control of parameter space is required. Here, high efficiency Y-series acceptors, as used in this chapter, may hold the key, due to their unusual thickness tolerance. Promisingly, recent records have displayed efficiencies exceeding 10% for 1000 nm thick solar cells, even over an area of 4 cm².² Clearly this is a growing and exciting segment of research, and one that spray coating is well placed to contribute to.

In **Chapter 5**, some of the links between solvent, drying time, and aggregation shown above were focused on more narrowly by examining a new non-fullerene acceptor (NFA) based system. Here the influence of a solvent additive, DIO, and the acceptor identity of a system, on performance, morphology, and device stability, were examined. It was found that non-fullerene acceptor (NFA) based OPVs trapped DIO more significantly than those based on a fullerene acceptor. This trapping contributed to significant and unfavourable aggregation, reducing performance over certain concentrations of solvent additive. Increased solvent additive was also shown to cause increased degradation in NFA based OPVs compared to those based on fullerene, linked again to improper morphology. This work contributes to the initial aims of the thesis by using understanding of morphology to identify factors negatively impacting device performance and stability.

Future work developing these conclusions should explore the influence of a range of solvent additives on a range of NFAs. Additives with different solubilising power for the components, different boiling points, and different impacts on morphology, would all change the outcome of the experiment with interesting results. Elucidating the exact mechanism of DIO trapping would also be noteworthy, as preventing this would be important for commercial scale up of many solvent additive-based systems. Exploring alternatives to high boiling point additives is also likely to be important for the future of OPVs. Significant attention has already been paid to more volatile solvent additives,³ solid solvent additives,⁴ and replacing solvent additives by tuning chemical structure⁵ or other processing conditions.⁶ It is considered likely that for solution processable OPVs to become commercial, solvent additives will have to be replaced completely, due to possible issues with maintaining batch-to-batch consistency with volume contents of only 0.5 – 3%.⁷ Therefore, a useful next step for this work would be to find a scalable method to improving the phase separation in the PBDB-T:ITIC devices, in replacement of DIO. This work provides a useful template of the morphology required, and that to avoid, when tuning for performance.

In **Chapter 6**, the morphological stability discussed in chapter 5 is discussed in greater depth. Here, the morphological stability of a range of NFAs is explored, and linked to their kinetic and miscibility differences. Positive burn-in is found for multiple systems, and is

suggested to occur due to a combination of high donor:acceptor immiscibility, and slow but apparent de-mixing, as a result of specific T_g values. This work illustrates that both kinetic and thermodynamic stability are important when choosing stable OPV systems, factors that will become increasingly important if OPVs are to be commercialised. This chapter compliments the other chapters, and the aims of the thesis by examining phase separation and its causes, and linking this morphology to performance and stability.

Immediate future work in regards to this chapter would involve verifying the calculated Flory-Huggins values using a more established method such as scanning transmission X-ray microscopy (STXM).⁸ Verifying whether the relationships between chemical structure and miscibility exist between other closely related acceptor analogues could also be valuable. On a wider scale, understanding morphological instability, and how it can be prevented, is likely to be vital for the future of OPVs. High efficiency Y-series acceptors have been shown to undergo fast de-mixing in a bulk heterojunction, due to their high Flory-Huggins values and low T_g values.⁹ Therefore, stabilisation of these systems, for example by use of a ternary blend, or tuning to increase Y-series T_g values, is an important next step. Understanding of morphological instability is likely to be furthered by computational methods such as machine learning, allowing for selection of donor:acceptor combinations based on their miscibility and kinetic hindrance.¹⁰

Together, these chapters illustrate the multi-faceted influence of morphology on OPV performance and stability, and reinforce that its control is the keystone to stable and scalable, commercial OPVs. However, there remains significant work to be done before this becomes a reality. Beyond the topics discussed above, key areas of research include reduction in synthetic complexity,¹¹ replacement of brittle and rare ITO,¹² and improving flexible OPV efficiencies.¹³ Whilst it remains to be seen if wide-spread OPV commercialisation will ever take place, small companies such as German based Heliatek have already seen success in niche applications such as building integrated PV (BIPV).¹⁴ From this, and the significant steps taken in recent years in terms of efficiency and stability, there remains hope that OPVs will play some role in our collective quest for net zero.

This research significantly increases our understanding of the impact of morphology on OPVs in a wide range of contexts, and brings the fields one step closer to commercial realisation.

7.2 References

1. Qin, F. *et al.* 54 cm² Large-Area Flexible Organic Solar Modules with Efficiency Above 13%. *Adv. Mater.* **33**, 2103017 (2021).
2. Ma, L. *et al.* High-Efficiency Nonfullerene Organic Solar Cells Enabled by 1000 nm Thick Active Layers with a Low Trap-State Density. *ACS Appl. Mater. Interfaces* **12**, 18777–18784 (2020).
3. Ye, L. *et al.* Ferrocene as a highly volatile solid additive in non-fullerene organic solar cells with enhanced photovoltaic performance. *Energy Environ. Sci.* **13**, 5117–5125 (2020).
4. Lee, D. H. *et al.* Solid-solvent hybrid additive for the simultaneous control of the macro- and micro-morphology in non-fullerene-based organic solar cells. *Nano Energy* **93**, 106878 (2022).
5. Chang, W. H. *et al.* A selenophene containing benzodithiophene- alt -thienothiophene polymer for additive-free high performance solar cell. *Macromolecules* **48**, 562–568 (2015).
6. Zhang, H., Yao, H., Zhao, W., Ye, L. & Hou, J. High-Efficiency Polymer Solar Cells Enabled by Environment-Friendly Single-Solvent Processing. *Adv. Energy Mater.* **6**, 1–6 (2016).
7. McDowell, C., Abdelsamie, M., Toney, M. F. & Bazan, G. C. Solvent Additives: Key Morphology-Directing Agents for Solution-Processed Organic Solar Cells. *Adv. Mater.* **30**, 1707114 (2018).
8. Peng, Z. *et al.* Measuring temperature-dependent miscibility for polymer solar cell blends: An easily accessible optical method reveals complex behavior. *Chem. Mater.* **30**, 3943–3951 (2018).
9. Qin, Y. *et al.* The performance-stability conundrum of BTP-based organic solar cells. *Joule* **5**, 2129–2147 (2021).
10. Mahmood, A., Irfan, A. & Wang, J. L. Machine learning and molecular dynamics simulation-assisted evolutionary design and discovery pipeline to screen efficient small molecule acceptors for PTB7-Th-based organic solar cells with over 15% efficiency. *J. Mater. Chem. A* **10**, 4170–4180 (2022).
11. Yu, Z. P. *et al.* Simple non-fused electron acceptors for efficient and stable organic solar cells. *Nat. Commun.* **10**, 1–9 (2019).
12. Guo, J. & Min, J. A Cost Analysis of Fully Solution-Processed ITO-Free Organic Solar Modules. *Adv. Energy Mater.* **9**, 1–9 (2019).
13. Fukuda, K., Yu, K. & Someya, T. The Future of Flexible Organic Solar Cells. *Adv. Energy Mater.* **10**, 1–10 (2020).
14. Solar films on a round heat storage of a heat power plant in Marburg *Heliatek* <https://www.heliatek.com/en/news/detail/solar-films-on-a-round-heat-storage-of-a-heat-power-plant-in-marburg/> (2021, accessed June 2022).